Coulomb interaction and electronic quantum coherence in solid-state interferometers

Hadrien Duprez

Université de Paris

Ecole doctorale n°564 Physique en Île-de-France (EDPIF)

Centre de Nanosciences et de Nanotechnologies (C2N) - CNRS

Coulomb interaction and electronic quantum coherence in solid-state interferometers

par

Hadrien Duprez

Thèse de doctorat en spécialité de Physique, dirigée par Anne Anthore et Frédéric Pierre,
présentée et soutenue publiquement à Palaiseau le 16 décembre 2020

Devant un jury composé de :

Christopher Bäuerle – Directeur de recherche Institut Néel, CNRS	Rapporteur
Xavier Waintal – Directeur de recherche Quantum Photonics Electronics and Engineering Laboratory, CEA Grenoble	Rapporteur
Mitali Banerjee – Professeure assistante École Polytechnique Fédérale de Lausanne	Examinatrice
Piet Brouwer – Professeur Université Libre de Berlin	Examinateur
Patrice Roche – Directeur de Recherche Service de Physique de l'État Condensé, CEA Saclay	Président du Jury, Examinateur
Anne Anthore – Enseignante-chercheuse Université de Paris	Co-directrice
Frédéric Pierre – Directeur de Recherche Centre de Nanosciences et Nanotechnologies, CNRS	Co-directeur

Titre : *Interaction de Coulomb et cohérence quantique dans des interféromètres électroniques*

Résumé :

Le transport électronique dans les circuits de petites dimensions et plongés à basse température sont gouvernés par les lois de la mécanique quantique, pour lesquelles la nature ondulatoire des électrons ne peut être ignorée. Les effets qui en résultent sont bien expliqués lorsque le transport électronique est exprimé en termes de canaux de conductions élémentaires, analogues aux modes optiques dans un guide d'onde. Les canaux de Hall quantiques sont une implémentation directe de ce type de canaux électroniques et constituent par conséquent une plateforme de choix pour l'étude du transport électrique à un niveau fondamental. Notamment, ils peuvent être utilisés pour fabriquer des interféromètres électroniques, et en particulier, l'analogue de l'interféromètre de Mach-Zehnder, qui entre autres réalisations, illustre une route prometteuse vers la réplication d'expériences d'optique quantique avec des électrons. Une différence cruciale avec l'optique gît cependant dans l'interaction coulombienne, omniprésente dans les circuits électroniques et qui à la fois limite la cohérence quantique des électrons, et fait émerger des phénomènes corrélés exotiques.

Dans cette thèse, des canaux de Hall ont été agencés dans une géométrie de Mach-Zehnder afin d'observer les effets de l'interaction coulombienne sur la cohérence quantique. Les résultats obtenus se scindent en deux volets. Premièrement, il est démontré l'efficacité d'une stratégie basée sur la suppression du couplage entre canaux médié par l'interaction de Coulomb, dans le but d'augmenter la longueur de cohérence quantique. Il en résulte une longueur de cohérence augmentée de plus d'un ordre de grandeur, atteignant la longueur macroscopique de 0.25mm, une longueur visible à l'œil nu, à basse température (10mK). Dans une seconde expérience, un îlot métallique est introduit sur l'un des deux chemins d'un interféromètre électronique de Mach-Zehnder. Un électron est retenu au cœur d'un tel îlot bien plus longtemps que son temps quantique, ce qui empêche normalement toute propagation cohérente d'électrons le traversant. Cependant, lorsqu'un seul canal électronique est connecté à un tel îlot et que la capacitance de celui-ci est suffisamment petite pour geler toute fluctuation de sa charge globale, une transmission parfaite de l'état quantique des électrons à travers l'îlot est prédite. Cette prédiction contre-intuitive fut expérimentalement démontrée au cours de cette thèse. Alors que le premier résultat illustre comment l'interaction coulombienne peut être nuisible à la cohérence quantique des électrons, le second montre au contraire comment cette interaction de Coulomb peut être exploitée pour préserver la cohérence quantique.

Mots clefs :

Physique de l'état condensé, physique mésoscopique, transport quantique, interférences quantiques, effet Aharonov-Bohm, cohérence quantique, interaction de Coulomb, effet Hall quantique, optique quantique électronique

Title : *Coulomb interaction and electronic quantum coherence in solid-state interferometers*

Abstract :

Electronic transport in low temperature and low scale solid-state devices is governed by the laws of quantum mechanics. In this regime, the wavelike nature of electrons is prominent. The resulting effects are well explained when electronic transport is expressed in terms of elementary conductive channels. These are analogous to optical modes in a waveguide. Quantum Hall edge channels are a direct implementation of such electronic channels and consequently are a platform of choice to study electrical transport at the fundamental level. Notably, they can be used to implement electronic interferometers and in particular, the analogue of a Mach-Zehnder interferometer. Among other realizations, such devices draw a promising route toward reproducing quantum optics experiments with electrons. A crucial difference with optics is that Coulomb interaction is ubiquitous in electronic circuits, which both limits the electron quantum coherence and gives rise to exotic correlated phenomena.

In this thesis, quantum Hall edge channels were arranged in a Mach-Zehnder geometry to study the effect of Coulomb interaction on the electronic quantum coherence. The obtained results are two-fold. First, a strategy based on the suppression of the Coulomb mediated coupling between co-propagating edge channels to highly increase the coherence length was demonstrated. The resulting observed coherence length was enhanced by over one order of magnitude, reaching a macroscopic length of 0.25 mm, a distance distinguishable with the naked eye, at low temperature (10 mK). In a second experiment, a small metallic island was introduced on one of the two paths of an electronic Mach-Zehnder interferometer. An electron remains within such an island much longer than its quantum lifetime, which normally prohibits any quantum coherent propagation of electrons across it. However, it was strikingly predicted that a perfect transmission of the electron quantum state across the island can be achieved when two conditions are fulfilled. First, a single channel has to be connected to this island, and second, the latter's capacitance needs to be small enough to freeze any fluctuation of its global charge. This regime was experimentally achieved for the first time in this thesis, demonstrating the validity of the aforementioned prediction.

While the first result illustrates how Coulomb interaction can be detrimental to quantum coherence, the second one, on the contrary, shows that it can be harnessed to preserve quantum coherence.

Keywords :

Condensed Matter Physics, mesoscopic physics, quantum transport, quantum interference, Aharonov-Bohm effect, quantum coherence, Coulomb interaction, quantum Hall effect, electron quantum optics

Contents

List of abreviations

Abreviation	Meaning
2DEG	Two-Dimensional Electron Gas
AB	Aharonov-Bohm
AL	Anderson Localization
FPI	Fabry-Perot Interferometer
HBT	Hanburry-Brown-Twiss
HOM	Hong-Ou-Mandel
MZI	Mach-Zehnder Interferometer
QH	Quantum Hall
QPC	Quantum Point Contact
TL(L)	Tomonaga-Luttinger (Liquid)
UCF	Universal Conductance Fluctuations
WL	Weak Localization

List of recurrent notations

Notation	Designation
$\mathcal{A}$	Interferometer area
B	Magnetic field
e	Elementary charge
E_F	Fermi energy
G	Conductance
h	Planck constant
$\mathcal{H}$	Hamiltonian
k_B	Boltzmann constant
l	Elastic mean free path
L	Device length
L_ϕ	Coherence length
R_K	Klitzing quantum of resistance ($= h/e^2$)
v_F	Fermi velocity
v_d	QH drift velocity
$\mathcal{V}$	Visibility
S	Current noise
Δ	Energy level separation (for a quantum dot or a metallic island)
$\hat{\phi}$	Bosonic operator
$\hat{\psi}$	Fermionic operator
ψ	Wavefunction
ρ	Electronic density
$\rho(x)$	Local density fluctuation operator
μ_e	Electronic mobility
ν	Filling factor
τ	Transmission probability
τ_ϕ	Coherence time

Introduction

Electrons are particles that behave according to the laws of quantum mechanics. As such, they also have a wavelike nature, which can give rise to interference phenomena. However, observing this quantum behaviour requires that the coherence of particles — including their wave character — is preserved along their path. In practice, electrons interact with their surroundings, potentially leading to decoherence — and consequently the loss of their wavelike character. That is especially true in solid-state circuits, where interactions can couple electrons to external degrees of freedom on numerous occasions. In particular, Coulomb interaction is unavoidable between the numerous electrons in solid-state systems, and due to its long-range attribute is generally the number one culprit for decoherence effects. For instance, in normal metals, at low temperature, it is well established that electron-electron interaction is the dominant decoherence mechanism. However, in such materials, the observed interferences are due to many different electron paths. Since about two decades, it is possible to fabricate electronic circuits with electrons guided along only a few, and even down to one, well-controlled paths. These make it possible to study and control the transport of electrons at the most fundamental level of a single transport channel. The two experimental works presented in this manuscript make use of such circuits, and reveal that Coulomb interaction can have two antagonistic effects on electron quantum coherence: it can either lead to its suppression or, more surprisingly, to its protection.

Before jumping to the obtained experimental results, this introductory chapter first skims through the concept of interferences. Then, it gives some examples of the manifestations of the wave-like nature of electrons, shortly presents the field of 'electron quantum optics' and highlights two Coulomb effects that are tightly related to each of both works further detailed in this manuscript. Finally, the concept of coherence is introduced more formally.

Interferences and the Aharonov-Bohm effect

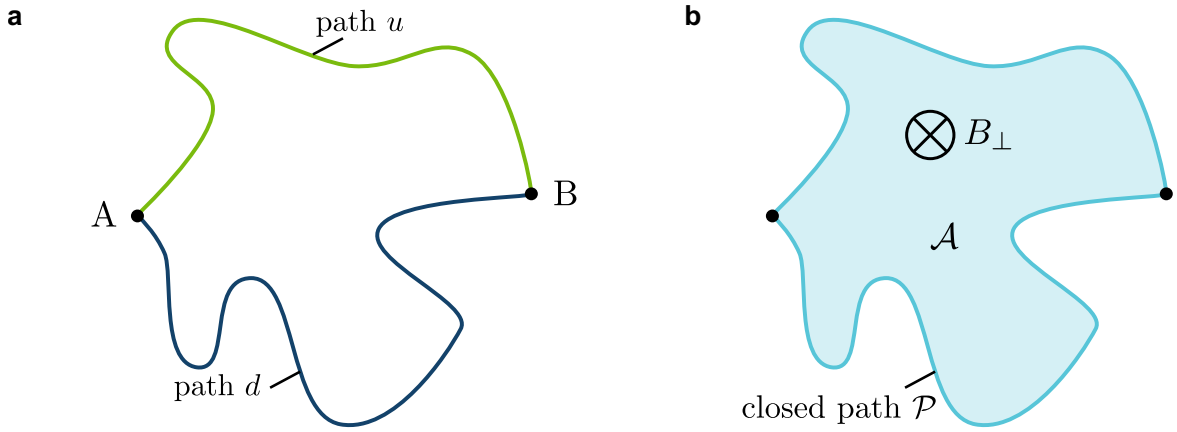

Figure 1: **a** Schematic of an initial wavefunction $|\psi_\mathrm{A}\rangle$ that splits in two at some point of space and time, these two parts are further recombined after each acquiring a path-dependent phase. **b** The Aharonov-Bohm, geometric phase acquired along a closed path $\mathcal{P}$ depends on the magnetic flux $\mathcal{A}B_\perp$ threading the area $\mathcal{A}$ perpendicular to the magnetic field $B_\perp$.

To illustrate what interferences are, we take the simplest example possible. Suppose that to go from point A to B, an electron can follow two distinct and independent paths u or d as sketched in figure 1 a. The probability amplitude associated to each path is of the form

$$a_{u,d} = A_{u,d} e^{i\phi_{u,d}} \tag{1}$$

and the probability for an electron to transfer from point A to point B is given by

$$P_{\mathrm{A}\to\mathrm{B}} = \sum_{i,j} a_i^* a_j = |A_u|^2 + |A_d|^2 + 2\mathrm{Re}\{A_u^* A_d e^{i(\phi_u - \phi_d)}\} \tag{2}$$

where the first two terms together represent the classical probability of transmission for the electron from A to B and the third term is the quantum interference term. The probability of finding the electron at point B therefore oscillates sinusoidally as a function of the phase difference between the two paths. This remains true as long as coherence is preserved.

A simple way to modify the phase difference between both paths is to take advantage of the Aharonov-Bohm effect. First outlined by W. Ehrenberg and R. Siday [1], and then explained more explicitly by Y. Aharonov and D. Bohm [2], this effect implies that the wavefunction of particles with a charge q will acquire a phase ϕ along a closed path $\mathcal{P}$ according to

$$\phi = \frac{q}{\hbar} \oint_{\mathcal{P}} (-V dt + \mathbf{A} \cdot d\mathbf{x}) \tag{3}$$

where V and $\mathbf{A}$ are the scalar and vector potentials respectively (from which are defined the electric and magnetic field). In practice, only the magnetic part of this effect is used (the second term in equation 3). It can be re-expressed in terms of the area enclosed in

the closed path $\mathcal{A}$ and the component of the magnetic field perpendicular to this area $B_\perp$ as illustrated in figure 1 b

$$\phi = \frac{q}{\hbar}\mathcal{A} \times B_\perp$$

Manifestations of electron coherence

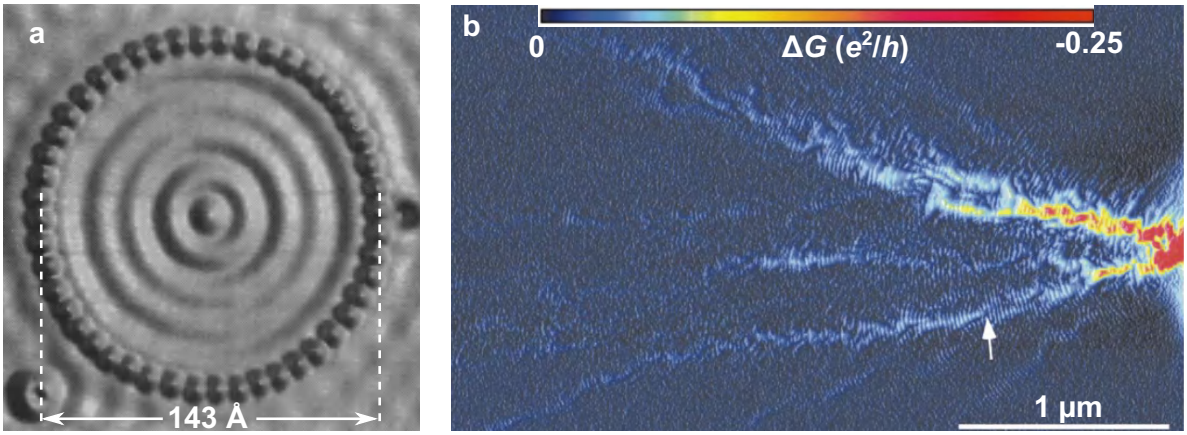

Figure 2: Electronic quantum ripples. **a** Scanning Tunneling Microscopy (STM) image of an atomic corral formed from 48 iron atoms on top of a copper (111) surface. The ripples observed are due to the distribution of electronic states within the corral (taken from [3]). **b** Scanning Gate Microscopy (SGM) image of the branched flow through a QPC. The small observable ripples are due to interferences of several electron paths (taken from [4]).

The wave-like nature of electrons was ascertained by a collection of experiments. Each of these observations involved at least two electron paths, so that the coherence was preserved at least at the scale of these paths. The first to demonstrate the wavelike nature of electrons was the 1927 Davisson & Germer experiment [5,6], where they observed that the diffraction pattern of electrons on a Nickel crystal resembled that of X-rays, in agreement with de Broglie's prediction that particles should also show a wave-like behaviour [7]. A similar demonstration of the electron's wave character is the Feynman-Young double slit experiment [8], which was reproduced several times, using either a bi-prism [9–11], or more recently, a true double slit [12,13]. In solid-state, it was observed in the famous atomic corral formed from iron atoms at the surface of copper [3], and where the electronic surface states formed the beautiful symmetric pattern shown in figure 2 a. It was also possible to see similar ripples in the transmission of a quantum point contact [4], where the branched flow of electrical current is governed by the impurities on the way, which also cause interferences as can be seen in figure 2 b. There are other markers of the electron wave-like nature in solid-state systems, although less visually appealing. These can show in transport measurements such as the Altshuler-Aronov-Spivak effect, weak-localization magnetoresistance or universal conductance fluctuations. They can also show up in the system's magnetization as for persistent currents in metals or the Landau diamagnetism. These evidences are described in further details in section 1.2.

Electron quantum optics

More recently, circuits with an essentially total control over the electrons' trajectory, becoming more and more common, have enabled refined experiments exploiting their quantum coherence. These experiments fall within the field of 'electron quantum optics', that is briefly reviewed here (a more complete review is accomplished in sections 2.2, 3.2). This analogy between optics and electronics makes sense first and foremost because there is a set of essential components such as sources, beam splitters, and waveguides that have their electronic counterparts. Specifically, this manuscript focuses on electronic waveguides that can be achieved by plunging a two-dimensional electron gas in a large perpendicular magnetic field, to reach the Quantum Hall (QH) regime. Another possibility is to use channels defined by lateral confinement without the need of a magnetic field (as e.g. [14]). QH edge channels are very convenient as they provide electron waveguides topologically protected from backscattering. A series of experiments in electron quantum optics consisted in making electronic versions of Fabry-Perot [15–19] and Mach-Zehnder [20,21] interferometers, and in reproducing emblematic quantum optics experiments such as Hanburry-Brown-Twiss [22] or Hong-Ou-Mandel [23,24] interferometry. Nonetheless, this field extends beyond a mere reproduction of quantum optics experiments with electrons, as the Coulomb interaction, inexistent for photons, is ubiquitous in solid-state systems and gives rise to rich emerging phenomena.

Ubiquity of Coulomb interaction

This section is divided in two parts which might appear to be focusing on overly specific effects at such an early point of the manuscript. However, each of these two parts is strongly tied to the two experimental works constituting the core of this manuscript, and that are summarized in the next section. Here I try to give only the essential physical points, and consequently ask the reader to bear with me as the purpose of emphasizing these particular effects will become clear soon after.

Inter-channel coupling in the QH regime

Many electron quantum optics experiments make use of QH edge channels as electronic waveguides. As far as it is known, electrons propagating within these behave according to the Tomonaga-Luttinger liquid model. The latter describes the elementary excitations of such a liquid as collective excitations (as opposed to the Fermi liquid model in higher dimensions, for which elementary excitations are dressed free and independent quasi-particles). Remarkably, when there are several QH edge channels next to each other, they are capacitively, strongly coupled together due to Coulomb interaction and their small spatial separation [25–28], and cannot be considered independent. In the simplest case of only two channels, the resulting elementary excitations are therefore

distributed over both of them, giving rise to an essentially charged mode and an essentially neutral one (see figure 3). It is then possible to picture a charge density wave injected in one of the two channels at one point of space. That will oscillate between both channels (although with no net dc current transmitted from one channel to another), similarly to the electric field's intensity in an optical coupler. In these kinds of circuits, based on QH edge channels, inter-channel coupling plays a major role on the transport properties, and signs show in several experiments, under a variety of forms, of which we list a few below. In Mach-Zehnder interferometers, this shows in the lobe pattern as a function of the bias voltage [29–33]. In Hong-Ou-Mandel experiments, the Pauli dip does not fully develop when two channels are coupled to each other [23], in contrast with the same experiment but when no edge channels are involved [24]. In experiments where non-equilibrium distributions are injected in one of the two channels, it is observed that energy can relax in the adjacent one [26,34,35].

Noticeably, several experiments where a non-equilibrium electron distribution or a quasiparticle was injected in one channel reported a missing amount of energy within the channels even for small propagation lengths [25,28,35–38]. This suggests that relaxation towards other external degrees of freedom plays a significant role in electron quantum optics [36–38].

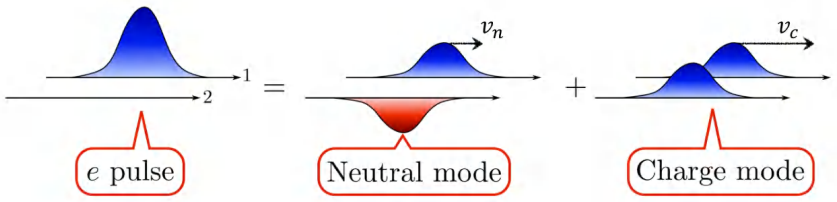

Figure 3: Schematics of an initial electronic excitation that gets decomposed in a charge and a neutral mode due to a coupling mechanism, taken from [39].

Electron correlations mediated by an island's large charging energy

The decomposition in charged and neutral modes as pictured in figure 3 is not restricted solely to the capacitive inter-channel coupling described above. Effectively, a different inter-channel coupling mechanism, mediated by a metallic island possessing a large charging energy results in a similar mode decomposition. A major difference with the aforementioned capacitive coupling mechanism is that the different channels are here electrically connected together through this metallic island. One of the only illustrations of this mechanism to date is the thermal Coulomb blockade of a ballistic channel [40]. In this experiment, it was observed that when N electronic channels connect the heated island to the cold reservoirs, the thermal conductivity remarkably amounts to only

$G^{\text{th}} = (N-1)G_Q^{\text{th}}$ (where $G_Q^{\text{th}} = \pi^2 k_B^2 T/3h$ is the quantum of thermal conductance), consisting in a reduction of the naively expected thermal conductivity by exactly one channel. The physical explanation lies in that the N available electronic modes can be decomposed in $N-1$ neutral modes and 1 charged mode. The latter cannot escape the island as it would involve a fluctuation of the island's global charge, which requires a too large energy ($E_C \gg k_B T$), and consequently only $N-1$ modes are available for thermal conductivity. A natural question that arises then is: what happens in the case where a single channel is connected ? Shall the heat transport be entirely suppressed even though the hot island is connected to cold reservoirs with one electronic channel ? This single-channel regime was not accessible to the experimental realization of [40] for practical reasons. However, it is explored in chapter 4 in a different, yet tightly related way.

Experimental investigations of this PhD thesis

In this PhD thesis, we explore the effect of both these Coulomb-mediated coupling mechanisms on the electron quantum coherence in two distinct experimental works. In a first experiment, inter-channel coupling was essentially suppressed to enable a larger coherence length. In a second experiment, we demonstrate a coherent transmission of electrons across a small metallic island, that is rendered possible by the Coulomb interaction. This section is dedicated to giving the key points of both experiments, and to situate the obtained result in a broader context.

Macroscopic electron coherence length in a solid-state circuit

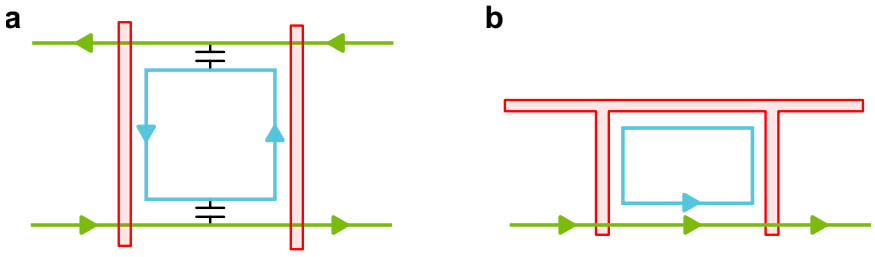

Figure 4: Schematics of gating strategies for confining the inner channel in small loops with a discrete energy spectrum. The top gates are represented in light red, the outer channels are in green and the inner ones in blue. **a** Strategy used in [41] where the loop mediates a long-distance coupling between counter-propagating outer channels. **b** Strategy used in this work [42] where the inner channel loop mediates no coupling towards any other propagating channel.

The goal of this experiment was to highly suppress inter-channel coupling in order to achieve a large coherence length in a QH edge channels based circuit. To this aim,

the adopted strategy consisted in confining the inner channel into small loops, with therefore a discrete energy spectrum of spacing $\Delta \gg k_B T$. This strategy was already adopted in an earlier experiment [41]; however, in this case, the loops introduced a long-distance coupling between counter-propagating channels as illustrated in figure 4 a. This consequently did not enable a large improvement of the coherence length. In this work, we implemented the same strategy but taking care not to introduce any coupling towards other propagating channels as illustrated in figure 4 b.

This work demonstrated a macroscopic coherence length of $L_\phi \approx 250\,\mu\text{m}$ for electrons in QH edge channels circuits, the confinement strategy enabling an increase of L_ϕ by over an order of magnitude. This shows that the inter-channel coupling is the primary source of decoherence in such circuits, and that the remaining coupling to the top gate does not provide for a decoherence mechanism as powerful as a co-propagating channel. On the other hand, the measured interferences were very noisy and unstable, which we can ascertain to be due to phase noise thanks to current noise measurements in the MHz range. A natural extension of this work would be to use this method in single electron interference experiments.

Coherent transmission of electrons across a metallic island

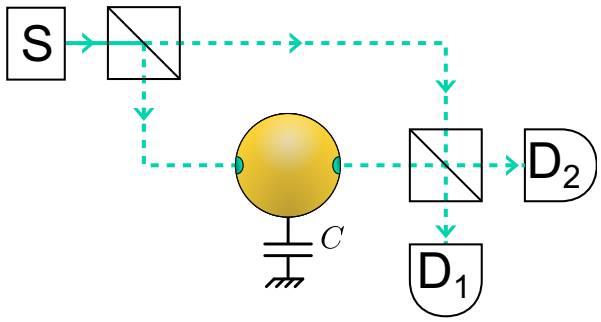

Figure 5: Schematics of a Mach-Zehnder interferometer with a small, floating metallic island interrupting one of the two paths.

This work aimed at demonstrating the puzzling coherent probe (as opposed to Büttiker's dephasing probe [43–45]) regime of a metallic island as predicted by [46,47] (and also, in a very similar prediction by [48]). These papers predict that electrons should be coherently transferred across a metallic island that has an electron dwell time much larger than the electron coherence time ($\tau_{\text{dwell}} \ggg \tau_\phi$), provided that two conditions are fulfilled:

- the island's charging energy must be much larger than the electrons' energy ($E_C \gg k_B T$, eV)
- only a single channel is connected to the island

It was found that these predictions are indeed correct, and this work experimentally demonstrates them by interrupting one of the two paths of a Mach-Zehnder interferom-

eter with a metallic island, as illustrated on the schematic of figure 5. Remarkably, as soon as a second channel is connected to the island, the fully incoherent probe regime is reached again. Another observation worthy of attention is that upon changing by one elementary electron charge the global charge of the metallic island (which can be changed continuously thanks to the ballistic coupling to the connected channel) a 2π phase shift in the interference pattern was observed, as expected by the theory [46,49].

The physical mechanism for this phenomenon is that, for decoherence to occur, an electronic excitation needs to couple to at least one degree of freedom of the island. This is usually provided by the island's continuous density of states that supplies an essentially infinite phase space for the electronic excitation to relax, mediated by electron-electron interactions. However, at low enough temperature, the large charging energy of the island does not allow for any fluctuations of its charge, and thus also prevents coupling of an incoming electronic excitation to the island's many internal degrees of freedom.

To put this result into perspective, it is interesting to underline the similarities that it bears with the proposal [50], which consists in a single topologically protected channel connected to a superconducting island with a large charging energy, such that a non-local correlation is established between the two distant points connecting the island by emerging Majorana bound states. This nonlocal correlation is the underlying mechanism for an electron teleportation. Does our result also demonstrate an electron teleportation ? From the prediction [47], it is clear that at finite temperature, the transfer is not fully coherent, thereby ruling out a pure teleportation, however, at zero temperature, the coherence should actually be entirely preserved, indicating a perfect transfer of the electron state from a first point to another distant one. This suggests that our observation at low temperature is approaching the regime of a pure electron teleportation that can only be reached at zero temperature.

This result therefore completes the model of the dephasing probe initially pictured by Büttiker as any floating contact, as this result makes it clear that the charging energy and the number of connected channels cannot be overlooked to predict whether it will effectively break the electron coherence. It also comes as a good illustration that the charging energy of an island hosting a continuous density of states is a crucial element for electron coherence as underlined in the proposal of L. Fu [50]. Finally, this result completes the heat Coulomb blockade experiment [40] described above, as it consists in connecting a single channel to a metallic island with a large charging energy. The island is not heated here, so that no thermal transport is at stake. However, the quantum coherent transmission of electrons across the island indicates that there is no information exchange between the electrons of the channel and the many electrons of the metallic island. As a consequence, and similarly to what was observed in the thermal Coulomb blockade experiment where heat exchange was diminished between the electrons within the channels and those within the island, here, information exchange is essentially suppressed. This illustrates the deep physical link between heat and information, usually explored in Maxwell demon's experiments.

Electronic coherence in relation to the environment

Similarly to the two preceding sections, this one is again divided in two parts.

The coherence of a particle can be described as their ability to interfere (note that it is question of first-order coherence here, for a more general definition, see [51] that is applicable to fields, but can be extended to particles: [52]). Interference of electrons were briefly introduced in the first few paragraphs of this introduction. From this standpoint, it is possible to take two different approaches to express how the quantum information is carried from point A to point B, as exposed in [53,54].

Coherence enclosed in the wavefunction

Equation 1 described the probability amplitude of an electron path with a simple generic phase. However, in general, an electronic wavefunction can evolve according to a Hamiltonian $\mathcal{H}(t)$ that characterizes the interaction of the particle described by the wavefunction $|\psi(t)\rangle$ with its environment such that:

$$|\psi(t)\rangle = \exp\left(-\frac{i}{\hbar}\int_0^t \mathcal{H}(t')dt'\right)|\psi(0)\rangle \tag{4}$$

This expression can very well lead to a simple static phase factor in the wavefunction, just as in equation 1. Nevertheless, a quantum uncertainty can arise in the state of the environment due to its interaction with the particle. It translates to an uncertainty in the Hamiltonian that must then be averaged over its multiple possible states and the acquired phase then becomes a statistical variable that is averaged over multiple values. The resulting phase can be decomposed in a static average part ϕ, and a statistical part $\delta\varphi$ described by a distribution function $P(\delta\varphi)$ such that the oscillating factor in equation 1 can be re-written as:

$$\exp\left(-\frac{i}{\hbar}\int_0^t \langle\mathcal{H}(t')\rangle\, dt'\right)|\psi(0)\rangle = e^{i\phi}\int d\delta\varphi P(\delta\varphi)e^{i\delta\varphi}|\psi(0)\rangle \tag{5}$$

The interference term of equation 2 then becomes:

$$2\mathrm{Re}\{A_u^* A_d e^{i\phi}\langle e^{i\delta\varphi}\rangle\} \tag{6}$$

in which the average value $\langle e^{i\delta\varphi}\rangle \leq 1$, acts as a reducing factor to the amplitude of the interferences from A to B and represents a measure of decoherence originating from the uncertainty induced in the environment's state. The closer it is to zero, the smaller is the interference contrast, the more classical the electron behaviour is, and the quantum coherence gets lost.

One of the consequences of decoherence is therefore to change the quantum phase in a

statistical variable, which, in turn, reduces the interferences contrast. Measuring this effect can be difficult as several other factors can lead to a reduction of this contrast as exemplified by our measurements of chapter 3.

Coherence enclosed in the environment

Above, coherence was presented from the point of view of a wavefunction that acquires a time-dependent phase, which can get blurred by a fluctuating environment. It is however possible to equivalently express the loss of coherence as a footprint that the propagating wavefunction leaves on its environment. Instead of expressing the paths' probability amplitudes as in equation 1, it is possible to express them as:

$$a_{u,d} = A_{u,d} e^{i\phi_{u,d}} \otimes \chi_{u,d}(\eta)$$

where η is the environment's set of coordinates. This time, the interference term is given by:

$$2\mathrm{Re}\left\{A_u^* A_d e^{i\phi} \int d\eta \chi_u^*(\eta)\chi_d(\eta)\right\}$$

This formulation is perfectly equivalent to the previous one [53], implying that

$$\langle e^{i\delta\varphi} \rangle = \int d\eta \chi_u^*(\eta)\chi_d(\eta)$$

Interestingly, in this expression, the integral on the environment variables is a scalar product between the two environment states. Initially, the scalar product of these two states has to be 1 because they describe the same environment and are consequently identical. When the wavefunctions each travel along their path, they might interact with the environment, changing its state each in a different way. In the extreme case where the scalar product becomes zero, then both environment states are orthogonal, meaning that it is possible to completely identify which path was taken by the electron simply from the imprint it left on the environment. Because quantum mechanical interferences rely on the path's uncertainty, when the uncertainty is lifted, no interferences can occur. As a consequence, this second interpretation formally expresses that when coherence is lost, the environment must have been modified in the process. So-called which-path experiments are precisely based on this principle and further discussed in section 4.1. Remarkably, the second experiment presented in this manuscript, the focus of chapter 4, looks at first sight like a which-path experiment, but yields surprising results.

In the former two paragraphs, coherence was presented in general terms, and that coherence loss could be seen as resulting either from a blurr of the electron phase or a modification to the environment.
Depending on the context, one or the other point of view is more adapted.

Outline of this manuscript

The structure of this introductory chapter reflects rather well the organization of this manuscript, it is therefore summarized here and the chapters that echo the corresponding part are emphasized.

First, the concept of interference was succinctly covered, along with the Aharonov-Bohm effect, absolute cornerstones of this whole PhD thesis. A few hallmark manifestations of electron coherence were then presented, in both free-space and solid-state. Several other signs of it are further detailed in chapter 1. The field of electron quantum optics was also briefly introduced, particularly in the context of quantum Hall edge channels based circuits, which is precisely the topic chapter 2 concentrates on. We then highlighted that this field does not consist in a pale copy of original quantum optics experiments but rather is a playground with rich physical effects, emerging from the ubiquitous Coulomb interaction, the second unifying theme of this PhD thesis. The two experimental works constituting the core of the present manuscript, and detailed in chapters 3 and 4, were then summarized and consist in good illustrations of the effects of such emerging phenomena on the electron quantum coherence. Finally, quantum coherence was introduced in more formal terms, and from two different yet equivalent perspectives, each of which will be adopted in the following, where they are the most appropriate.

1

Quantum Coherence in Solid-State Circuits

In vacuum, it comes as no surprise that electrons can interfere. In the solid-state, however, it is far less obvious. Effectively, electrons travelling through a solid state circuit encounter many occasions to interact with other degrees of freedom. Each such scattering event is an opportunity for the electrons to entangle with their environment, thus blurring their quantum phase. According to the formal description of coherence given in the introduction, this means that electrons can lose their coherence in such processes. In particular, the many electrons in a conductive material can scatter each other. The electrons are also affected by the vibrations of the ionic structure, giving rise to electron-phonon scattering. One may wonder then, if it is possible to have electrons retaining their coherence on relatively large scales in the solid state. This chapter provides an outlook on several experiments investigating electron coherence in solid-state circuits. It also illustrates how the presence of random scattering can give rise to specific interference effects (such as the Altshuler-Aronov-Spivak effect for example).

The first section of this chapter deals with the limiting mechanisms for the electronic coherence. As the electron quantum phase can be controlled with the Aharonov-Bohm effect, coherence effects are better illustrated when the magnetic flux is a well-controlled quantity. This is achievable in conducting samples with a hole of a known area relatively large compared to the metal's section width (like a conductive cylinder or ring). The second section is precisely devoted to the presentation of coherence effects that survive in presence of static disorder or even emerge thanks to it. These effects are also present in simply connex geometries (with no hole in the conducting material), where they manifest in distinctly different ways that constitute the topic of the third section. The

fourth section finally shows the several ways that these manifestations are used to measure the actual coherence length of electrons in the device.

1.1 Limiting mechanisms of L_ϕ

One may think that an electron loses its coherence as soon as it gets scattered, limiting the coherence length to the electron mean free path. That is incorrect, however, and while some scattering events indeed do destroy the coherence, the elastic scattering on static potentials (crystallographic defect, impurity...) does not. The coherence length therefore does not simply reduce to the mean free path. To illustrate this, let us recast the phase acquired by the electron as originating from a potential V originating from the environment:

$$\phi = -\frac{q}{\hbar}\int V(t)dt$$

If an electron causes no quantum uncertainty in the environment's state, its acquired phase is a static, well-defined quantity. On the other hand, if a quantum uncertainty in the environment's state is generated, an uncertainty is also induced in the electron's wavefunction phase, causing decoherence. When energy is exchanged with the environment, this necessarily happens upon coupling with its degrees of freedom, resulting in an uncertainty in the wavefunction's phase. As a consequence, it is natural to distinguish two categories in the scattering mechanisms: the scattering events during which the state of the electron environment is changed and those that do not affect it. Some examples of scattering events that do affect the environment are e-e, e-ph, e-TLS (Two Level Systems) interactions, which therefore tend to cause decoherence of the electrons. These are inelastic events, during which energy is exchanged with the environment, so that they undeniably affect its state. On the other hand, elastic scattering events can be associated to static, well-defined potentials, which affect the electrons' phase in a deterministic way. The phase, thus shifted by a fixed amount, remains well-defined and the coherence is preserved. An example of such non-dephasing mechanisms is the interaction of an electron with a lattice defect such as a dislocation, a grain boundary, an interstitial atom, an atomic vacancy or impurity, that induces a static variation of the potential without any energy exchange. It would be incorrect nonetheless to assume that only inelastic events can be responsible for decoherence. Effectively, quasi-elastic mechanisms, that do not involve energy exchange between the electron and the environment, can also be responsible for causing an uncertainty in the environment's state. Quasi-elastic scattering can flip an electron in a degenerate orthogonal state, thereby causing decoherence without affecting its energy. Two such examples are spin-flip events (provided no external magnetic field is applied) and inter-valley scattering (in graphene for example, where the valley degree of freedom introduces another degeneracy).

Each type of scattering is characterized by the average time elapsing between the occurence of two such events. It is possible to define the coherence time τ_ϕ in terms of

independent dephasing events times as such:

$$\frac{1}{\tau_\phi} = \frac{1}{\tau_{\text{e-e}}} + \frac{1}{\tau_{\text{e-ph}}} + \frac{1}{\tau_{\text{TLS}}} + \frac{1}{\tau_{\text{s-f}}} + \frac{1}{\tau_{\text{v-f}}}$$

where $\tau_{\text{e-e}}$ and $\tau_{\text{e-ph}}$ are the electron-electron and electron-phonon scattering times respectively, τ_{TLS} is the two-level system scattering time, $\tau_{\text{s-f}}$ and $\tau_{\text{v-f}}$ are the spin-flip and valley-flip times respectively. Note that the above expression's validity is conditionned to the fact that all these dephasing mechanisms are independent from each other. From there, it is possible to define the coherence length as:

- $L_\phi = \sqrt{D\tau_\phi}$ if in a diffusive medium, with D the diffusion coefficient
- $L_\phi = v_F\tau_\phi$ in the ballistic regime, with v_F the electronic velocity at the Fermi energy.

As a conclusive remark, it is stressed that the elastic scattering time τ_{el} may be much smaller than the coherence time τ_ϕ, enabling diffusive coherent transport.

1.2 Aharonov-Bohm manifestations of electron quantum coherence in the solid-state

In solid-state circuits, electron quantum coherence can be investigated even in media where many elastic scattering events occur, such as normal metals. These were historically the first playground for electron quantum coherence studies. In such diffusive metals, electrons can propagate along many different paths. The transport properties are obtained by summing on the probability amplitudes of each possible path. For paths smaller than L_ϕ, coherent effects will show. Inevitably, some of the possible paths take the form of loops along which coherence is retained, making the transport properties sensitive to an external magnetic field through the Aharonov-Bohm effect. That is exactly what is exposed in this section, where the presented effects specifically take advantage of a controlled doubly-connected geometry (with a hole in the conductor), such that the Aharonov-Bohm flux is well-defined.

1.2.1 $h/2e$ oscillations of the conductance: the Altshuler-Aronov-Spivak effect

The first kind of experiment that unambiguously revealed the wavelike behaviour of electrons to also show in the solid-state was performed by Sharvin and Sharvin in 1981 [55]. It consisted of a cylindrical metallic wire along which the electrical conductance was measured as a function of a magnetic field applied along the cylinder's rotation axis (see figure 1.1 **a**). In such a wire, among the multitude of possible trajectories, some of them contain loops that wind around the cylinder. Electrons therefore have the

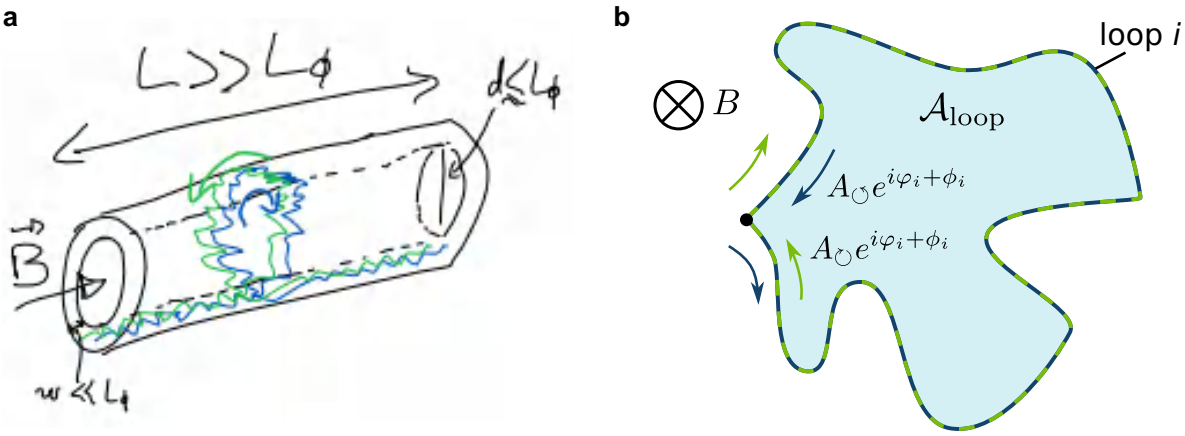

Figure 1.1: Schematics of **a** AAS paths in a cylinder **b** AAS loop of length $L_{\text{loop}} \lesssim L_\phi$ projected in a plane perpendicular to the magnetic field B, offering two possible directions for an electron: clockwise and counter-clockwise. The resulting probability amplitudes contain an Aharonov-Bohm phase factor ϕ_i proportional to the loop area $\mathcal{A}_{\text{loop}}$.

possibility to go around these loops in both directions: clockwise and anti-clockwise, each constituting the time-reversed trajectory of the other. Interferences therefore occur between electrons taking opposite directions. In the Sharvin experiment [55], the cylinder's dimensions respected two conditions:

- the cylinder's diameter d was at most comparable to the coherence length: $d \lesssim L_\phi$, in order for loops to form around it and along which the electron coherence is retained.
- the width of the metal w was significantly smaller than the cylinder's diameter $w \ll d$ in order for the Aharonov-Bohm flux to be well-defined, close to the flux threading the hollow cylinder's body.

Remarkably, the authors observed periodic oscillations in the cylinder's conductance with a periodicity $\Delta B = h/e2\mathcal{A}_\oslash$. The periodicity is related to twice the cylinder's cross-section area $\mathcal{A}_\oslash$, hence the name '$h/2e$ oscillations'.

To get a better grasp of this effect, it is instructive to calculate the expression of the total probability for an electron located at some point of space to return to this initial location, as illustrated in figure 1.1 b. It is noted R (for reflection probability), and is given by the squared modulus of the sum of each possible path's probability amplitude A_i:

$$R = \left| \sum_i A_i \right|^2$$

In particular, we highlight that each loop i can be taken clockwise or anti-clockwise by an electron, such that

$$A_i = A_{\circlearrowleft,i} e^{i(\varphi_i + \phi_i)} + A_{\circlearrowright,i} e^{i(\varphi_i - \phi_i)}$$

where the $A_{p,i}$ are the probability amplitudes for the electron to be scattered along path i in the clockwise or anti-clockwise direction as indicated by $\circlearrowleft$, $\circlearrowright$, and constituting the

time-reversed path of each other. φ_i and ϕ_i are respectively the static potential and the pure Aharonov-Bohm phases acquired by the electron along path i, yielding

$$R = \sum_i \left(|A_{\circlearrowleft,i}|^2 + |A_{\circlearrowright,i}|^2 + 2\mathrm{Re}(A_{\circlearrowleft,i} A_{\circlearrowright,i}) \cos(2\phi_i) \right) + \sum_{i \neq j} \left(\sum_{\{p,q\}=\{\circlearrowleft,\circlearrowright\}} A^*_{p,i} A_{q,j} e^{i(\varphi_j + \phi_j - \varphi_i - \phi_i)} \right) \tag{1.1}$$

From this expression, it is possible to see that the second sum vanishes due to the averaging of the different static phases and Aharonov-Bohm ones due to the inevitably many different possible loop paths along a cylinder that is much longer than the coherence length $L \gg L_\phi$. Remarkably, an interfering term survives even for long cylinders, with a periodicity proportional to twice the cylinder's cross-sectional area $\Delta B_\perp = 1/\mathcal{A}_\oslash \times h/2e$, resulting from the interference multiple pairs of time-reversed symmetric paths, each encircling the area $\mathcal{A}_\oslash$. In what is left, the first two terms together represent the classical probability for the electron to be reflected to its initial location. This reasoning holds for a single channel and the sum on all the available channels has to be taken to obtain the conductance via the Landauer formula. Upon this summation, all interference terms contribute in phase with each other as they do not depend on the random static phases, explaining the effect's robustness to ensemble averaging often mentioned in the literature.

This AAS effect was first observed by Sharvin & Sharvin [55] as predicted by the AAS theory [59]. The experiment was then reproduced several times by independent groups, with very good quantitative agreement with theory as for example [60], see also [61, pp. 381–383] for a review. The effect of spin-orbit interaction can also be clearly seen from such transport experiments in metallic cylinders. It is effectively expected that in absence (presence) of strong spin-orbit interaction, the conductance should always boast a maximum (minimum) at zero magnetic field. Such opposite behaviour was confirmed by magnetoresistance measurements in lithium metallic cylinders (with negligible spin-orbit interaction) [57,62], in comparison with the magnesium cylinders (with strong spin-orbit) used in the original Sharvin & Sharvin paper [55] or cadmium as demonstrated later [62] (see figure 1.2 a). Regardless of the spin-orbit interaction in the material, AAS oscillations are suppressed with only a modest value of the magnetic field (up to only $\approx 20\,\mathrm{mT}$ in [63] and $B \approx 8\,\mathrm{mT}$ in [64]), which is in good agreement with the theory [65, sec. 7]. This sensitivity to an external magnetic field can be intuitively understood as a gradual breaking of the time-reversal symmetry between the interfering paths at the root cause of $h/2e$ oscillations. AAS oscillations were also observed almost twenty years later in carbon nanotubes [58], which constitute a very natural object of study for such an effect (see figure 1.2 b). In this case, a maximum of the conductance is observed at zero magnetic field, as expected in absence of spin-orbit interaction like in graphene. Additionally, a rather large magnetic field $\sim 8\,\mathrm{T}$ is required to observe just one $h/2e$ oscillation, due to the very small diameter of the carbon nanotube $\approx 8\,\mathrm{nm}$.

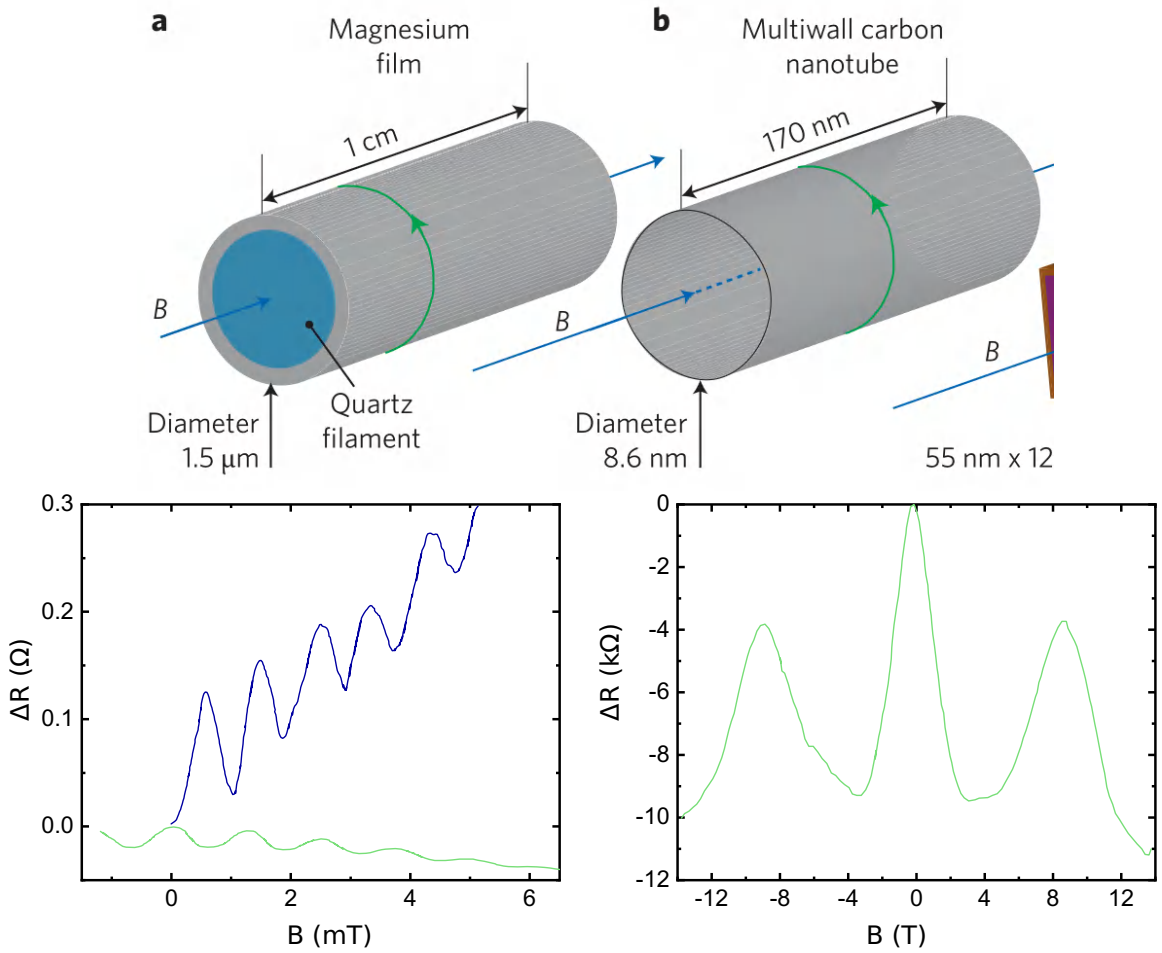

Figure 1.2: Sketch taken from [56]. AAS oscillations of the magnetoresistance in **a** Mg cylinders with strong spin-orbit interaction (blue, data from [55]) and Li cylinders with weak spin-orbit interaction (green, data from [57]) **b** carbon nanotube (data from [58])

1.2.2 h/e oscillations of the conductance

Despite the excellent agreement of various experiments with the AAS theory, a naive expectation is that h/e oscillations should also be observed in the cylinders experiments. Effectively, in such cylinders, one would expect some different processes than those implied in the AAS effect, and which are only encircling the cylinder's area once. To be more specific, among all the possible trajectories in the cylinders, some of them will separate at one point, one winds around the cylinder clockwise while the other winds around it counter-clockwise, before joining again, following two distinct paths as illustrated in figure 1.1 b. It was predicted that in the case of a ring comporting a single channel (only a single path on each side of the ring is available to the electrons), h/e oscillations should indeed be observed [66,67]. However, this single-channel case is purely theoretical and in real systems as those measured in the mentioned experiments, many channels, i.e. many possible paths for the electrons, contribute to the conductance. The following paragraph explains why they were not observed, in the spirit of [68, sec. V].

It is possible to consider electrons that take either a path i or a path j in separate upper (u) or down (d) arm in the ring as illustrated in figure 1.3 b (but the two paths could also take the same arm). The number of electronic channels M hosted by the ring is $\propto w \times t$, the cross-section area of the ring's wires. The outgoing electronic wave in the channel p is given by

$$\psi_p = \sum_i^M A_{u,i} e^{i(\varphi_i + \phi_u)} + \sum_j^M A_{d,j} e^{i(\varphi_j + \phi_d)}$$

where $\varphi_{i,j}$ are static, random phases associated with the detailed paths and $\phi_{u,d}$ are the pure Aharonov-Bohm phases (that is considered equal for all paths in each arm, this neglects the ring's width w, which is appropriate when $w \ll d$, the ring's diameter). The total transmission for a single channel is therefore:

$$\begin{aligned} T =& |\psi_p|^2 \\ =& \sum_i |A_{u,i}|^2 + \sum_j |A_{d,j}|^2 \\ &+ 2\sum_{i \neq i'} \mathrm{Re}\{A^*_{u,i} A_{u,i'}\} \cos(\varphi_{i'} - \varphi_i) + 2\sum_{j \neq j'} \mathrm{Re}\{A^*_{d,j} A_{d,j}\} \cos(\varphi_{j'} - \varphi_j) \\ &+ 2\sum_{i,j} \mathrm{Re}\{A^*_{u,i} A_{d,j}\} \cos(\varphi_i - \varphi_j + \phi_u - \phi_d) \end{aligned}$$

For a single Aharonov-Bohm ring, with a well-defined area (i.e. its diameter is large compared to the wire's width: $d \gg w$), the purely Aharonov-Bohm phase is given by $\phi = \phi_u - \phi_d = \mathcal{A}B/(\hbar/e)$, with $\mathcal{A}$ the ring's area. The transmission probability above is the sum of three terms: a classical probability (cl.) coming from $2M$ incoherent terms, a probability coming from the $2M^2$ fluctuating terms (fl.) in each arm with incoherent

contributions such that they contribute in $\sqrt{2M^2}$ to the transmission probability and an Aharonov-Bohm component (AB) that also contain $2M^2$ incoherent terms contributing to $\sqrt{2M^2}$. The transmission probability can then be re-expressed in a simpler form:

$$T = a_{(\text{cl.})} + 2a_{(\text{fl.})}\cos(\varphi) + a_{(\text{AB})}\cos(\phi + \varphi)$$

where φ are random phases originating from the static, flux-independent components of the phase. Due to the arguments above, the three amplitudes $a_{(\text{cl.})}$, $a_{(\text{fl.})}$ and $a_{(\text{AB})}$ are considered of equal magnitude a.
The conductance is then given by the Landauer Formula, by summing the transmission probabilities of all M channels:

$$\begin{aligned} G =& \frac{2e^2}{h}\sum_{p,q}^{M} T_{pq} \\ =& \frac{2e^2}{h}\left[\sum_{p,q} a_{pq} + \sum_{p,q} a_{pq}\cos(\varphi_{pq}) + \sum_{p,q} a_{pq}\cos(\phi + \varphi_{pq})\right] \end{aligned} \tag{1.2}$$

Once again, it is possible to use the fact that φ_{pq} is uncorrelated from one channel to another, so that the M^2 randomly oscillating terms contribute to the transmission probability to an amount of $\sqrt{M^2}$. Moreover, in the case where transport is as equiprobable along each channel (which is a realistic assumption in diffusive metals), we have $a_{pq} \propto 1/M$, such that

$$G \propto \frac{2e^2}{h}\left[M + \cos(\varphi) + \cos(\theta + \phi)\right]$$

where the first term is the average conductance ($\propto M$ as expected), the second term causes the universal conductance fluctuations that we come back to in section 1.3.2, and the third term is the Aharonov-Bohm term that is of interest here. This last term is the only one to be magnetic-field sensitive. In a two-terminal conductor, time-reversal symmetry imposes $G(B) = G(-B)$ (and thus that $G(\phi) = G(-\phi)$), consequently, θ is either 0 or π, and is randomly either one of the other, the randomness coming from the random character of the static phases. From this, it is possible to understand why h/e oscillations are not seen in long cylinders where the AAS effect is observable. It is effectively possible to picture the long cylinder as a collection of multiple, uncorrelated sections of thickness L_ϕ, in each of which θ takes random 0 or π value. The h/e oscillating conductance of all the contributing independent rings thereby averages to zero. This shows that this type of interferences is not robust to ensemble averaging.

Such h/e oscillations were observed in what is sometimes referred to as "1-D" rings in the literature – they are 1-D in the sense that $w, t \ll L_\phi, L_T$ – unambiguously for the first time in 1985 by Webb and colleagues [69]. This was further confirmed by several other observations in other metals such as silver [63,70] and tin [71,72], as well as in III-V semiconductors 2DEG [73]. In such experiments, it is also sometimes possible to

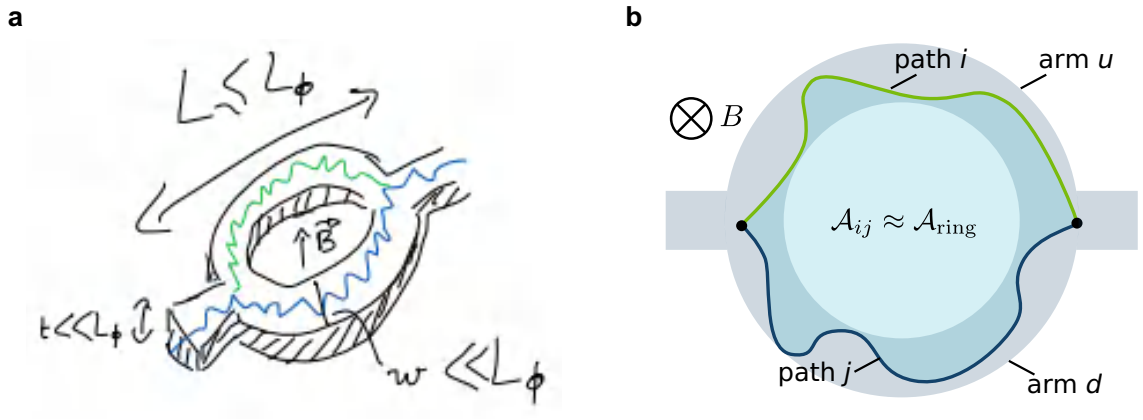

Figure 1.3: **a** Schematic of an AB ring **b** Schematic of two specific paths i, j respectively exploring the upper (u) and down (d) arm of an Aharonov-Bohm ring. The area enclosed in between the two paths drawn $\mathcal{A}_{ij}$ is approximately equal to the ring's area $\mathcal{A}_{\text{ring}}$

see oscillations of the conductance periodic in $h/2e$ at high magnetic fields, but of much weaker amplitude. Those are distinct from AAS oscillations however, and are rather due to harmonics of the same effect: pairs of different paths that separate at one point, circle the ring one full turn (instead of just half a turn for h/e), and then recombine and interfere. Effectively, contrary to the AAS oscillations, these do not rely on the indistinguishability of time-reversed paths, and can therefore survive to arbitrarily large magnetic fields.

1.2.3 Persistent Currents in Metallic Rings

It is possible to observe non-dissipative currents in metallic (non-superconducting!) rings when immersed in a magnetic field. This can seem puzzling as in metals, transport is normally dissipative, apparently preventing the circulation of any net current without a voltage bias. However, non-vanishing currents can indeed persist indefinitely even in a dissipative medium. This effect is only possible thanks to the electron quantum coherence [74]. The idea is that in a ring with a perimeter length smaller than the coherence length, the electrons' wavefunctions will be periodic. The current associated to each energy band n is then given by:

$$I(\Phi) = \sum_n \frac{\partial \epsilon_n}{\partial \Phi}$$

where the ϵ_n are the eigenenergies of each band and Φ is the magnetic flux threading the ring [75–78]. As the band structure $\epsilon_n(\phi)$ is constituted of non-flat bands with their derivatives that are mostly of alternating signs, currents are generated in both directions that consequently cancel. That is at the exception of the last few bands which are the only responsible for this effect, explaining its tiny amplitude. It is also predicted that disorder (elastic collisions) should only reduce the amplitude of the effect

but not prevent it entirely. This persistent current results in a magnetization of the ring, which can be measured. More precisely, it is the change in the magnetization upon a change in the externally applied magnetic field that is measured in experiments. The first measurement of this effect was performed in 1990 [79], and a periodicity of $h/2e$ was observed. The most accurate and unambiguous measurements of those magnetizations were performed rather recently, in 2009, both on rings arrays at high magnetic fields [80] as well as on several individual rings at low magnetic fields [81]. Both measurements boasted an h/e periodicity.

1.3 Quantum Corrections to the Conductance in diffusive conductors

The three effects presented above illustrate the physics of interferences in solid-state circuits, by showing how the combination of quantum interferences and random paths can give rise to these specific effects. So far, however, these effects were discussed in terms of a well-defined Aharonov-Bohm flux due to the doubly connected geometry of the systems. In a singly connected disordered metal (with no hole), like a simple wire, no precise Aharonov-Bohm flux is identifiable. A reasonable question that arises therefore is: do these quantum effects still show? The answer is yes, and they show in three distinct effects: in the magnetoresistance of the device, the Universal Conductance Fluctuations (UCF) and in Landau diamagnetism, the first two of which are presented in this section.

1.3.1 Weak-localization Magnetoresistance of Mesoscopic Wires and Films: a Signature of the AAS Effect

In simple metallic wires or films, it is also possible to have trajectories containing loops with a starting and ending point placed at the same location, just as for the AAS effect. In this case however, there is no well-defined preferential magnetic flux due to the system's geometry. As a consequence, no periodicity will stand out in its transport properties. All electron trajectories forming loops of length l_{loop} such that $l_{\text{loop}} \lesssim L_\phi$ can still interfere, and do affect the transport [82].

Due to the dependence of the AAS effect on interferences of time-reversed symmetric paths, an external magnetic field, which tends to destroy this symmetry, gives rise to a non-trivial dependence of the conductance (see eq.1 in [83]). At this point, it is interesting to look back at the data plotted in figure 1.2. It is very clear that superposed to the oscillations is a slowly drifting background. It is this part of the conductance dependence that we get interested in now. These are due to paths smaller than L_ϕ that loop around on themselves within the metal's thickness, but do not wind around the cylinder's perimeter. As a consequence, these loops are condemned to enclose a

much smaller magnetic flux than those that do wind around the cylinder, explaining the magnetic field's effect resulting in a slowly drifting background compared to the rapid $h/2e$ oscillations. Looking in more details, it appears that in the Mg cylindrical wire, the differential magnetoresistance (dR/dB) is positive with increasing B while in the Li wire, it is negative. This is due to the spin-orbit interaction, essentially absent in Li while strong in Mg, and such consideration illustrates the two opposite, yet linked effects: anti-weak and simple weak localization. In a nutshell, in absence of spin-orbit, both interfering trajectories will acquire the same relative phase, resulting in constructive interferences every time. On the contrary, in presence of spin-orbit interaction, the spin of the clockwise propagating electrons will get shifted of always the exact opposite angle than the anti-clockwise propagating electrons. This always result in destructive interferences, which can be seen as anti-trapping whence the terminology anti-weak localization (see [84, p. ch.7.4] for the detailed calculation).
When the magnetic field is turned on, the (anti-)weak localization effect is gradually killed. As a result, a negative (positive) magnetoresistance is observed in absence (presence) of spin-orbit interaction (see e.g. [82] for more details). In wires and films, this translates into a dependence of the resistance/conductance on B that is well captured by the AAS theory [85,86] (for complementary theoretical sources, see [87, pp. 203–206] for a discussion in terms of Feynman paths amplitudes, [87, pp. 222–241] for the derivation in terms of Green's function, and for a very different approach [Montambaux, pp.84-86] discussing the same matter in terms of Hikami boxes). Weak-localization is a thoroughly investigated effect and the induced magnetoresistance has even become the object of quantum simulation [88].

1.3.2 Universal Conductance Fluctuations: a reminiscence of h/e oscillations

When measuring the conductance of a disordered metal such that its dimensions do not exceed the coherence length, it is possible to observe fluctuations in the conductance upon varying an external parameter. It can be a magnetic field [89] or a nearby gate voltage [90] (the latter only works in semiconductors, as in metals, the large screening prevents a gate to have any effect). Remarkably, those aperiodic fluctuations are reproducible within a single sample. Regardless of the material, the amount of disorder in that material, or the sample's dimensions L (as long as $l \ll L \ll L_\phi$, where l is the mean free path), those conductance fluctuations will always remain of the order of the conductance quantum e^2/h. To a certain extent, the amplitude of those fluctuations are also independent of the sample's dimensionality [91], as in all three possible cases: 3D ($L_{x,y,z} \gg L_\phi$), 2D ($L_{x,y} \gg L_\phi, L_z \lesssim L_\phi$) or 1D ($L_x \gg L_\phi, L_{y,z} \lesssim L_\phi$), the conductance fluctuations remain of the order of e^2/h. For all these reasons, those fluctuations are called universal. Universal Conductance Fluctuations (UCF) were observed in 1D [90], 2D [90,92] and in 3D [93], upon changing an external parameter such as the voltage of a nearby gate [90] or a magnetic field [89,94]. They were observed in metals [[95];

[69];], in Si MOSFET [89,90,92,94] and more recently in graphene [96–99] as well as in some topological insulators as e.g. [100]. It is worth noting that in graphene, the valley degree of freedom (absent in normal metals) can drastically affect the UCF by enhancing them or suppressing them entirely (see [101, sec. II.C.3])

Just as in the case of h/e oscillations in 1-D rings, UCF are due to interferences between different pairs of paths that cross each other twice [102,103]. The effect of varying a nearby gate as in [90] is to modify the electrochemical potential μ of the propagating electrons. On the other hand, the effect of varying a magnetic field B, as in [89,94], is to change the relative phase of the different interfering paths. UCF therefore constitute a fingerprint of the particular microscopic arrangement of the material's impurities, and to which electronic interferences are sensitive. In this regard, this effect is analogous to the speckle effect in optics, a seemingly random interference pattern due to the scattering of coherent light through a diffusive medium [[102]; Montambaux, pp.94-100]. Such fluctuations were responsible for the ambiguity of the first attempt at measuring h/e conductance oscillations in ref. [95] because the ratio of the hole's area to the area of the metallic wire perpendicular to the magnetic field was around unity. As a consequence, h/e oscillations were buried in a background of noise which was ironically due to the exact same physical effect the experimentalists wanted to put in evidence.

To conclude this section it is simply mentionned that the analogue of persistent currents in simply connected geometries translates into Landau diamagnetism [104, chap. 4,105, chap. IV]

1.4 Measurement of the Electron Coherence Length

Because all the effects described above originate from quantum interferences, each can be used to quantify the coherence length L_ϕ. However, in practice, some are more precise and quatitative than others. In what follows, it is briefly covered how.

1.4.1 WL magnetoresistance, a quantitative probe

The weak-localization theory [106,107] predicts different behaviors of the magnetoresistance depending on the device dimensionality, as well as the transport regime (diffusive or ballistic). Below are listed a two examples for different regimes of the simplest geometry:

- in quasi-1D metallic wires, where the transverse dimensions of the wire: thickness t and width w are smaller or comparable to L_ϕ , the magnetoresistance is predicted to have the form of eq.1 in [83] for quasi-1D wires in the diffusive regime.
- For quasi-1D wires in the semi-ballistic regime, see eq.10 in [85], which also explores the cross-over between both diffusive and semi-ballistic regimes.

The equations are not printed here as we are not interested in the details. We simply point that in all these formulas, the magnetoresistance is based on just a few parameters which are:

- the wire's width w, which is the transverse dimension of the wire that is perpendicular to the applied magnetic field, and is a known parameter in an experiment
- the spin-orbit length, which characterises the strength of the spin-orbit coupling and is characteristic of the material that can be determined by fitting the localization theory
- the coherence length L_ϕ which is precisely the parameter of interest, also determined by fitting with the theory

The main feature in (anti-)WL magnetoresistance measurements is a peak (dip), whose relative amplitude and width are related to the coherence length L_ϕ (see fig.2 in ch.6 of [108] for the exact shape in quasi-1D wires).

Studying such systems gained interest again in the late 1990s after a it was suggested in [109,110] that the observed saturation of the coherence length at low temperatures was caused by zero-point fluctuations of phase coherent electrons. This controversy is very well summarized in [106]. It was further shown that such an assumption was not necessary to account for this saturation and even that the saturation could actually be explained by the presence of of magnetic impurities in such minute concentration that it could not be detected by other means [83].

1.4.2 Universal Conductance Fluctuations

On the other hand, it is difficult to be quantitative on L_ϕ with UCF, as there is no model as universal as that for WL and containing as few parameters, that enables to determine a well-defined value for L_ϕ from the UCF amplitude. There are consequently only a few examples where UCF measurements were used as quantitative probes (e.g. [97,111]), but were also always completed with WL ones, and most of times only served as a consistency check. It is however used as an indicative tool with its dependence upon varying temperature as in [111] or bias voltage, as in [112,113]. UCF measurements are therefore a must-do in any new materials, as they attest that the observed transport phenomena in the material are not spurious. Notable examples are in graphene [97,99], and some topological insulators such as Bi_2Te_2Se [100] and Bi_2Te_2S [114].

1.4.3 Multiple-path Interferometers

Another possibility is to rely on the amplitude of the h/e conductance oscillations in rings to evaluate L_ϕ. Once again, this technique is not as quantitative as WL measurements and is often performed along with WL measurements as for example in [71]. On the other hand, interferometers, although showing no particular advantage over

WL to quantify the coherence length, enable to explore what can affect the quantum coherence in which-path experiments thanks to their well-controlled geometry.

An example of such experiment is [115] (and another similar one [86] in copper) where a metal ring was doped with Manganese and Chrome. These are magnetic species with Kondo temperatures much lower than the experimentally explored range to ensure no screening of the spin impurities takes place. All these magnetic impurities act as a sensing environment by potentially exchanging their spin state with conduction electrons. By turning up the magnetic field, the magnetic impurities' spin gradually align with the field and get harder to flip (energy cost is $\propto B$), and interferences are recovered. The same experiment is performed on simply connex geometry in the same paper and by measuring UCF, it is shown that they are recovered at high magnetic field.

It is also possible to apply this technique in other types of two-path interferometers such as the series of experiments realized at the Weizmann institute which are solid-state implementations of the double-slit experiment [116,117]. Another, even more controlled experiment, consists in placing a quantum dot along one of the paths of a solid-state two-slit interferometer as in [118,119]. The quantum dot is itself capacitively coupled to a QPC, of which the sensitivity is tunable as a function of the voltage bias applied across it. The observed interference contrast diminished as the sensitivity of the QPC was tuned, elegantly demonstrating how sensing the quantum state by the environment can cause decoherence.

The difficulty for these as well as for metallic rings resides in the fact that there are several different channels interfering with each other. The final measured quantity is therefore always an average of the transport in several channels. The ideal situation would be to have a single channel for electrons to circulate and interfere within this single channel. This is precisely what the quantum Hall regime enables to do and is the subject of the next chapter.

2

The Quantum Hall Edge Channels and Electron Quantum Optics

So far, interferences were presented with numerous quantum channels interfering together. For example, the cross-section of an Aharonov-Bohm ring hosts many electronic modes. An ideal configuration for the quantum manipulation of electrons would be to have a system where single electronic modes can be controllably combined. This nevertheless requires to confine electrons to one-dimensional channels. However, in doing so, the influence of Coulomb interaction is dramatically increased. Effectively, in two- and three-dimensional conductors, their behaviour at low energy ($\ll E_F$, the Fermi energy) is usually well described in terms of free quasi-particles excitations with a renormalized mass, according to the Fermi liquid theory [120]. In one dimension, the free quasi-particle approach breaks down. An intuitive way to understand this is to picture that if one were to put electrons in a pipe thin enough so that they cannot go around each other, then due to Coulomb interaction, pushing just one electron will move all the others, resulting in a collective excitation. In effect, in one-dimensional conductors, electrons' behaviour is described by the Tomonaga-Luttinger (TL) liquid theory, which tracks the collective electrons' motion rather than the single-particle dynamics [121]. How could this be compatible with the coherent transport of electrons ? It turns out that for spinless and chiral conductors such as quantum Hall edge channels, the TL theory predicts the intra-channel interactions to only renormalize the electron velocity (eq. 1.44 in [121]), and therefore to have no undesirable decoherence side-effects. In this type of conductors, the electron decoherence at low temperature involves the coupling to other states, such as adjacent electronic channels (as will be discussed in chapter 3). Therefore, QH edge channels seem to constitute an ideal platform for exploiting

electron quantum coherence.

In what follows, it is explained how one-dimensionnal electronic systems, can be experimentally obtained. First, it is presented how one-dimensional confinement of electron can be achieved, restricting to the specific case of the QH regime. Then, the field of electron quantum optics is presented through a set of experiments, most of which take advantage of the one-dimensional QH channels for electron quantum manipulations. Finally, we introduce how these can be used to realize true two-path interferometers.

2.1 1-D Electronic Channels

This part shortly describes how 1D electronic channels can be obtained with 2DEG driven in the quantum Hall regime (for extensive review of this effect, I highly recommend reading R. Rodriguez's PhD thesis [122, chap. 2] as well as D. Tong lecture notes [123], other helpful resources are [124–127] and [128, chap. 3]).

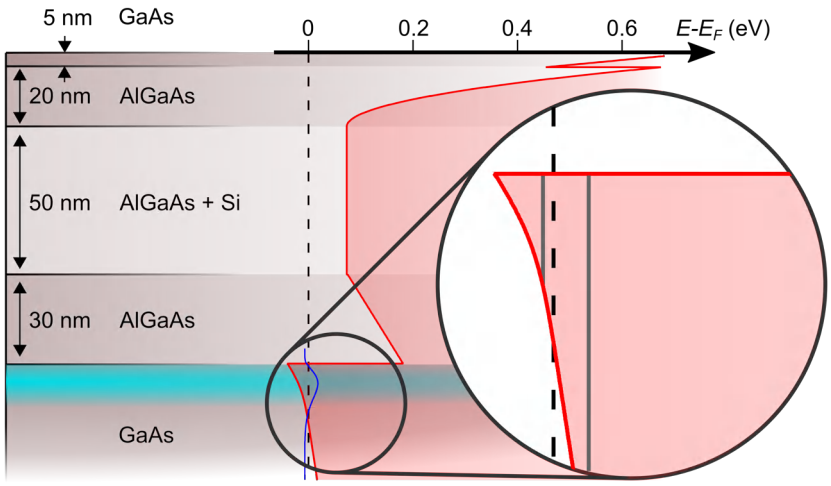

Figure 2.1: Sketch, to scale, of the SC structure used in the first study of this thesis. The bottom of the conduction band calculation was determined by solving the Poisson equation, assuming a homogeneous donors density in the Si doped layer, courtesy of Ulf Gennser. The zoomed-in part highlights that a potential well is created at the AlGaAs/GaAs interface and that only the fundamental level lies below the fermi energy.

The first step in confining electrons in one dimension is to confine them to two dimensions. State of the art two-dimensionnal electron gas are obtained by band engineering in epitaxied Si-doped AlGaAs heterostructures as illustrated in figure 2.1. They are epitaxied on a GaAs substrate from very pure materials and with a control of the thickness down to the atomic layer. Such purity and epitaxial growth guarantee an extreme scarcity of grain boundaries and lattice defects in the crystal, thereby preventing many elastic collisions for conduction electrons. The transport of electrons in such 2DEG is therefore ballistic typically up to several tens of microns at low temperature, which means they experience no scattering on shorter length scales. To get to the

one-dimensional confinement, two routes are possible. The first one consists in using a lateral confinement, however in this case, backscattering progressively increases towards an insulating regime as the temperature is reduced, except for perfectly ballistic systems, according to the TL theory. Another possibility is to take advantage of the topological protection of the quantum Hall edge channels against backscattering. In the following is described how to reach such a regime.

Immersing a high-mobility AlGaAs 2DEG with low carrier densities in a perpendicular magnetic field leads to a splitting of the electrons energy levels in highly degenerate Landau levels

$$E_{n,\sigma_\pm} = \hbar\omega_c(n + 1/2) \pm g\mu_B B/2 \tag{2.1}$$

where $\sigma_+(\sigma_-)$ stands for spin (anti-)aligned with the magnetic field, $\omega_c = eB/m^*$ is the cyclotron frequency, $m^* \approx 0.067m_e$ the electron effective mass, $g \approx -0.4$ the Landé factor, and μ_B the Bohr magneton. The first term in equation 2.1 is the Landau splitting, ~ 75 times larger than the second term, which is the Zeeman splitting, due to the small electron effective mass in those systems. To obtain a well-defined Landau level population, the thermal energy needs to be much smaller than the level separation: $k_B T \ll \hbar\omega_c$ (e.g. the temperature needs be $T \ll 100\,\mathrm{K}$ at $B = 5\,\mathrm{T}$, while Zeeman-split levels require a smaller temperature: $T \ll 1.3\,\mathrm{K}$ at $B = 5\,\mathrm{T}$). In the bulk, the energy levels lying below (above) the Fermi energy are fully populated (completely empty). Near the edges, the confining potential progressively increases towards the work function (~ 4.7 eV$\approx k_B \times 54$ kK [129,130], which is virtually infinite on the energy scales relevant to the transport regime we are interested in). The Landau levels therefore bend up and those populated in the bulk necessarily cross the Fermi energy near the edges (this would not be possible for large samples without any disordered-induced localized states in the bulk). The only propagative low energy states are therefore localized along the edges, at these crossing points. In practice, these edge states constitute small conducting channels, one for each populated Landau level, where electrons are only going one way, and are called edge channels. The backscattering within a single Laundauer-Büttiker channel is therefore only possible through the bulk by variable range hopping, which is essentially entirely suppressed whenever a conductance plateau is observed [131–133].

2.2 Electron quantum optics

2.2.1 The eletronics-optics analogy

Three of the characteristics of the quantum Hall regime permit to draw an analogy with the optical light. As a consequence, the QH regime provides a path for an electron implementation of quantum optics experiments. First, the quantum Hall channels are topologically protected against backscattering, similarly to how photons propagate in a transparent medium. Second, adjustable edges allow for guiding electrons along

controllable paths, similarly to photons in optical fibers. This can be achieved either by etching the 2DEG to the desired geometry or by field-effect. Third, it is possible to control the number of propagating modes, simply by tuning the magnetic field, while for photons, this would be controlled by the waveguide's dimensions.

This analogy with optics can be pushed further in that some electronic components can be identified to usual optical components, enabling the achievement of so-called electron quantum optics experiments. As further detailed below, it is possible to make coherent sources of (single) electrons, the electronic equivalent of beam-splitters, and photo-detectors.

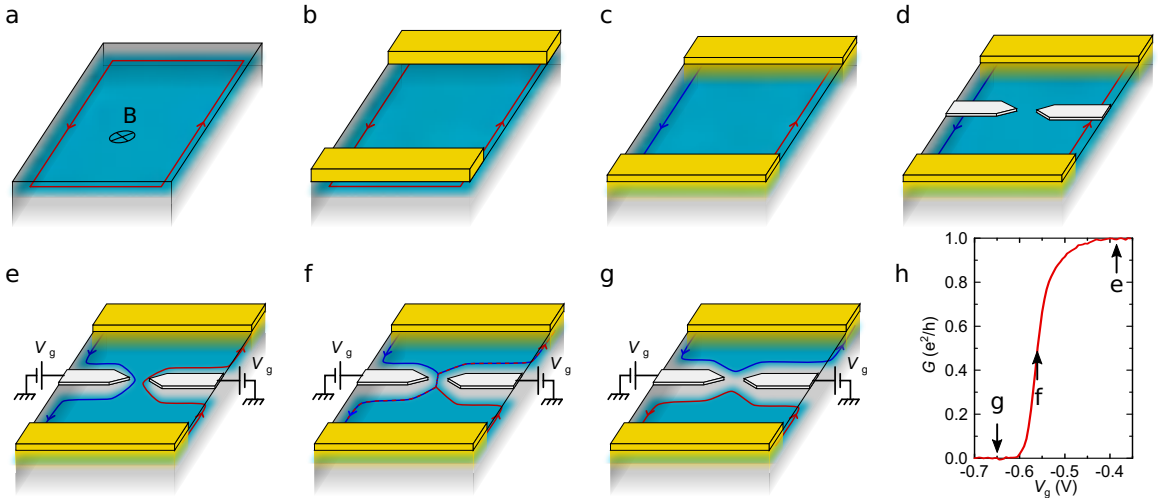

Figure 2.2: Sketches of the different steps to process ohmic contacts and Quantum Point Contacts (QPC). **a** 2DEG immersed in a perpendicular magnetic field, quantum Hall channel forms along the edges. Ohmic contacts are made as such: **b** An eutectic mix of Au & Ge is deposited on top of the structure, Ni is added for good adhesion to the surface. **c** The metal diffuses into the semiconductors thanks to a thermal annealing, so that the quantum Hall channels can be contacted electrically with wires through these contacts. **d** Al is deposited on top of the structure, constituting electrostatic gates. **e,f,g** Applying a negative voltage to these gates repels the electrons of the 2DEG located underneath, and enables to vary the transmission of the quantum Hall channels across them.

Electronic Beam-Splitters

The electronic equivalent of optical beam-splitters are quantum point contacts (QPC). They consit of metallic gates deposited on top of the semiconductor structure such that they are electrically disconnected from the 2DEG. By field effect, it is possible to repel electrons located below them, the two gates constituting the QPC are specially designed such that they end with sharp tips pointing at each other, enabling to gradually narrow the separation between counter-propagating edges channels.
When both electrostatically defined edges are close enough to each other, tunneling can occur between the forward and backward moving electrons, inducing backscattering. The amount of backscattering can be precisely controlled by the voltage applied to the

split gates, giving complete control on the transmission probability accross the QPC. In essence, a QPC is a fully tunable beam-splitter for electrons. A typical transmission curve is plotted in figure figure 2.2 h.

DC Sources and Detectors

The DC sources and detectors consist of ohmic contacts, that is, metallic electrodes that are electrically connected to the 2DEG. The coherence of the source is ensured by the low temperature of the device. The temporal width of an electronic wavepacket is $\sim \hbar/2k_BT$, which makes it a $\hbar v_F/2k_BT \sim 20\,\mu$m wide at 10 mK (taking a standard drift velocity for electrons in QH channels of $v_F \approx 5.10^4 \mathrm{m.s}^{-1}$ [134,135]).

Single Electron Sources

Single electron sources were implemented in essentially three different forms. The first type is constituted of a gate-defined quantum dot [136,137]. Playing with the voltage applied to the gates allows to capture and then emit a single electron at a well-defined energy or time. The second type of sources is also constituted of a quantum dot but this time, the electron emission is triggered by a surface acoustic wave along which the electrons subsequently travels with [14]. The third type of single electron sources simply consists in an ohmic contact, just as the ones described for the DC source. It is then required to apply a particular voltage excitation (of lorentzian shape in the time domain, with a particular width), such that the wavepacket contains exactly one elementary charge [24].

Single Electron Detectors

It is possible to detect electrons one by one by simply using a QPC, nearby the region to be monitored as in [138]. Any charge located in the QPC surroundings acts as a gate, as a consequence, an excess charge entering or leaving the nearby region provokes a change in the QPC's transmission, that can be monitored. For maximum sensitivity, the QPC is tuned at its sharpest transconductance value (the goal is to maximize $\partial G_{\mathrm{qpc}}/\partial V_{\mathrm{qpc}}$). This kind of detection is however generally limited to low frequencies [139]. To increase the detection rate, it is possible to connect the sample with an impedance-matched RF circuit, enabling detection in the 100 MHz range as in [140].
These schemes remain however too slow to detect flying electrons (going at $\sim 5 \cdot 10^4\,\mathrm{m.s}^{-1}$ in devices that are typically tens of microns long). This is why some proposals were made to be able to perform this kind of flying single electron measurements such as [141], in which electrons are made to propagate alternatively below two large metallic gates, resulting in a non-destructive ac detection signal. See also [142, sec. 5.2], for a review of other possible methods.

2.2.2 A few milestone experiments

Using the aforementioned tools, it was possible to the mesoscopic community to realize equivalents of a few quantum optics experiments, in what follows, several striking ones are presented.

Hong-Ou-Mandel Experiment

Time resolved single electron sources, rendered possible to collision two indistinguishable single particles at a QPC, analogous to the photons collisions performed on an optical beam-splitter [143]. The rate of coincidence of two particles impinging on the two output detectors is measured as a function of their arrival time difference at the beam-splitter. When both particles arrive at the beam-splitter with a large delay, they do not see each other and act as single particles. In the measured low-frequency electronic noise, this translates into simple shot-noise. However, when they both arrive at the same time on the QPC, it is their two-body wavefunction that drives the outcome. This two-body wavefunction $\Psi(\boldsymbol{r_1}, \boldsymbol{r_2})$ (with $\boldsymbol{r_i}$ the single particles' set of coordinates) depends on the particles' nature and more precisely on their exchange statistics, which is defined by the phase acquired θ upon the two particles exchange, and reads:

$$\Psi(\boldsymbol{r_1}, \boldsymbol{r_2}) = e^{i\theta}\Psi(\boldsymbol{r_2}, \boldsymbol{r_1}) \tag{2.2}$$

For bosons $\theta = 2\pi$ and for fermions $\theta = \pi$, such that the probability of finding two particles at the same position $\boldsymbol{r}$, given by $|\Psi(\boldsymbol{r}, \boldsymbol{r})|^2$, is unity for bosons ($\theta = 2\pi$) and it vanishes for fermions ($\theta = \pi$). The fermions' anti-bunching behaviour leads to a suppression of the partition noise whenever two indistinguishable fermions arrive at the same time at the QPC, as observed in [23,24] (although in [23], the Pauli dip did not go to zero due to hole-type excitations and Coulomb mediated interaction with the environment).
Interestingly, it was also possible to observe an intermediate behaviour between the bosons' bunching and the fermions' antibunching in a similar collision experiment, with anyons possessing an intermediate exchange statistics $\theta = 1/3$ [144] (note however a major difference: the single-particle sources were voltage biased QPCs, giving no control on the single-particle delays, the exchange statistics could however be probed with the cross-correlation noise).

Mach-Zehnder and Fabry-Perot Interferometers

The above experiments put forward the particle-nature of the electronic excitations, it is also possible to probe their wavelike nature, thanks to interferometers, just like in optics. The first true two-paths electronic interferometer to be implemented was the Mach-Zehnder interferometer of the Weizmann Institute in 2003 [20], the principle of which is detailed in section 2.3. As far as now, this kind of interferometer remains the

only kind of true two-paths interferometers for electrons in conductors as it involves only a single channel. Any other type rely on interferences of several paths implying different electronic channels. It is also possible to make Fabry-Perot interferometers using the same principle (see section 2.3 for details).

Hanburry-Brown-Twiss Experiment

The principle of the Hanburry-Brown-Twiss (HBT) interferometry is that correlations between indistinguishable particles can develop along their way to the detectors, even if they are emitted by two spatially incoherent sources. It is possible to realize a similar interferometry experiment with electrons, which relies on coupling two Mach-Zehnder interferometers via one of their paths [22]. This enables to entangle an electron in the first MZI to an electron in the second one. The double MZI geometry involves four detectors, two of which are put to ground, and the two others are each an output of a different MZI. Electron correlations can be measured through the electronic cross-correlation signal between these two detectors. Remarkably, although no single particle can travel a path enclosing both MZI areas, the observed cross-correlation noise shows an Aharonov-Bohm periodicity consistent with this total, double MZI area, demonstrating the correlated nature of the indistinguishable electrons that entangled within the double MZI.

2.3 Electronic Interferometers

In electronics, one major manifestation of quantum mechanics is the wavelike nature of electrons. Interferometry is a simple and elegant way to reveal it. Quantum Hall channels can be used to realize interferometers that are analogous to optical ones, here the focus is specifically on the Mach-Zehnder and Fabry-Perot interferometers.

2.3.1 Electronic Mach-Zehnder Interferometer

With the tools described above, it is possible to make interferometers that are similar to their optical counterparts, such as Mach-Zehnder interferometers as illustrated in figure 2.3 b. A first QPC is used to separate an incoming beam of electrons into two beams that each follow a distinct path. Those two are further recombined on a second QPC before ending on two detectors. The observed intensity of the signal transmitted from source S to detector D_1 (be it for the electromagnetic field module or the electrical current) will be a sinusoidal curve:

$$I = \bar{I}[1 + \mathcal{V}cos(\phi)] \tag{2.3}$$

where $\bar{I}$ is the average current, ϕ is the phase difference acquired along both paths and $\mathcal{V}$ is the interferences visibility defined from the maximum and minimum intensity

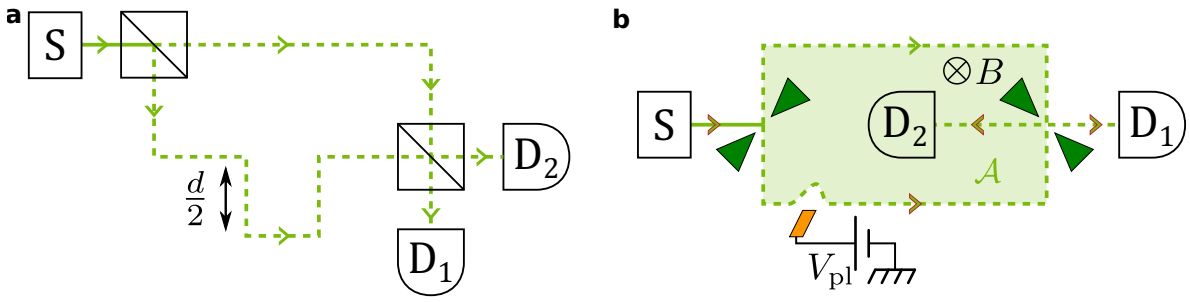

Figure 2.3: Schematics of Mach-Zehnder interferometers: **a** In an optical system, a source (S) emits a beam of classical light or photons that is separated in two at a first beam-splitter. These are further recombined on a second beam-splitter before hitting two detectors (D1,D2). The path difference (d) drives the phase difference, which determines the observed interference pattern. **b** In a solid state electronic circuit, a source (S) emits a beam of electrons (in a quantum Hall channel) that is separated in two at a QPC (pair green triangles facing each other) and further recombined on a second QPC before ending on two detectors (D1,D2). The phase setting the interferences is driven by the magnetic flux $\mathcal{A} \times B$ threading the area $\mathcal{A}$ enclosed between both paths, with B the magnetic field perpendicular to the plane of the area $\mathcal{A}$. Two knobs are therefore available to modulate the magnetic flux: the perpendicular magnetic field B as well as the area $\mathcal{A}$ thanks to an electrostatic gate voltage V_{pl} that can repel away one of the propagating channels by field-effect.

measured as:

$$\mathcal{V} = (I_{\max} - I_{\min})/(I_{\max} + I_{\min}) \tag{2.4}$$

In the ideal case, without decoherence and with beam-splitters tuned to half transmission, the contrast is perfect, which translates in a visibility that is unity. For an optical MZI, the phase difference is due to the paths length difference d, while for the electronic MZI, it is an Aharonov-Bohm phase that is picked up and which is given by:

$$\phi = \frac{e}{\hbar}\mathcal{A}B \tag{2.5}$$

where $\mathcal{A}$ is the area comprised in between both of the interferometer's arms while B is the perpendicular component of the external magnetic field applied to the interferometer. Note that in equation 2.5, only the pure Aharonov-Bohm phase is taken into account and the geometric phase due to a possible path length difference bewteen both arms is neglected. To vary the magnetic flux, one can vary either the magnetic field B or the area $\mathcal{A}$ enclosed between the interfering paths. In practice, the two knobs that are accessible to modulate the interferences' Aharonov-Bohm phase: the magnetic field, and the voltage of a gate coupled to one of the interferometer's paths (which can vary the area as shown in figure 2.3 b by the small bump along the lower path). In general, the dependence of these two parameters can be written as:

$$\frac{d\phi}{2\pi} = \frac{\partial}{\partial B}\left(\frac{\mathcal{A}B}{h/e}\right)dB + \frac{\partial}{\partial V_{\mathrm{pl}}}\left(\frac{\mathcal{A}B}{h/e}\right)dV_{\mathrm{pl}} \tag{2.6}$$

In the simple case, where only the magnetic field is changed, the area of a simple MZI interferometer is not affected by it and a 2π phase shift corresponds to

$$\Delta B = \frac{h/e}{\mathcal{A}}$$

and is therefore inversely proportional to the interferometer's area.

Mach-Zehnder interferometers present the advantage of having one of the two detecting contacts playing the role of a charge sink, thereby preventing any charging effects. These are a major concern in Fabry-Perot type interferometers as argued below.

2.3.2 Electronic Fabry-Perot Interferometer

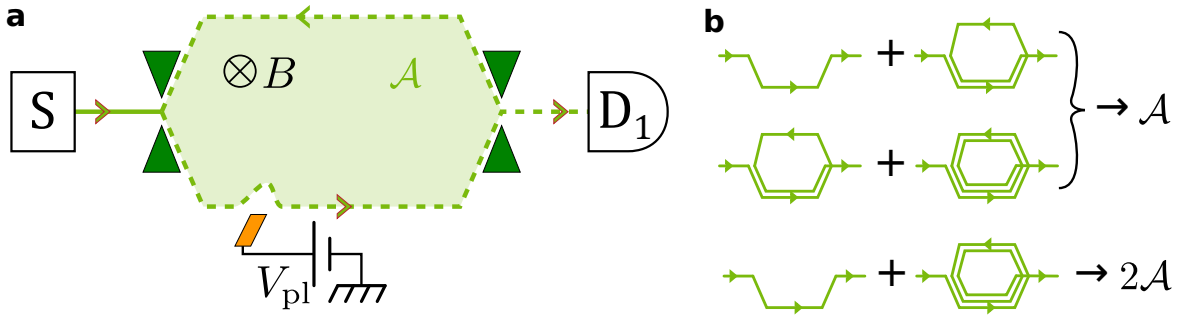

Similarly to Mach-Zehnder interferometers, Fabry-Perot Interferometers (FPI) can be built in the quantum Hall regime [16,17]. They also rely on the presence of two QPCs in series. This time however, interferences between multiple paths can occur as illustrated in figure **??**. In the limit where the QPCs are tuned to reflect only a small fraction of the current ($R_2, R_1 \ll 1$, with R_i the reflection probability of each QPC), the current through a FPI is given by:

$$I_{\mathrm{FPI}} \approx \bar{I}_{\mathrm{FPI}} \left(1 + 2\sqrt{R_2 R_1}\cos\phi\right)$$

where ϕ is the phase acquired for a single loop in the cavity.

Contrary to Mach-Zehnder interferometers, the interfering paths in Fabry-Perot cavities encircle an area containing no charge sink (a role played by contact D_2 on figure 2.3 b). Consequently, Coulomb repulsion effects within the cavity can become significant, and modifying the magnetic field or a side gate voltage not only affects the Aharonov-Bohm pattern but also the total charge enclosed inside the cavity Q_{cav}. In the case of a cavity with only the outer channel connected to the outside through the QPCs, the total charge Q_{cav} can be decomposed in the addition of three terms:

$$Q_{\mathrm{cav}} = Q_{\mathrm{ions}} + Q_{\mathrm{in}} + Q_{\mathrm{out}}$$

with Q_{ions} the fixed charge of the donor ions, $Q_{\mathrm{in}} = eN_{\mathrm{in}}$ is the electrons charge localized

in the cavity bulk (with therefore an integer number N_{in} of elementary charges) and Q_{out} is the charge carried by the outer, interfering channel, which is not restricted to an integer number of electrons. In the integer QH regime, the charge contained in each channel (in particular in the outer one) is given by $Q_{\text{out}}/e = B\mathcal{A}/(h/e)$. In the Coulomb-dominated regime, Q_{cav} is primarily determined such that it minimizes the charging energy of the cavity $Q_{\text{cav}}^2/2C$, with C the capacitance of the cavity towards its surroundings, i.e $Q_{\text{cav}} = 0$. In the particular case of changing the magnetic field, being in the Coulomb-dominated regime implies

$$\frac{\partial Q_{\text{cav}}}{\partial B} = 0$$

The magnetic field does not affect the background ionic charge and therefore $\partial Q_{\text{ions}}/\partial B = 0$, leaving only

$$\begin{aligned} \frac{\partial Q_{\text{in}}}{\partial B} &= -\frac{\partial Q_{\text{out}}}{\partial B} \\ \frac{\partial N_{\text{in}}}{\partial B} &= -\frac{\partial}{\partial B}\left(\frac{\mathcal{A}B}{h/e}\right) \\ &= -\frac{1}{2\pi}\frac{\partial \phi}{\partial B} \end{aligned} \tag{2.7}$$

where ϕ is the phase of the oscillating conductance, that can therefore only change in steps of 2π, in the Coulomb-dominated regime, resulting in an interference pattern independent of B. What physically happens is that the term $\partial \mathcal{A}B/\partial B = B\partial\mathcal{A}/\partial B + \mathcal{A}$ has to vanish, so that the area enclosed by the outer channel needs to shrink progressively as B is sweeped. When the area has contracted of $\Delta\mathcal{A}$ such that $B\Delta\mathcal{A}/(h/e) = 1$, N_{in} jumps by one e and the area abruptly relaxes, resulting in a phase jump of 2π, invisible in conductance measurements.

Here, the situation considered was only in the very particular case of a Coulomb-dominated QH FPI constituted by the outer channel, upon varying only the magnetic field. A general model for QH FPIs can be found in [145], where variations of a gate voltage, the number of free propagating channels, and regimes where the charging energy of the cavity does not dominate, are also considered. Explorations in several regimes were accomplished, [18,146–148] resulting in oscillatory patterns with distinct signatures, in good agreement with theory [145].

This kind of charging effects can be suppressed by adopting a few stategies: one of them is to place a charge sink in the middle of the interferometer under the form of a micron-scale ohmic contact [146]. Another strategy is to screen Coulomb charging energy by placing a nearby top-gate as in [18,146]. The latter strategy can be taken a step further in very small cavities, that require screening planes to be disposed very close to the transport plane, as was accomplished with a triple quantum well in an AlGaAs heterostructure [149] and for which a pure Aharonov-Bohm interference pattern was

observed. Finally, let us point to very recent results in two independent groups that reported the successful realization of Fabry-Perot interferometers in graphene [150,151]. Those do not suffer from any charging effects, thanks to the hole channels that run under their gates and are capacitively very well-coupled to the interfering channels due to their very small spatial separation, acting as efficient Coulomb screens. Such 2D material platform might therefore be ideal to study anyons in the future.

2.4 Coulomb induced correlations in electron quantum optics

So far in this chapter, a parallel was established between electrons in solid-state circuits and photons, a few examples of experiments common to both fields were also given. One should however note a caveat of such an analogy: contrary to interactionless photons, electron-electron interactions play a major role in one-dimensional electronic conductors. While this interaction can be detrimental to the electron coherence, it can also give rise to exotic physical effects that have no equivalent in optics. Below, a few examples highlight that the interests of electron quantum optics goes beyond the mere reproduction of optical experiments.

2.4.1 Measurement of the Anyonic Statistics by Interferometry

The most striking case of such emerging phenomena is probably the fractional quantum Hall effect that arises in 2DEG with low carrier densities and high mobilities due to Coulomb interaction as electrons pair with several flux quanta. These emerging quasiparticles can have anyonic statistics, which can be probed by interferometry as described below. One of the appeal of interferometry is to directly measure the exchange statistics of anyonic quasiparticles [152, sec. 7]. Although attempts were made in MZI [153,154], they remained unfruitful, maybe because of edge reconstruction [155,156] occuring and destroying the fragile anyonic quasi-particles. It appears that anyonic quasi-particles cannot propagate on long distances in the fractional quantum Hall regime (this is the reason why source QPCs were placed in close proximity to the collision QPC in [144]).

Another approach is to use FPI that allow for significantly smaller path lengths than MZI. Several attempts at measuring the anyonic statistics were made with a Fabry-Perot interferometer [157–162], and while some elements point to an effectively measured anyonic statistic, charging effects render these measurements ambiguous [18,145,163]. The Manfra screening strategy [149] suppresses the Coulomb charging energy of the cavity, enabling the authors to unambiguously measure the braiding of anyonic quasiparticles in the fractional quantum Hall regime at $\nu = 1/3$ [164]. In this regime, electronic excitations of the fractional quantum Hall state are of anyonic nature with an exchange phase (equation 2.2) of $\theta = \pi\nu = \pi/3$. Although first order interferences

in a FPI involve single anyons going around the cavity, by doing so, the interfering quasi-particle encircles all N_{qp} quasi-particles localized in the bulk of the cavity. This process can be shown to be equivalent to two two-particle position exchange, called a braiding operation [152,165], and the resulting picked-up phase by the interfering anyon is: $\phi = 2\pi\nu[\mathcal{A}B/(h/e) - N_{\mathrm{qp}}]$ [152, sec. 7] (where $\mathcal{A}$ is the interferometer's area). Upon changing the magnetic field or a nearby plunger gate voltage, the number of bulk quasi-particles (which is a well-defined integer number due to their localization) can jump by one, provoking a $2\pi/3$ jump in the interferometric pattern and which is precisely the measured signature in [164]. Let's stress that the aforementioned experiment results from an absolute tour de force in the heterostructure growth, as well as in the device fabrication, involving techniques unavailable to any other research group at the moment.

2.4.2 Perspectives for electronic flying qubits

QH edge channels provide a mean to perform quantum operations based on single electrons [142,166], indeed, they are analogous to optical waveguides and allow for an efficient coupling thanks to the Coulomb interaction. It is effectively possible for example, to imagine a quantum CNOT gate based on two coupled Mach-Zehnder interferometer [166]: the principle of a classical CNOT gate being to control the output of a bit with the state of a second one. A quantum CNOT gate is exactly the same, but with qubits, that can therefore be in a superposition of both states. In a MZI, the electron can be in a superposition of being present in one path and being present in the other. As a consequence, two MZI coupled together along one of their paths such that when both electrons are in the coupled path, they pick up a π phase shift, represents a quantum CNOT gate.

2.4.3 Luttinger spin-charge separation

As already discussed for anyons, the dimensionality of a physical system can drastically affect its behaviour. Similarly, electrons confined to one dimension act very differently compared to higher dimensions. As a matter of fact, electrons in quantum Hall edge channels implement a chiral Tomonaga-Luttinger liquid [121]. Several experiments were performed to reveal some of the characteristics of such systems, such as the so-called spin-charge separation that we adress in more details in section 3.2. Note that the Tomonaga-Luttinger liquid model also applies to systems different from quantum Hall edge channels such as laterally confined 2DEG (see e.g. [167]). Note also that the spin-charge separation is only valid for particular systems and although this terminology conveys the idea that no single particle excitations can exist in 1D systems (as these would carry both charge and spin), we stress here that the spin degree of freedom plays no other role in this effect than providing distinct energy degenerate states. In the following, we prefer to talk about the separation between a charge mode and a neutral mode.

3

Macroscopic electron quantum coherence in a solid state circuit

This chapter describes the experimental demonstration of a macroscopic electron coherence length in a solid-state circuit which, more specifically, was demonstrated using quantum Hall edge channels. It is said to be macroscopic in the sense that such a length ($250\,\mu m$) is visible to the naked eye, by comparison, a hair is typically $50 - 100\,\mu m$ wide. In addition, this experiment sheds light on the difficulty to access the real, intrinsic coherence length through simple conductance measurements, and how current noise measurements in the MHz range can be used to draw stronger conclusions.

First, the reasons that motivated this work are briefly presented, then an overview of the knowledge of the behaviour of electrons in quantum Hall edge channels is given. From this standpoint, we adopt a strategy to minimize decoherence in a QH edge states based circuit, and experimentally demonstrate its efficiency with a MZI.

3.1 Motivations

The first motivation for this work is fundamental and falls within the broad context of understanding and pushing further the bounds where quantum physics manifests [168]. More specifically, we address the question of how much distance can an electron cover in a solid-state circuit while keeping its quantum character.
In principle, there is no fundamental limit to that distance. In practice however, the electron coherence length is limited to typically below a few tens of microns regardless of the material. It is interesting in itself to identify and understand the mechanisms

that ultimately limit the quantum behaviour.

A second main motivation for unlocking the quantum coherence of electron is the potential technological avenue it would open, in particular, in using electronic flying q-bits for quantum computing applications [39,142]. The larger the distance an electron can travel keeping its quantum integrity, the greater the number of operations that can be performed on it, enabling more advanced calculations.

Finally, the choice of QH channels as a test-bed for this kind of measurements is to take advantage of both, the flexibility they offer as electron physical guides, and the absence of backscattering.

3.2 Electron-electron interactions in QH channels

In the QH regime, electronic transport occurs along the edges of the sample in spatially separated, one-dimensional channels, and is protected from backscattering thanks to the chirality. As such, it can be thought to be well-described by the Tomonaga-Luttinger Liquid (TLL) model where interactions between counter-propagating channels (the g_1 and g_2 types described in [121, sec. 1.3]) can be dropped as they are typically separated by a large insulating bulk, and only those between electrons going in the same direction (the g_4 types) are kept. The Hamiltonian $\mathcal{H}$ of co-propagating QH channels can therefore be described in terms of the local density fluctuation operator $\rho_\alpha(x)$ in each channel α (see [121, sec. 2.1] or [169, sec. 3.1.2] for a formal definition of $\rho(x)$):

$$\mathcal{H}_{\mathrm{QH}} = \pi\hbar \sum_{\alpha} \left[v_d^{(\alpha)} \int \rho_\alpha^2(x)dx + v_{\alpha\alpha} \int \rho_\alpha^2(x)dx \right] + \pi\hbar \sum_{\alpha<\beta} \int u_{\alpha\beta}\rho_\alpha(x)\rho_\beta(x)dx \qquad (3.1)$$

where the sum runs over the α co-propagating physical channels. In this expression, the first term is the interactionless part of the Hamiltonian, with $v_d^{(\alpha)}$ the interactionless particles' drift velocity in channel α. The second term is the intra-channel interactions part, the effect of which is only to renormalize the electron drift velocity to a new one in each channel: $v_\alpha = v_d^{(\alpha)} + v_{\alpha\alpha}$. The last term describes the inter-channel interactions, these render the hamiltonian non-diagonal with respect to the elementary excitations in each separate channel. Note that the two interaction terms of equation 3.1 bear three differences with eq. 2.94 in [121]: the first one is that it only considers one type of movers (either leftgoers or rightgoers) as we specified above. The second is that the sum on spins was replaced by a sum that runs on an arbitrary number of channels, while the TLL model considers only two (one for each spin). The third is that it allows for different intra- and inter-channel coupling constants from channel to channel, because we know that QH channels correspond to non-degenerate states, while the TLL model considers electrons that are spin-degenerate.

Most of the electron quantum optics experiments were performed at filling factor of

two, in this case, the hamiltonian of equation 3.1 reads

$$\mathcal{H}_{\text{2ch.}} = \pi\hbar \int \left(v_o \rho_o^2(x) + v_i \rho_i^2(x) + u \rho_o(x) \rho_i(x) \right) dx$$

where $\rho_{o,i}$ and $v_{o,i}$ are respectively the density fluctuation operator and renormalized electron drift speed of the outer (o) and inner (i) channel, and u is the coupling constant between both channels with units of a velocity. This hamiltonian is diagonalized like so:

$$\mathcal{H}_{\text{2ch.}} = \pi\hbar v_c \int \rho_c^2(x) dx + \pi\hbar v_n \int \rho_n^2(x) dx$$

by new density fluctuation operators $\rho_{c,n}$ which are linked to the physical channels' fluctuation operators $\rho_{o,i}$ in the following way:

$$\begin{pmatrix} \rho_c \\ \rho_n \end{pmatrix} = \begin{pmatrix} \cos\theta & \sin\theta \\ \sin\theta & -\cos\theta \end{pmatrix} \begin{pmatrix} \rho_o \\ \rho_i \end{pmatrix} \qquad \text{with} \qquad \begin{aligned} v_c &= (v_o + v_i)/2 + \sqrt{(v_o - v_i)^2/4 + u^2} \\ v_n &= (v_o + v_i)/2 - \sqrt{(v_o - v_i)^2/4 + u^2} \end{aligned}$$

where $\theta \in [0, \pi/2]$ is a parameter that fully characterizes the asymmetry between both channels, defined as:

$$\tan(2\theta) = \frac{2u}{v_o - v_i} \tag{3.2}$$

The value $\theta = \pi/4$ corresponds to the special case where the physical channels are degenerate: $v_o = v_i$ (which never occurs for QH channels). In this particular case, ρ_c is the charge mode, carrying all the charge and ρ_n is the neutral mode (also commonly referred to as the spin mode as it carries all the spin) which constitute the ideal TLL charge and spin modes. For $\theta = 0, \pi/2$, both channels are independent from each other and the notions of charged and neutral modes do not make sense anymore. In between these two extreme cases of fully degenerate and fully independent channels, there exist a continuous variety of pairs of natural modes that closely resemble the ideal TLL charged/neutral modes when θ is close to $\pi/4$. Note that in the QH regime, $v_o > v_i$, but even in this case, where channels are non-degenerate ($v_o \neq v_i$), the modes can become very close to the ideal TLL ones provided the interchannel coupling u is strong (as can be seen from equation 3.2). Physically, the coupling strength u is related to the inter-channel capacitance: the larger it is, the larger will be the coupling (see [170, chap. 4], [25,26,28,171,172] and [122, chap. 3.3] and references therein for details).

In the following, experiments in the integer QH regime at filling factor $\nu = 2$ that showed inter-channel coupling between two quantum Hall channels to be strong, and consequently that the natural excitations are a (mostly) charged mode and a (mostly) neutral mode, are briefly presented. Then, we turn to a few other experiments that demonstrate the consequences of such a strong coupling on several observables. Finally, different strategies aiming at circumventing these effects are presented and their limitations are discussed.

3.2.1 Experimental demonstrations of the strong inter-channel coupling at $\nu = 2$

Frequency Dependent Characterization of Charge Separation

The first experiment of this kind was performed by Bocquillon and colleagues [25]. The setup consists of a simple QPC that is tuned to reflect either both channels or a single one. On one side of the QPC, a quantum capacitor driven with a sinusoidal excitation voltage at a frequencies ranging from 0.7 to 9 GHz excites charge density waves solely in the outer channel. These then propagate on 3.2 µm in close proximity to a co-propagating channel before reaching the QPC where the outer channel is filtered out. The collected current is that solely due to what is present in the inner channel, where nothing was injected directly. As a consequence, this frequency dependent current is entirely due to the coupling with the inner channel. The authors are capable to extract an inter-channel coupling parameter of $\theta \approx \pi/4$, thereby attesting of the strong coupling between both channels (note that the authors' definition of θ in their paper is different from our's by a factor 2).

Noise measurement of charge fractionalized wave-packets

In the experiment [26], the coupling parameter is extracted from shot-noise measurements. Shot-noise is injected on one channel through a first biased QPC set to half transmission. This channel is left to co-propagate for 8 µm near an adjacent one, which originates from grounded contact. In this process, due to inter-channel interactions, the individual charges that cross the first QPC fractionalize and distribute over the two channels in such a way that there is no net dc current on the second channel. However, this effectively heats up the second channel. This heating is detected by varying the transmission of a second QPC and monitoring the resulting shot-noise on the second channel. The indirectly generated shot-noise is found to be following a $[\tau(1-\tau)]^{\gamma}$ dependence with γ a parameter that can be linked to the coupling θ, which is then found to be $\theta \approx \pi/7$, markedly below the $\pi/4$ value required to observe the pure charge-neutral mode separation.

Revival of a quasi-particle peak

In a different experiment [28], a quantum dot was positioned so as to inject electrons in the outer channel at a well-defined energy above the Fermi sea. These then excite the natural plasmonic modes of the two coupled channels and the energy distribution is measured further downstream by performing spectroscopy through a second quantum dot. In general, what is observed is that as the injected energy peak is increased, the measured peak becomes smaller, then it eventually vanishes and revives at even higher energies.

This corresponds to the naive picture of a fast charge mode catching up with a slow neutral mode, that eventually leads to a first extinction of the quasiparticle peak in the outer channel when the condition

$$E_{in} \sim \frac{h v_c v_n}{(v_c - v_n)L} \left(\approx \frac{h v_n}{L} \text{ if } v_c \gg v_n \right) \tag{3.3}$$

is fulfilled (with E_{in} the input quasiparticle energy, and L the co-propagation length). The authors could also extract a parameter θ for each of their sample, ranging from 0.11π to 0.17π.

Time-resolved Spin Pulses

Probably the most emblematic experiment of this series, is the time-resolved detection of the spin-charge separation in QH channels of Hashisaka and colleagues [172]. In this experiment, a short current pulse is generated in one channel which then co-propagates with a second channel initially at equilibrium, for 260 µm. The coupling between both channels decomposes the initial single channel charge pulse in a fast charged pulse with essentially no spin polarization, and a slow, mostly neutral one which is spin polarized. The propagation speed of both pulse types being different, the time-resolved current measured at a detector QPC clearly shows two peaks when the initial excitation was injected on the measured channel and a peak followed by a dip when the initial excitation was injected on the channel adjacent to the measured one. In both measurements, the times of arrival of the first two peaks are synchronized and almost symmetrical. The second peak and the trough are also synchronized and almost anti-symmetric. This experiment convincingly demonstrates that an initial electronic excitation located in one channel decomposes in a fast charged mode and a slower neutral mode in two co-propagating quantum Hall channels. The extracted coupling parameter from this experiment is $\theta \approx \pi/5$.

Although there is a marked disparity among the coupling parameter θ extracted from the different experiments, each of these values attest of a significant coupling between both channels. In the following section, some visible consequences of such a coupling are briefly reviewed.

3.2.2 Consequences of the strong inter-channel coupling

Energy Relaxation

In [35], Le Sueur and colleagues introduce a double-step fermi function in the outer channel thanks to a first voltage biased QPC tuned to an intermediate transmission probability τ. This channel hosting a non-equilibrium particle distribution co-propagates next to the inner QH channel on a distance that can be tuned to four different values: 0.8 µm, 2.2 µm, 10 µm and 30 µm. After these different propagation lengths, a quantum

dot is used to perform the spectroscopy of the energy distribution of the outer channel. When this distance is small (0.8, 2.2 µm), a clear signature of the injected double-step distribution function is observed. On the other hand, when the propagation length is longer (10 µm or 30 µm), this signature vanishes, attesting of the relaxation of the initial double-step distribution to an energy distribution resembling a hot thermal Fermi function. In a more recent experiment [37], Itoh and colleagues showed that the resulting distribution function was a metastable, non-equilibrium one, with on a moderately large propagation length (15 µm).

HOM experiment's imperfect Pauli dip

In the HOM experiment described in section 2.2.2, [23], it was found that the Pauli dip was imperfect (in contrast with the experiment performed with levitons, but not in the QH regime [24]). This imperfect dip is compatible with decoherence caused by inter-channel coupling as argued in [173–175]. In [173], the current noise HOM dip is studied by performing collision with both the inner and outer channels, while always injecting a charge pulse only in the outer channel. The simple fact that a HOM dip can be seen on the inner channel while no charge pulse was originally injected along it convincingly demonstrates the inter-channel coupling mechanism. In [174], the experiment is repeated at filling factor of $\nu = 3$ where it is found that the dip on the outer channel is even more suppressed than at $\nu = 2$, compatible with the idea that inter-channel interactions will be even larger with more channels.

Interference dephasing

Injecting shot noise on a channel adjacent to one of the interfering channels of an electronic MZI, it was found that dephasing could be introduced [22,176,177], suggesting that the inter-channel coupling is indeed a predominant source of dephasing. Note that the observed dephasing is probably a mixture of phase averaging and pure decoherence. These MZI experiments are further described and discussed in section 4.1.

Multiple side Lobes in the interference visibility of MZI

Inter-channel interactions also show when a dc voltage is applied to the interfering channel of a MZI [32,33] when the co-propagating (non-interfering) channel is kept to ground on both sides of the MZI. Effectively, in these experiments, the visibility vanishes at several values of V_{dc}. This a priori peculiar lobe pattern can be qualitatively understood in terms of the fast charged mode catching up with the slower neutral mode over the length L of the MZI. The first QPC of the interferometer partitions electrons at an energy eV_{dc} (where V_{dc} is the bias voltage of the source contact), such that when $eV_{\mathrm{dc}} \sim hv_c v_n/(v_c - v_n)L$, the charge density wave that was initially in the outer channel gets transferred entirely to the inner channel, preventing any recombination of the splitted initial density wave at the second QPC.

3.2.3 Control of the inter-channel coupling

In regard of the previous experiments, the inter-channel coupling is responsible of several marked effects, and it consequently appears to be the dominant mechanism for electron decoherence. As a consequence, it would be desirable to control it. An overview of the several strategies already adopted is given in what follows.

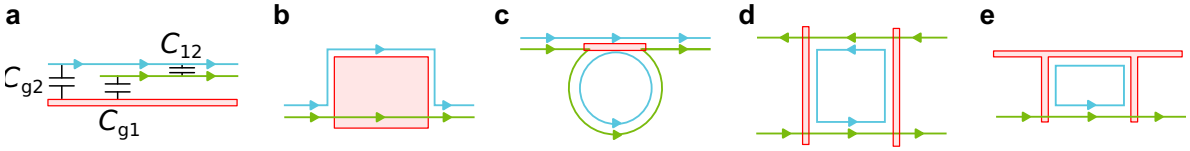

Figure 3.1: Schematics of the different strategies adopted to tune inter-channel coupling, the outer channel is drawn in green, the inner channel in blue and the top gates are in red. **a** The channels are pushed away from the side gate, resulting in smaller capacitances $C_{g1,g2}$ that tend to screen the interchannel coupling C_{12}, used in [172]. **b** A large top gate tunes the density of the 2DEG below to reach an effective filling factor of $\nu = 1$, such that the inner channel is repelled far away from the inner one, used in [28] **c** Loop strategy employed in [35] which resulted in an essentially supressed energy relaxation. The inner channel is confined into a small loop behind a gate while the outer channel is free to flow. **d** Strategy used in the MZI of [41]. The inner channel is confined into small loops but is capacitively coupled to both counter-propagating channels. **e** Strategy used in this work [42]: the inner channel is confined into small loops and coupled to a single outer channel.

Changing the filling factor for $\nu = 1$

The most obvious solution to get rid of inter-channel coupling would be to keep just one channel as it is clearly expected from equation 3.1 that the intra-channel interactions only renormalize the drift velocity and should therefore not affect the electron coherence. However, this was observed to yield lower quantum interference visibility $\mathcal{V}$ than for 2 co-propagating channels. For example, in MZIs the visibility of interferometers at $\nu = 1$ is significantly smaller than at $\nu = 2$ (e.g. in [32] $\mathcal{V}(\nu = 1) \approx 23\%$ while $\mathcal{V}(\nu = 2) \approx 45\%$). The real reasons for this are not clearly identified, but there are several hypothesis. First, the bulk being ferromagnetic at $\nu = 1$, it is possible that the channel interacts with spin textures (such as skyrmions) within the bulk, this cannot occur at $\nu = 2$ as the bulk is not ferromagnetic. Another possibility is interactions with other bulk degrees of freedom such as trapped charges, which is less likely at $\nu = 2$ than at $\nu = 1$ due to the much greater Landau cyclotron gap compared to the Zeeman gap. Also edge reconstruction, when one channel divides into a combination of downstream and upstream channels, is another possible reason for a poorer visibility.

Screening interactions with a metallic gate

In their time-resolved experiment, Hashisaka and colleagues vary the voltage of a side gate located just near their two co-propagating channels [172]. In applying a voltage

more and more negative, the channels are pushed further and further away from the gate (see figure 3.1 a). In doing so, the capacitance of both channels towards this gate is gradually diminished, consequently increasing the relative inter-channel capacitance, and thereby their relative coupling strength. This increased relative inter-channel coupling then shows in the velocity of the charged mode that can be increased by a factor of ~ 2.5 while the neutral mode's velocity remains roughly constant. This shows the importance of screening: by placing a metallic gate in close proximity to the co-propagating channels, one can significantly diminish their relative coupling.

Pushing one channel away from the other

In [28], a large top gate can be used to locally tune the underlying 2DEG at an effective filling factor of $\nu = 1$, thereby pushing the co-propagating channel far away from it as illustrated in figure 3.1 b. The observed quasiparticle peak is much larger under these conditions compared to when both channels are left to co-propagate next to each other as in the $\nu = 2$ configuration. The much smaller energy relaxation indicates that the inter-channel coupling is reduced. Moreover, when both channels are separated, the peak's vanishing and revival previously mentioned is not observed anymore. This attests that inter-channel interactions are responsible for this vanishing and revival, consistent with the picture of a fast charge mode catching up with a neutral mode in such a way that the electronic excitation is essentially suppressed at some energies defined by equation 3.3.

Constraining one channel into small loops

It is possible to minimize the long range inter-channel interactions by closing the trajectory of the inner channel into a loop small enough that it forms a quantum dot. Its energy level spacing is given by $\Delta = hv_d/L$ with L the loop length and v_d the drift velocity ($v_d \approx 10^4 - 5.10^5\,\mathrm{m.s^{-1}}$ in GaAs). By engineering the dot so that $\Delta \gg k_B T, eV$, it is possible to prevent any excitations to be generated within it, thereby effectively freezing inter-channel interactions. This was implemented in [34] (see figure 3.1 c), where the energy relaxation was found to be drastically reduced when the co-propagating channel was made to loop around on itself in a quantum dot, even for a propagation length as large as 8 µm (corresponding to $\Delta \approx 52\,\mu\mathrm{eV} \gtrsim eV \gg k_B T$).

That inspired the work [41], in which this strategy was implemented in a MZI to minimize interactions between the interfering (outer) channel and the inner one by segmenting it into multiple small loops (see figure 3.1 d). However, in this case, only a disappointing factor of two was gained on the visibility by using this strategy compared to the standard case where the inner channel was let free. It is suspected that the formed loops can mediate a coupling between the two counter-propagating outer channels as can be seen in figure 3.1 d.

3.2.4 Other possible decoherence mechanisms

Below, we list other potential mechanisms for decoherence in QH edge channels:

- long range intra-channel interactions [178–182],
- long range interactions between distant channels [36,183],
- edge reconstruction that predicts the existence of new modes, that could act in a similar way as those described above [155,156],
- bulk degrees of freedom that are not well identified.
- interactions with optical phonons [38], although that was only demonstrated for very large electron energy ($\sim 10 - 100\,\mathrm{meV}$),

In this section, several experiments were presented, the first few of which clearly demonstrate the significant inter-channel coupling occuring between two QH channels at filling factor of $\nu = 2$. Then, another set of experiments was presented to show the multiple manners in which this strong coupling can manifest. Even though these are not necessarily directly linked to decoherence, it is obvious that if energy relaxation occurs, for example, then it won't allow for coherence to be preserved. On the other hand, a controlling strategy successfully achieving a reduction or even a suppression of the inter-channel energy relaxation does not necessarily protect against decoherence and to be sure, one needs to check and it is precisely the purpose of the study we present in the remaining of this chapter.

3.3 Principle of the experiment

As presented above, inter-channel coupling is responsible for many peculiar behaviour of the electrons in QH channels. It is thus possible to learn from these past experiments, in particular the MZI one that tried to isolate the inner channel in small loops [41] and adopt a strategy that would remedy to the possible coupling between the counter-propagating channels by completely isolating the inner channel loops as illustrated in figure 3.1 e. To test whether this strategy is efficient to significantly minimize decoherence, it is possible to use a MZI as explained below.

3.3.1 The electronic Mach-Zehnder interferometer as a coherence length measurement tool

Several strategies can be used to determine the coherence length of electrons in a solid-state circuit, and more specifically along QH channels. The most direct way however remains the two-paths interferometer [21], and more precisely the Mach-Zehnder interferometer as is illustrated in figure 2.3 b (for exotic alternatives to infer the coherence length, see e.g. the proposal [184] or, the experiment [185]). Indeed, we recall that the current across such an interferometer is given by equation 2.3 where the visibility

(equation 2.4) is unity only if there is no dephasing. However, in practice the visibility never reaches this ideal value, thus giving information about the coherent propagation of electrons. A large visibility therefore indicates that the electrons conserved their coherence.

Coherent transport across mesoscopic devices can be described by the scattering theory. In this framework, the expression for the current across a MZI reads (see appendix section C for full derivation)

$$I_{\mathrm{MZI}} = I_{\mathrm{in}} \left(R_2 R_1 + T_2 T_1 + 2\sqrt{R_2 R_1 T_2 T_1} \cos(\phi_d - \phi_u) \right) \tag{3.4}$$

where R_i, T_i are respectively the reflection and transmission probabilities at QPC i (with $T_i + R_i = 1$). From equation equation 3.4, it is possible to see that at $T_1 = T_2 = 0.5$ ($R_1 = R_2 = 0.5$), the scattering theory predicts oscillations with perfect contrast ($\mathcal{V} = 1$): the current I_{MZI} should oscillate between 0 and the injected current at the source I_{in}. This prediction does not account for the inevitable decoherence mechanisms that will take place in a real device however, and needs to be refined. Within the scattering formalism, decoherence can be introduced by inserting a dephasing probe on one of the two paths as was done by Marquardt and colleagues [186]. However, the authors point out that such an approach gives no information on the microscopic dephasing mechanisms, and that what the dephasing probe physically mimics is hard to picture. A more fundamental approach, still by Marquardt, consists in introducing a coupling between the electrons going through the MZI and a quantum bath [187,188], this nevertheless requires assuming the nature of the quantum bath.

The usual experimentalists' approach is to introduce an exponential reduction prefactor in front of the oscillatory term: e^{-2L/L_ϕ} [21], where L is the length of one arm of the device, and L_ϕ the coherence length. This prefactor ensures that the visibility is capped to 1 in the case of an infinite coherence length and the exponential decay assumes a Poisson process of dephasing events along the propagation paths, which is the simplest assumption possible. With this new element, it is possible to rewrite eq equation 3.4 as

$$I_{\mathrm{MZI}} = I_{\mathrm{in}} \left(R_2 R_1 + T_2 T_1 + 2e^{-2L/L_\phi} \sqrt{R_2 R_1 T_2 T_1} \cos(\phi_d - \phi_u) \right) \tag{3.5}$$

which, by analogy with formula equation 2.3 enables us to establish a link between the visibility and the coherence length:

$$\mathcal{V} = 2 \frac{1}{R_2 R_1 + T_2 T_1} e^{-2L/L_\phi} \sqrt{R_2 R_1 T_2 T_1} \tag{3.6}$$

Before moving on, we raise a point on what the experimental visibility $\mathcal{V}_{\mathrm{exp}}$ actually measures. The interference contrast can effectively be diminished via two possible mechanisms:

- **intrinsic decoherence**, when the electrons are affected by their environment and lose their quantum coherence,
- **phase averaging** over the measurement integration time, during which many one-electron interferences can take place.

It is not simple to tell apart one mechanism from the other, as a consequence throughout this manuscript, the term dephasing is used to qualify the combination of both decoherence and phase averaging.

3.4 Devices specificities

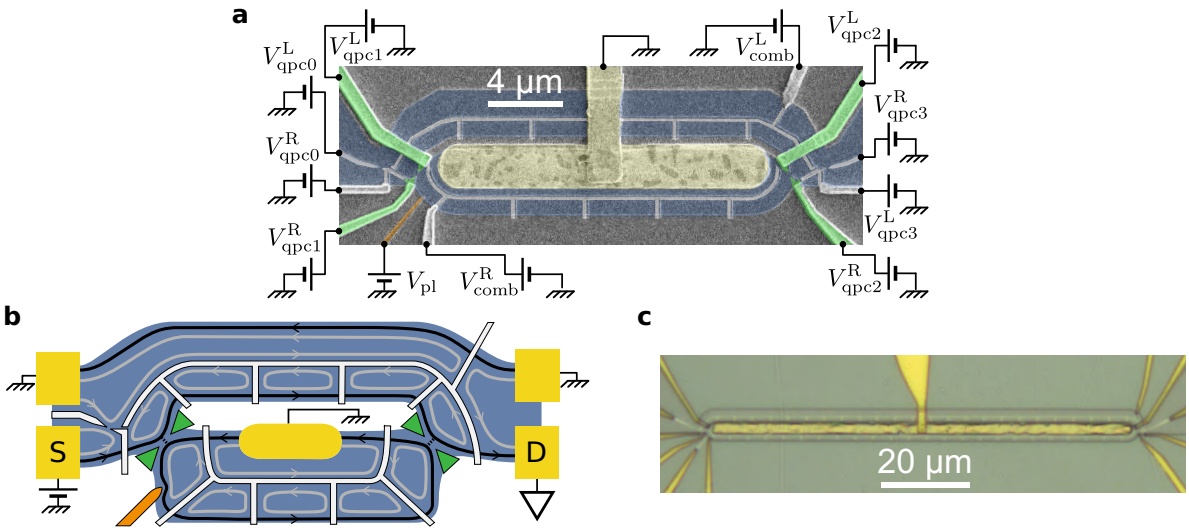

Figure 3.2: **a** False colored SEM picture of the 24 μm long device. QPC 0 and 3 (white) are always tuned to fully transmit either the outer or both channels. The two QPC used as beam-splitters for interferences are QPC 1 and 2 (green), the gates $QPC^{L}_{1,2}$ are connected via air-bridges that span the mesa. The central ohmic contact (ligth yellow), sole element in this picture to be in electrical contact with the 2DEG, is linked to ground via another air-bridge (visible in the center top). **b** Simplified schematic of the MZI, with the trajectories of the outer channel (black) and inner channel (grey), when the device is tuned to form loops with the inner channel. QPC3 is not shown here as it was left fully open for the whole study. **c** Optical image of the 100 μm long device, the comb-shaped gates can be distinguished faintly (appearing white and very thin), the elongated horizontal golden piece of metal is the central ohmic contact, linked to ground via the air bridge.

Two devices were used for this study. An SEM scan of the first device and an optical image of the second are shown in figure 3.2 a & c, respectively. Both electronic MZI were measured in the integer QH regime at filling factor of two, at a magnetic field of 4.3 T (see figure A.1 in appendix for the plateau). They were both nanofabricated simultaneously, from the same 2DEG with a mobility $\mu_e \approx 10^6\,\mathrm{cm^2V^{-1}s^{-1}}$ and density $2.5 \times 10^{11}\,\mathrm{cm^{-2}}$, on the same chip, just separated by a few mm from one another. The first device has an arm-length of 24 μm and the second of 100 μm. Special care was taken such that both arms of each device have equal length (at least in the lithographic design)

in order to minimize the energy dependence of the interferences. It was checked that the outer channel was well-coupled to the central ohmic contact (see section A.2). The originality of these electronic MZI resides in the comb-shaped metallic gates deposited along the paths of both interfering channels. To be in the regime where the inner channel is confined in small loops as depicted in figure 3.2 b, it is necessary to characterize the transmission across the comb gates as a function of the applied voltage. These curves are shown for the comb-shaped gates in figure 3.3 a,b as well as the $\mathrm{QPC}_0^{\mathrm{R}}$ and $\mathrm{QPC}_3^{\mathrm{L}}$ gates in figure 3.3 c,d.

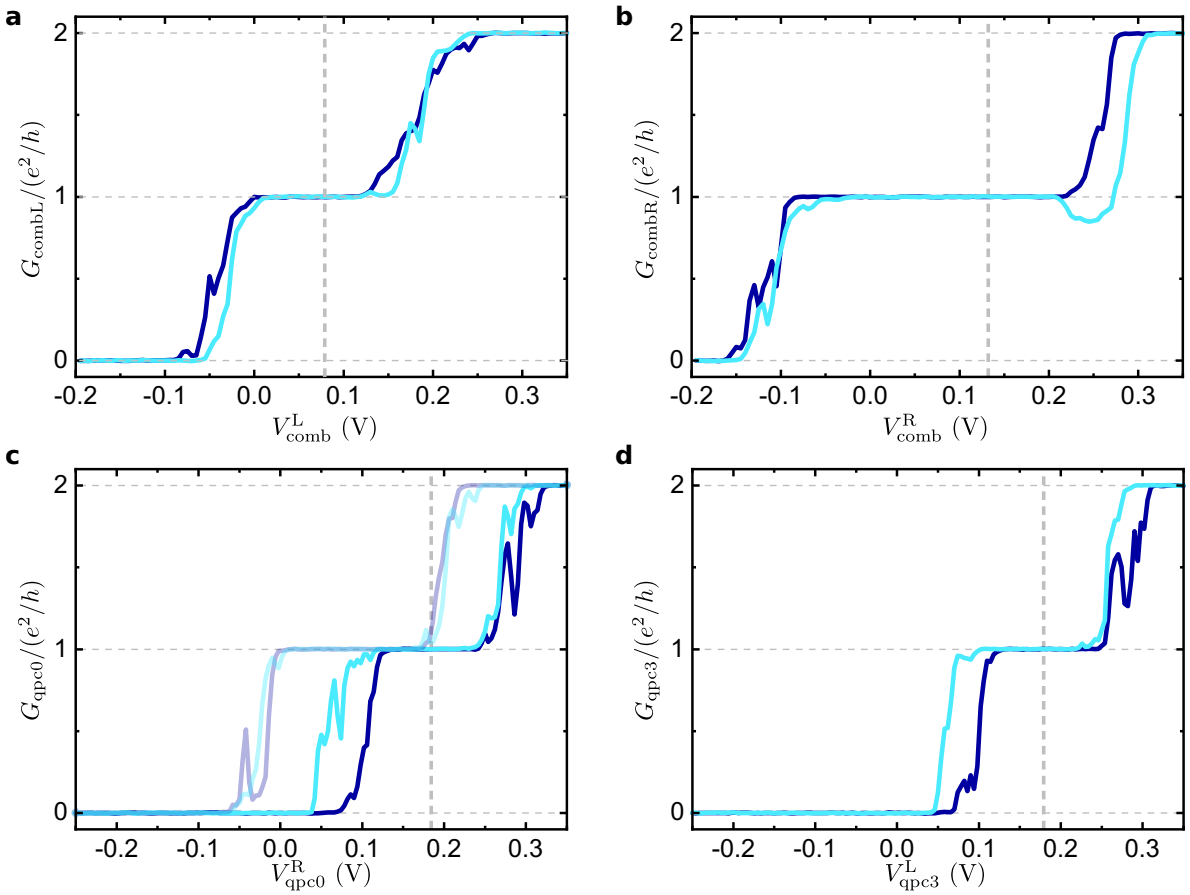

Figure 3.3: Conductance across the metallic gates of the 24 µm long device (dark blue) and the 100 µm long device (light blue). **a,b** Conductance across the comb-shaped gates. **c,d** Conductance across the QPC 0 & 3, in **c** the left gate of QPC 0 was set to a voltage $V^{\mathrm{L}}_{\mathrm{qpc0}} \approx 0\,\mathrm{V}$. The difference between the full and faded curves is that only $V^{\mathrm{R}}_{\mathrm{qpc1}}$ was set to $-0.85\,\mathrm{V}$, and $+0.35\,\mathrm{V}$, respectively, illustrating that significant cross-talk occurs between gates located next to each other. In **d**, the right QPC 3 gate was set to a voltage $V^{\mathrm{R}}_{\mathrm{qpc3}} \approx +0.35\,\mathrm{V}$.

Plateaus in the conductance can be observed as a function of the gate voltage at e^2/h and $2e^2/h$. The first plateau occurs when these gates let only a single channel through, and this spans a large set of electrostatic voltages. It can be puzzling for the reader to see that the plateau at e^2/h occurs at positive values of gate voltage. That is because the gates were polarized at $+0.35\,\mathrm{V}$ during the cooldown while the 2DEG is kept to the ground. This is a common practice to avoid putting too negative voltages on the

gates, it is also thought to help empty charge traps that could trigger more noise in the measurements. Therefore, applying a gate voltage smaller than this +0.35 V reference value effectively reduces the electronic density in the 2DEG below. Now, let's turn to the QPCs, the electrostatic voltages of each side provide two levers for each QPC. The transmission map as a function of both gate voltages is plotted in figure 3.4. Regions where a relatively smooth transition from zero to full transmission are seeked, as sharp features often indicate energy-dependent resonances that are sensitive to spurious noise in the sample, thereby potentially affecting the QPC transmission in an uncontrolled manner. For practical matters, we usually then fix one gate voltage and sweep the other to reach the desired transmission. The curves of figure 3.4 e and f respectively present the transmission of QPC 2 and 1 for both devices when varying the voltage of the right QPC gate, for a fixed voltage of the left gate. The dashed lines indicate data taken when a DC bias was applied to the incoming channel, illustrating that the transmission varies as a function of energy but only by a few percents. This ascertains that the chosen working points are free of spurious changes in transmission. What can be observed from all the curves of figures 3.3, 3.4 is that they are fairly similar in both samples, with the transitions between plateaux occuring at very close values of gate voltage. This reproducibility is reassuring as the lithographic parameters were the same for both samples.

3.5 MZI interferences

Conductance oscillations in the standard MZI configuration (no loops)

The goal of this study is to find out whether confining the inner channel into small loops is effective at strongly enhancing the electronic quantum coherence. As a reference experiment, we start by measuring MZI interferences for which the inner channel is left co-propagating next to the outer one. Both MZI QPCs (1&2) are tuned to half transmission, in order to maximize the visibility. A sketch of the devices tuned in this configuration is depicted in figure 3.5 b. The observed interferences, plotted in terms of the outer channel transmission across the whole MZI in figure 3.5 d (in dark red), have a visibility of around 6% in the 24 μm long device, which corresponds to a 17 μm coherence length. This is at the level of previously measured values in similar systems, at comparable temperatures (e.g. [21]). In the larger device (light red curve in figure 3.5 e), no interferences can be observed as expected from the fact that it is 5-6 times larger than the coherence length measured on the smaller device. A striking feature of this measurement is that it slightly varies around the 40% transmission mark, lower than the expected flat 50% signal. This is due to inter-channel tunneling. When co-propagating over such large distances, the probability for electrons to tunnel from one channel to the adjacent one becomes significant even though such events require a spin-flip [189,190]. The amount of tunneling is characterized in section A.3. On the other hand, when the device is tuned so that comb-shaped gates only transmit the outer channel and force

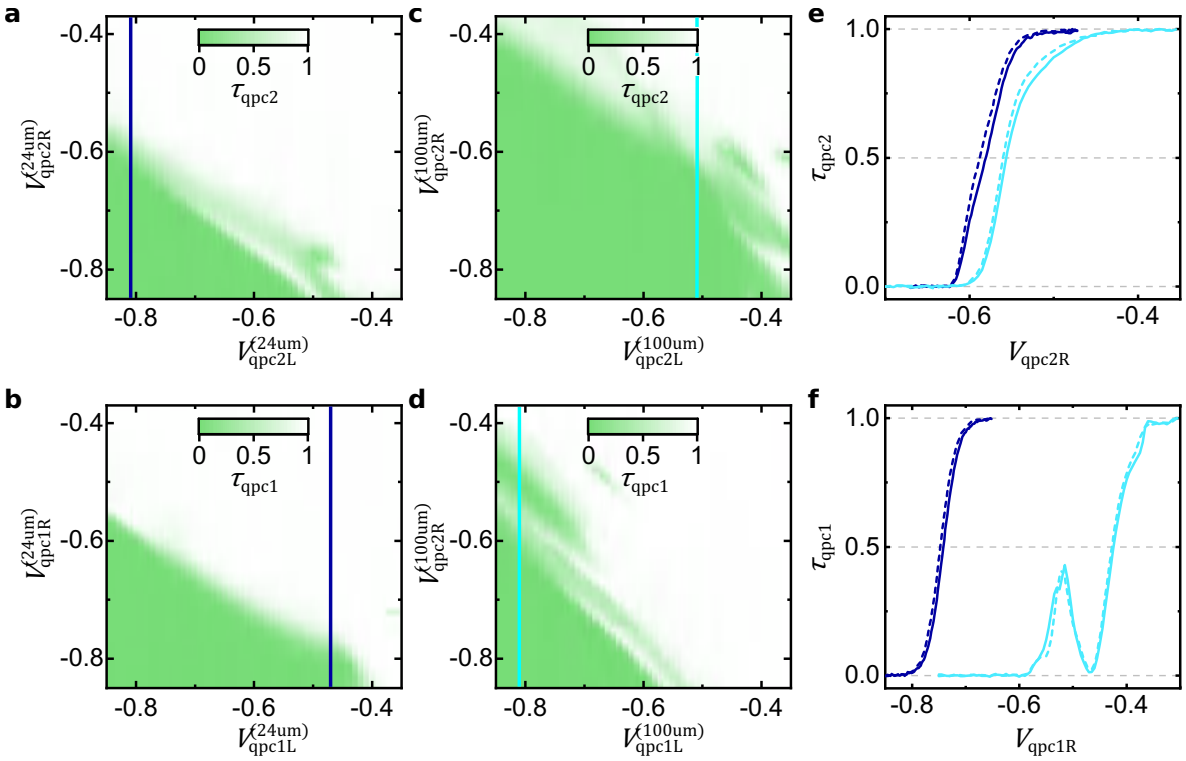

Figure 3.4: Transmission curves of the quantum point contacts in both MZI devices. **a,b,d,f** 2D maps of the QPC transmission in the 24 µm device (**a,b**) as well as in the 100 µm device (**c,d**) as a function of both gate voltages. For practical purposes, it is easier to fix one of the gate voltages and vary the second one, as displayed on **e,f**. The full lines are cuts of the conductance 2D plot by fixing the left gate voltage each time at a value indicated by the colored lines in **a-d**. Dark blue lines are for the small (24 µm) device, while light blue are for the long (100 µm) device. Dashed lines indicate transmission curves taken when applying a finite dc voltage to the injected electrons (47 µV and 35 µV respectively in the small and large device). The transmission is therefore energy dependent, but this dependence is reasonably small

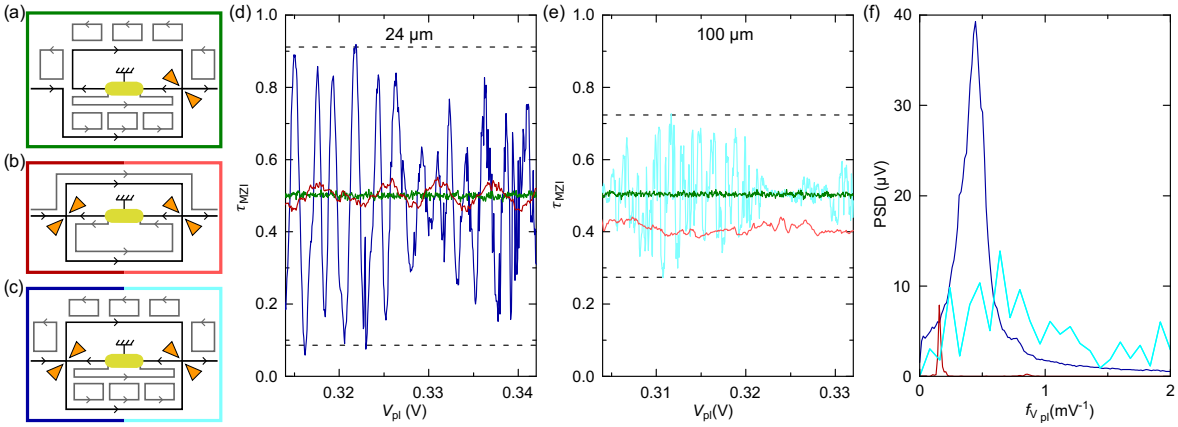

Figure 3.5: **a-c** Schematics of the different MZI configurations. Frames' colors correspond to the colors of the curves measured in the corresponding configuration. **d,e** Aharanov-Bohm interferences in the 24 µm and 100 µm device respectively, when both QPCs are tuned to half transmission $\tau_{QPC1,2} \approx 1/2$. **f** Fourier transform power spectrum of the interference signals for the 24 µm device with a co-propagating inner channel (dark red), inner channel forced into loops (dark blue) and the 100 µm device with the inner channel forced into loops (light blue). For the latter, the analysis was restricted to regions of high visibility, spanning 6 expected MZI periods.

the inner channel into loops, tunneling events are suppressed. Data acquired in this regime with the first (second) MZI QPC set to fully-(half-)transmit the outer channel (schematic of figure 3.5 a), in order to avoid any interferences, is displayed in green in figure 3.5 d,e. The noise level of this signal also indicates our measurement uncertainty $\sim 1\%$.

Conductance oscillations with closed inner channel loops

The device tuned so that comb-shaped gates only transmit the outer channel, and both MZI QPCs are set to half-transmission. Representative data of the observed signal upon varying the plunger gate voltage V_{pl} is shown for both devices in figure 3.5. The data for the smaller $L = 24\,\mu m$ device shows oscillations of a large visibility, up to 82% (dark blue curve), with a period about three times smaller than that observed when both channels are co-propagating. This change in the periodicity has already been observed in a similar context [18] and can be explained by the difference in the screening of V_{pl} by the inner channel. When the plunger gate voltage is gradually made more negative, the capacitively coupled edge channels are pushed away. As the electronic density decreases locally, an excess of negative charges needs to be evacuated. When both channels are co-propagating, both channels are affected similarly by the plunger gate voltage and the excess charge is expulsed towards the ohmic contacts. The corresponding decrease of the local density in the inner channel itself therefore partially screens the effect of the plunger gate. In the case where the inner channel is confined in small loops, the excess charge cannot be evacuated but must be redistributed along the loop. The inner channel's screening effect is thereby much reduced, and the effect of V_{pl} on the

interfering outer channel is consequently enhanced.

Instability of the oscillations

A striking feature of our data with closed loops is the noisy character of the oscillations as well as the fact that few of the observed ones reach the 82% visibility mark, while many are much smaller. Such behaviour can be accounted by what we will call phase noise. This corresponds to fluctuations on the MZI phase that take place on time scales shorter or comparable than the measurement time ($\sim 100\,\mathrm{ms}$) but longer than the propagation time of electrons along the MZI ($\lesssim 1\,\mathrm{ns}$). It could result from some moving charges along the two paths. Such moving charges would act as local gates, varying the effective area enclosed in between the two paths. Such an effect can be accounted for by adding a fluctuating phase term $\delta\varphi(t)$ in equation 3.4:

$$I_{\mathrm{MZI}}(t) = \bar{I}(1 + \mathcal{V}\cos(\phi + \delta\varphi(t)) \tag{3.7}$$

The actually measured current will however be averaged on our measurement time window $\Delta t \approx 100\,\mathrm{ms}$ corresponding to the integration time for each data point:

$$I_{\mathrm{MZI}}^{\mathrm{meas}} = \langle I_{\mathrm{MZI}} \rangle = \int_0^{\Delta t} I_{\mathrm{MZI}}(t)dt \tag{3.8}$$

If the phase noise is gaussian, it results in a reduction factor in front of the interference term (see [53] although it was discussed there in terms of pure decoherence):

$$\langle I_{\mathrm{MZI}} \rangle = \bar{I}[1 + \mathcal{V}e^{-\langle \delta\varphi^2 \rangle/2}\cos(\phi)] \tag{3.9}$$

where $\langle \delta\varphi^2 \rangle$ is the variance of the phase fluctuations. From equation 3.9, it seems a priori impossible to distinguish pure decoherence (here included in $\mathcal{V}$) from phase averaging by a simple conductance measurement scheme. The intrinsic, decoherence limited, $\mathcal{V}$ only constitutes an upper bound to the experimental visibility $\mathcal{V}_{\mathrm{exp}}$ that can only be approached when $\langle \delta\varphi^2 \rangle$ is reduced ($\ll 1$). As we will see in the following, the presence of such phase noise can be directly evidenced by current noise measurements. First, we concentrate on conductance measurements.

Phase noise has already been observed in electronic MZI interferometers, as in [33] where clear Aharonov-Bohm interferences could not be observed in the conductance. The distribution of conductance data points were nonetheless mainly distributed around a maximum and a minimum conductance values. This is expected for a phase noise with a relatively small amplitude ($\langle \delta\varphi^2 \rangle \ll (2\pi)^2$) as the MZI conductance exhibits only a small phase dependence around its maximum and minimum values. Such an analysis can be performed in both configurations: with and without the loops as shown on figure 3.6 a,b. As can be seen, the distribution of conductance points is effectively peaked around extrema values in the conductance in the no-loops, $L = 24\,\mu\mathrm{m}$ case (a). However, in the loop-case (figure 3.6 b), the distribution tends to be more peaked around

the center, despite some clear oscillations visible in the left panel. This behaviour can still be explained by phase noise. If $\langle \delta\varphi^2 \rangle \sim (2\pi)^2$, the phase averaged current then approaches the mean current $\bar{I}$. From the left panel of figure 3.6 b, it is also possible to deduce that for some gate voltage values or some time, $\langle \delta\varphi^2 \rangle$ is smaller, corresponding to the regions of high visibility oscillations.

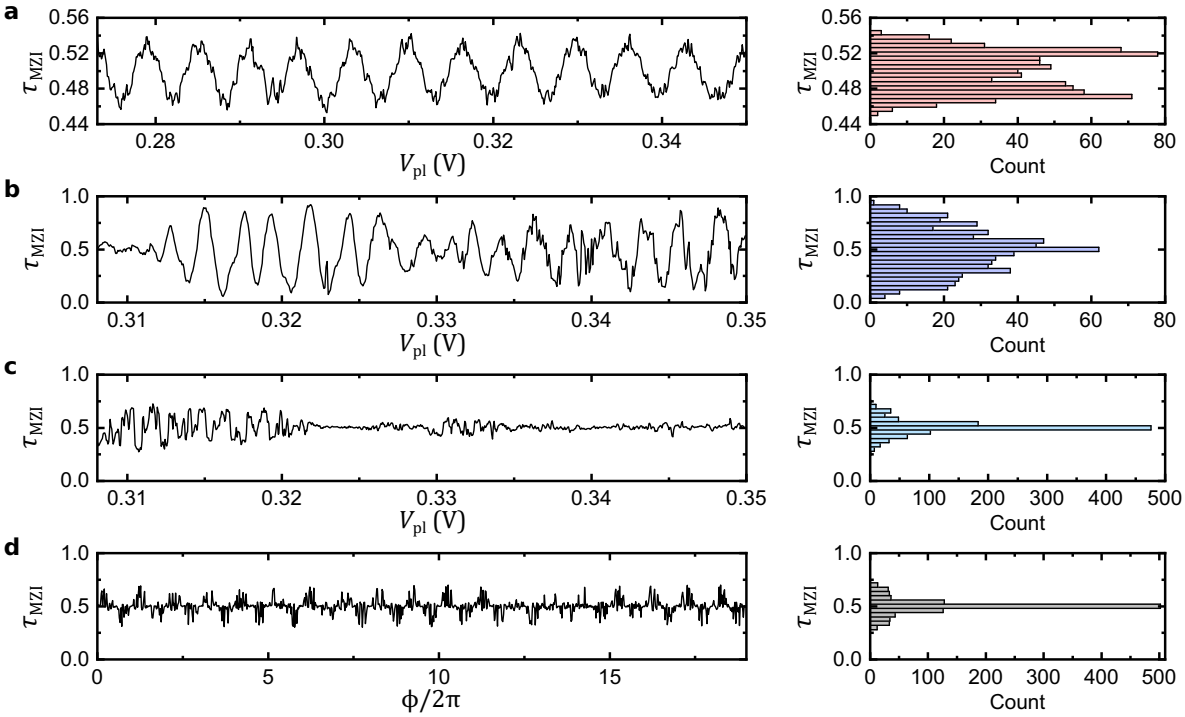

Figure 3.6: **a,b,c** Left panel: renormalised conductance traces as a function of plunger gate voltages in **a** the 24 µm device with two copropagating channels **b**&**c** respectively the 24 & 100 µm device with the inner channel confined into loops. Right panel: histograms of the corresponding conductance data points displayed on the left. The histogram of **a** boasts maxima at the extrema of conductance as in [33]. On the contrary, histograms **b** & **c** are peaked around the mean conductance value, which can be explained by phase averaging. **d** Left panel: a simulated conductance trace according to the model $I_{\mathrm{MZI}} = 1/2\varphi \int_{\phi-\varphi}^{\phi+\varphi} dx 1/2(1 + 0.4\sin(x))$ where φ is a pseudo-random number following a normal distribution with a variance of $2\pi/1.1$. This variance was chosen such that the histogram shown in the right panel approximately reproduces the distribution of our measured conductance data shown in **c**. Note that the discretization was chosen to be the same than that of the measured data in **c** (45 points per period) and that the span is also the same as in **b**&**c** (19 periods).

The noisy character of the conductance is even more pronounced in the 100 µm long device as displayed on figure 3.6 c, and the associated histogram is even more peaked. To convince ourselves that such a histogram can be reproduced simply with phase averaging, a simulated conductance trace is generated and plotted in figure 3.6 d, using equation 3.8 that we re-write: $I_{\mathrm{MZI}} = 1/2\varphi \int_{\phi-\varphi}^{\phi+\varphi} dx 1/2(1 + 0.4\sin(x))$ with φ a pseudo-random number following a normal distribution with a variance of $2\pi/1.1$ specially chosen to approximately reproduce the histogram of the measured data in figure 3.6 c. In this model, a uniform distribution of phase, independent of V_{pl} and uncorrelated

in time, was assumed, which is clearly inadequate to fully reproduce the data. This model, shows that the histogram representation can vary drastically depending on $\langle\delta\varphi\rangle$. The comparison with the data also suggests that $\delta\varphi$ is either time and/or gate voltage dependent.

While we have just seen that phase noise can explain the irregular behaviour of our conductance data, let us stress that intrinsic decoherence would not create such features. Effectively, phase noise locally/temporarily limits the observed visibility, while decoherence imposes a hard upper limit to the visibility that cannot be overcome. Taking advantage of the irregular phase noise $\delta\varphi$, the intrinsic, decoherence-limited visibility is more closely approached by the maximum measured experimental visibility: $\mathcal{V}_{\rm exp}^{(\rm max)} \approx 82(45)\%$ for the $L = 24(100)\,\mu$m long device. These values correspond to a coherence length of $L_\phi \approx 240(250)\,\mu$m, using equation 3.6. The deduced $L_\phi \approx 250\,\mu$m is possibly under-estimated, but the concording values deduced from two devices of different lengths suggests that the intrinsic value of L_ϕ is closely approached.

3.6 Visibility dependence as $\sim \sqrt{\tau_{\rm qpc}(1-\tau_{\rm qpc})}$

To further establish the presence of true Aharonov-Bohm interferences in our devices, as well as the claimed $L_\phi \approx 250\,\mu$m, we present additional conductance measurements.

A first important test is to confirm that the observed oscillations in $I_{\rm MZI}$ effectively result from MZI quantum interferences and not from some spurious source like, for example, noisy QPCs. For this purpose, the dependence of the amplitude of the MZI quantum interferences is measured versus the transmission probability of one of the two beam-splitters. The expected dependence can be obtained from the expression of the visibility of equation 3.6, in which the transmission probabilities of each QPC are substituted: $T_i \equiv \tau_i$ as well as $R_i = 1 - T_i \equiv 1 - \tau_i$. Fixing the transmission of the right QPC at $\tau_{\rm QPC2} = 0.5$, the average current becomes $\bar{I}_{\rm MZI} = I_{\rm in}/2$ and by one gets for the visibility:

$$\mathcal{V} = 2e^{-2L/L_\phi}\sqrt{\tau_{\rm QPC1}(1-\tau_{\rm QPC1})} \tag{3.10}$$

To check that the visibility indeed behaves according to equation 3.10 (as has been checked on different MZIs [20,33,191]), we acquired conductance data as a function of the plunger gate voltage (as shown in figures 3.5, 3.6) for several values of $\tau_{\rm qpc1}$, while fixing $\tau_{\rm qpc1} = 0.5$. Each scan was cut into intervals corresponding to the length of a period in plunger gate voltage 2.26 mV extracted from the Fourier transform (figure 3.5 f). A local visibility was extracted from the maximum and minimum values of the conductance within each of these intervals. To ensure that no maximum visibility was missed, an overlap of half a period was taken from interval to interval. Each extracted local visibility corresponds to one data point of figure 3.7. As can be seen from directly looking at our conductance data, the local visibilities range from very small values to much larger ones. Assuming a phase noise on the MZI interferences, the saturation

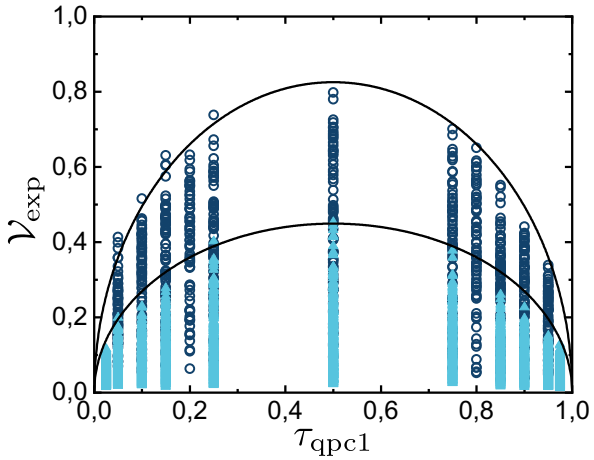

Figure 3.7: Each individual dark (light) blue symbol, measured in the $L = 24(100)\,\mu$m device, is a local visibility (see text) of Aharonov-Bohm interferences as a function of the transmission of QPC_1 when QPC_2 is kept constant at half transmission. Full black lines are obtained from equation 3.10 by inserting each device length for $L = 24, 100\,\mu$m and the same coherence length $L_\phi = 250\,\mu$m.

values of the visibility should follow the trend of equation 3.10. The full black lines are direct plots of equation 3.10 with $L = 24, 100\,\mu$m and $L_\phi = 250\,\mu$m. This attests that our observed conductance fluctuations are indeed due to electronic interferences. Moreover, the fact that the observed $\sqrt{\tau_{\rm qpc}(1-\tau_{\rm qpc})}$ trend can be quantitatively linked to a single value of $L_\phi = 250\,\mu$m on both devices of very different sizes, suggests that the maximum values of the visibility closely approach the intrinsic, decoherence-limited visibility $\mathcal{V}$ (note that otherwise, the intrinsic L_ϕ would be larger than $250\,\mu$m).

3.7 MZI Current noise as a function of voltage bias.

In section 3.5, it was shown that conductance data can partially differentiate intrinsic decoherence from phase averaging. In the following, we show that the presence of phase noise in our MZI devices can be directly established, by measuring the current noise across the MZI, in the MHz range (over a 180 kHz bandwidth centered on 855 kHz to be precise).

Incoherent MZI

Let's first see what one would expect for the noise if the MZI was perfectly incoherent. Following Marquardt & Bruder [186], a first naive expectation for the voltage dependent part of the noise $S(V_{\rm dc})$ would be to consider the incoherent transmission on the MZI and treat it as a unique scatterer (see [186,192, sec. II.D]):

$$S(V_{\rm dc}) = \frac{eV_{\rm dc}}{R_K}\tau_{\rm MZI}^{\rm inc.}(1-\tau_{\rm MZI}^{\rm inc.})\coth\left(\frac{eV_{\rm dc}}{2k_BT}\right) \tag{3.11}$$

where $\tau_{\mathrm{MZI}}^{\mathrm{inc.}} = \tau_1\tau_2 + (1-\tau_1)(1-\tau_2)$ is the MZI transmission probability in the purely incoherent case (i.e. when the oscillating term vanishes). Note that this corresponds to eq. 64 a in [186]. In the same work, Marquardt derives another formula, where decoherence is mimicked by a classical environment (i.e. without quantum uncertainty) rapidly fluctuating on time scales smaller than the temporal width of the wavepackets ($\min(h/k_BT, h/eV) \approx 5\,\mathrm{ns}$ at $10\,\mathrm{mK}$ & $0\,\mathrm{V}$):

$$S(V_{\mathrm{dc}}) = \frac{eV_{\mathrm{dc}}}{R_K}\frac{(\tau_{\mathrm{qpc2}} - (1-\tau_{\mathrm{qpc2}}))^2}{4}\coth\left(\frac{eV_{\mathrm{dc}}}{2k_BT}\right) \tag{3.12}$$

which is independent of the transmission of the first QPC. Note also that [186] provides yet another expression, not exposed here as the authors themselves qualify it as artificial and which differs from the two above only by the Fano factor. The key point here is that, in any case, at large voltage bias ($V_{\mathrm{dc}} \gg k_BT$), the noise $S(V_{\mathrm{dc}})$ is linear in V_{dc}, and the difference always lie in the Fano factor.

Coherent MZI without phase noise

In the case of a perfectly coherent MZI, without phase noise, it is possible to consider the whole MZI as an elastic, coherent scatterer, such that the noise it creates is given by

$$S(V_{\mathrm{dc}}) = \frac{eV_{\mathrm{dc}}}{R_K}\tau_{\mathrm{MZI}}(1-\tau_{\mathrm{MZI}})\coth\left(\frac{eV_{\mathrm{dc}}}{2k_BT}\right)$$

with here (in contrast to equation 3.11), $\tau_{\mathrm{MZI}} = \tau_1\tau_2 + (1-\tau_1)(1-\tau_2) + \sqrt{\tau_1\tau_2(1-\tau_1)(1-\tau_2)}\cos\phi$, with ϕ the pure Aharonov-Bohm phase. In this case, the noise is also linear in V_{dc}.

Phase noise in a coherent MZI

Now what happens with the phase noise contribution to the current noise across a coherent MZI ? It is possible to plug equation 3.7 in the expression for current noise:

$$S(\omega) = \mathcal{F}\{\langle I_{\mathrm{MZI}}(t)I_{\mathrm{MZI}}(t+\tau)\rangle - \bar{I}_{\mathrm{MZI}}^2\}$$

with $\mathcal{F}\{...\}$ denoting the Fourier transform, and perform an expansion around $\delta\varphi \approx 0$, after some algebra (detailed in section A.4), one obtains:

$$S(\omega) \approx \bar{I}^2\mathcal{V}^2\langle\delta\varphi^2(\omega)\rangle\sin^2\phi \tag{3.13}$$

which is valid for $\delta\varphi \ll 1$. Note however, that all higher order terms are also proportional to $\mathcal{V}^2\bar{I}_{\mathrm{MZI}}^2 (= \mathcal{V}^2V_{\mathrm{dc}}^2/\bar{R}_{\mathrm{MZI}}^2)$ (as shown in section A.4). It is possible to get rid of the dependence in the pure Aharonov-Bohm phase ϕ by averaging over a whole period.

Then, one gets a noise that is proportional to V_{dc}^2:

$$\langle S_{\mathrm{MZI}} \rangle_\phi \propto V_{\mathrm{dc}}^2 \mathcal{V}^2 \langle \delta\varphi^2 \rangle \tag{3.14}$$

which is the expression for the average phase noise in a coherent MZI.

Measured MZI current noise

In practice, the averaging on the Aharonov-Bohm phase ϕ is accomplished by acquiring data for several gate voltages on a few periods. Such a measurement was performed and is shown on figure 3.8.

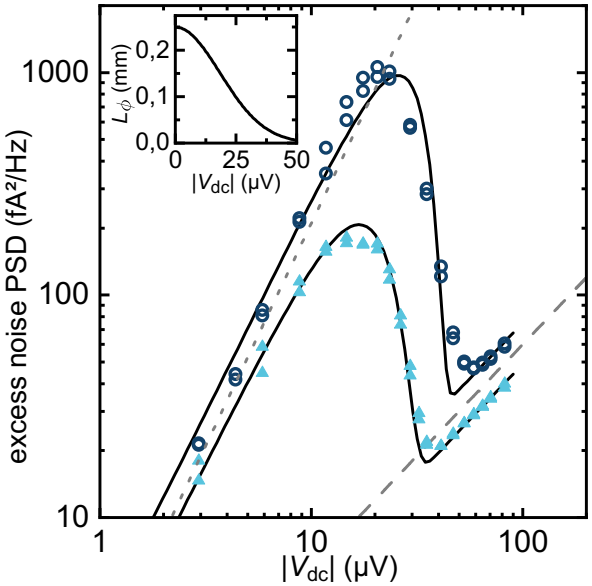

Figure 3.8: Measurement of MHz excess current noise with respect to the noise at zero bias, as a function of the dc voltage V_{dc} applied to the source contact, plotted as open dark blue circles (full light blue triangles) for the $L \approx 24(100)\,\mu$m device . The gray dotted (dashed) line indicates a $\propto |V_{\mathrm{dc}}|^2(|V_{\mathrm{dc}}|)$ trend, full black lines are obtained from equation 3.16. Inset: gaussian dependence used for $L_\phi(|V_{\mathrm{dc}}|)$ given by equation 3.15, that is used to obtain the full black lines of the main panel.

On figure 3.8, it is possible to identify three qualitatively different regimes. In the limit of small voltages, a V_{dc}^2 dependence can be observed (as indicated by the dotted line) for both interferometers, as expected from equation 3.14 assuming $\mathcal{V}$ remains constant in this limit. This V_{dc}^2 dependence further establishes the picture of a coherent MZI subject to phase noise. At large dc voltages, a linear dependence in V_{dc} is recovered (dashed line) as expected for a fully incoherent MZI (equation 3.11). Such a transition to an incoherent MZI is driven by a reduction of L_ϕ, which is generally expected as the phase space for the scattering of electrons increases with the applied bias V_{dc}. In an attempt to obtain the characteristic voltage scale V_ϕ for the reduction of L_ϕ, we tried different expressions for $L_\phi(V_{\mathrm{dc}})$. We find that a naive extension $L_\phi(V_{\mathrm{dc}}) \sim 1/V_{\mathrm{dc}}$ of the $L_\phi(T) \propto 1/T$ observed in the presence of two co-propagating channels [21] is

much too progressive to reproduce the noise data (not shown). It turns out that a phenomenological gaussian decay of the coherence length:

$$L_\phi(V_{\rm dc}) = e^{-(V_{\rm dc}/V_\phi)^2} \times 250\,\mu{\rm m} \tag{3.15}$$

with $V_\phi = 26\,\mu{\rm V}$ (plotted in inset of figure 3.8) provides a good fit to our data. Effectively, to obtain the full black lines of figure 3.8, the expression of equation 3.15 was plugged in the addition the following:

$$S^{\rm exc} = f_2 \frac{V_{\rm dc}^2}{R_K^2} \mathcal{V}_0^2 e^{-\frac{4L}{L_\phi}} + f_1 \frac{eV_{\rm dc}}{R_K} \tag{3.16}$$

where $\mathcal{V}_0$ is the visibility at zero bias and we leave two free parameters: f_1 and f_2. f_1 is a Fano factor that multiplies the term of the incoherent MZI noise (equation 3.11) and f_2 a factor which appears in front of the coherent MZI phase noise term (equation 3.14]). These two parameters f_1, f_2 were adjusted by hand and are given in table 3.1. The corresponding full lines in figure 3.8 closely reproduce our data.

Let us first point out that the same expression for $L_\phi(V_{\rm dc})$ (equation 3.15) was used for both MZI sizes. This further confirms that $L_\phi \approx 250\,\mu{\rm m}$ is close to the intrinsic, decoherence-limited coherence length and also that the characteristic voltage scale $V_\phi = 26\,\mu{\rm V}$ is device independent. Second, we note that the value of the cutoff dc voltage on the visibility V_ϕ corresponds to the loops energy spacing: $V_\phi = 26\,\mu{\rm V} \approx \Delta/e = hv_d/Le$ (using the loop perimeter $L \approx 8\,\mu{\rm m}$ and a drift velocity of $5.10^4\,{\rm m.s}^{-1}$). This suggests that the observed increase of dephasing at large $V_{\rm dc}$ results from the activation of the loops' internal degrees of freedom.

Let us now comment on the values of the obtained parameters f_1, f_2 for each device. First, we look at the linear $V_{\rm dc}$ dependence, for which the found Fano factor f_1 for each interferometer is far less than what one would expect from equation 3.11: $\tau_{\rm MZI}^{\rm inc}(1 - \tau_{\rm MZI}^{\rm inc}) \simeq 0.25$ (with $\tau_{\rm MZI}^{\rm inc} = R_1R_2 + T_1T_2 = 0.5$). This significant reduction is in qualitative agreement with equation 3.12 that predicts, for a decoherence by a rapidly fluctuating field, a fully suppressed noise at our working point: $\tau_{\rm qpc2} \approx 0.5$. Concerning the second, quadratic f_2 parameter, it is expected to be $\propto \langle \delta\varphi^2 \rangle$. Microscopically, phase noise must be due to fluctuations of some sort, like some moving charges in the vicinity of the paths or fluctuations in the magnetic flux threading the interferometer. A probable phase fluctuation mechanism is moving charges along the paths, (possibly charges entering and leaving the inner-channel loops formed by the long comb-shaped gates). The number of independent fluctuators should then scale as L, and therefore one would expect $f_2 \propto \langle \delta\varphi^2 \rangle \propto L$. From the values in table 3.1, we can see that $f_2^{100\mu{\rm m}}/f_2^{24\mu{\rm m}} = 6.5$, which does not deviate too much from the geometrical ratio of 4.

Table 3.1: Parameters used in equation 3.16 to obtain the full lines of figure 3.8

MZI arm length (µm)	f_1	f_2
24	0.12	$4 \cdot 10^{-9}$
100	0.08	$26 \cdot 10^{-9}$

A few words on the different time scales

As a summary, we recall the different time scales involved in these measurements. First, experimental time scales are: (i) the lock-in integration time is set to $\tau_{\mathrm{LI}} = 100\,\mathrm{ms}$, (ii) the current noise is sensitive to events on the scale of $\tau_S \approx 1/855\mathrm{kHz} \approx 1\,\mu\mathrm{s}$. Second, the microscopic time scales are: (iii) the time of flight of electrons through the interferometer $\tau_{\mathrm{tof}} = L/v_d \approx 0.5-2\,\mathrm{ns}$, (iv) the time in between two events causing the erratic behavior of the interference pattern $\tau_{\delta\varphi}$ and which is a priori unknown.

Our conductance measurements indicate that at some times and/or certain MZI settings, $\tau_{\delta\varphi} \ll \tau_{\mathrm{LI}}$ so that noisy events are fast enough (and $\langle\delta\varphi^2\rangle$ large enough) to fully blur the measured interferences with our lock-in amplifiers. In other cases, these events are slow or small enough such that we can observe large visibility interferences. Our MHz measurements at small V_{dc} clearly show that phase fluctuations do occur at least on the µs scale: $\tau_{\delta\varphi} \sim \tau_S$. The only effect of these events at $\tau_{\delta\varphi} \ll \tau_{\mathrm{tof}}$ are to blur the measured visibility of conductance oscillations, but do not impact the intrinsic coherence. Note that similar fluctuations could also occur on time scales comparable to the traversal time of the electron in the MZI which then destroys their quantum character.

3.7.1 Reconstructed interference visibility vs dc bias voltage from phase noise

In order to compare the robustness of the visibility against bias voltage with the loops confinement strategy, the differential visibility – the visibility of dI/dV oscillations – is reconstructed from the noise measurement averaged over several periods. This reconstructed visibility is shown in figure 3.10 b. The step by step process to arrive to such a result is explained in what follows. First, the data of figure 3.8 is recast in figure 3.9 a, in linear scales, where the quadratic (linear) dependence of the noise, at small (large) bias voltage, is easily identifiable. The individual (non-averaged over ϕ) data points are also displayed in small, semi-transparent points to show the extent of the dependence of phase noise on the Aharonov-Bohm phase. Second, the dc visibility (of conductance oscillations in I/V) is obtained by isolating $\mathcal{V}$ in equation 3.16. Instead of using the f_1, f_2 parameters listed above, we fit these more closely to the data, and check that there is no major discrepancy. To do so, the linear component of the noise, that is the focus of figure 3.9 b and plotted in full dark (light) blue lines is subtracted from the averaged noise of the 24 µm (100 µm) MZI, as this component of the noise

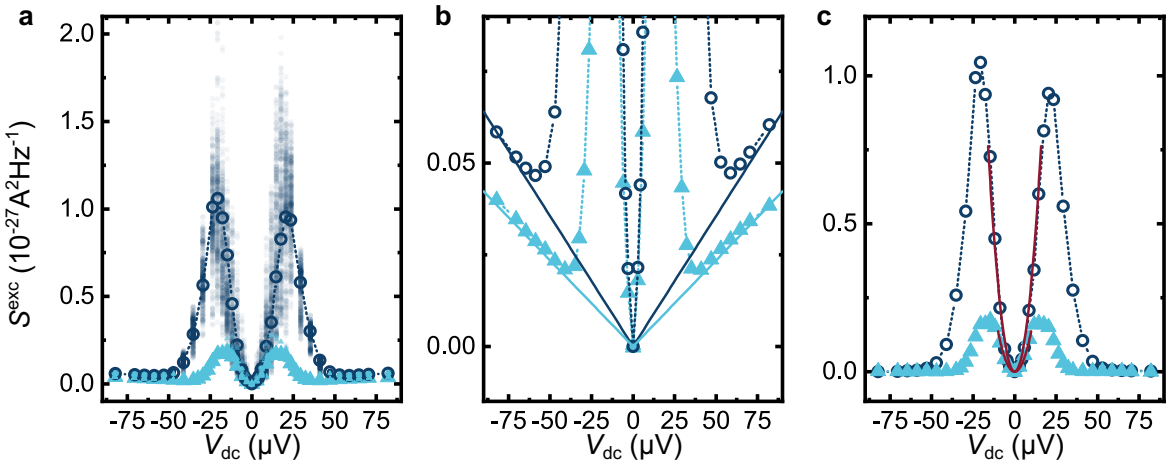

Figure 3.9: Measured excess current noise in the 24 µm (dark blue open circles) and 100 µm (ligth blue full triangles) device as a function of the applied bias voltage V_{dc}. Dotted lines are only a guide for the eye. **a** Individual small semi-transparent data point represent the measured current noise for a given plunger gate voltage V_{pl}. Open circles and full triangles are the average at a given V_{dc}. **b** Focus on the linear component of the average noise. **c** Average current noise with the linear component subtracted, full red lines are quadratic fits used to reconstruct the dc visibility.

is purely due to partition noise and not to the phase noise in a coherent MZI (the thermal rounding is here neglected). This yields the pure phase noise S_ϕ, plotted in figure 3.9 c, and on which a quadratic fit is performed on a restricted range of V_{dc} where the quadratic (and is essentially equal to f_2 of equation 3.16). It is then possible to isolate the visibility in equation 3.14 $\mathcal{V} \propto \sqrt{\langle S_{\mathrm{MZI}}\rangle_\phi \langle \delta\varphi^2\rangle}$. To obtain the data points of figure 3.10 a, it is assumed that $\langle\varphi^2\rangle$ remains constant over the whole explored V_{dc} range, and the proportionality factor is then adjusted by hand so that the calculated dc visibility at small V_{dc} approximately matches the measured differential visibility at zero bias voltage. Finally, the differential visibility is obtained from the dc one by the expression:

$$\mathcal{V}_{\mathrm{diff}} = \left| \mathcal{V} + V_{\mathrm{dc}} \frac{\partial \mathcal{V}}{\partial V_{\mathrm{dc}}} \right| \tag{3.17}$$

which is derived in section A.5. The resulting differential visibility is displayed in figure 3.10 b. The differential visibility for the 24 µm MZI with two co-propagating channels (and keeping QPC 0 open to a single channel only), measured by conductance measurements is also displayed in light green. In comparison with the visiblity in the MZI without the loops, it is striking how the interferences are more robust to a dc bias when the inner channel is forced into loops.

3.8 Conclusion

To put this result into perspective, it is interesting to compare it with state of the art works in the same area. Figure 3.11 shows graphs with a non-exhaustive set of repre-

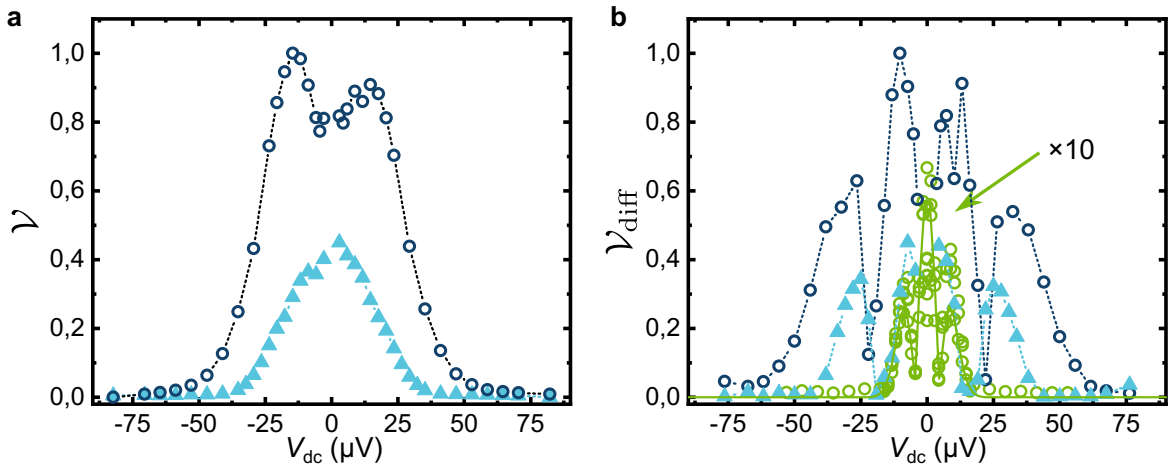

Figure 3.10: Using the same symbol code as before: dark blue open circles (light blue full triangles) are used in the $L = 24(100)\,\mu m$ device. Extracted **a** dc visibility extracted from the measured phase noise of the MZI (see text) and **b** differential visibility obtained from equation 3.17 and data in a, are in blue. Light green data points correspond to the differential visibility obtained from standard conductance measurements with two co-propagating channels in the $L = 24\,\mu m$ device.

sentative coherence lengths observed in various systems and materials. For example, it includes an AlGaAs based MZI (the Ji article [20] previously held the record of the largest coherence length among all subsequent QH realizations except for this work), as well as the more recent implementation of a MZI in graphene in the Yacoby group [193] (blue hexagon on figure 3.11). A proper comparison of the different coherence lengths should only be done at the same temperature, as regardless of the system, the coherence length tends to increase with a lowered temperature. The full line on figure 3.11 a displays a T^{-1} trend, passing through our result. This trend is known to adequately describe the dependence of the coherence length on temperature in QH channels [21], as well as in other ballistic systems [194]. However, this trend should only be taken as indicative as it is not universal. For example, Aharonov-Bohm diffusive metallic rings follow a $T^{-1/2}$ trend, and diffusive metallic wires a $T^{-1/3}$ one [195]. Among all the listed results, four points lie above the black line, suggesting a larger coherence length could be achieved in these systems if they were cooled down to 10,mK, as our devices were. Nonetheless, three of these points were obtained in samples much smaller than the claimed coherence length as shown in figure 3.11 b (where the vertical scale is identical to panel a for an easy matching of each data point). This is illustrated in figure 3.11 b by the full line dividing the graph in two, the lower, green part is a safe zone where the measured coherence length is smaller than three times the device length. In this light, a single other study reports a coherence length that surpasses all other works, including ours, by at least an order of magnitude, and was possibly limited by the sample size. However, such a large coherence length, obtained in a plateau to plateau transition in the QH regime, where electrons are essentially localized, was indirectly derived in the framework of Anderson Localization [196].

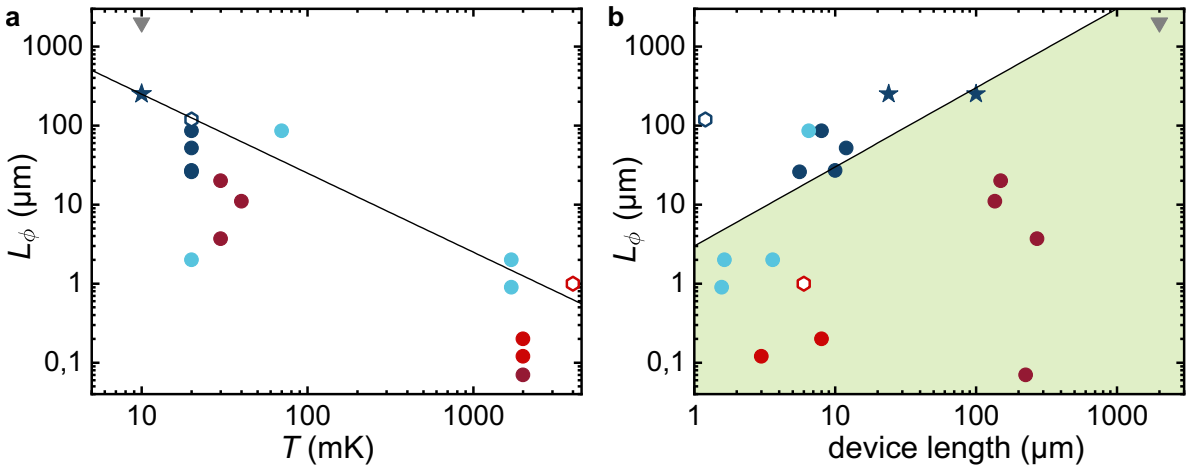

Figure 3.11: Comparison of electron coherence length L_ϕ reached in our work (stars) compared to other works in various materials such as graphene (empty hexagons), and using different measurement techniques (see table A.1 for exact values and references). Colors correspond to: quantum Hall channels MZI (dark blue), diffusive metallic and AlGaAs Aharonov-Bohm rings (light blue), diffusive metallic wires (dark red) and wires in small exotic materials (light red). The dark grey triangle corresponds to Anderson Localization measurements in AlGaAs 2DEG (see text for details). The coherence lengths are presented as a function of **a** temperature, where the black line $\propto 1/T$, serves as a guide for the eye, and **b** device length where the line delimitates a safe zone in green where the claimed coherence length is smaller than three times the device length.

The present work is the first to directly demonstrate a macroscopic electron coherence length in a solid-state circuit. By engineering the environment of the interfering quantum Hall channel, inter-channel electron-electron interactions are drastically supressed, thereby increasing the coherence length by a factor of 15. It also confirms that electron-electron interactions between adjacent channels is by far the main decoherence mechanism in such circuits. However, this kind of engineering came with a drawback in our study: a large phase noise was generated when forming inner channel loops. This complicates the exploitation of the large obtained L_ϕ, especially at low-frequencies. Such limitation may be overcome using smaller loops of even larger level-spacing, suppressing possible tunnel events. Another approach, not fully explored, would be to use wide gates, allowing to repel the inner channel away from the outer one. Such a strategy has recently proved efficient at minimizing energy relaxation [28]. Finally, a natural follow-up to this work would be to use this type of engineering for single electron interference experiments, as the observed phase noise in our dc experiment might not affect the short, $\sim 50\,\mathrm{ps}$ wide, electron pulses commonly used in such experiments [24,167,197].

4

Electron quantum state transfer accross a metallic island

As discussed in the introduction of this manuscript, whenever a propagating electron induces a change in its environment, it (at least partially) lifts the uncertainty on the path taken, thereby washing out the quantum coherence. Such modification to the environment has to be mediated by an interaction of some nature. This is the reason why interactions in general are intuitively associated to decoherence. Moreover, in solid-state circuits, Coulomb interaction is inescapable, and is consequently widely perceived as the nemesis of coherent transport of electrons. A good example of how Coulomb interaction limits the electronic coherence is actually the whole experiment described in the previous chapter, where its effect was effectively reduced in order for the coherence length to be increased. In this chapter, we report on an experiment that challenges this intuitive view and in which Coulomb interaction strikingly acts as the main ingredient enabling for the electron coherence to be preserved.

4.1 Which-path experiments in electronic MZI

Taking a step back, and in order to illustrate that Coulomb interaction usually drives decoherence in solid-state circuits, we introduce which-path experiments. These typically consist in voluntarily introducing an element in the environment that lifts the uncertainty on the electrons' path. Below, a few examples that were explored in electronic Mach-Zehnder interferometer devices are discussed. This detour is justified by the fact that the experiment reported on in this chapter a priori looks like a which-path

one, as will be clear from the sample presentation.

4.1.1 Dephasing with a coupled Mach-Zehnder

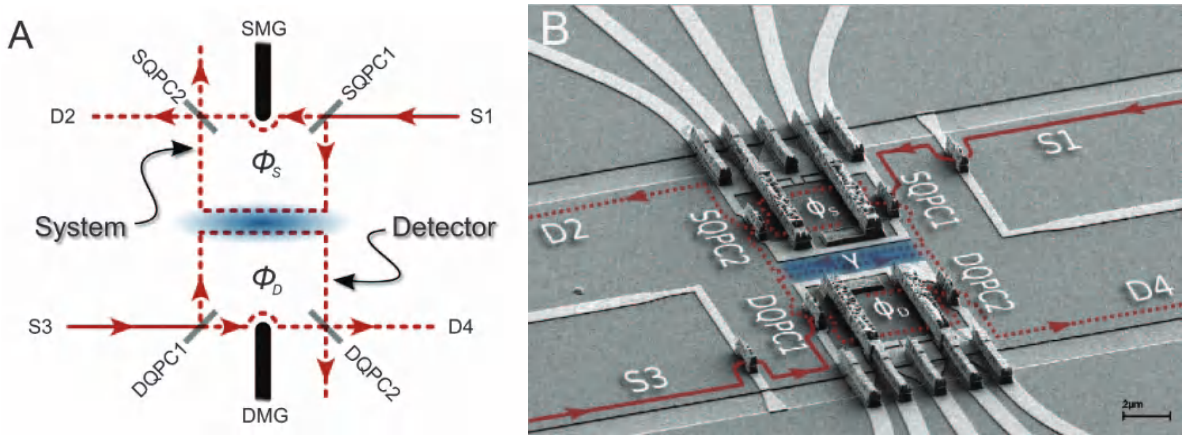

Figure 4.1: Two MZI with one of their path capacitively coupled together realized at $\nu = 2$ [198]. **a** Schematic of the circuit: electrons couple within the blue region where the two MZI arms are close to each other. **b** SEM scan of the device. The outer QH channels are drawn in red.

It is possible to couple a path of a Mach-Zehnder interferometer together with one path of a second MZI, taking advantage of Coulomb interaction as illustrated in figure 4.1. As a consequence, the states of the electrons in the two separate interferometers are entangled and due to the system's symmetry, each MZI can be seen as part of other's environment. In each MZI, electrons can either be in the interacting path or in the non-interacting one. When present in the interacting path, electrons act as a small gate on the other MZI, adding a phase shift γ to its interference pattern. The entanglement between both MZI results in an interference term, for each MZI, that is the average of two interference patterns phase-shifted by γ. As a consequence, when $\gamma \neq 0$, each MZI gains information about the other, thereby reducing the visibility of each of the measured interferences pattern. The phase shift γ can be tuned by increasing the dc current in one of the two interferometers, as doing so increases the number of electrons crossing the interferometer per unit time, and therefore increasing its local gate effect on the other interferometer. Although increasing the current could be interpreted as simple phase averaging, the authors argue that the amount of dephasing can be tuned by post-selecting the information measured by the MZI serving as a detector, simply by tuning its phase via the magnetic flux or, equivalently, a plunger gate voltage. When doing so, the visibility of the probed MZI is alternatively almost fully suppressed, and recovered to its almost environment-free value. This is interpreted by the authors as the knowledge of the which-path detector, that can be tuned so as to cause decoherence (when which-path knowledge is maximum) or not (when no which path knowledge is gained) of the electrons propagating in the other interferometer.

4.1.2 Shot-noise induced dephasing

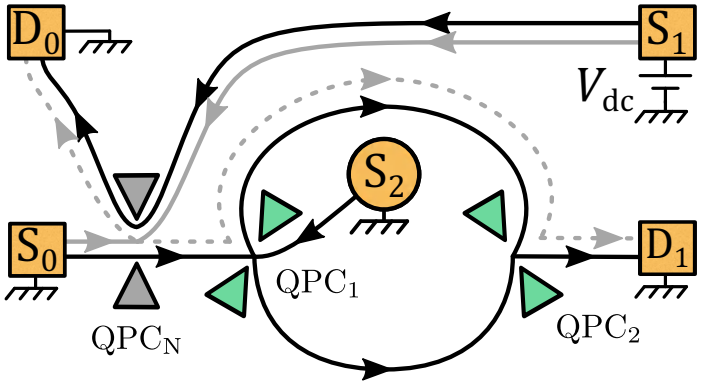

Figure 4.2: Schematic of a MZI dephased by shot-noise in a channel adjacent to one of the two paths. QPC_N is biased with voltage V_{dc}

By introducing electronic noise on the channel co-propagating with one of the interfering channels, it is possible to blur the phase of the interfering electrons through the capacitive coupling between both channels [176,177,199]. The idea is to generate shot-noise thanks to a biased QPC (QPC_N on figure 4.2) set to a partial transmission probability for the inner channel. As a consequence, through the inter-channel capacitive coupling described in the previous chapter, the noise can also be generated on the interfering channel, on time scales that induce decoherence. It can also be thought of differently: the interfering electrons can affect the noise in the adjacent channel, meaning that it is possible to determine which path the electrons take in the interferometer, this information destroys the quantum superposition on which interferences rely. The noise in the co-propagating channel therefore acts as a which-path sensor, which is controllably tunable through the voltage bias at QPC_N that drives the available phase space.

In these experiments however, phase averaging also occurs. That is hard to distinguish from true decoherence: the noisy channel can be thought of as acting as a gate on the interfering channel, when noise is increased (with the dc voltage). As a consequence, the interferometer area is slightly varied many times on the time scale of the conductance measurements, with typical integration times of $\sim 0.1 - 1\,\mathrm{s}$, and phase averaging occurs, resulting in a reduction of the observed visibility. The agreement of the visibility reduction with a model assuming a gaussian phase distribution (that assumes independent phase randomizing events) in [177] supports the idea that many uncorrelated electrons are involved in the process. A discrepancy with such a model was however measured in [176,199] at high bias voltage, which the authors argue is a signature of true decoherence by the tunneling electrons in the noisy channel.

All in all, these results illustrate how a which-path experiment can be implemented, but also that it can be hard to distinguish true decoherence from simple phase averaging.

4.1.3 The dephasing probe

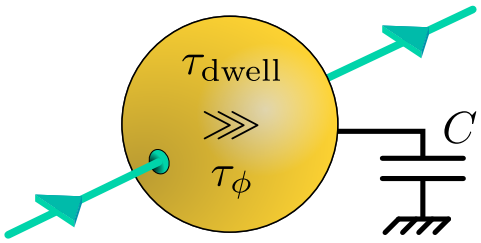

Figure 4.3: Schematic of a metallic 'voltage' or 'dephasing' probe connected to a single electronic channel.

The dephasing probe is a theoretical tool, introduced by Büttiker to take into account dephasing processes within the non-interacting scattering formalism [43–45]. In these works, Büttiker describes the probe as having a floating electrochemical potential, determined by that of the leads to which it is connected. Additionally, it plays the role of an inelastic scatterer in the sense that it breaks down the quantum coherence, as absorbed electrons are distinguishable from re-emitted ones. This approach is successful to describe the crossover from purely quantum coherent transport given by the Landauer formula to the purely classical result where series resistors are added [44,45]. For realistic purposes, Büttiker argues that this abstract object of a dephasing probe can actually be simply realized by an electron reservoir, a piece of metal, disconnected from the ground. This dephasing relies on the fact that the dwell time of electrons within the metal τ_{dwell} is much larger than their coherence time τ_ϕ in this medium. It was subsequently demonstrated, using a MZI, that such an object indeed does blur the quantum phase of electrons in good agreement with the scattering theory [200].

4.2 The *coherent* probe

In the above description of a dephasing probe, Coulomb interactions are completely neglected, although they can become of paramount importance. Effectively, any such piece of metal necessarily possesses a capacitance towards its surrounding. This capacitance C defines the energy necessary to add an elementary charge to it $E_C = e^2/2C$, the charging energy. Whenever $k_BT \ll E_C$, the global charge of the piece of metal is frozen. In the very particular case of a single channel connected to the metal subject to the conditions $\Delta \ll k_BT \ll E_C$, it was predicted that inelastic scattering with the metallic island's many degrees of freedom is effectively suppressed[1] and that the coherence is preserved between electrons arriving into the island and indistinguishable electrons simultaneously exiting [46–48].

All three papers [46–48] rely on the idea that in one dimension, low-energy electronic

[1]Note that inelastic scattering still occurs for the electrons contained within the metal, and that this effective suppression only concerns the impinging electrons from the outside.

excitations (low-energy here means $\ll E_F$, the Fermi energy), naturally expressed as single-particle fermionic fields, can be re-expressed in terms of collective bosonic fields (see [121,201] for references textbooks and [202,203] for more pedagogical presentations). This presents the advantage that some problems that are intractable expressed in terms of fermionic fields, become much easier when recast as bosonic ones. That is especially true when electron-electron interactions are at play, because the interaction hamiltonian then contains terms that are quartic in fermion fields, which become quadratic in bosonic fields, and therefore exactly solvable. Treating quantum Hall edge channels this way is a successful strategy to account for the effects of Coulomb interactions in such systems (see [204] for several examples). In particular, this approach enables to keep track of the quantum phase in presence of interactions in the T-junction geometry of [46], but also in the ohmic contact of [47] or strong interaction region of [48] embedded in a MZI.

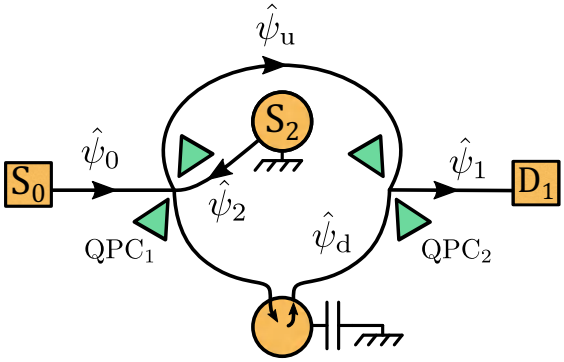

Figure 4.4: Schematic of a MZI interferometer with the lower arm coupled to a metallic island.

In what follows, we introduce the very basis of the formalism and try to convey the physical ideas that can be drawn from it in the particular context of a MZI coupled to a metallic island as illustrated in figure 4.4. As stated above, the main idea relies on the fact that fermion fields $\hat{\psi}_{u,d}(x)$ (which verify the canonical anti-commutation relations $\{\hat{\psi}_i^\dagger(x), \hat{\psi}_j(y)\} = \delta_{\mathrm{i,j}}\delta(x-y)$) can be re-expressed in terms of the boson fields $\hat{\phi}_{\mathrm{u,d}}(x)$ in the following way:

$$\hat{\psi}_{u,d}(x) = \frac{1}{\sqrt{a}} e^{i\hat{\phi}_{\mathrm{u,d}}(x)}$$

with a a renormalization constant, such that the bosonic operator can be physically interpreted as the electron's quantum phase. Another physical meaning can be tied to these bosonic fields: it is possible to express the fluctuation electronic density operator (defined as the departure from the mean density) in the following way:

$$\hat{\rho}_i(x) = \hat{\psi}_i^\dagger(x)\hat{\psi}_i(x) - \langle\hat{\psi}_i^\dagger(x)\hat{\psi}_i(x)\rangle = \frac{1}{2\pi}\partial_x\hat{\phi}_i(x) \tag{4.1}$$

where the index i denotes the channel.

With these two ingredients, it is possible to grasp what happens at the level of the metallic island when the condition $k_B T \ll E_C$ is fulfilled. Effectively, the latter con-

dition states that any charge fluctuations of the island is frozen. This implies that, whenever an incoming charge pulse $\delta\hat{\rho}_{\text{in}} = \hat{\rho}_{\text{in}} - \langle\hat{\rho}_{\text{in}}\rangle$ penetrates the island, another one $\delta\hat{\rho}_{\text{out}}$ has to be expelled such that it contains the exact same amount of charge.
When a single channel is connected to the island, the outgoing charge pulse is necessarily exactly equivalent to the incoming one, which means that $\hat{\rho}_{\text{in}} = \hat{\rho}_{\text{out}}$, and through equation 4.1 that $\partial_x\hat{\phi}_{\text{in}}(x) = \partial_x\hat{\phi}_{\text{out}}(x)$. As a consequence, the incoming bosonic field is equal to the outgoing one and, by extension, the quantum phase is preserved between the electrons constituting the incoming and outgoing charge pulses. On the other hand, when more than one channel are connected to the island, it is possible for the incoming charge pulse to re-arrange among all the available channels, the outgoing charge pulse is different from the incoming one and the information on the phase is lost. Note a complementary insightful physical discussion in [205, sec. 2].

4.3 Sample characterization

4.3.1 MZI configurations

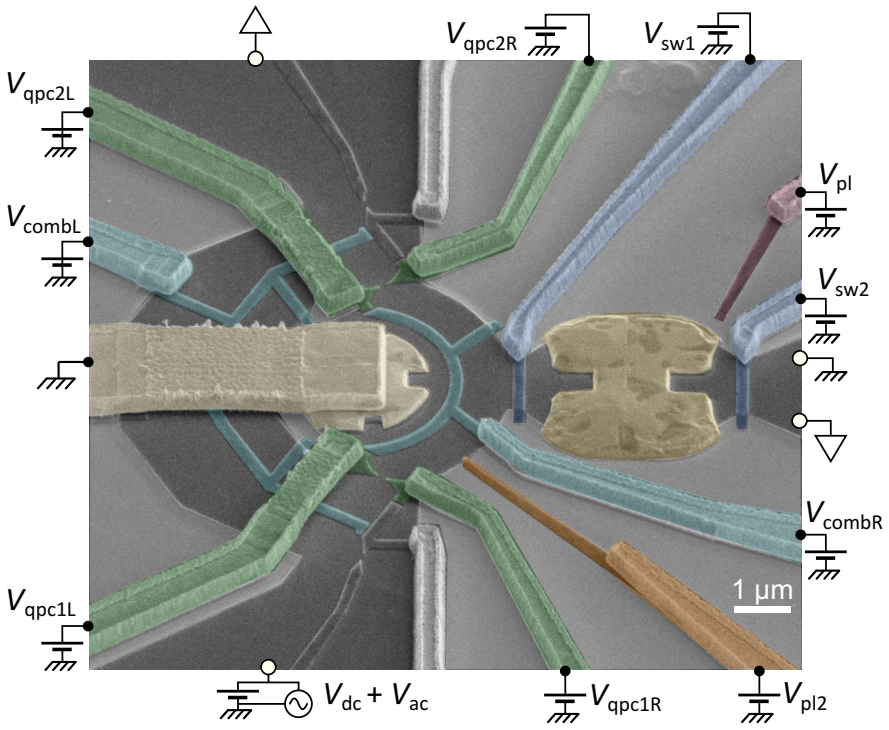

Figure 4.5: SEM scan of the sample. The two QPCs (in green) are the MZI's beam-splitters. The central ohmic contact on the left (light gold) is connected to ground via an air bridge. Sources and drains are not visible in this picture but materialized by the white dots.

Idrisov et al. [47] propose to test their prediction in a Mach-Zehnder geometry which is exactly what we have done. In figure 4.5 an SEM scan of the sample is printed, it consists in a Mach-Zehnder interferometer defined by the two QPCs (colored in green)

and a central ohmic contact (in light gold) that is connected to ground via an air-bridge. On the right side, another small ohmic contact is present, it is electrically connected to the outside world only via the 2DEG and will be used as the 'probe'. By looking closely, one can see a shallow trench in the middle of this ohmic contact. That is where the heterostructure was etched before the metal deposition to garantee no electrons can pass from one side to the other of the island through the 2DEG, thereby bypassing the metal. The two dents on each side of the island are there to increase the length of the metal/2DEG interface so as to make the interface as transparent as possible. A large magnetic field ($B \approx 5\,\mathrm{T}$) is applied perpendicular to the sample so as to reach the quantum Hall regime at filling factor $\nu = 2$ (and close to the lower B-field plateau edge). Just like in the previous study, two top gates in the shape of combs (light blue) were deposited along both interferometer's arms but those are not used in what follows. There are two plunger gates, the first one in dark red is well coupled to the island and badly coupled to the interferometer's paths, while the second one in orange is badly coupled to the island and well coupled to the right MZI path. Two top gates (dark blue) permit to controllably open or block the flow of electrons towards and away from a metallic island on each of its two sides. These enable to tune the device in three different configurations as illustrated in figure 4.6. The first configuration (figure 4.6 a,d) consists in coupling the channel defining the right path of the interferometer, as well as a second channel on the other side of the island. In this case, theory predicts the electron coherence should not be preserved. The second configuration (figure 4.6 b,e) consists in a simple MZ interferometer: the blue barring gate is closed on the interferometer's side and will serve as a control experiment. The third configuration (figure 4.6 c,f) consists in plugging only the right interfering channel of the interferometer to the island, it is for this configuration that theory counter-intuitively predicts a preservation of the phase coherence.

Note that the first configuration does not realize the ideal dephasing probe as part of the current is lost to the island's other side, while in the ideal case, all the current is recovered, like in [200]. However, it is simply not possible to connect two channels to a probe without losing some signal in the standard electronic MZI geometry where a central grounded contact is required.

4.3.2 Metallic island

The island's charging energy being a crucial parameter, it can be characterized by tuning the device in a Single Electron Transistor (SET) regime such that it is connected to the outer world by very weak tunnel junctions as illustrated on figure 4.7 a. Upon varying both the energy of incident electrons through V_{dc} and the plunger gate voltage V_{pl}, we obtain the Coulomb diamonds of figure 4.7 b. The height of the Coulomb diamonds ($e/C \approx 50 \pm 3\,\mu\mathrm{V}$) enable to deduce the island's charging energy: $E_C = e^2/2C \approx k_B \times 285 \pm 15\mathrm{mK}$, where C is the island's total capacitance towards its surroundings.

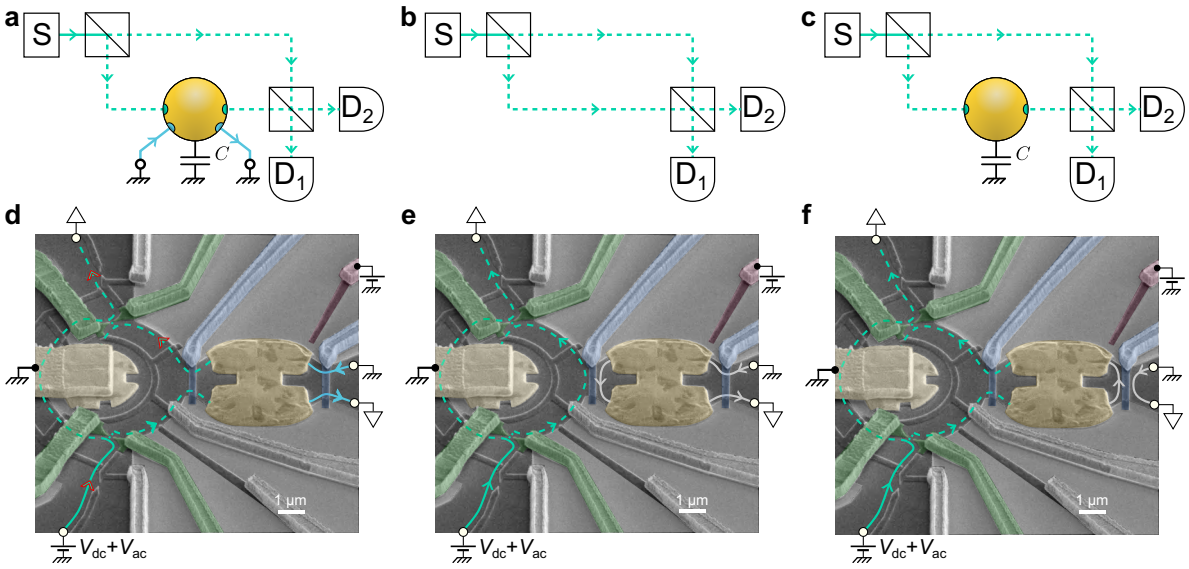

Figure 4.6: **a-c** Schematics of the three possible configurations of the sample and **d-f** corresponding trajectories of the outer quantum Hall channel drawn on the sample's false colored SEM scan. **a,d** Two channels are coupled to the island, the metallic island should act as a dephasing probe.

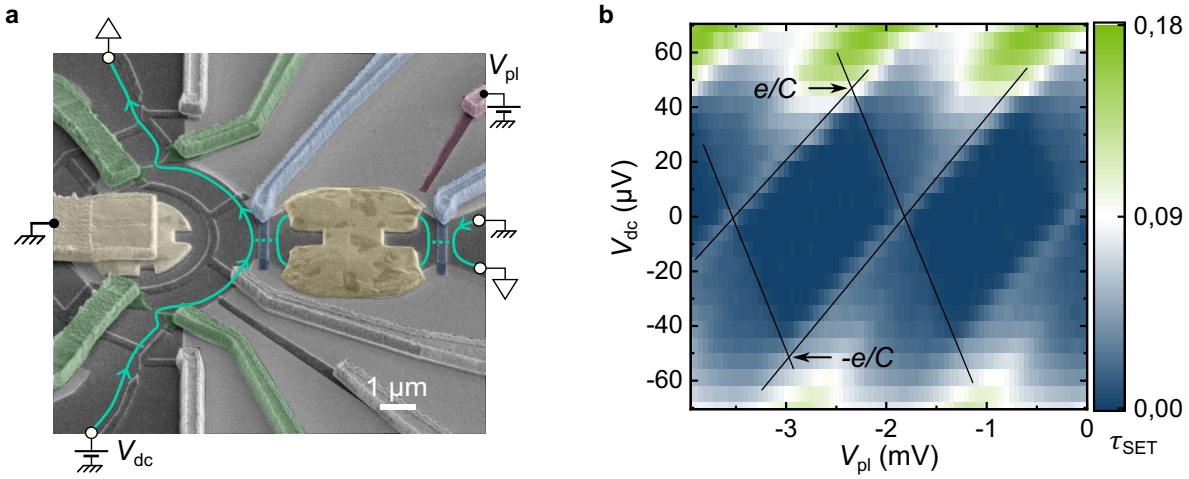

Figure 4.7: **a** Sample tuned in a SET configuration: both blue switch gates are tuned in the tunnel regime (very low transmission), the outer channel is sketched in light green, the inner channel is not drawn but fully reflected at every interface **b** Coulomb diamonds obtained for the metallic island when the device is tuned as a SET. The total island's capacitance, and consequently its charging energy, is deduced from the diamonds V_{dc} extension ($eC \approx 50 \pm 3\,\mu\mathrm{m}$).

It is also possible to estimate the island's level spacing: $\Delta = 1/\rho_F\Theta$, with Θ the island's volume and ρ_F the electronic density of states per unit volume and energy (in gold $\rho_F \approx 1.14 \cdot 10^{47}\,\mathrm{J}^{-1}.\mathrm{m}^{-3}$). Here, $\Theta \approx 3\,\mu\mathrm{m}^3$, such that the level spacing is $\Delta \approx k_B \times 0.2\,\mu\mathrm{K} \lll k_B T$.

4.3.3 Small Ohmic Contacts Interface Characterization

For this experiment, it is crucial that the ohmic contacts are well connected to the quantum Hall channels. While the source and drain contacts are large and have essentially perfect interfaces with the 2DEG, it is not necessarily the case of the two micron-scale ohmic contacts in our MZI,.

Central ohmic contact

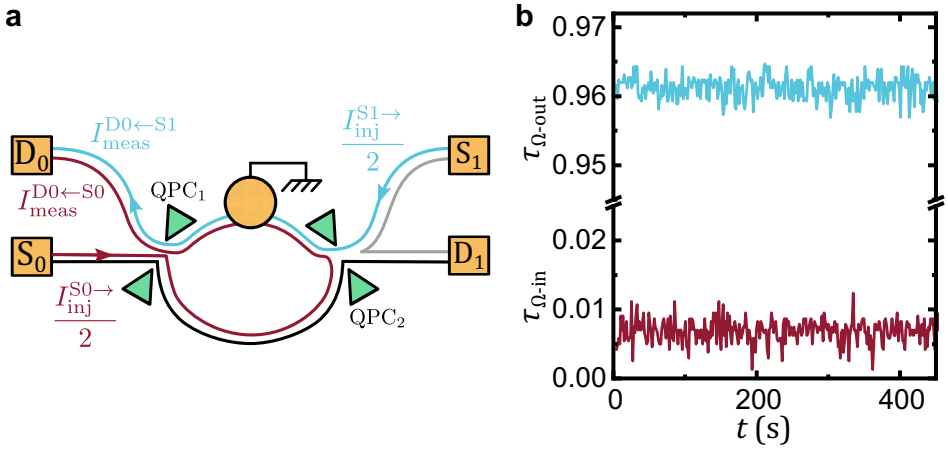

Figure 4.8: Measurements over time of the transmission coefficients at the metal/2DEG interface for the outer channel ($\tau_{\Omega-\mathrm{out}}$) as well as for the inner one ($\tau_{\Omega-\mathrm{in}}$) **a** Schematic of the gate configuration and the channels trajectories. QPC1 is fully open. Only the halves of the injected current relevant to the calculation of the transmission coefficients are indicated in red and blue (see text). The other half of the current emerging from contact S_0 (S_1) is injected in the outer (inner) channel, colored in black (grey) and end up on contact D_1. **b** Measurement of $\tau_{\Omega-\mathrm{in,out}}$. The measurements take place between contacts S_1 and D_0 for the outer channel (in light blue on the schematic) and S_0 and D_0 for the inner one (dark red).

One of them is the central contact connected to the ground via the air bridge, which needs to be small due to the small size of the interferometer. The other one is the metallic island, that needs to remain small so as to boast a large charging energy. In itself, realizing micron-scale ohmic contacts in good electrical contact with the 2DEG is a challenging task, this is why it is necessary to ensure that these interfaces are of good quality. It is possible to retrieve the transmission coefficient of the quantum Hall channels at the 2DEG/metal interface. To do so, the interface is treated as an elastic scatterer, and the device is tuned in different configurations to find the different transmission coefficients.

By tuning the device in the configuration sketched in figure 4.8 a, it is possible to characterize the interface of the central ohmic contact for both the outer and the inner channels independently and simultaneously thanks to our homodyne detection scheme. The quantities $\tau_{\Omega-\text{out,in}}$ plotted in figure 4.8 b are the transmission probabilities between the outer/inner channel and the inside of the metallic island. The values of $\tau_{\Omega-\text{out,in}}$ are obtained by measuring at contacts $D_{0,1}$ the part of the current $I^{0,1}_{\text{meas}}$, that remains of the injected current $I^{0,1}_{\text{inj}}$ at contacts $S_{0,1}$. As $I^{0,1}_{\text{inj}}$ is equally distributed between the inner and outer channel, we get

$$\tau_{\Omega-\text{out}} = 1 - \frac{I^{\text{D0}\leftarrow\text{S1}}_{\text{meas}}}{I^{\text{S1}\rightarrow}_{\text{inj}}/2} \qquad \text{and} \qquad \tau_{\Omega-\text{in}} = 1 - \frac{I^{\text{D0}\leftarrow\text{S0}}_{\text{meas}}}{I^{\text{S0}\rightarrow}_{\text{inj}}/2}$$

It can be observed that the inner channel is very little coupled to the grounded central contact, with just a 1% transmission probability. While unexpected, this very poor coupling of the inner channel to the central contact is however not a big concern as only the outer channel is intended to be used for interferometry. The outer channel, while being much better coupled to it isn't perfect and boasts a 96% transmission probability. This value is however high enough to prevent charging effect within the interferometer and greatly suppress any second order interference.

Metallic Island

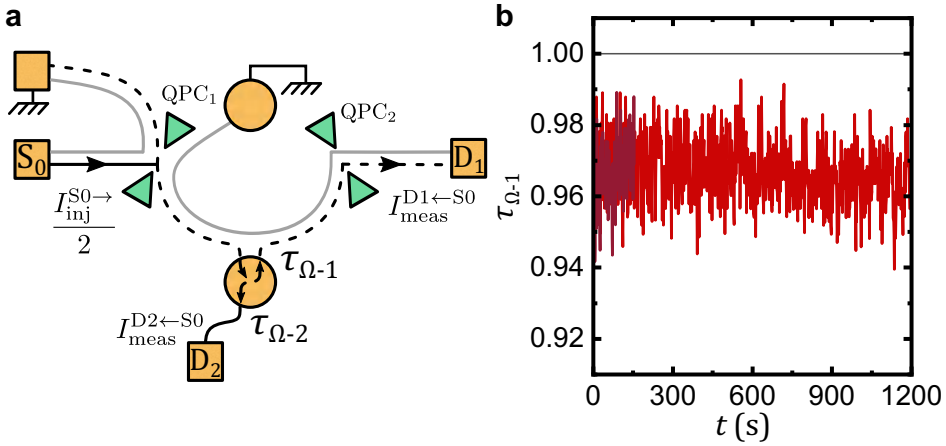

Figure 4.9: **a** Schematic of the gate configuration and channels trajectories: QPC^{L} is set to half transmission such that it lets only half of the current injected in the outer channel go through, which makes $I^{\text{S0}\rightarrow}_{\text{inj}}/4$. **b** Measurement over time of the transmission coefficients at the metal/2DEG interface for the outer channel ($\tau_{\Omega-1}$).

The coupling of the outer channel with the floating island can be estimated in a similar fashion. From complementary measurements (shown in section B.1), the transmission probability inside the ohmic contact was seen to slightly depend on the nearby gate voltages. Therefore, the device is tuned in a configuration as close as possible to the MZI configuration by setting the first QPC to half transmission on the outer channel, which only lets through a current $I^{\text{S0}\rightarrow}_{\text{inj}}/4$. In this case however, there are two interfaces

in series and it is impossible to infer separately $\tau_{\Omega-1}$ and $\tau_{\Omega-2}$ (see figure 4.9 a). The series transmission probability is

$$\tau_{\Omega}^{\text{series}} = \left(\frac{1}{\tau_{\Omega-1}} + \frac{1}{\tau_{\Omega-2}}\right)^{-1} = \frac{I_{\text{meas}}^{\text{D2}\leftarrow\text{S0}}}{I_{\text{inj}}^{\text{S0}\rightarrow}/4} = 1 - \frac{I_{\text{meas}}^{\text{D1}\leftarrow\text{S0}}}{I_{\text{inj}}^{\text{S0}\rightarrow}/4}$$

Note that in the case $\tau_{\Omega-1} = \tau_{\Omega-2} = 1$, $\tau_{\Omega}^{\text{series}} = 1/2$ as expected from the equi-repartition of current in both connected channels following from the Kirchoff law applied to the island, considered as a circuit node. Some elements (such as the current redistribution when changing each of the switch gates voltages and the absence of residual charge quantization oscillations, detailed in section B.1), indicate that the interface of the island opposite to the MZI is near perfect. This is the reason why we assume: $\tau_{\Omega-2} \simeq 1$, which makes $\tau_{\Omega-1} \simeq \tau_{\Omega}^{\text{series}}/(1 - \tau_{\Omega}^{\text{series}})$. Experimentally, $\tau_{\Omega-1}$ is therefore given by:

$$\tau_{\Omega-1} \simeq \frac{I_{\text{meas}}^{\text{D2}\leftarrow\text{S0}}}{I_{\text{meas}}^{\text{D1}\leftarrow\text{S0}}}$$

We can then plot the traces of figure 4.9 b and conclude that the metal/2DEG interface of the floating island on the side of the MZI reflects ~3% of the impinging electrons. Additional elements shown and discussed in section B.1 indicate that the coupling of the inner channel is very bad on the MZI side of the island while it is very good on the outer side.

For both ohmic contacts, a slight variation of the transmission is observed as a function of the surrounding gates voltages (not shown here). This effect remains however small and is further discussed in section B.1.

Because both transparencies of the metal/2DEG interfaces are not perfect, it is possible that some measurement artifacts arise. However, their relatively low deviation from the ideal case should not affect much the interference patterns.

4.4 Experimental results

4.4.1 Magnetic field oscillations

Now, the device is tuned as a Mach-Zehnder interferometer for the outer channel: both QPCs are tuned to half transmission (the inner channel is fully reflected) and both paths are open (the comb gates are set to 0V). First, the device is tuned in a Mach-Zehnder such that one of its path is interrupted by the island, and the island is also connected to a second channel as depicted in the schematic of figure 4.10 a. The average signal measured at the output detector of the MZI is of around $\tau_{\text{MZI}} \approx 3/8$, indicated on figure 4.10 as the dashed black line. This is expected from both QPCs tuned to 1/2 transmission probability and from the current equi-redistribution at the the floating island, between both channels connected. The light blue signal oscillates around the

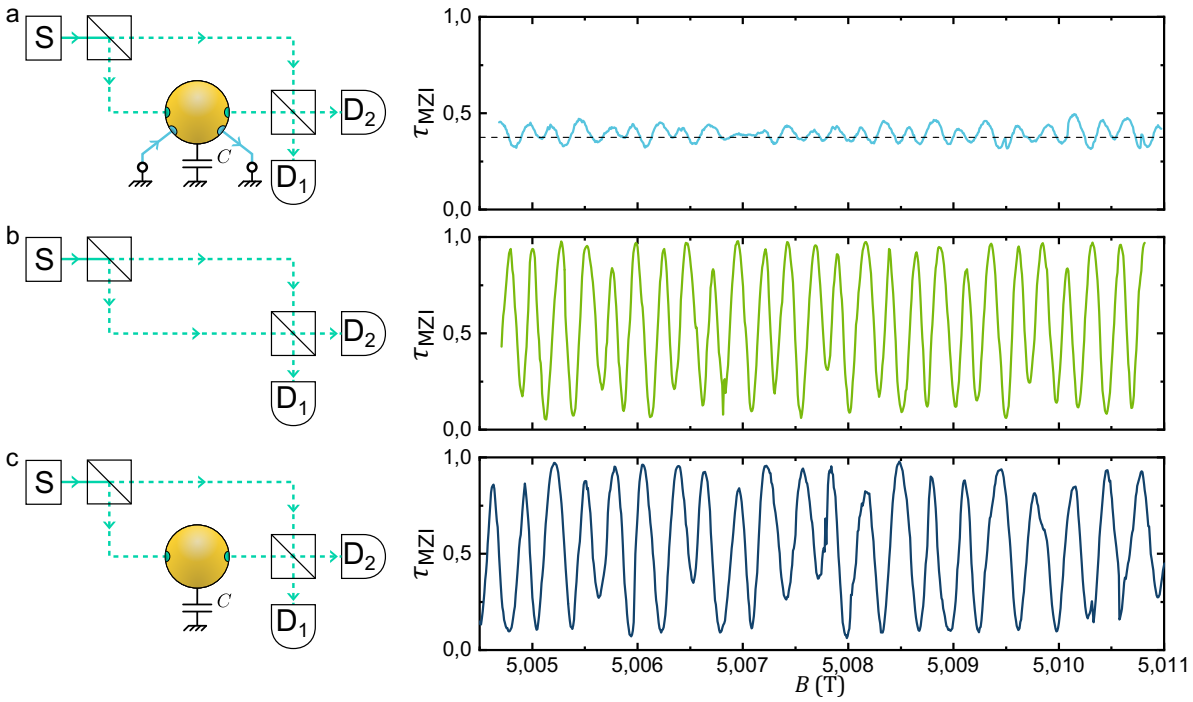

Figure 4.10: Mach-Zehnder oscillations as a function of the perpendicular magnetic field are presented in the right panel when the device is tuned in the configuration sketched in the left panel: **a** when two channels are connected to the island, **b** in the simple MZI case, **c** when only a single channel is connected to the island.

3/8 value with a maximum visibility of $\approx 20\%$, suggesting residual coherent transport across the interferometer although theory predicts that none should subsist. These can be explained by the residual reflection on the island contact: electrons that do not penetrate the metal keep their quantum state intact and can interfere. The value of 20% visibility for these oscillations is compatible with a 3% reflection at the ohmic contact interface as characterized above (the residual oscillations' visibility is expected to scale as the square root of the reflection probability [200], see section B.4 for the exact expected expression in this case). The fact that no interferences should subsist when electrons are well-coupled to the island can be intuitively understood with a 'which-path' interpretation. In effect, the interferences rely on the uncertainty on which of the two paths an electron took. As some signal leaks out of the interferometer along one the the paths as is the case here, it is possible to determine which path an electron took, thereby destroying the interferences. Note a difference with a true which-path experiment where no signal should be lost, just like in [199,200,206].

The second configuration consists in simply closing the gate separating the interferometer's right path from the island, resulting in a simple MZI as depicted in figure 4.10 b. In this case, oscillations of visibility of up to 90% can be observed, which serves as a reference. Turning towards the third configuration, where a single channel is connected to the metallic island, it is possible to see in figure 4.10 c that the visibility of the resulting oscillations is, at our resolution, as large as in the simple MZI case, show-

ing that the coherence of the electrons along the right path is preserved even though they are coupled to the metallic island. This means that the latter does not act as a dephasing probe, contrary to the situation in [200]. Consequently, this configuration does not constitute a which-path experiment, in spite of its appearance. This implies that no matter how close one would monitor the state of the metallic island, it is not possible to tell which path the electron took and the charge state of the island remains unaffected by electrons crossing the MZI. This is due to the island's very large charging energy that freezes the island's global charge. Taking a closer look at figure 4.10 b & c, it is clear that the periodicities do not match. The power spectral density of the Fourier transform of all three signals is drawn in figure 4.11 a. Noticeably, the peaks of the simple MZI (light green) as well as the MZI connected to the island (dark blue) oscillations are at clearly different values. The evolution of flux enclosed between both MZI paths being given by equation 2.6 that we re-write here:

$$\frac{d\phi}{2\pi} = \frac{\partial}{\partial B}\left(\frac{\mathcal{A}B}{h/e}\right)dB + \frac{\partial}{\partial V_{\mathrm{pl}}}\left(\frac{\mathcal{A}B}{h/e}\right)dV_{\mathrm{pl}}$$

here by varying only the magnetic field, only the first term of the right hand side of this expression is relevant and a full oscillation period is obtained when

$$\frac{h}{e} = \frac{\partial(\mathcal{A}\cdot B)}{\partial B}\Delta B$$

where ΔB is the magnetic field periodicity. In a MZI, the area does not vary as a function of the magnetic field, leaving only

$$\frac{h}{e} = \mathcal{A}\Delta B$$

which implies that the periodicity as a function of magnetic field is inversely proportional to the area enclosed between the two interferometer's arms. In the simple MZI case (light green), this peak corresponds to a flux periodicity of $241 \pm 3\,\mu\mathrm{T}\times\mathcal{A}_{\mathrm{MZI}} \approx 0.98h/e$, with the interferometer's lithographically defined area of $\mathcal{A}_{\mathrm{MZI}} = 16.8\,\mu\mathrm{m}^2$. This is in agreement, within 2%, with the expected unit flux quantum per period, that is represented in figure 4.11 b as a vertical dashed light green line. When the island is connected (dark blue), the flux periodicity is $305 \pm 4\,\mu\mathrm{T}\times\mathcal{A}_{\text{MZI-island}} \approx 1.35h/e$, when assuming a naive area of $\mathcal{A}_{\text{MZI-island}} = 18.4\,\mu\mathrm{m}^2$ that is depicted on figure 4.11 c. This is a large, 35% deviation to a single flux quantum per period, materialized by the vertical dashed dark blue line on figure 4.11 a. Note that in this case, the area that should be considered is not clear as the well-defined QH edge path is interrupted by the metallic island that couples the incoming and outgoing channels through its surface plasmons, that cannot be associated to a well-defined electron path. Nonetheless, any electrical current path necessarily encloses an area that is at least larger than that of the simple MZI (figure 4.11 b). Here, the measured magnetic field periodicity is substantially larger, by 27%, than that of the simple MZI, corresponding to a smaller area. This

puzzling result is incompatible with a simple Aharonov-Bohm phase, suggesting that another effect is happening. On the bright side, this unexpected periodicity further confirms that electrons along the right path of the interferometer are indeed well coupled to the island and that the observed large visibility does not come from a mere reflection at the metal interface, at which frequency we see no peak at all.

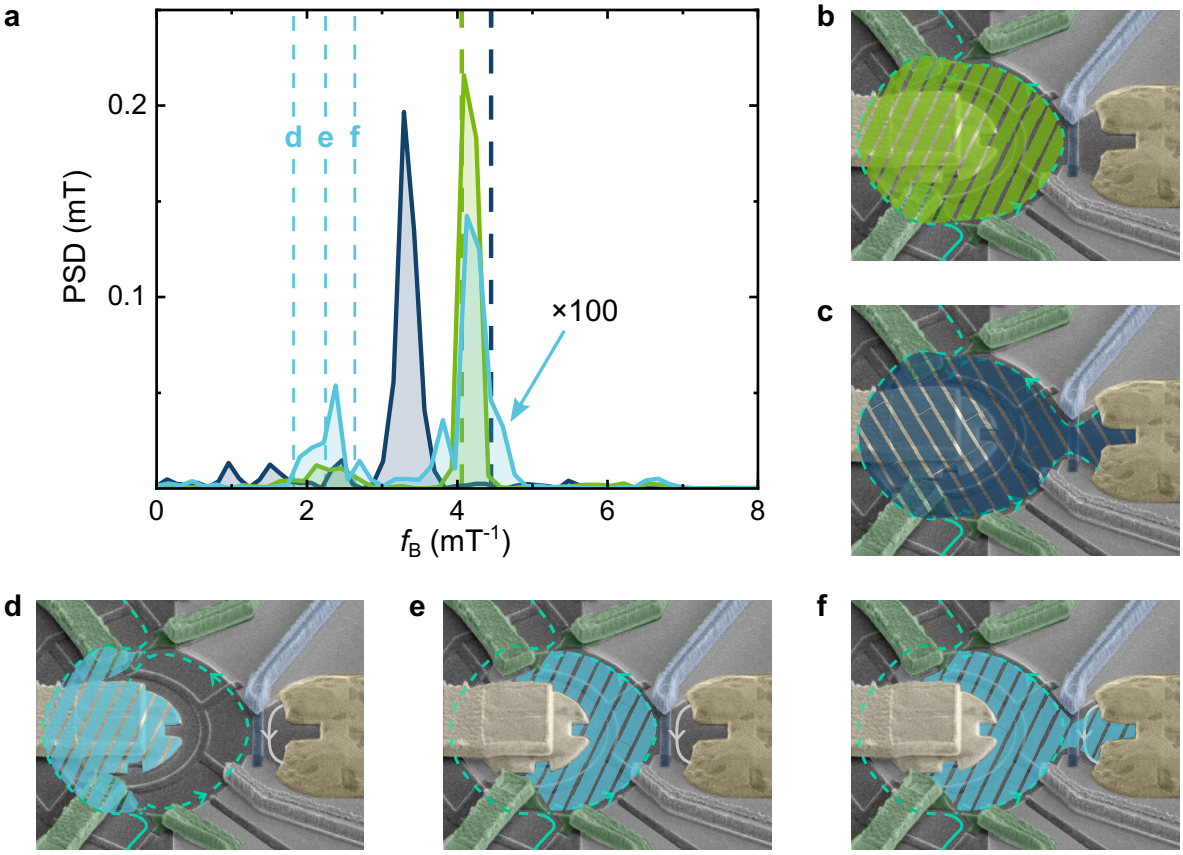

Figure 4.11: **a** Fourier transform of the data of figure 4.10 using the same color code to identify each configuration. **b** Simple MZI area. **c** Area with a single channel connected to the island in a naive approach. **d-f** Three areas of possible Fabry-Perot interferences whose first order component explain the secondary peak of the light blue FFT (when two channels are connected to the island).

Turning to the case where two channels are connected to the island, first, the area of its primary FFT-power peak is about two orders of magnitude smaller than that of the two others. This is compatible with the observed smaller contrast of the residual oscillations ($\lesssim 20\%$) as the FFT power is proportional to the squared amplitude of oscillations. Second, its FFT is peaked around the same frequency as the simple MZI case. One would expect it to be peaked around the dark blue dashed line as the reflected electrons at the metal/2DEG interface should enclose the whole dark blue area of figure 4.11 c. The sligthly lower frequency, matching that of the standard MZI, suggests that the electrons are reflected at the level of the switch gate, or that something else is happening as is further discussed in section B.2. As reflected electrons apparently contribute to oscillations with the simple MZI periodicity, then one would

also expect to see a small peak in the Fourier transform of the dark blue signal, when the island is coupled to the MZI. The reason it cannot be seen is that, with a 90% visibility, the inevitable phase noise in this MZI is responsible for noise at all other frequencies, thereby drowning this secondary peak in a higher noise background. This is clear when looking at the FFTs in log-scale where the light blue one is not rescaled: its dominant peak then lies below the noise level of the dark blue one (see figure **??** in section B.2.3).

Finally, the secondary, lower frequency peak of the two-channel case (light blue), is compatible with a first order Fabry-Perot interferences present due to the small reflections at the ohmic contacts interfaces. The possible frequencies from the areas depicted in figure 4.11 d-f are identified with the vertical light blue dashed lines in figure 4.11 a.

4.4.2 Controlling the transmitted electron phase with the island's charge

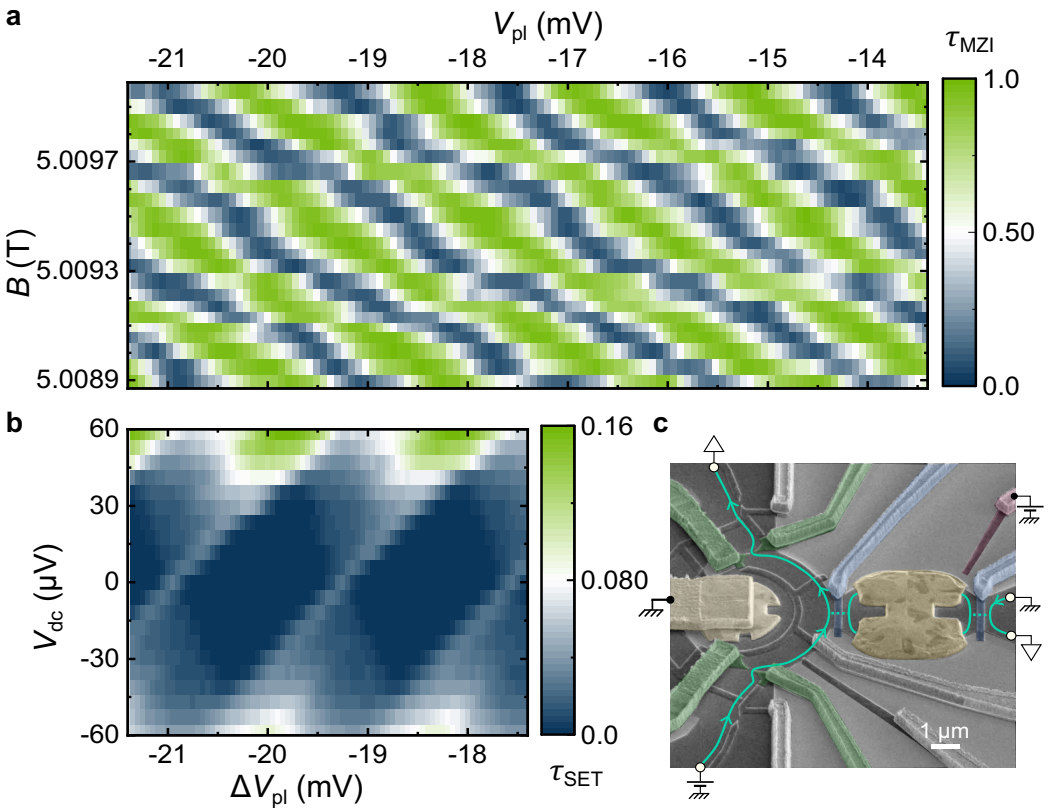

Figure 4.12: **a** Transmission across the MZI τ_{MZI} as a function of both the plunger gate voltage V_{pl} and perpendicular magnetic field B. The negative slope of the constant phase lines indicate an Aharonov-Bohm regime. **b** Coulomb diamonds of the metallic island when it is tuned in a SET regime (just like in figure 4.7) with its V_{pl} axis offset to match that of the plot in **a**. The matching periodicity with V_{pl} between the Coulomb diamonds and the MZI interferences indicate a 2π phase shift for a change of one elementary charge within the island.

We turn now to investigate the influence of the charge state of the island on the interference pattern in the configuration where the MZI is coupled to the island. Effectively, theory predicts that a modification of the island's charge by one elementary charge e should result in a 2π phase shift in the interference pattern [49]. Modifying the charge on the island can be achieved by changing the voltage applied to the gate labeled 'pl' on figure 4.5, which is close to the island and is therefore strongly coupled to it capacitively. Continuously changing the voltage of this gate enables to modify the macroscopic charge of the island, which is changed continuously because of its (almost) ballistic coupling to the quantum Hall outer channel.
On figure 4.12 a is displayed the interference pattern obtained upon changing both the magnetic field and the voltage of the plunger gate best coupled to the island. Such a measurement is standard in interferometers [18,20,193]. However, usually the plunger gate is placed in close proximity to one of the two interfering paths, while here it is mainly coupled to the island. The smooth oscillations as a function of V_{pl} show that the charge on the island is indeed changed continuously, and the negative slope of the constant phase lines indicate that the interferometer operates in the Aharonov-Bohm regime [145,146], as expected for a MZI as opposed to the Coulomb dominated regime that often take place in Fabry-Perot interferometers.

A natural question that arises is: to what corresponds the periodicity in V_{pl} ? figure 4.12 b shows Coulomb diamond of the metallic island when the device is tuned to be a single electron transistor as illustrated in figure 4.12 c. In this configuration, the two QPCs are tuned to transmit a full channel and no interferences take place, the two blue gates on each side of the island are tuned to be tunnel barriers, with very low transmission probabilities. The abscissa axis of figure 4.12 b is shifted by 17.4 mV in order for it to match that of figure 4.12 a. Remarkably, the periodicity in V_{pl} in the interference pattern of figure 4.12 a matches perfectly with the V_{pl} periodicity in the Coulomb diamonds. This demonstrates that a continuous modification of exactly one elementary charge in the island's total charge results in a 2π phase shift in the interference pattern. This is predicted by theory and is consistent with the Friedel sum rule [49]. The equivalent role between the magnetic field and the plunger gate voltage demonstrated by figure 4.12 a, together with the fact that the periodicity in gate voltage is equivalent to changing the charge on the island by exactly e further supports the good coupling between the island and the interfering channel even in the MZI regime.

In order to ascertain that V_{pl}'s influence is overwhelmingly on the island's charge, it is possible to look at the effect of this plunger gate also when in the simple MZI configuration. Its effect is illustrated on figure 4.13 a, boasting a periodicity of 270 mV, while the data in the case when the island is coupled is on figure 4.13 b, where the periodicity is the aforementionned 1.7 mV, the same as that of Coulomb diamonds. The factor ~160 between the two demonstrates that the coupling of the quantum Hall edge channel to this plunger gate is poor and much enhanced when the island is connected to it. This further shows that the interfering electrons are indeed well-coupled to the

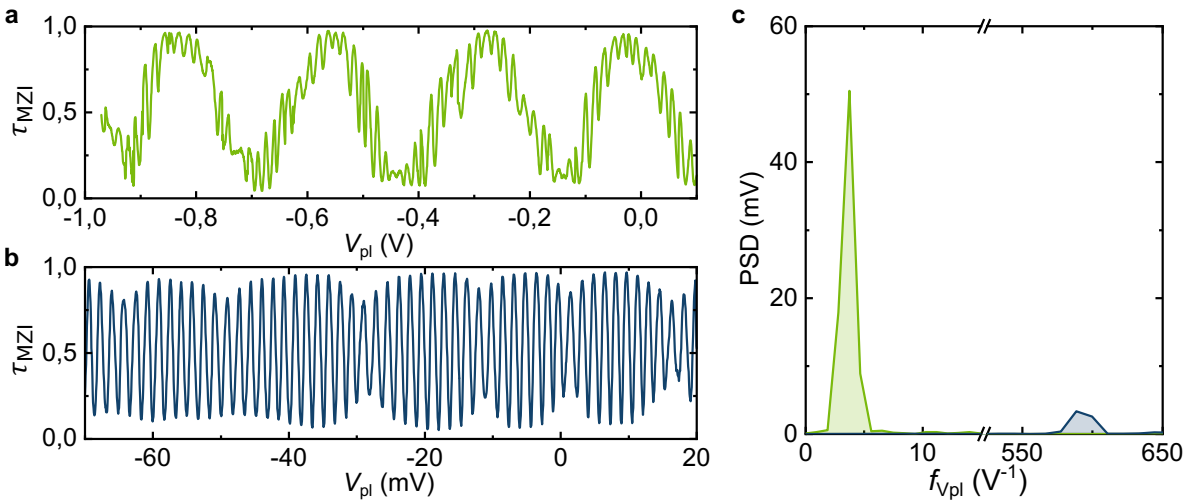

Figure 4.13: MZI interferences of **a** the MZI in the simple regime **b** the MZI with a single channel connected to the island. **c** Fourier transform of both signals in **a,b**

metallic island when the blue gate leading to it is open. Note a secondary periodicity of about 14 mV and much smaller amplitude (which consequently would not show on figure 4.13 c, which is the same in both cases suggesting that the plunger gate addresses another object, although it is not clear what this could be.

4.5 Conclusion

This experimental work therefore demonstrates a coherent transmission of the quantum state of electrons through a metallic island with a characteristic dwell time orders of magnitude larger than the typical coherence time in the island. This puzzling effect is only possible thanks to Coulomb interaction, that, through the island's large charging energy, prevents impinging electrons from coupling to the many degrees of freedom within the metal. The parallel with the proposal of L. Fu [50] (with an experimental attempt in [207]) is tantalizing considering that the charging energy also plays a crucial role in this electron teleportation scheme. A major difference with our experiment is that in this proposal, the mechanism for non-local quantum correlations involves Majorana bound-states.

This work is also strongly tied to the Coulomb blockade of heat observed in [40,208], in which a part of the electronic heat transport between a heated metallic island and cold reservoirs was blocked due to the island's large charging energy. Effectively, in this case, the correlations between all N physical channels, induced by the metallic island connecting them all, causes a decomposition in a single charged mode and $N-1$ neutral modes. The heat, in their experimental conditions, can only be carried by electrons, and therefore consists in current fluctuations. The charged ones are consequently blocked due to the charging energy, that prevents fluctuations of the island's charge. In this study, the single channel regime could not be attained for practical reasons, but the

experiment described above closes this gap as it shows no quantum information can flow between the island and the connected single channel. This implies that no heat can be exchanged either between these two, as Maxwell's demon can testify.

References

[1] W. Ehrenberg and R. E. Siday, "The Refractive Index in Electron Optics and the Principles of Dynamics," Proc. Phys. Soc. B **62**, 8–21 (IOP Publishing, 1949).

[2] Y. Aharonov and D. Bohm, "Significance of Electromagnetic Potentials in the Quantum Theory," Phys. Rev. **115**, 485–491 (American Physical Society, 1959).

[3] M. F. Crommie, C. P. Lutz, and D. M. Eigler, "Confinement of Electrons to Quantum Corrals on a Metal Surface," Science **262**, 218–220 (American Association for the Advancement of Science, 1993).

[4] M. A. Topinka, B. J. LeRoy, R. M. Westervelt, S. E. J. Shaw, R. Fleischmann, E. J. Heller, K. D. Maranowski, and A. C. Gossard, "Coherent branched flow in a two-dimensional electron gas," Nature **410**, 183–186 (Nature Publishing Group, 2001).

[5] C. Davisson and L. H. Germer, "The Scattering of Electrons by a Single Crystal of Nickel," Nature **119**, 558–560 (Nature Publishing Group, 1927).

[6] C. Davisson and L. H. Germer, "Diffraction of Electrons by a Crystal of Nickel," Phys. Rev. **30**, 705–740 (American Physical Society, 1927).

[7] L. de Broglie, "Recherches sur la théorie des Quanta," PhD thesis (Université de Paris, 1924).

[8] R. P. Feynman, R. B. Leighton, and M. Sands, The Feynman Lectures on Physics, The New Millenium (Basic Books).

[9] C. Jönsson, "Electron Diffraction at Multiple Slits," American Journal of Physics **42**, 4–11 (American Association of Physics Teachers, 1974).

[10] O. Donati, G. P. Missiroli, and G. Pozzi, "An Experiment on Electron Interference," American Journal of Physics **41**, 639–644 (American Association of Physics Teachers, 1973).

[11] A. Tonomura, T. Matsuda, R. Suzuki, A. Fukuhara, N. Osakabe, H. Umezaki, J. Endo, K. Shinagawa, Y. Sugita, et al., "Observation of Aharonov-Bohm Effect by Electron Holography," Phys. Rev. Lett. **48**, 1443–1446 (American Physical Society, 1982).

[12] S. Frabboni, A. Gabrielli, G. Carlo Gazzadi, F. Giorgi, G. Matteucci, G. Pozzi, N. S. Cesari, M. Villa, and A. Zoccoli, "The Young-Feynman two-slits experiment with single electrons: Build-up of the interference pattern and arrival-time distribution using a fast-readout pixel detector," Ultramicroscopy **116**, 73–76 (2012).

[13] R. Bach, D. Pope, S.-H. Liou, and H. Batelaan, "Controlled double-slit electron diffraction," New J. Phys. **15**, 033018 (IOP Publishing, 2013).

[14] S. Hermelin, S. Takada, M. Yamamoto, S. Tarucha, A. D. Wieck, L. Saminadayar, C. Bäuerle, and T. Meunier, "Electrons surfing on a sound wave as a platform for quantum optics with flying electrons," Nature **477**, 435–438 (Nature Publishing Group, 2011).

[15] B. Chenaud, C. Chaubet, B. Jouault, L. Saminadayar, D. Mailly, G. Faini, and A. Cavanna, "Edge states interferometer: An electronic Fabry–Perot," Physica B: Condensed Matter **346–347**, 488–492 (2004).

[16] F. E. Camino, W. Zhou, and V. J. Goldman, "Aharonov-Bohm electron interferometer in the integer quantum Hall regime," Phys. Rev. B **72**, 155313 (American Physical Society, 2005).

[17] F. E. Camino, W. Zhou, and V. J. Goldman, "Quantum transport in electron Fabry-Perot interferometers," Phys. Rev. B **76**, 155305 (American Physical Society, 2007).

[18] N. Ofek, A. Bid, M. Heiblum, A. Stern, V. Umansky, and D. Mahalu, "Role of interactions in an electronic Fabry–Perot interferometer operating in the quantum Hall effect regime," PNAS **107**, 5276–5281 (2010).

[19] J. Nakamura, S. Liang, G. C. Gardner, and M. J. Manfra, "Direct observation of anyonic braiding statistics," Nature Physics **16**, 931–936 (Nature Publishing Group, 2020).

[20] Y. Ji, Y. Chung, D. Sprinzak, M. Heiblum, D. Mahalu, and H. Shtrikman, "An electronic Mach–Zehnder interferometer," Nature **422**, 415–418 (2003).

[21] P. Roulleau, F. Portier, P. Roche, A. Cavanna, G. Faini, U. Gennser, and D. Mailly, "Direct Measurement of the Coherence Length of Edge States in the Integer Quantum Hall Regime," Phys. Rev. Lett. **100**, 126802 (2008).

[22] I. Neder, N. Ofek, Y. Chung, M. Heiblum, D. Mahalu, and V. Umansky, "Interference between two indistinguishable electrons from independent sources," Nature **448**, 333 (2007).

[23] E. Bocquillon, V. Freulon, J.-M. Berroir, P. Degiovanni, B. Plaçais, A. Cavanna, Y. Jin, and G. Fève, "Coherence and Indistinguishability of Single Electrons Emitted by Independent Sources," Science **339**, 1054–1057 (American Association for the Advancement of Science, 2013).

[24] J. Dubois, T. Jullien, F. Portier, P. Roche, A. Cavanna, Y. Jin, W. Wegscheider, P. Roulleau, and D. C. Glattli, "Minimal-excitation states for electron quantum optics using levitons," Nature **502**, 659–663 (2013).

[25] E. Bocquillon, V. Freulon, J. M. Berroir, P. Degiovanni, B. Plaçais, A. Cavanna, Y. Jin, and G. Fève, "Separation of neutral and charge modes in one-dimensional chiral edge channels," Nature Communications **4**, 1839 (2013).

[26] H. Inoue, A. Grivnin, N. Ofek, I. Neder, M. Heiblum, V. Umansky, and D. Mahalu, "Charge Fractionalization in the Integer Quantum Hall Effect," Phys. Rev. Lett. **112**, 166801 (2014).

[27] M. Hashisaka, N. Hiyama, T. Akiho, K. Muraki, and T. Fujisawa, "Waveform measurement of charge- and spin-density wavepackets in a chiral Tomonaga–Luttinger liquid," Nature Physics **13**, 559–562 (2017).

[28] R. H. Rodriguez, F. D. Parmentier, D. Ferraro, P. Roulleau, U. Gennser, A. Cavanna, M. Sassetti, F. Portier, D. Mailly, et al., "Relaxation and revival of quasiparticles injected in an interacting quantum Hall liquid," Nature Communications **11**, 2426 (Nature Publishing Group, 2020).

[29] E. Bieri, M. Weiss, O. Göktas, M. Hauser, C. Schönenberger, and S. Oberholzer, "Finite-bias visibility dependence in an electronic Mach-Zehnder interferometer," Phys. Rev. B **79**, 245324 (2009).

[30] A. Helzel, L. V. Litvin, I. P. Levkivskyi, E. V. Sukhorukov, W. Wegscheider, and C. Strunk, "Counting statistics and dephasing transition in an electronic Mach-Zehnder interferometer," Phys. Rev. B **91**, 245419 (2015).

[31] L. V. Litvin, A. Helzel, H.-P. Tranitz, W. Wegscheider, and C. Strunk, "Phase of the transmission amplitude for a quantum dot embedded in the arm of an electronic Mach-Zehnder interferometer," Phys. Rev. B **81**, 205425 (American Physical Society, 2010).

[32] I. Neder, M. Heiblum, Y. Levinson, D. Mahalu, and V. Umansky, "Unexpected Behavior in a Two-Path Electron Interferometer," Phys. Rev. Lett. **96**, 016804 (2006).

[33] P. Roulleau, F. Portier, D. C. Glattli, P. Roche, A. Cavanna, G. Faini, U. Gennser, and D. Mailly, "Finite bias visibility of the electronic Mach-Zehnder interferometer," Phys. Rev. B **76**, 161309 (2007).

[34] C. Altimiras, H. le Sueur, U. Gennser, A. Cavanna, D. Mailly, and F. Pierre, "Tuning Energy Relaxation along Quantum Hall Channels," Phys. Rev. Lett. **105**,

226804 (2010).

[35] H. le Sueur, C. Altimiras, U. Gennser, A. Cavanna, D. Mailly, and F. Pierre, "Energy Relaxation in the Integer Quantum Hall Regime," Phys. Rev. Lett. **105**, 056803 (2010).

[36] T. Krähenmann, S. G. Fischer, M. Röösli, T. Ihn, C. Reichl, W. Wegscheider, K. Ensslin, Y. Gefen, and Y. Meir, "Auger-spectroscopy in quantum Hall edge channels and the missing energy problem," Nat Commun **10**, 1–6 (2019).

[37] K. Itoh, R. Nakazawa, T. Ota, M. Hashisaka, K. Muraki, and T. Fujisawa, "Signatures of a Nonthermal Metastable State in Copropagating Quantum Hall Edge Channels," Phys. Rev. Lett. **120**, 197701 (2018).

[38] T. Ota, S. Akiyama, M. Hashisaka, K. Muraki, and T. Fujisawa, "Spectroscopic study on hot-electron transport in a quantum Hall edge channel," 23 February 2019, <http://arxiv.org/abs/1902.08743> (27 February 2019).

[39] E. Bocquillon, V. Freulon, F. D. Parmentier, J.-M. Berroir, B. Plaçais, C. Wahl, J. Rech, T. Jonckheere, T. Martin, et al., "Electron quantum optics in ballistic chiral conductors," Annalen der Physik **526**, 1–30 (2014).

[40] E. Sivre, A. Anthore, F. D. Parmentier, A. Cavanna, U. Gennser, A. Ouerghi, Y. Jin, and F. Pierre, "Heat Coulomb blockade of one ballistic channel," Nature Physics **14**, 145–148 (2018).

[41] P.-A. Hyunh, F. Portier, H. le Sueur, G. Faini, U. Gennser, D. Mailly, F. Pierre, W. Wegscheider, and P. Roche, "Quantum Coherence Engineering in the Integer Quantum Hall Regime," Phys. Rev. Lett. **108**, 256802 (2012).

[42] H. Duprez, E. Sivre, A. Anthore, A. Aassime, A. Cavanna, A. Ouerghi, U. Gennser, and F. Pierre, "Macroscopic Electron Quantum Coherence in a Solid-State Circuit," Phys. Rev. X **9**, 021030 (American Physical Society, 2019).

[43] M. Büttiker, "Small normal-metal loop coupled to an electron reservoir," Phys. Rev. B **32**, 1846–1849 (American Physical Society, 1985).

[44] M. Büttiker, "Role of quantum coherence in series resistors," Phys. Rev. B **33**, 3020–3026 (American Physical Society, 1986).

[45] M. Büttiker, "Absence of backscattering in the quantum Hall effect in multiprobe conductors," Phys. Rev. B **38**, 9375–9389 (1988).

[46] A. A. Clerk, P. W. Brouwer, and V. Ambegaokar, "Interaction-Induced Restoration of Phase Coherence," Phys. Rev. Lett. **87**, 186801 (2001).

[47] E. G. Idrisov, I. P. Levkivskyi, and E. V. Sukhorukov, "Dephasing in a Mach-Zehnder Interferometer by an Ohmic Contact," Phys. Rev. Lett. **121**, 026802 (2018).

[48] S.-Y. Lee, H.-W. Lee, and H.-S. Sim, "Visibility recovery by strong interaction in an electronic Mach-Zehnder interferometer," Phys. Rev. B **86**, 235444 (2012).

[49] A. Clerk, "ASPECTS OF ANDREEV SCATTERING AND KONDO PHYSICS IN MESOSCOPIC SYSTEMS" (Cornell University, 2001).

[50] L. Fu, "Electron Teleportation via Majorana Bound States in a Mesoscopic Superconductor," Phys. Rev. Lett. **104**, 056402 (2010).

[51] R. J. Glauber, "The Quantum Theory of Optical Coherence," Phys. Rev. **130**, 2529–2539 (1963).

[52] B. Roussel, "Autopsy of a quantum electrical current," Theses (Université de Lyon, 2017).

[53] A. Stern, Y. Aharonov, and Y. Imry, "Phase uncertainty and loss of interference: A general picture," Phys. Rev. A **41**, 3436–3448 (American Physical Society, 1990).

[54] A. Stern, Y. Aharonov, and Y. Imry, "Linear Response and Dephasing by Coulomb Electron-Electron Interactions," in Quantum Coherence in Mesoscopic Systems, B. Kramer, Ed. (Springer US, Boston, MA, 1991).

[55] D. Y. Sharvin and Y. V. Sharvin, "Magnetic flux quantization in a cylindrical film," JETP Lett. **34**, 272–275 (1981).

[56] T. Ihn, "Oscillations in the ribbons," Nature Materials **9**, 187–188 (Nature Publishing Group, 2010).

[57] B. L. Altshuler, A. G. Aronov, B. Z. Spivak, D. Y. Sharvin, and Y. V. Sharvin, "Observation of the Aharonov-Bohm effect in hollow metal cylinders," JETP Lett. **35**, 588–590 (1982).

[58] A. Bachtold, C. Strunk, J.-P. Salvetat, J.-M. Bonard, L. Forró, T. Nussbaumer, and C. Schönenberger, "Aharonov–Bohm oscillations in carbon nanotubes," Nature **397**, 673–675 (Nature Publishing Group, 1999).

[59] B. L. Altshuler, A. G. Aronov, and B. Z. Spivak, "The Aharonov-Bohm effect in disordered conductors," JETP Lett. **33**, 94–97 (1981).

[60] M. Gijs, C. Van Haesendonck, and Y. Bruynseraede, "Resistance Oscillations and Electron Localization in Cylindrical Mg Films," Phys. Rev. Lett. **52**, 2069–2072 (American Physical Society, 1984).

[61] S. Washburn and R. A. Webb, "Aharonov-Bohm effect in normal metal quantum coherence and transport," Advances in Physics **35**, 375–422 (Taylor & Francis, 1986).

[62] Y. V. Sharvin, "Weak localization and oscillatory magnetoresistance of cylindrical metal films," Physica B+C **126**, 288–293 (1984).

[63] C. P. Umbach, C. Van Haesendonck, R. B. Laibowitz, S. Washburn, and R. A.

Webb, "Direct observation of ensemble averaging of the Aharonov-Bohm effect in normal-metal loops," Phys. Rev. Lett. **56**, 386–389 (American Physical Society, 1986).

[64] V. Chandrasekhar, M. J. Rooks, S. Wind, and D. E. Prober, "Observation of Aharonov-Bohm Electron Interference Effects with Periods $\frac{h}{e}$ and $\frac{h}{2e}$ in Individual Micron-Size, Normal-Metal Rings," Phys. Rev. Lett. **55**, 1610–1613 (American Physical Society, 1985).

[65] S. Chakravarty and A. Schmid, "Weak localization: The quasiclassical theory of electrons in a random potential," Physics Reports **140**, 193–236 (1986).

[66] M. Büttiker, Y. Imry, and M. Y. Azbel, "Quantum oscillations in one-dimensional normal-metal rings," Phys. Rev. A **30**, 1982–1989 (American Physical Society, 1984).

[67] Y. Gefen, Y. Imry, and M. Y. Azbel, "Quantum Oscillations and the Aharonov-Bohm Effect for Parallel Resistors," Phys. Rev. Lett. **52**, 129–132 (American Physical Society, 1984).

[68] M. Büttiker, Y. Imry, R. Landauer, and S. Pinhas, "Generalized many-channel conductance formula with application to small rings," Phys. Rev. B **31**, 6207–6215 (American Physical Society, 1985).

[69] R. A. Webb, S. Washburn, C. P. Umbach, and R. B. Laibowitz, "Observation of $\frac{h}{e}$ Aharonov-Bohm Oscillations in Normal-Metal Rings," Phys. Rev. Lett. **54**, 2696–2699 (1985).

[70] A. D. Benoit, S. Washburn, C. P. Umbach, R. B. Laibowitz, and R. A. Webb, "Asymmetry in the Magnetoconductance of Metal Wires and Loops," Phys. Rev. Lett. **57**, 1765–1768 (American Physical Society, 1986).

[71] F. P. Milliken, S. Washburn, C. P. Umbach, R. B. Laibowitz, and R. A. Webb, "Effect of partial phase coherence on Aharonov-Bohm oscillations in metal loops," Phys. Rev. B **36**, 4465–4468 (American Physical Society, 1987).

[72] S. Washburn, H. Schmid, D. Kern, and R. A. Webb, "Normal-metal Aharonov-Bohm effect in the presence of a transverse electric field," Phys. Rev. Lett. **59**, 1791–1794 (American Physical Society, 1987).

[73] D. Mailly, C. Chapelier, and A. Benoit, "Experimental observation of persistent currents in GaAs-AlGaAs single loop," Phys. Rev. Lett. **70**, 2020–2023 (1993).

[74] I. O. Kulik, "Flux quantization in a normal metal," JETP Lett. **11**, 275–277 (1970).

[75] M. Büttiker, Y. Imry, and R. Landauer, "Josephson behavior in small normal one-dimensional rings," Physics Letters A **96**, 365–367 (1983).

[76] H. Bouchiat, G. Montambaux, L. P. Levyt, G. Dolan, and J. Dunsmuir, "Persistent Currents in Mesoscopic Rings: Ensemble Average and Half-Flux-Quantum Periodicity,"

in Quantum Coherence in Mesoscopic Systems, B. Kramer, Ed. (Springer US, Boston, MA, 1991).

[77] E. Akkermans and G. Montambaux, Mesoscopic Physics of Electrons and Photons (Cambridge University Press, 2007).

[78] W. Nolting and A. Ramakanth, Quantum Theory of Magnetism (Springer Berlin Heidelberg, Berlin, Heidelberg, 2009).

[79] L. P. Lévy, G. Dolan, J. Dunsmuir, and H. Bouchiat, "Magnetization of mesoscopic copper rings: Evidence for persistent currents," Phys. Rev. Lett. **64**, 2074–2077 (American Physical Society, 1990).

[80] A. C. Bleszynski-Jayich, W. E. Shanks, B. Peaudecerf, E. Ginossar, F. von Oppen, L. Glazman, and J. G. E. Harris, "Persistent Currents in Normal Metal Rings," Science **326**, 272–275 (American Association for the Advancement of Science, 2009).

[81] H. Bluhm, N. C. Koshnick, J. A. Bert, M. E. Huber, and K. A. Moler, "Persistent Currents in Normal Metal Rings," Phys. Rev. Lett. **102**, 136802 (American Physical Society, 2009).

[82] G. Bergmann, "Weak localization in thin films: A time-of-flight experiment with conduction electrons," Physics Reports **107**, 1–58 (1984).

[83] F. Pierre, A. B. Gougam, A. Anthore, H. Pothier, D. Esteve, and N. O. Birge, "Dephasing of electrons in mesoscopic metal wires," Phys. Rev. B **68**, 085413 (2003).

[84] F. PIERRE, "Interaction électron-électron dans les fils mésoscopiques," Theses (Université Pierre et Marie Curie - Paris VI, 2000).

[85] Y. Niimi, Y. Baines, T. Capron, D. Mailly, F.-Y. Lo, A. D. Wieck, T. Meunier, L. Saminadayar, and C. Bäuerle, "Quantum coherence at low temperatures in mesoscopic systems: Effect of disorder," Phys. Rev. B **81**, 245306 (2010).

[86] F. Pierre and N. O. Birge, "Dephasing by Extremely Dilute Magnetic Impurities Revealed by Aharonov-Bohm Oscillations," Phys. Rev. Lett. **89**, 206804 (American Physical Society, 2002).

[87] S. Datta, Electronic Transport in Mesoscopic Systems (Cambridge University Press, 1997).

[88] Y. Chen, P. Roushan, D. Sank, C. Neill, E. Lucero, M. Mariantoni, R. Barends, B. Chiaro, J. Kelly, et al., "Emulating weak localization using a solid-state quantum circuit," Nature Communications **5**, 5184 (Nature Publishing Group, 2014).

[89] S. B. Kaplan and A. Hartstein, "Universal Conductance Fluctuations in Narrow Si Accumulation Layers," Phys. Rev. Lett. **56**, 2403–2406 (American Physical Society, 1986).

[90] A. B. Fowler, A. Hartstein, and R. A. Webb, "Conductance in Restricted-Dimensionality Accumulation Layers," Phys. Rev. Lett. **48**, 196–199 (American Physical Society, 1982).

[91] P. A. Lee and A. D. Stone, "Universal Conductance Fluctuations in Metals," Phys. Rev. Lett. **55**, 1622–1625 (American Physical Society, 1985).

[92] J. C. Licini, D. J. Bishop, M. A. Kastner, and J. Melngailis, "Aperiodic magnetoresistance oscillations in narrow inversion layers in Si," Phys. Rev. Lett. **55**, 2987–2990 (American Physical Society, 1985).

[93] A. Ghosh and A. K. Raychaudhuri, "Universal Conductance Fluctuations in Three Dimensional Metallic Single Crystals of Si," Phys. Rev. Lett. **84**, 4681–4684 (American Physical Society, 2000).

[94] W. J. Skocpol, P. M. Mankiewich, R. E. Howard, L. D. Jackel, D. M. Tennant, and A. D. Stone, "Universal conductance fluctuations in silicon inversion-layer nanostructures," Phys. Rev. Lett. **56**, 2865–2868 (American Physical Society, 1986).

[95] C. P. Umbach, S. Washburn, R. B. Laibowitz, and R. A. Webb, "Magnetoresistance of small, quasi-one-dimensional, normal-metal rings and lines," Phys. Rev. B **30**, 4048–4051 (American Physical Society, 1984).

[96] D. W. Horsell, A. K. Savchenko, F. V. Tikhonenko, K. Kechedzhi, I. V. Lerner, and V. I. Fal'ko, "Mesoscopic conductance fluctuations in graphene," Solid State Communications **149**, 1041–1045 (2009).

[97] S. V. Morozov, K. S. Novoselov, M. I. Katsnelson, F. Schedin, L. A. Ponomarenko, D. Jiang, and A. K. Geim, "Strong Suppression of Weak Localization in Graphene," Phys. Rev. Lett. **97**, 016801 (American Physical Society, 2006).

[98] X. Wu, X. Li, Z. Song, C. Berger, and W. A. de Heer, "Weak Antilocalization in Epitaxial Graphene: Evidence for Chiral Electrons," Phys. Rev. Lett. **98**, 136801 (American Physical Society, 2007).

[99] Y.-F. Chen, M.-H. Bae, C. Chialvo, T. Dirks, A. Bezryadin, and N. Mason, "Magnetoresistance in single-layer graphene: Weak localization and universal conductance fluctuation studies," J. Phys.: Condens. Matter **22**, 205301 (IOP Publishing, 2010).

[100] Z. Li, T. Chen, H. Pan, F. Song, B. Wang, J. Han, Y. Qin, X. Wang, R. Zhang, et al., "Two-dimensional universal conductance fluctuations and the electron-phonon interaction of surface states in Bi 2 Te 2 Se microflakes," Scientific Reports **2**, 595 (Nature Publishing Group, 2012).

[101] S. Das Sarma, S. Adam, E. H. Hwang, and E. Rossi, "Electronic transport in two-dimensional graphene," Rev. Mod. Phys. **83**, 407–470 (2011).

[102] S. Feng and P. A. Lee, "Mesoscopic Conductors and Correlations in Laser Speckle Patterns," Science **251**, 633–639 (American Association for the Advancement of Science,

1991).

[103] Y. Imry, “Active Transmission Channels and Universal Conductance Fluctuations,” EPL **1**, 249–256 (IOP Publishing, 1986).

[104] D. T. Haar, Collected Papers of L.D. Landau (Gordon and Breach, 1965).

[105] J. H. Van Vleck, Theory of Electric and Magnetic Susceptibilities (Oxford University Press, 1932).

[106] I. L. Aleiner, B. L. Altshuler, and M. E. Gershenson, “Interaction effects and phase relaxation in disordered systems,” Waves in Random Media **9**, 201–239 (1999).

[107] B. L. Altshuler, A. G. Aronov, and D. E. Khmelnitsky, “Effects of electron-electron collisions with small energy transfers on quantum localisation,” J. Phys. C: Solid State Phys. **15**, 7367–7386 (IOP Publishing, 1982).

[108] A. Anthore, “Mécanismes de decohérence dans les conducteurs mésoscopiques / Decoherence mechanisms in mesocopic conductors,” Theses (Université Pierre et Marie Curie - Paris VI, 2003).

[109] P. Mohanty, E. M. Q. Jariwala, and R. A. Webb, “Intrinsic Decoherence in Mesoscopic Systems,” Phys. Rev. Lett. **78**, 3366–3369 (American Physical Society, 1997).

[110] D. S. Golubev and A. D. Zaikin, “Quantum Decoherence in Disordered Mesoscopic Systems,” Phys. Rev. Lett. **81**, 1074–1077 (American Physical Society, 1998).

[111] P.-Y. Yang, L. Y. Wang, Y.-W. Hsu, and J.-J. Lin, “Universal conductance fluctuations in indium tin oxide nanowires,” Phys. Rev. B **85**, 085423 (American Physical Society, 2012).

[112] A. van Oudenaarden, M. H. Devoret, E. H. Visscher, Y. V. Nazarov, and J. E. Mooij, “Conductance Fluctuations in a Metallic Wire Interrupted by a Tunnel Junction,” Phys. Rev. Lett. **78**, 3539–3542 (American Physical Society, 1997).

[113] P. Petit, A. Anthore, M. L. Della Rocca, and P. Lafarge, “Conductance fluctuations in metallic nanogaps made by electromigration,” Journal of Applied Physics **109**, 014307 (American Institute of Physics, 2011).

[114] T. Trivedi, S. Sonde, H. C. P. Movva, and S. K. Banerjee, “Weak antilocalization and universal conductance fluctuations in bismuth telluro-sulfide topological insulators,” Journal of Applied Physics **119**, 055706 (American Institute of Physics, 2016).

[115] A. Benoit, D. Mailly, P. Perrier, and P. Nedellec, “Effect of magnetic impurities of universal conductance fluctuations,” Superlattices and Microstructures **11**, 313–316 (1992).

[116] A. Yacoby, U. Sivan, C. P. Umbach, and J. M. Hong, “Interference and dephasing by electron-electron interaction on length scales shorter than the elastic mean free path,” Phys. Rev. Lett. **66**, 1938–1941 (American Physical Society, 1991).

[117] A. Yacoby, M. Heiblum, H. Shtrikman, V. Umansky, and D. Mahalu, "Dephasing of ballistic electrons as a function of temperature and carrier density," Semicond. Sci. Technol. **9**, 907–910 (IOP Publishing, 1994).

[118] E. Buks, R. Schuster, M. Heiblum, D. Mahalu, and V. Umansky, "Dephasing in electron interference by a 'which-path' detector," Nature **391**, 871–874 (Nature Publishing Group, 1998).

[119] L. Meier, A. Fuhrer, T. Ihn, K. Ensslin, W. Wegscheider, and M. Bichler, "Single-electron effects in a coupled dot-ring system," Phys. Rev. B **69**, 241302 (American Physical Society, 2004).

[120] P. Nozieres and D. Pines, Theory Of Quantum Liquids (Avalon Publishing, 1999).

[121] T. Giamarchi, Quantum Physics in One Dimension (Oxford University Press, Oxford, New York, 2003).

[122] R. H. Rodriguez, "Relaxation of quasiparticles injected above the Fermi sea of a Quantum Hall edge channel," Theses (Université Paris-Saclay, 2019).

[123] D. Tong, "Lectures on the Quantum Hall Effect," 21 June 2016, <http://arxiv.org/abs/1606.06687> (28 October 2017).

[124] R. E. Prange and S. M. Girvin, Eds., The Quantum Hall Effect, 2nd ed. (Springer-Verlag, New York, 1990).

[125] S. M. Girvin, "The Quantum Hall Effect: Novel Excitations and Broken Symmetries," 1 July 1999, <http://arxiv.org/abs/cond-mat/9907002> (8 June 2017).

[126] B. Douçot and V. Pasquier, "Physics in a Strong Magnetic Field," in The Quantum Hall Effect, B. Douçot, V. Pasquier, B. Duplantier, and V. Rivasseau, Eds. (Birkhäuser Basel, 2005).

[127] M. O. Goerbig, "Quantum Hall Effects," 10 September 2009, <http://arxiv.org/abs/0909.1998> (8 June 2017).

[128] "Gilles Montambaux's Homepage," <https://www.equipes.lps.u-psud.fr/Montambaux/X-meso.htm> (22 October 2018).

[129] D. Haneman, "Photoelectric emission and work functions of InSb, GaAs, Bi2Te3 and germanium," Journal of Physics and Chemistry of Solids **11**, 205–214 (1959).

[130] N. Inoue, T. Higashino, K. Tanahashi, and Y. Kawamura, "Work function of GaAs (001) surface obtained by the electron counting model," Journal of Crystal Growth **227-228**, 123–126 (2001).

[131] D. G. Polyakov and B. I. Shklovskii, "Variable range hopping as the mechanism of the conductivity peak broadening in the quantum Hall regime," Phys. Rev. Lett. **70**, 3796–3799 (American Physical Society, 1993).

[132] B. Huckestein, "Scaling theory of the integer quantum Hall effect," Rev. Mod. Phys. **67**, 357–396 (American Physical Society, 1995).

[133] K. Bennaceur, P. Jacques, F. Portier, P. Roche, and D. C. Glattli, "Unveiling quantum Hall transport by Efros-Shklovskii to Mott variable-range hopping transition in graphene," Phys. Rev. B **86**, 085433 (American Physical Society, 2012).

[134] R. C. Ashoori, H. L. Stormer, L. N. Pfeiffer, K. W. Baldwin, and K. West, "Edge magnetoplasmons in the time domain," Phys. Rev. B **45**, 3894–3897 (American Physical Society, 1992).

[135] M. Kataoka, N. Johnson, C. Emary, P. See, J. P. Griffiths, G. A. C. Jones, I. Farrer, D. A. Ritchie, M. Pepper, et al., "Time-of-Flight Measurements of Single-Electron Wave Packets in Quantum Hall Edge States," Phys. Rev. Lett. **116**, 126803 (American Physical Society, 2016).

[136] S. P. Giblin, M. Kataoka, J. D. Fletcher, P. See, T. J. B. M. Janssen, J. P. Griffiths, G. a. C. Jones, I. Farrer, and D. A. Ritchie, "Towards a quantum representation of the ampere using single electron pumps," Nature Communications **3**, 930 (Nature Publishing Group, 2012).

[137] G. Fève, A. Mahé, J.-M. Berroir, T. Kontos, B. Plaçais, D. C. Glattli, A. Cavanna, B. Etienne, and Y. Jin, "An On-Demand Coherent Single-Electron Source," Science **316**, 1169–1172 (2007).

[138] M. Field, C. G. Smith, M. Pepper, D. A. Ritchie, J. E. F. Frost, G. A. C. Jones, and D. G. Hasko, "Measurements of Coulomb blockade with a noninvasive voltage probe," Phys. Rev. Lett. **70**, 1311–1314 (American Physical Society, 1993).

[139] R. Schleser, E. Ruh, T. Ihn, K. Ensslin, D. C. Driscoll, and A. C. Gossard, "Time-resolved detection of individual electrons in a quantum dot," Appl. Phys. Lett. **85**, 2005–2007 (American Institute of Physics, 2004).

[140] D. J. Reilly, C. M. Marcus, M. P. Hanson, and A. C. Gossard, "Fast single-charge sensing with a rf quantum point contact," Appl. Phys. Lett. **91**, 162101 (2007).

[141] G. D. C., N. J., T. I., R. P., B. C., and W. X, "Design of a Single-Shot Electron detector with sub-electron sensitivity for electron flying qubit operation," 10 February 2020, <http://arxiv.org/abs/2002.03947> (24 September 2020).

[142] C. Bäuerle, D. C. Glattli, T. Meunier, F. Portier, P. Roche, Preden Roulleau, S. Takada, and X. Waintal, "Coherent control of single electrons: A review of current progress," Rep. Prog. Phys. **81**, 056503 (2018).

[143] C. K. Hong, Z. Y. Ou, and L. Mandel, "Measurement of subpicosecond time intervals between two photons by interference," Phys. Rev. Lett. **59**, 2044–2046 (American Physical Society, 1987).

[144] H. Bartolomei, M. Kumar, R. Bisognin, A. Marguerite, J.-M. Berroir, E. Bocquillon, B. Plaçais, A. Cavanna, Q. Dong, et al., "Fractional statistics in anyon collisions," Science **368**, 173–177 (American Association for the Advancement of Science, 2020).

[145] B. I. Halperin, A. Stern, I. Neder, and B. Rosenow, "Theory of the Fabry-Pérot quantum Hall interferometer," Phys. Rev. B **83**, 155440 (2011).

[146] I. Sivan, H. K. Choi, J. Park, A. Rosenblatt, Y. Gefen, D. Mahalu, and V. Umansky, "Observation of interaction-induced modulations of a quantum Hall liquid's area," Nature Communications **7**, 12184 (2016).

[147] M. P. Röösli, M. Hug, G. Nicolí, P. Märki, C. Reichl, B. Rosenow, W. Wegscheider, K. Ensslin, and T. Ihn, "Fractional Coulomb blockade for quasiparticle tunneling between edge channels," 26 May 2020, <http://arxiv.org/abs/2005.12723> (20 August 2020).

[148] M. P. Röösli, L. Brem, B. Kratochwil, G. Nicolí, B. A. Braem, S. Hennel, P. Märki, M. Berl, C. Reichl, et al., "Observation of quantum Hall interferometer phase jumps due to a change in the number of bulk quasiparticles," Phys. Rev. B **101**, 125302 (American Physical Society, 2020).

[149] J. Nakamura, S. Fallahi, H. Sahasrabudhe, R. Rahman, S. Liang, G. C. Gardner, and M. J. Manfra, "Aharonov–Bohm interference of fractional quantum Hall edge modes," Nat. Phys. **15**, 563–569 (2019).

[150] C. Déprez, L. Veyrat, H. Vignaud, G. Nayak, K. Watanabe, T. Taniguchi, F. Gay, H. Sellier, and B. Sacépé, "A tunable Fabry-P\'erot quantum Hall interferometer in graphene," 25 August 2020, <http://arxiv.org/abs/2008.11222> (27 August 2020).

[151] Y. Ronen, T. Werkmeister, D. Najafabadi, A. T. Pierce, L. E. Anderson, Y. J. Shin, S. Y. Lee, Y. H. Lee, B. Johnson, et al., "Aharonov Bohm Effect in Graphene Fabry P\'erot Quantum Hall Interferometers," 27 August 2020, <http://arxiv.org/abs/2008.12285> (30 August 2020).

[152] A. Stern, "Anyons and the quantum Hall effect—A pedagogical review," Annals of Physics **323**, 204–249 (2008).

[153] R. Bhattacharyya, M. Banerjee, M. Heiblum, D. Mahalu, and V. Umansky, "Melting of Interference in the Fractional Quantum Hall Effect: Appearance of Neutral Modes," Phys. Rev. Lett. **122**, 246801 (American Physical Society, 2019).

[154] I. Gurman, R. Sabo, M. Heiblum, V. Umansky, and D. Mahalu, "Dephasing of an electronic two-path interferometer," Phys. Rev. B **93**, 121412 (2016).

[155] I. L. Aleiner and L. I. Glazman, "Novel edge excitations of two-dimensional electron liquid in a magnetic field," Phys. Rev. Lett. **72**, 2935–2938 (American Physical Society, 1994).

[156] C. de C. Chamon and X. G. Wen, "Sharp and smooth boundaries of quantum Hall liquids," Phys. Rev. B **49**, 8227–8241 (American Physical Society, 1994).

[157] P. Bonderson, A. Kitaev, and K. Shtengel, "Detecting Non-Abelian Statistics in the $\ensuremath{\nu}=5/2$ Fractional Quantum Hall State," Phys. Rev. Lett. **96**, 016803 (American Physical Society, 2006).

[158] F. E. Camino, W. Zhou, and V. J. Goldman, "Aharonov-Bohm Superperiod in a Laughlin Quasiparticle Interferometer," Phys. Rev. Lett. **95**, 246802 (American Physical Society, 2005).

[159] F. E. Camino, W. Zhou, and V. J. Goldman, "Realization of a Laughlin quasiparticle interferometer: Observation of fractional statistics," Phys. Rev. B **72**, 075342 (American Physical Society, 2005).

[160] F. E. Camino, W. Zhou, and V. J. Goldman, "Transport in the Laughlin quasiparticle interferometer: Evidence for topological protection in an anyonic qubit," Phys. Rev. B **74**, 115301 (American Physical Society, 2006).

[161] F. E. Camino, W. Zhou, and V. J. Goldman, "$e/3$ Laughlin Quasiparticle Primary-Filling $\ensuremath{\nu}=1/3$ Interferometer," Phys. Rev. Lett. **98**, 076805 (American Physical Society, 2007).

[162] W. Zhou, F. E. Camino, and V. J. Goldman, "Flux-period scaling in the Laughlin quasiparticle interferometer," Phys. Rev. B **73**, 245322 (American Physical Society, 2006).

[163] B. Rosenow and B. I. Halperin, "Influence of Interactions on Flux and Back-Gate Period of Quantum Hall Interferometers," Phys. Rev. Lett. **98**, 106801 (2007).

[164] J. Nakamura, S. Liang, G. C. Gardner, and M. J. Manfra, "Direct observation of anyonic braiding statistics," Nature Physics **16**, 931–936 (Nature Publishing Group, 2020).

[165] C. Nayak, S. H. Simon, A. Stern, M. Freedman, and S. Das Sarma, "Non-Abelian anyons and topological quantum computation," Rev. Mod. Phys. **80**, 1083–1159 (2008).

[166] D. C. Glattli and P. S. Roulleau, "Levitons for electron quantum optics," physica status solidi (b) **254**, 1600650 (2017).

[167] G. Roussely, E. Arrighi, G. Georgiou, S. Takada, M. Schalk, M. Urdampilleta, A. Ludwig, A. D. Wieck, P. Armagnat, et al., "Unveiling the bosonic nature of an ultrashort few-electron pulse," Nature Communications **9**, 2811 (2018).

[168] A. Bassi, K. Lochan, S. Satin, T. P. Singh, and H. Ulbricht, "Models of wave-function collapse, underlying theories, and experimental tests," Rev. Mod. Phys. **85**, 471–527 (2013).

[169] J. Voit, "One-dimensional Fermi liquids," Rep. Prog. Phys. **58**, 977–1116 (IOP Publishing, 1995).

[170] E. Bocquillon, "Electron quantum optics in quantum Hall edge channels," PhD thesis (Université Pierre et Marie Curie - Paris VI, 2012).

[171] M. Hashisaka, K. Washio, H. Kamata, K. Muraki, and T. Fujisawa, "Distributed electrochemical capacitance evidenced in high-frequency admittance measurements on a quantum Hall device," Phys. Rev. B **85**, 155424 (American Physical Society, 2012).

[172] M. Hashisaka and T. Fujisawa, "Tomonaga–Luttinger-liquid nature of edge excitations in integer quantum Hall edge channels," Reviews in Physics **3**, 32–43 (2018).

[173] V. Freulon, A. Marguerite, J.-M. Berroir, B. Plaçais, A. Cavanna, Y. Jin, and G. Fève, "Hong-Ou-Mandel experiment for temporal investigation of single-electron fractionalization," Nature Communications **6**, 6854 (Nature Publishing Group, 2015).

[174] A. Marguerite, C. Cabart, C. Wahl, B. Roussel, V. Freulon, D. Ferraro, C. Grenier, J.-M. Berroir, B. Plaçais, et al., "Decoherence and relaxation of a single electron in a one-dimensional conductor," Phys. Rev. B **94**, 115311 (American Physical Society, 2016).

[175] A. Marguerite, E. Bocquillon, J.-M. Berroir, B. Plaçais, A. Cavanna, Y. Jin, P. Degiovanni, and G. Fève, "Two-particle interferometry in quantum Hall edge channels (Phys. Status Solidi B 3/2017)," physica status solidi (b) **254**, 1770215 (2017).

[176] I. Neder, M. Heiblum, D. Mahalu, and V. Umansky, "Entanglement, Dephasing, and Phase Recovery via Cross-Correlation Measurements of Electrons," Phys. Rev. Lett. **98**, 036803 (2007).

[177] P. Roulleau, F. Portier, P. Roche, A. Cavanna, G. Faini, U. Gennser, and D. Mailly, "Noise Dephasing in Edge States of the Integer Quantum Hall Regime," Phys. Rev. Lett. **101**, 186803 (2008).

[178] D. L. Kovrizhin and J. T. Chalker, "Exactly solved model for an electronic Mach-Zehnder interferometer," Phys. Rev. B **80**, 161306 (2009).

[179] D. L. Kovrizhin and J. T. Chalker, "Multiparticle interference in electronic Mach-Zehnder interferometers," Phys. Rev. B **81**, 155318 (2010).

[180] S. Ngo Dinh, D. A. Bagrets, and A. D. Mirlin, "Analytically solvable model of an electronic Mach-Zehnder interferometer," Phys. Rev. B **87**, 195433 (American Physical Society, 2013).

[181] M. Schneider, D. A. Bagrets, and A. D. Mirlin, "Theory of the nonequilibrium electronic Mach-Zehnder interferometer," Phys. Rev. B **84**, 075401 (2011).

[182] J. T. Chalker, Y. Gefen, and M. Y. Veillette, "Decoherence and interactions in an electronic Mach-Zehnder interferometer," Phys. Rev. B **76**, 085320 (2007).

[183] E. V. Sukhorukov and V. V. Cheianov, "Resonant Dephasing in the Electronic Mach-Zehnder Interferometer," Phys. Rev. Lett. **99**, 156801 (2007).

[184] I. Esin, A. Romito, and Y. Gefen, "Detection of quantum interference without interference," 20 November 2019, <http://arxiv.org/abs/1910.13705> (29 May 2020).

[185] T. Machida, H. Hirai, S. Komiyama, and Y. Shiraki, "Phase coherence of edge states over macroscopic length scales," Physica B: Condensed Matter **249-251**, 128–131 (1998).

[186] F. Marquardt and C. Bruder, "Effects of dephasing on shot noise in an electronic Mach-Zehnder interferometer," Phys. Rev. B **70**, 125305 (2004).

[187] F. Marquardt, "Fermionic Mach-Zehnder interferometer subject to a quantum bath," EPL **72**, 788 (IOP Publishing, 2005).

[188] F. Marquardt, "Equations of motion approach to decoherence and current noise in ballistic interferometers coupled to a quantum bath," Phys. Rev. B **74**, 125319 (American Physical Society, 2006).

[189] B. J. van Wees, E. M. M. Willems, C. J. P. M. Harmans, C. W. J. Beenakker, H. van Houten, J. G. Williamson, C. T. Foxon, and J. J. Harris, "Anomalous integer quantum Hall effect in the ballistic regime with quantum point contacts," Phys. Rev. Lett. **62**, 1181–1184 (American Physical Society, 1989).

[190] G. Müller, D. Weiss, A. V. Khaetskii, K. von Klitzing, S. Koch, H. Nickel, W. Schlapp, and R. Lösch, "Equilibration length of electrons in spin-polarized edge channels," Phys. Rev. B **45**, 3932–3935 (American Physical Society, 1992).

[191] P. Brasseur, "Mach Zehnder interferometry and coherent manipulation of the valley in a graphene PN junction," PhD thesis (Paris-Saclay, 2020).

[192] Y. M. Blanter and M. Büttiker, "Shot noise in mesoscopic conductors," Physics Reports **336**, 1–166 (2000).

[193] D. S. Wei, T. van der Sar, J. D. Sanchez-Yamagishi, K. Watanabe, T. Taniguchi, P. Jarillo-Herrero, B. I. Halperin, and A. Yacoby, "Mach-Zehnder interferometry using spin- and valley-polarized quantum Hall edge states in graphene," Science Advances **3**, e1700600 (2017).

[194] A. E. Hansen, A. Kristensen, S. Pedersen, C. B. Sørensen, and P. E. Lindelof, "Mesoscopic decoherence in Aharonov-Bohm rings," Phys. Rev. B **64**, 045327 (American Physical Society, 2001).

[195] T. Capron, C. Texier, G. Montambaux, D. Mailly, A. D. Wieck, and L. Saminadayar, "Ergodic versus diffusive decoherence in mesoscopic devices," Phys. Rev. B **87**, 041307 (American Physical Society, 2013).

[196] W. Li, C. L. Vicente, J. S. Xia, W. Pan, D. C. Tsui, L. N. Pfeiffer, and K. W.

West, “Scaling in Plateau-to-Plateau Transition: A Direct Connection of Quantum Hall Systems with the Anderson Localization Model,” Phys. Rev. Lett. **102**, 216801 (American Physical Society, 2009).

[197] E. Arrighi, “Time-resolved measurements of collective effects in quantum conductors,” PhD thesis (Université Grenoble Alpes [2020-....], 2020).

[198] E. Weisz, H. K. Choi, M. Heiblum, Y. Gefen, V. Umansky, and D. Mahalu, “Controlled Dephasing of an Electron Interferometer with a Path Detector at Equilibrium,” Phys. Rev. Lett. **109**, 250401 (American Physical Society, 2012).

[199] I. Neder, F. Marquardt, M. Heiblum, D. Mahalu, and V. Umansky, “Controlled dephasing of electrons by non-gaussian shot noise,” Nature Physics **3**, 534 (2007).

[200] P. Roulleau, F. Portier, P. Roche, A. Cavanna, G. Faini, U. Gennser, and D. Mailly, “Tuning Decoherence with a Voltage Probe,” Phys. Rev. Lett. **102**, 236802 (2009).

[201] A. O. Gogolin, A. A. Nersesyan, and A. M. Tsvelik, Bosonization and Strongly Correlated Systems (1999).

[202] J. von Delft and H. Schoeller, “Bosonization for beginners — refermionization for experts,” Annalen der Physik **7**, 225–305 (1998).

[203] S. Eggert, “One-dimensional quantum wires: A pedestrian approach to bosonization,” 1 August 2007, <http://arxiv.org/abs/0708.0003> (25 February 2019).

[204] I. Levkivskyi, “Mesoscopic Quantum Hall Effect” (Springer Berlin Heidelberg, 2012).

[205] M. Filippone, A. Marguerite, K. L. Hur, G. Fève, and C. Mora, “Phase-Coherent Dynamics of Quantum Devices With Local Interactions,” Entropy **22**, 847 (2020).

[206] E. Weisz, H. K. Choi, I. Sivan, M. Heiblum, Y. Gefen, D. Mahalu, and V. Umansky, “An electronic quantum eraser,” Science **344**, 1363–1366 (American Association for the Advancement of Science, 2014).

[207] A. M. Whiticar, A. Fornieri, E. C. T. O’Farrell, A. C. C. Drachmann, T. Wang, C. Thomas, S. Gronin, R. Kallaher, G. C. Gardner, et al., “Interferometry and coherent single-electron transport through hybrid superconductor-semiconductor Coulomb islands,” 19 February 2019, <http://arxiv.org/abs/1902.07085> (20 February 2019).

[208] É. Sivré, “Electrical fluctuations and heat flow in a quantum composite circuit,” PhD thesis (Université Paris Saclay (COmUE), 2019).

[209] M. Yamamoto, S. Takada, C. Bäuerle, K. Watanabe, A. D. Wieck, and S. Tarucha, “Electrical control of a solid-state flying qubit,” Nature Nanotechnology **7**, 247–251 (2012).

[210] A. B. Gougam, F. Pierre, H. Pothier, D. Esteve, and N. O. Birge, "Comparison of energy and phase relaxation in metallic wires," Journal of Low Temperature Physics **118**, 447–456 (2000).

[211] S. Jezouin, Z. Iftikhar, A. Anthore, F. D. Parmentier, U. Gennser, A. Cavanna, A. Ouerghi, I. P. Levkivskyi, E. Idrisov, et al., "Controlling charge quantization with quantum fluctuations," Nature **536**, 58–62 (2016).

[212] A. A. Clerk, X. Waintal, and P. W. Brouwer, "Fano Resonances as a Probe of Phase Coherence in Quantum Dots," Phys. Rev. Lett. **86**, 4636–4639 (American Physical Society, 2001).

[213] C. W. J. Beenakker, "Random-matrix theory of quantum transport," Rev. Mod. Phys. **69**, 731–808 (1997).

[214] U. Klaß, W. Dietsche, K. von Klitzing, and K. Ploog, "Imaging of the dissipation in quantum-Hall-effect experiments," Z. Physik B - Condensed Matter **82**, 351–354 (1991).

[215] M. Persson and J. Pettersson, "Submicron air-bridge interconnection process for complex gate geometries," Journal of Vacuum Science & Technology B: Microelectronics and Nanometer Structures Processing, Measurement, and Phenomena **15**, 1724–1727 (American Institute of Physics, 1997).

[216] T. Borzenko, F. Lehmann, G. Schmidt, and L. W. Molenkamp, "Metallic air-bridges on non-planar transport structures," Microelectronic Engineering **67-68**, 720–727 (2003).

[217] A. J. Keller, "Emergent Symmetries in Quantum Impurity Experiments," Doctoral Thesis (Stanford University, 2015).

[218] R. V. Gorbachev, A. S. Mayorov, A. K. Savchenko, D. W. Horsell, and F. Guinea, "Conductance of p-n-p Graphene Structures with 'Air-Bridge' Top Gates," Nano Lett. **8**, 1995–1999 (American Chemical Society, 2008).

[219] A. Helzel, "Dephasing and quantum noise in an electronic Mach-Zehnder interferometer," PhD thesis (2013).

[220] T. Borzenko, C. Gould, G. Schmidt, and L. W. Molenkamp, "Metallic air-bridges fabricated by multiple acceleration voltage electron beam lithography," Microelectronic Engineering **75**, 210–215 (2004).

[221] E. Girgis, J. Liu, and M. L. Benkhedar, "Fabrication of metallic air bridges using multiple-dose electron beam lithography," Appl. Phys. Lett. **88**, 202103 (American Institute of Physics, 2006).

A

Supplementary information for the macroscopic coherence length

A.1 Plateau $\nu = 2$

The B-field extent of the $\nu = 2$ plateau is displayed in figure A.1, using two different ohmic contacts located on the same side (dark blue) and on the opposite side of a top gate (green). The green data illustrates how a top gate, even grounded can slightly affect the plateau's extent. For the study described in chapter 3, the data was acquired at a magnetic field of $B = 4.3\,\mathrm{T}$, rather in the middle of the plateau.

A.2 Central ohmic contact characterization

The transmission probability of the inner channel towards the central grounded ohmic contact $\tau_{\Omega\text{-out}}$ can be obained by tuning the devices in the configuration depicted in figure A.2 a and then using:

$$1 - \tau_{\Omega\text{-out}} = \frac{I_{\mathrm{meas}}^{\mathrm{D1}\leftarrow\mathrm{S0}}}{I_{\mathrm{inj}}^{\mathrm{S0}\rightarrow}/2} - 1$$

The transmission probability $\tau_{\Omega\text{-out}} \approx (99.4(100) \pm 0.05)\%$ is (near) perfect, which shows that the central ohmic contact acts as a very good charge sink.

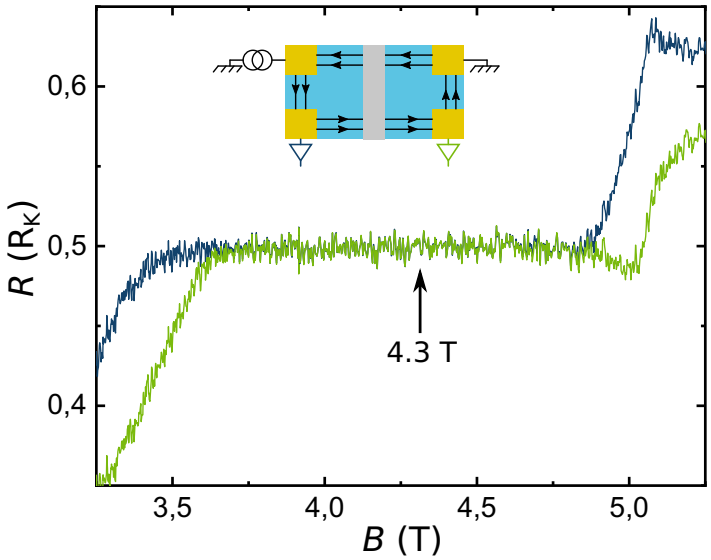

Figure A.1: Magnetic field extent of the plateau $\nu = 2$ for the 2DEG used in this experiment. Data were measured in a Van der Pauw geometry as illustrated in the inset schematic, on a device different from the MZI, with a geometry very similar to the depicted schematic and with a grounded top gate (light grey).

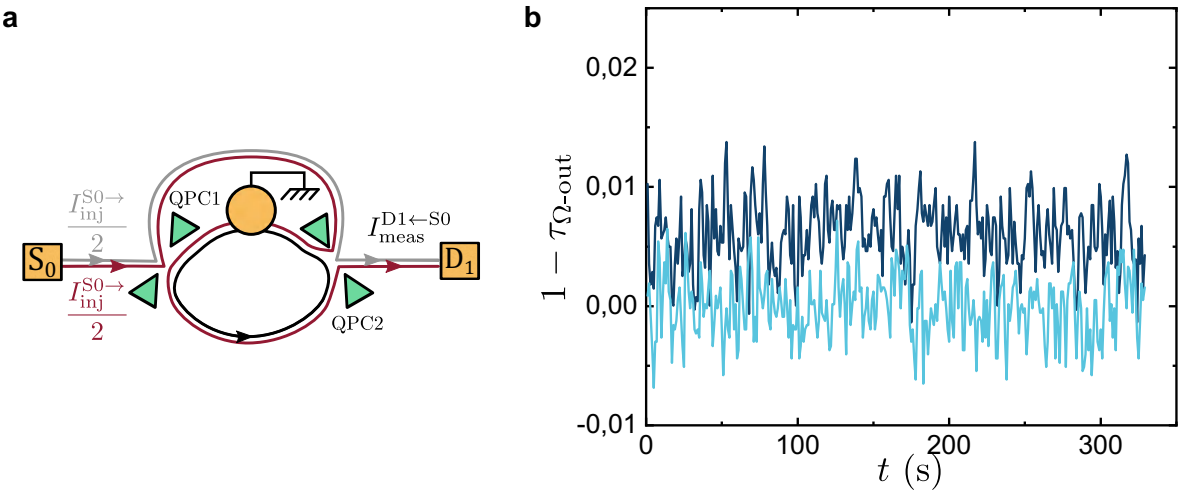

Figure A.2: Characterization of transmission probability for the outer channel at the central, grounded ohmic contact, obtained from the current originating from S0 and measured at D1, for the $L = 24\,\mu m$ (dark blue) and the $L = 100\,\mu m$ (light blue) devices. **a** Schematic of the device configuration for the determination of $\tau_{\Omega\text{-out}}$. The channel in red highlights the trajectory of interest. **b** The data shows that ≈ 0.006 of the outer channel is reflected at the metal/2DEG interface in the $L = 24\,\mu m$ long device, while nothing is reflected in the $L = 100\,\mu m$ long device to our experimental accuracy (relative error of 5×10^{-4} when averaging).

Although it is not at all crucial to this experiment, it is also possible to obtain $\tau_{\Omega\text{-in}}$ by configuring the devices as depicted in figure A.3 a with:

$$1 - \tau_{\Omega\text{-in}} = \frac{I_{\text{meas}}^{\text{D1}\leftarrow\text{S0}}}{I_{\text{inj}}^{\text{S0}\rightarrow}/2} - 1$$

yielding the data of figure A.3 b. The inner channel is therefore perfectly transmitted in the $L = 100\,\mu\text{m}$ device while $\tau_{\Omega\text{-in}} \approx 0.68 \pm 0.1$ in the $L = 24\,\mu\text{m}$ device, illustrating how small ohmic contacts can be hard to contact well electrically with QH channels.

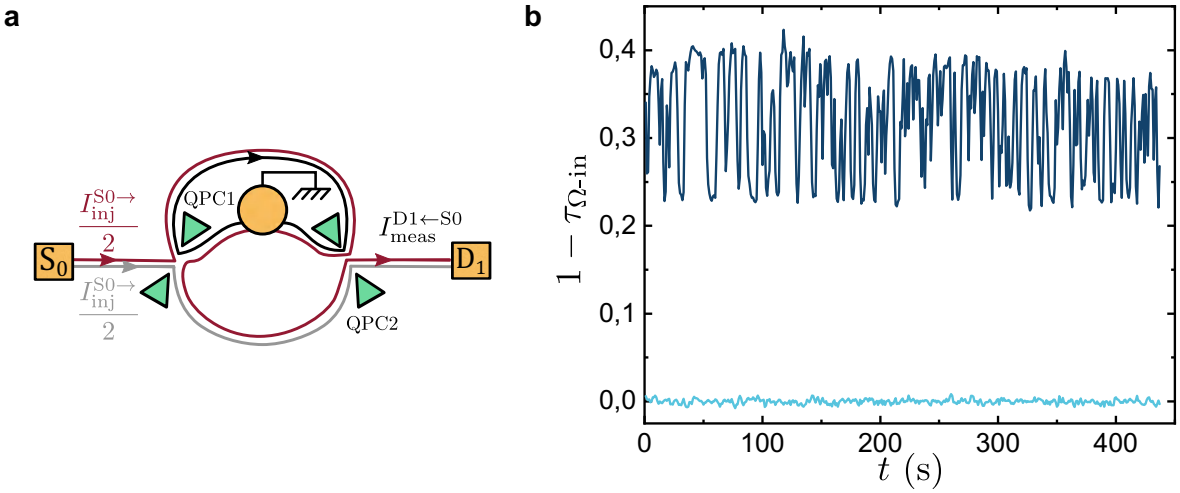

Figure A.3: Characterization of transmission probability for the inner channel at the central, grounded ohmic contact, obtained from the current originating from S0 and measured at D1, for the $L = 24\,\mu\text{m}$ (dark blue) and the $L = 100\,\mu\text{m}$ (light blue) devices. **a** Schematic of the device configuration for the determination of $\tau_{\Omega\text{-in}}$. The channel in red highlights the trajectory of interest. **b** The data shows that $\tau_{\Omega\text{-in}} \approx 0.32 \pm 0.1$ of the outer channel is reflected at the metal/2DEG interface in the $L = 24\,\mu\text{m}$ long device, while nothing is reflected in the $L = 100\,\mu\text{m}$ long device to our experimental accuracy (relative error of 5×10^{-4} when averaging).

A.3 Inter-Channel Tunneling

The interchannel tunneling can be observed by injecting a current in one channel, and none in the co-propagating one. After both channels are left to co-propagate for some length, they are separated again and either the remaining current in the original channel or the current in the co-propagating channel is measured. This kind of measurement was performed as illustrated in the top panels of figure A.4 a,b,c. In figure A.4 a&b, it is the tunneling along the upper path of the MZI that is measured, using both possible techniques. In the scheme of figure A.4 a, current is injected in the outer channel, which then co-propagates with the inner channel from QPC0 onwards, until they reach QPC2. At that point, the outer channel is directed towards the central grounded ohmic contact while the inner channel is directed towards the drain D, where the amount of

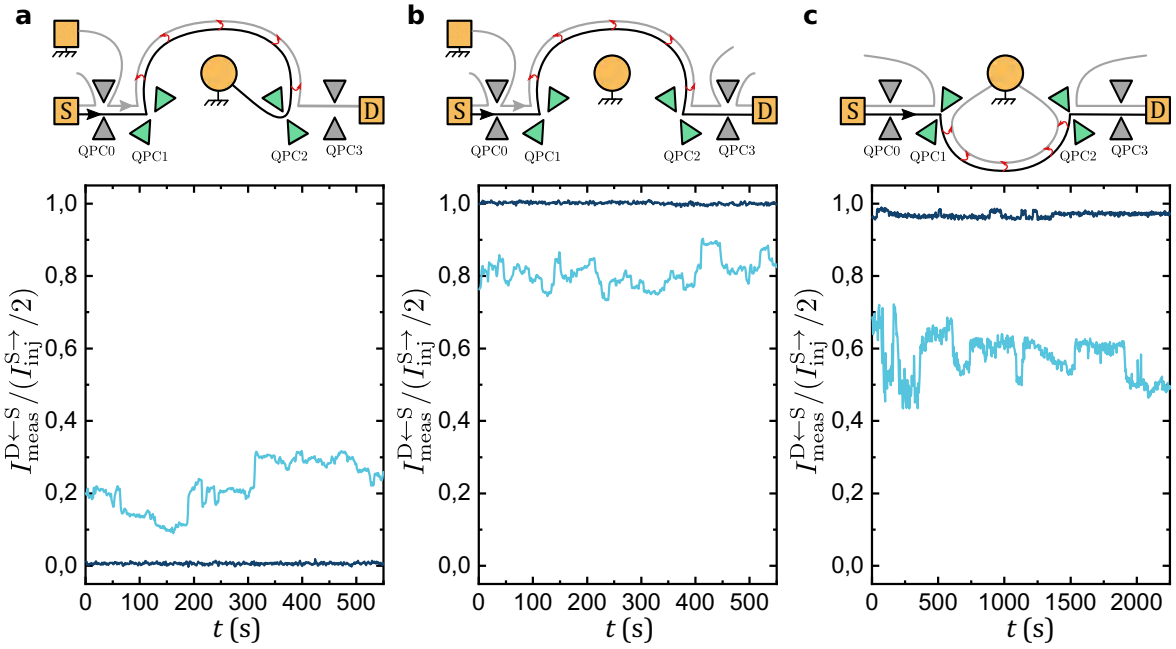

Figure A.4: **Upper panel:** Schematics of the device configuration for the measurements displayed in the lower panel. The outer (inner) channel is colored in black (grey). **Lower panel:** Measurements of inter-channel co-tunneling along the **a, b** upper (**c** lower) path of the MZIs. The curves are the normalised currents between source (S) and drain (D) measured as a function of time, for both the 24 μm (dark blue) and 100 μm (light blue) devices. Two methods are possible for the upper path: **a** the direct measurement of the amount of current that tunneled towards the inner channel and **b** the measurement of the amount of current that remained in the outer channel. Both methods are consistent and indicate a tunneling of $\lesssim 1\%(30\%)$ for the 24 μm (100 μm) device. **c** Along the lower path, it is only possible to proceed in one way: measuring the remaining signal in the outer channel. Tunneling on this path is slightly more important: $\lesssim 3.5\%(50\%)$

current coming from S (identified via homodyne detection), is measured. The tunneling probability along the co-propagating length $L \approx 24(100)\,\mu\text{m}$ is then given by

$$\tau_{\text{tunnel}} = \frac{I_{\text{meas}}^{\text{D}\leftarrow\text{S}}}{I_{\text{inj}}^{\text{S}\rightarrow}/2}$$

In the scheme of figure A.4 b, current is injected in the outer channel, which then co-propagates with the inner channel from QPC0 onwards, until they reach QPC3. At that point, only the outer channel is directed towards D while the inner one is re-directed towards a ground. The tunneling probability along the co-propagating length $L \approx 24(100)\,\mu\text{m}$ is then given by

$$\tau_{\text{tunnel}} = 1 - \frac{I_{\text{meas}}^{\text{D}\leftarrow\text{S}}}{I_{\text{inj}}^{\text{S}\rightarrow}/2} \tag{A.1}$$

Both measurements of figure A.4 a&b are consistent with a $\tau_{\text{tunnel}} \lesssim 1(30)\%$for a propagating length of $L = 24(100)\,\mu\text{m}$.

In figure A.4 c, the tunneling along the lower path is characterized and τ_{tunnel} is again given by equation A.1. In this case, $\tau_{\text{tunnel}} \lesssim 3.5(50)\%$ for a propagating length of $L = 24(100)\,\mu\text{m}$. Note that τ_{tunnel} cannot be superior to 50% as in this case, it means that both channels are at equilibrium and any tunneling from one channel to the other would be compensated by processes that go the other way around. Surprisingly, the tunneling along the lower path is substantially larger than that along the upper path. This kind of values for τ_{tunnel} is consistent with what has been measured in the past on comparable lengths [189,190].

In figure 3.5 e, the irregular τ_{MZI} signal in light red that is centered around ≈ 0.4 can be explained by such tunneling. The light red curve of figure 3.5 e was obtained by leaving both co-propagating channel in the upper path to impinge on the detector D, such that it is not affected by tunneling along the upper path. On the contrary, along the lower path, the electrons tunneling from the outer to the inner channel will end in the central grounded contact. The $\tau_{\text{MZI}} \approx 0.4$ (of the light red curve of figure 3.5 e) therefore suggests a $\tau_{\text{tunnel}} \approx 0.4$ along the lower path, a value compatible with the $\tau_{\text{tunnel}} \in [0.3, 0.5]$ obtained from the data displayed in figure A.4 c.

A.4 Current noise power spectral density in a coherent MZI with phase noise

The current noise measured is the symmetrised power spectral density $S(\omega) + S(-\omega)$ that respectively correspond to absorption and emission of current noise as it is not possible to distinguish one from the other at low frequency (as in our setup with

$\omega \approx 1\,\mathrm{MHz}$). The power spectral density $S(\omega)$ is itself obtained through the Wiener-Kintchine theorem as the fourier transform of the current correlation function $\mathcal{C}(\tau)$ defined in general as

$$\begin{aligned}\mathcal{C}(\tau) &= \langle \Delta I(t) \Delta I(t+\tau) \rangle \\ &= \langle I(t) I(t+\tau) \rangle - \bar{I}^2\end{aligned}$$

In particular, the current going through a coherent MZI with phase noise is given by

$$I_{\mathrm{MZI}}(t) = \bar{I}[1 + \mathcal{V}\cos(\phi + \delta\varphi(t))]$$

and the auto-correlation function at the detector is

$$\begin{aligned}\mathcal{C}_{\mathrm{MZI}}(\tau) &= \langle I_{\mathrm{MZI}}(t) I_{\mathrm{MZI}}(t+\tau) \rangle - \bar{I}^2 \\ &= \bar{I}^2 \left\langle [1 + \mathcal{V}\cos(\phi + \delta\varphi(t)][1 + \mathcal{V}\cos(\phi + \delta\varphi(t+\tau))] \right\rangle\end{aligned} \tag{A.2}$$

We take an expansion of the cos terms around $\delta\varphi = 0$:

$$\cos(\phi + \delta\varphi) \approx \cos\phi - \delta\varphi \sin\phi - \frac{\delta\varphi^2}{2}\cos\phi$$

Plugging this in equation A.2 will yield terms that can be collected in the powers of $\delta\varphi$. By construction, $\langle \delta\varphi \rangle = 0$, we then obtain:

$$\begin{aligned}\mathcal{C}_{\mathrm{MZI}}(\tau) \approx & \bar{I}^2 \Big\{ (1 + \mathcal{V}\cos\phi)^2 + \mathcal{V}^2 \langle \delta\varphi(t)\delta\varphi(t+\tau) \rangle \sin^2\phi \\ & + \mathcal{V}^2 \left[\mathcal{O}\left(\langle \delta\varphi(t)\delta\varphi^2(t+\tau) \rangle \right) + \mathcal{O}\left(\langle \delta\varphi^2(t)\delta\varphi(t+\tau) \rangle \right) \right] \Big\} - \bar{I}^2 \\ \approx & \bar{I}^2 \left\{ (1 + \mathcal{V}\cos\phi)^2 + \mathcal{V}^2 \langle \delta\varphi^2 \rangle \sin^2\phi + \mathcal{V}^2 \mathcal{O}\left(\langle \delta\varphi^3 \rangle \right) \right\} - \bar{I}^2\end{aligned}$$

where it was assumed in the last step that $\delta\varphi$ does not vary much over time. The power spectral density is then the Fourier transform of this result:

$$\begin{aligned}S(\omega) &= \int_{-\infty}^{\infty} \mathcal{C}_{\mathrm{MZI}}(\tau) e^{-i\omega\tau} d\tau \\ &\approx \bar{I}^2 \mathcal{V}^2 \left\{ \langle \delta\varphi^2(\omega) \rangle \sin^2\phi + \mathcal{O}\left(\langle \delta\varphi^3(\omega) \rangle \right) \right\}\end{aligned} \tag{A.3}$$

Taking the average in ϕ, over several Aharonov-Bohm periods, we obtain:

$$\langle S(\omega) \rangle_\phi \approx \bar{I}^2 \mathcal{V}^2 \left\{ \frac{\langle \delta\varphi^2(\omega) \rangle}{2} + \mathcal{O}\left(\langle \delta\varphi^3(\omega) \rangle \right) \right\}$$

A.5 Link between direct and differential visibility

Starting with the direct current through a MZI defined as:

$$I_{\mathrm{MZI}} = \bar{I}(1 + \mathcal{V}\cos\phi)$$

the differential conductance, that is the usual measured quantity in MZIs will consequently be given by:

$$\frac{dI_{\mathrm{MZI}}}{dV_{\mathrm{dc}}} = \frac{d\bar{I}}{dV_{\mathrm{dc}}}(1 + \mathcal{V}\cos\phi) + \bar{I}\frac{d}{dV_{\mathrm{dc}}}(1 + \mathcal{V}\cos\phi)$$

In general, we consider a dc visibility $\mathcal{V}$ that depends on the voltage bias V_{dc} (but the dependence $\phi(V_{\mathrm{dc}})$ is ignored as the upper and lower paths are symmetric), so that

$$\frac{dI_{\mathrm{MZI}}}{dV_{\mathrm{dc}}} = \frac{d\bar{I}}{dV_{\mathrm{dc}}} + \left(\mathcal{V}\frac{d\bar{I}}{dV_{\mathrm{dc}}} + \bar{I}\frac{d\mathcal{V}}{dV_{\mathrm{dc}}}\right)\cos\phi$$

Since here $\bar{I} = V_{\mathrm{dc}}(d\bar{I}/dV_{\mathrm{dc}})$ (assuming the beam-splitters' transmissions do not depend on V_{dc}), then:

$$\frac{dI_{\mathrm{MZI}}}{dV_{\mathrm{dc}}} = \frac{d\bar{I}}{dV_{\mathrm{dc}}}\left[1 + \left(\mathcal{V} + V_{\mathrm{dc}}\frac{d\mathcal{V}}{dV_{\mathrm{dc}}}\right)\cos\phi\right]$$

from which we identify the term multiplying the oscillating part of the differential conductance to be the differential visibility:

$$\mathcal{V}_{\mathrm{diff}} = \left|\mathcal{V} + V_{\mathrm{dc}}\frac{d\mathcal{V}}{dV_{\mathrm{dc}}}\right| \tag{A.4}$$

where the absolute value comes from the fact that the visibility is by definition positive. Interestingly, it is straightforward to see from equation A.4 that a monotonously decreasing $\mathcal{V}(V_{\mathrm{dc}})$ will always yield one side lobe in the differential visibility $\mathcal{V}_{\mathrm{diff}}$. Multiple side lobes (more than one) in the differential visibility are due to inter-channel interactions and will be linked to at least one side lobe in the dc visibility $\mathcal{V}$.

A.6 Overview of Coherence Lengths Measurements

Table A.1: List of representative coherence lengths measured with different techniques in various materials, that are displayed on the graphs of figure 3.11. 'Int.' stands for Interferometry, 'WL' for Weak Localization, 'AL' for Anderson Localization and 'UCF' for Universal Conductance Fluctuations.

Technique	Material	Geometry	Article	L_ϕ (µm)	T (mK)	L (µm)
Int.	AlGaAs	MZI	us [42]	250	10	24
Int.	AlGaAs	MZI	us [42]	250	10	100
Int.	AlGaAs	MZI	Roulleau2008 [21]	26	20	5.6
Int.	AlGaAs	MZI	Ji 2003 [20]	52	20	12
Int.	AlGaAs	MZI	Huynh 2012 [41]	27	20	10
Int.	AlGaAs	MZI	Neder 2007 [32]	86	20	8
Int.	Graphene	MZI	Wei 2017 [193]	119	20	1.2
Int.	AlGaAs	AB ring	Yamamoto 2012 [209]	86	70	6.5
WL & Int.	Sb	AB ring	Miliken 1987 [71]	2	20	1.64
WL & Int.	Al	AB ring	Chandrasekhar 1985 [64]	2.00	1700	3.6
WL & Int.	Ag	AB ring	Chandrasekhar 1985 [64]	0.9	1700	1.57
WL	AlGaAs	Wire	Niimi 2010 [85]	20	30	150
WL	doped Si	Wire	Ghosh 2000 [93]	0.07	2000	225
WL	Ag	Wire	Gougam 2000 [210]	11	40	136
WL	Cu	Wire	Gougam 2000 [210]	3.7	30	271
WL & UCF	Graphene	Monolayer	Morozov 2006 [97]	1	4000	6
WL & UCF	Bi2Te2Se	Micro-flake	Li 2012 [100]	0.12	2000	3
WL & UCF	Bi2Te2S	Micro-flake	Trivedi 2016 [114]	0.2	2000	8
AL	AlGaAs	Wire	Li 2009 [196]	2000	10	2000

B

Complementary measurements for the island embedded in the MZI

B.1 Further measurements of the ohmic contacts interfaces

B.1.1 Dependence on the nearby gates voltages

figure B.1 presents the transmission coefficient of both channels characterized in different gate configurations schematized in the corresponding upper pannel. From figure B.1 a, it is possible to see that the outer channel is rather well coupled to the central ohmic contact ($\tau_{\Omega-\text{out}} \approx 0.96$) while the inner channel is almost entirely reflected ($\tau_{\Omega-\text{in}} \approx 0.01$). The light blue curve of figure B.1 a was acquired in the configuration illustrated in the corresponding schematic and simultaneously to the dark red curve. The dark blue curve was acquired with the device tuned slightly differently: QPC1 was set to transmit only one channel (instead of two), the corresponding lower transmission coefficient measured however suggests that it is dependent on the voltage of the nearby gates, in a small but measurable way.
For the data of figure B.1 b, QPC0 & QPC1 only let the outer channel through and QPC2 is fully closed so that any signal measured on contact D_0 can be attributed to a reflection on the central contact. In this case, both blue traces were taken in the same

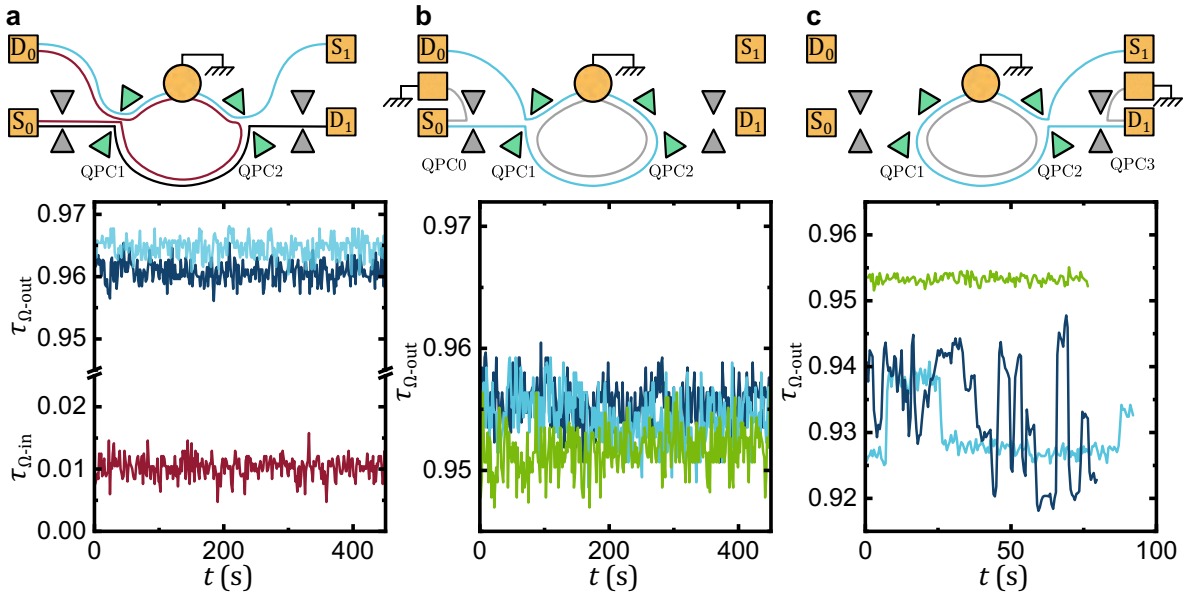

Figure B.1: Measurements over time of the transmission coefficients at the metal/2DEG interface of the grounded central ohmic contact, for both the outer channel ($\tau_{\Omega-\text{out}}$) and the inner one ($\tau_{\Omega-\text{in}}$) in different gates configurations. **a** The measurements take place between contacts S_1 and D_0 for the outer channel (in light blue on the schematic) and S_0 and D_0 for the inner one (dark red). **b** Measurement of $\tau_{\Omega-\text{out}}$.

configuration some time apart, attesting the reproducibility. The value measured is however slightly below that of configuration a) of figure B.1 confirming that the voltage applied to the top gates located near the ohmic contact can affect its interface transparency. That is even more confirmed by the green trace in figure B.1 b was taken with the right comb-shaped gate tuned to let only a single channel through.
A final test is the symmetric version of the last one, presented in figure B.1 c. Once again, both blue traces were taken at different times and both boast telegraphic noise, pointing towards a few impurities that are periodically excited and enhance or reduce the transmission towards the central contact. These telegraphic features are suppressed when the comb-shaped gate is set to transmit a single channel (green curve), further attesting the importance of the gate configuration on the metal/2DEG interface transparency. Interestingly, these kind of two-level system excitations give an order of magnitude for the potential problems arising in the device: these amount to only ~2% of the transmission of one channel.

Similarly, it is possible to characterize the metal/2DEG interface of the floating metallic island, those are displayed in figure B.2. In this case, even though there are two interfaces between the metal and the electron gas, one on each side of the island ($\tau_{\Omega-1}$ for the transmission of the outer channel towards the metallic island on the MZI side, and $\tau_{\Omega-2}$ for the side opposite to the MZI), it is not possible to characterize them independently as they are in series with each other. In the data displayed in figure B.2, it is assumed that the transmission towards the side of the island that is opposite to the interferometer is perfect: $\tau_{\Omega-2} = 1$. This assumption is supported by data of figure B.4

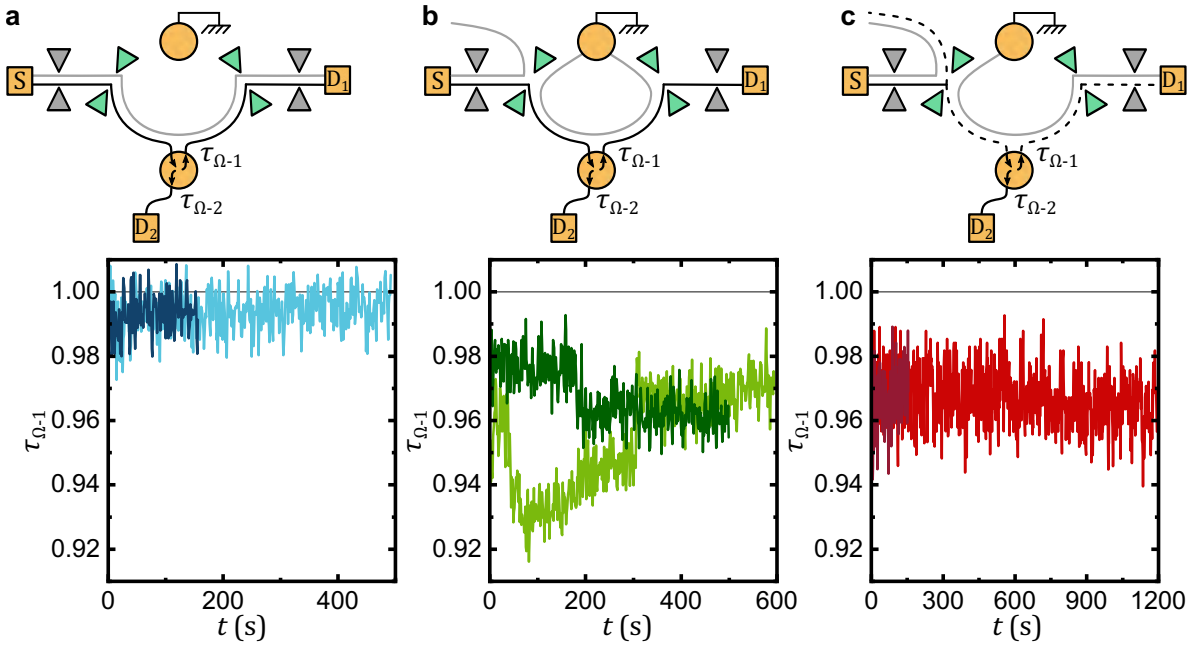

Figure B.2: Measurement of the floating island's interface transmission probability $\tau_{\Omega-1}$ over time (assuming $\tau_{\Omega-2} = 1$) and in different top gates configurations as illustrated by the schematics in the upper part. Displayed transmission probabilities result from the current measured at contact D_2 (a consistency check, not shown, is performed by measuring the current at contact D_1). **a** QPC 1 and 2 are set to transmit two channels and the transmission towards the ohmic contact is close to 1. **b** QPC 1 and 2 are set to transmit a single channel **c** QPC1 is set to transmit half a channel and QPC2, two channels. For the light red signal, the upper 'Loop' gate was also varied linearly over the 1200 s between -0.45 V and -0.47 V (to check for an eventual artifact from the upper path: none can be detected).

(see also the associated discussion). Once again, it is possible to see that the transmission probability towards the metal depends in a small but significant way on the voltages applied to the nearby gates (see figure B.2 a-c). In an attempt to characterize it in a configuration as close to the one used in the interferometry, both MZI QPCs are tuned to half transmission as illustrated in the schematic of figure B.2 c and the upper path is closed, using the comb-shaped gate, to ensure no interferences can occur. The resulting measured transmission probability is $\tau_{\Omega-1} \approx 97\%$.

B.1.2 Sweeping the switch gates voltages

First, let us recall how current redistribution should occur at the floating island. The current redistribution occuring at any contact can be derived simply from current conservation (Kirchoff's nodes law). In the general case of a contact connected to N leads, each hosting M channels, the current from lead α to lead β reads:

$$I^{D\beta\leftarrow S\alpha} = I_{\text{inj}}^{S\alpha\rightarrow} \frac{\sum_i^M \tau_{\alpha,i}}{M} \frac{\sum_i^M \tau_{\beta,i}}{\sum_\gamma^N \sum_i^M \tau_{\gamma,i}}$$

where $\tau_{\alpha,i}$ is the probability for the current coming from channel i in lead α to enter inside the contact, which is assumed to be symmetric (note that an asymmetric transmission probability is not standard), implying that it is also the probability for the current coming from the contact to be transmitted to channel i in lead α.

Switch gate on the MZI side (sw1)

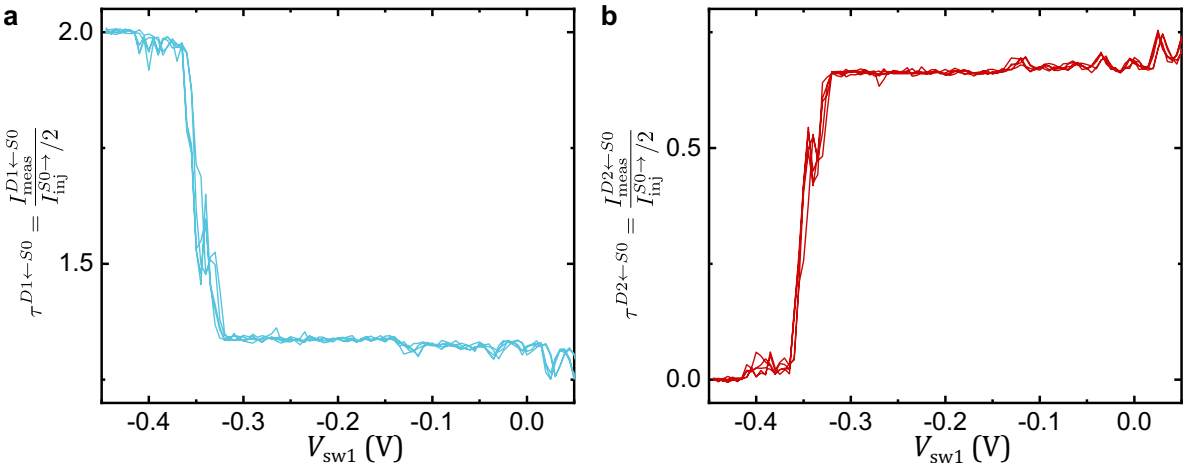

Figure B.3: **a** Normalized current measured at D_1 while sweeping V_{sw1} such that the outer switch goes from fully closed ($-0.45\,V$) to fully open ($0\,V$) while the inner switch is fully open ($V_{sw2} = 0\,V$. **b** normalized current measured at D_2, data taken simultaneously with data in **a**. Both of the MZI QPCs are set to full transmission for these measurements.

figure B.3 shows the normalized current measured at drain D_2 while sweeping the inner switch gate voltage V_{sw1} while the outer switch voltage is kept at $V_{sw2} = 0$. The

step-like behaviour is expected and characteristic of the quantum Hall edge channels. The observed plateau at $\tau_{D1\leftarrow S0} \approx 2$ occurs at the most negative voltages when both quantum Hall channels are reflected at the level of inner switch gate. The blue plateau at $\tau_{D1\leftarrow S0} \approx 1.33$ is expected from the addition of the current of a fully reflected inner channel and that of a very well transmitted outer channel into the island, that redistributed equally between all three channels connected to the island. Two are on the opposite side to the MZI and end on detector D_2, hence the red plateau at $\tau_{D2\leftarrow S0} \approx 0.66$ and the other one is the outer channel on the MZI side of the island end up on detector D_1 accounting for the remaining third. This indicates a very good coupling of the island with all these three channels. At $V_{\mathrm{sw1}} \approx -0.15V$, the plateau $\tau_{D1\leftarrow S0} \approx 1.33$ drops slightly, then slowly downwards with more and more positive voltage, indicating that the inner channel starts to be transmitted, however it never reaches a plateau. A perfect transmission of the inner channel should result in an equal redistribution of the total current between all four channels connected, which would translate to $\tau_{D1\leftarrow S0} = \tau_{D2\leftarrow S0} = 1$. The observed value indicates that the inner channel is only very poorly coupled to the island (but it is slightly, otherwise there would be no dip (bump) in the blue (red) curve of figure B.3), maybe due to a malfuctionning switch gate (although quite improbable, c.f. end of this section) or more probably, that the inner channel is badly coupled to it. Note that this is not an unusual situation: from experience, in a GaAs 2DEG driven in the quantum Hall regime, when the metal/2DEG interface of an ohmic contact isn't perfect, the outer channel is always better transmitted than the inner one.

Switch gate on the opposite side of the MZI (sw2)

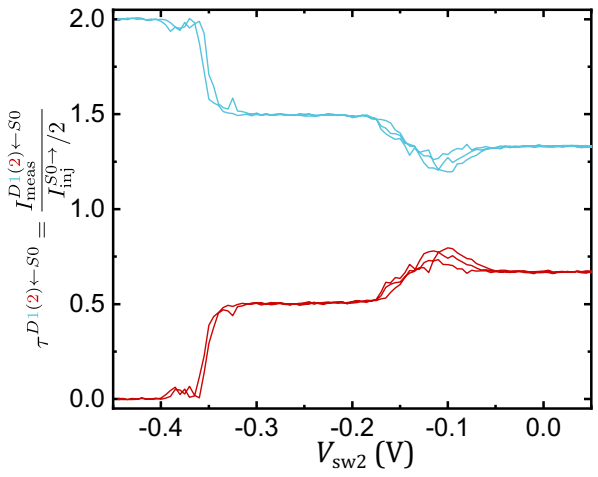

Figure B.4: Normalized current measured at D_1 while sweeping V_{sw2} such that the outer switch goes from fully closed ($-0.45\,\mathrm{V}$) to fully open ($0\,\mathrm{V}$) while the inner switch is fully open ($V_{\mathrm{sw1}} = 0\,\mathrm{V}$). Both of the MZI QPCs are set to full transmission for these measurements.

figure B.4 shows the normalized current measured at drain D_1 while sweeping the outer switch gate voltage V_{sw2} while the inner switch voltage is kept at $V_{\mathrm{sw1}} = 0$. The

observed plateau in the normalized conductance at $g_{\mathrm{D2}\leftarrow\mathrm{S0}} \approx 2$ occurs at the most negative voltages when both quantum Hall channels are reflected at the level of the outer switch gate. No information can be gained from this plateau: it is impossible what proportion of the current is reflected at the island's interface or at the gate. The fact that there is a plateau lying at $g_{\mathrm{D1}\leftarrow\mathrm{S0}} \approx 1.5$ is fully consistent with what we said above. It can effectively result from the current of an almost entirely reflected inner channel on the inner side of the MZI plus that of an outer channel very-well coupled to the island, which is then equally redistributed in the outer channel of the opposite side of the MZI (red plateau at $g_{D2\leftarrow S0} \approx 0.5$) and the outer channel on the MZI side.

As a final remark, one can note that the transition from one plateau to another occur around the same gate voltage for both switches (which share an identical lithographic design): the first transition occurs at $V_{\mathrm{sw1,2}} \approx -0.35\,\mathrm{V}$ and second one at $V_{\mathrm{sw1,2}} \approx -0.15\,\mathrm{V}$. This indicates that there is indeed no major problem with the inner gate and that rather, the reflection occurs at the island's interface.

B.1.3 No measurable residual charge quantization in the island

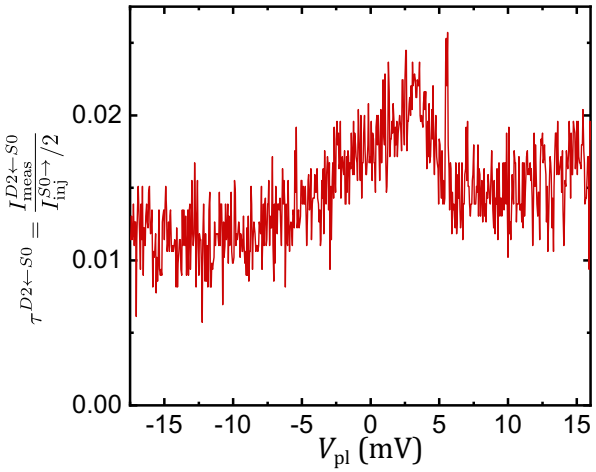

Figure B.5: Transmission through the island upon varying the plunger gate voltage V_{pl} with the inner switch gate set at a very low transmission probability ($V_{\mathrm{sw1}} \approx -0.3665\,\mathrm{V}$), while the outer switch gate is fully transmitting only the outer channel ($V_{\mathrm{sw2}} \approx -0.25\,\mathrm{V}$).

Would the outer channel be imperfectly connected to the island, residual charge quantization oscillations should subsist with a periodicity equal to that of the Coulomb diamond, (i.e $\Delta V_{\mathrm{pl}} \approx 1.7\,\mathrm{mV}$) [211]. Such oscillations are clearly absent of figure B.5 that boasts a broad peak instead, and that we cannot relate in any way to charge quantization (and it is unclear where this peak comes from). Note that such a measurement is very sensitive and that even a minute deviation from ballistic coupling results in an appreciable signal (e.g. assuming a $\tau_{\mathrm{sw1}} < 5\%$, which is clearly the case, a 1% reflection of the outer channel on the opposite side to the MZI would yield oscillations of over 30%, see [211, fig. 3]). This, in line with the previous section, further attests that

the outer channel is essentially perfectly coupled to the island and that our analysis of section 4.3.3 to deduce $\tau_{\Omega-1}$ is valid.

B.2 About the observed anomalous periodicities of A-B oscillations

B.2.1 Periodicity of the reflected electrons at the metallic island interface

We consider here the situation with two channels connected to the island, and give a reasonable argument for why the periodicity of the interference pattern is different from what is a priori expected.

Let's precisely start with what is expected. The measured phase of the interference pattern due to the reflected electrons at the island's interface is naively expected to be

$$\begin{aligned}\phi &= \frac{B(\mathcal{A}_{\mathrm{MZI}} + \mathcal{A}_{\mathrm{dot}})}{\hbar/e} \\ &= \phi_{\mathrm{MZI}} + \phi_{\mathrm{dot}}\end{aligned}$$

with $\mathcal{A}_{\mathrm{MZI}}$ the simple MZI area (in green in figure 4.11 b), and $\mathcal{A}_{\mathrm{dot}}$ the area of the small region comprised between the metallic island and the switch gate located closest to the MZI (sw1) (corresponding to the difference in the blue area of figure 4.11 c and the green one of figure 4.11 b). We observe nonetheless that it is as if $\mathcal{A}_{\mathrm{dot}}$ is not contributing.

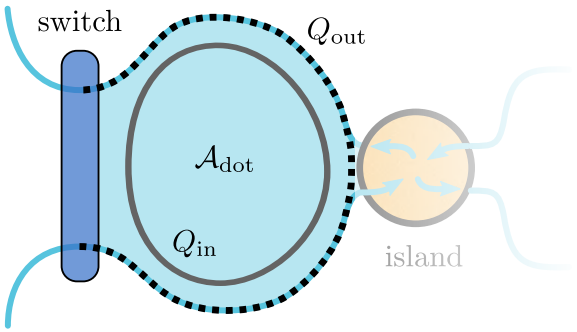

Figure B.6: Schematic, not to scale, of the Coulomb dominated area between the switch gate (in dark blue) and the island (yellow disk) that we consider to play no role in this model and is therefore faded. It is here totally disconnected from the inner channel which carries a Q_{in} localized charge. The reflected part of the outer channel (black dotted line) is also considered entirely disconnected from the island and to carry a charge Q_{out}. The part of the outer channel that is well-connected to the island, which does not play a role in the model (see text), is depicted in light blue.

As discussed in section 2.3.2, the charging energy of a region can be large enough to prevent any charge modification in the considered region. It is possible to think that this kind of effect takes place in the small region comprised in between the metallic island and the switch gate located on the MZI side (sw1), for the reflected electrons. For this, the fraction of electrons in the outer channel reflected at the metallic island interface, is assumed to be completely disconnected from the island as illustrated in figure B.6. The second assumption is that the inner channel is also completely disconnected from the island, which is a good approximation as attested by the characterization measurements discussed in section B.1. Its charge, confined to this very small region, is therefore defined by an integer number N_{dot} of e. The third assumption is the most speculative as we have no numbers to put in: it consists in considering the charging energy of this small region as dominating and forcing this small region to be in the Coulomb-dominated regime. The very small dot size, constituted of two QH channels, cannot have a large capacitance with its surroundings, making this last assumption realistic.

Under these assumptions, it is possible to directly use equation 2.7 applied to this small dot region:

$$\frac{\partial N_{\mathrm{dot}}}{\partial B} = -\frac{1}{2\pi}\frac{\partial \phi_{\mathrm{dot}}}{\partial B}$$

As a consequence, the magnetic field phase acquired in this region cancels $\partial\phi_{\mathrm{dot}}/\partial B = 0$.

B.2.2 Periodicity of the MZI interrupted by the metallic island

It is tempting to perform a reasoning similar to the above to try to explain the puzzling increase in the magnetic field periodicity when a single channel is connected to the island.

In this configuration, it is safe to consider the whole region comprised in between both switch gates to be in the Coulomb dominated regime considering the island's large charging energy. However, this regime can only account for a cancellation of the Aharonov-Bohm phase due to the Coulomb-blockaded area. In our case, this should lead to, in the extreme case, an effective area $\mathcal{A}_{\mathrm{eff}}$ that matches that of the simple MZI $\mathcal{A}_{\mathrm{MZI}}$, and not a smaller one, as observed. It therefore seems that something else is at play, and that the geometric coincidence pointed above is not linked to the observed periodicity.

We note a simple geometric observation: if one were to attribute the observed periodicity in this configuration to an effective area $\Delta B = (h/e)/\mathcal{A}_{\mathrm{eff}}$, then it corresponds to $\mathcal{A}_{\mathrm{eff}} \approx 13.5 \pm 0.2\,\mu\mathrm{m}^2$. This corresponds to a reduction of the simple MZI nominal area of $\mathcal{A}_{\mathrm{MZI}} - \mathcal{A}_{\mathrm{eff}} \approx 16.8 - 13.5 \approx 3.3\,\mu\mathrm{m}^2$. This difference corresponds, within uncertainties, to the area of the 2DEG comprised between the two switch gates $2\mathcal{A}_{\mathrm{dot}} \approx 3.1\,\mu\mathrm{m}^2$ (extracted from the lithographic design). This might be a mere coincidence, as it is hard to find a physical explanation for such a correspondance, but I thought worth to mention it in case it gives someone else an idea on a possible microscopic mechanism

that would involve geometrical arguments.

B.2.3 FFT power spectral density in log scale

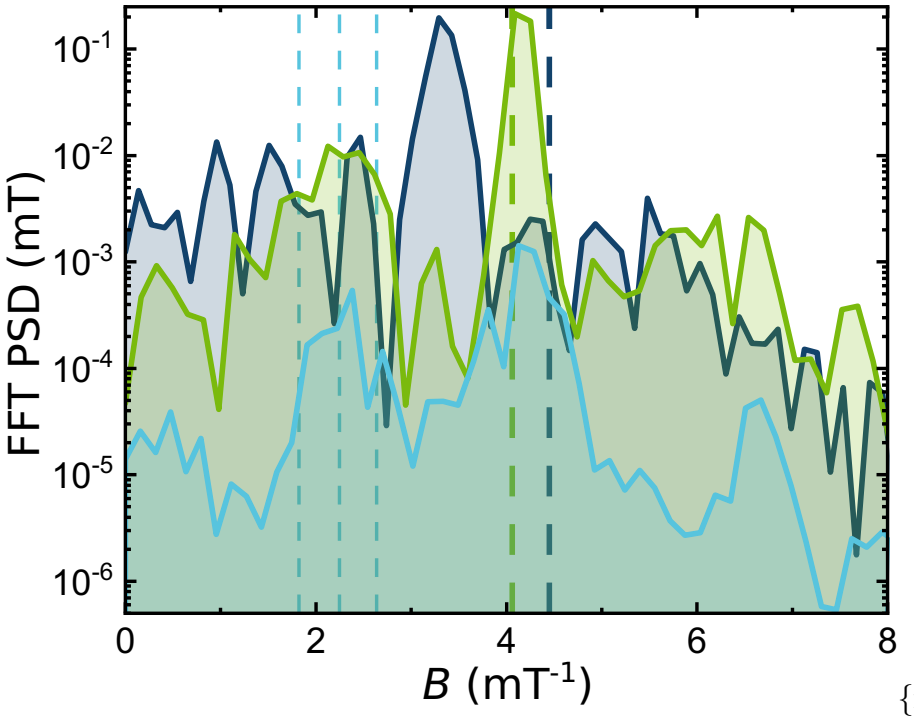

{fig:FFT-log width=50%}

B.3 Plunger gates oscillations

It is possible to use the other knobs at hand to try get a better picture of this device.

B.3.1 Gate coupled only to one path

By varying V_{combL}, we obtain the data printed in figure B.7 a-c, as this gate is only coupled to the left path and separated from the island by a set of other gates, it is well screened and its capacitance towards the island should be very small. In effect, upon varying its voltage, it is clear from figure B.7 d that there is a single periodicity, as one would expect, regardless of the configuration the MZ is set in.

B.3.2 Gate coupled to both a path and the island

It is also possible to use $V_{\text{pl-2}}$ as a modulation knob for the interference pattern, the acquired data is visible on figure B.8 a-c, using the usual color code for all three configurations. Interestingly, the periodicity when a single channel is connected to the island (dark blue) is smaller than in the simple MZI case (light green). This can be understood

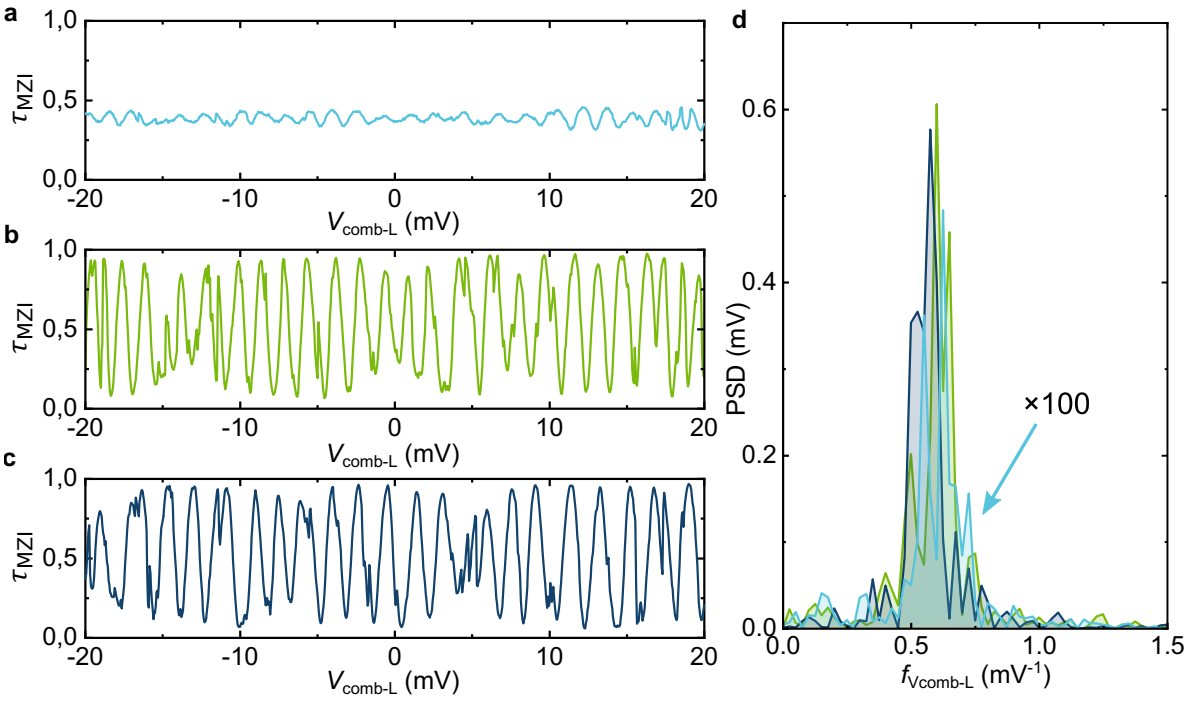

Figure B.7: MZI interferences as a function of V_{combL} following the same color code as in the main text.

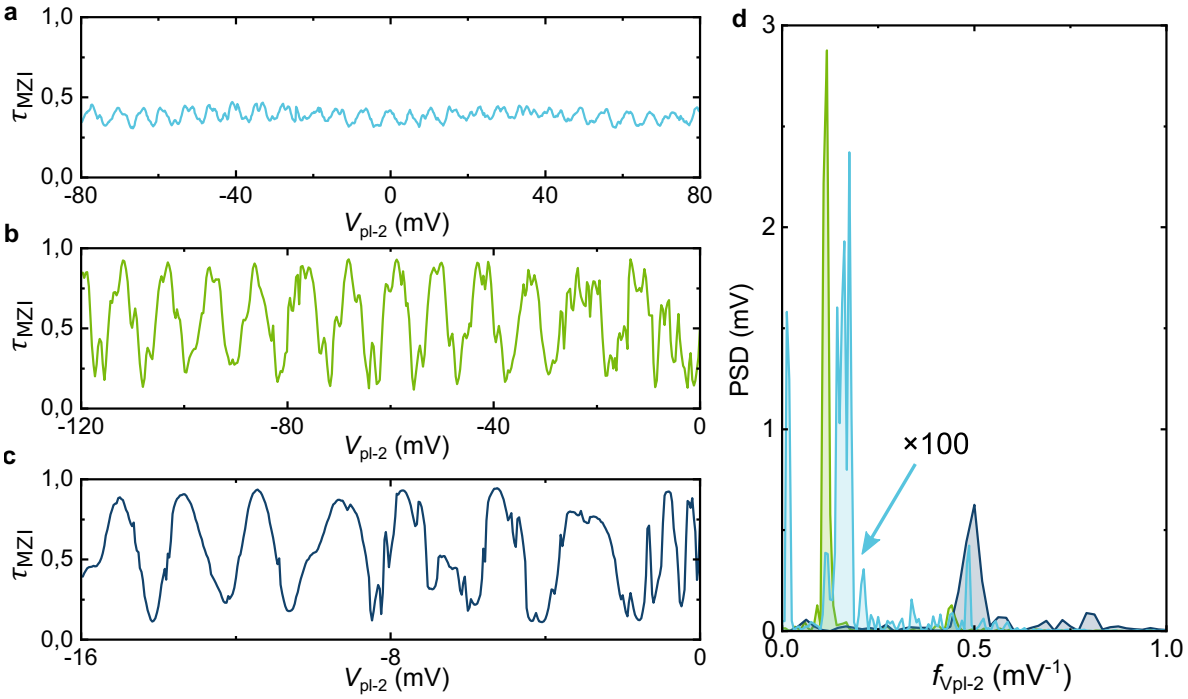

Figure B.8: MZI interferences as a function of V_{pl2} following the same color code as in the main text.

as the fact that not only $V_{\text{pl-2}}$ acts on the area enclosed between both paths, but it also modifies the charge state of the island alltogether, resulting in a smaller periodicity. The main peak observed for the 2-channel case, because of its slightly higher frequency, is compatible with a path slightly more coupled to this gate than the simple MZI path but also well decoupled from the island as it remains far from the much higher frequency of the 1-channel case. Together these two elements go in the sense of a reflection occuring at the metal/2DEG interface and that the observed anomalous periodicity in magnetic field comes from a cancellation of the small area enclosed between the island and the top barring gate.

B.4 Visibility dependence as a function of the inner switch gate transmission

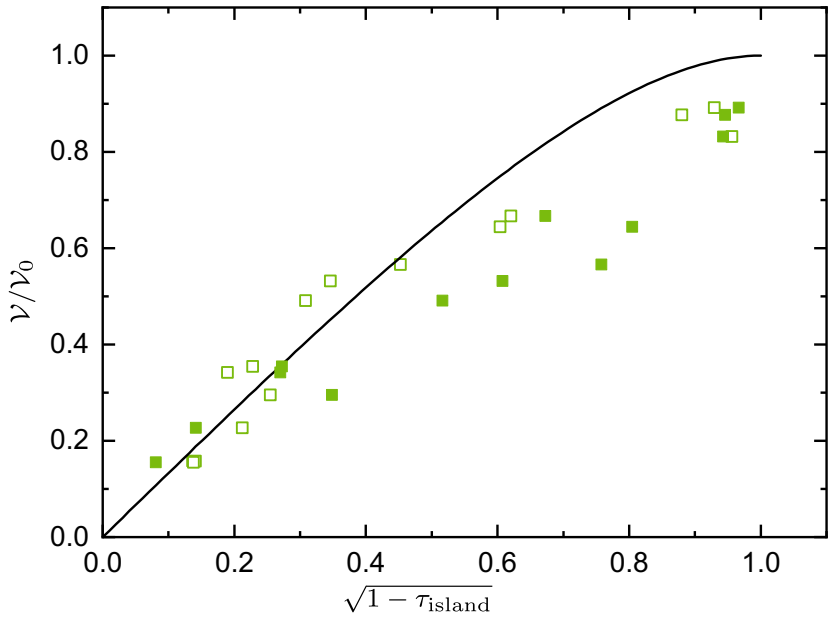

Figure B.9: Visibility of the measured interference visibility $\mathcal{V}$ normalized to the maximum visibility $\mathcal{V}_0 = \mathcal{V}(\tau_{\text{island}} = 0) \approx 89\%$ as a function of the transmission probability of the interfering channel to the island τ_{island} when a second channel is ballistically connected to it. The full black line is obtained directly from equation C.5 evaluated in $\tau_R = \tau_L = 1/2$. The full (open) symbols are obtained by extracting the value of τ_{island} from two different methods (see text).

When the outer switch gate (sw2) is open to couple one channel to the island, and that the inner switch gate (sw1) is gradually opened with transmission probability τ_{island}, the MZI becomes incoherent following equation C.5. It is hard to precisely know the transmission probability of the switch gate (sw1) as a function of the voltage applied to it V_{sw1}, due to large and rapid fluctuations of $\tau_{\text{island}}(V_{\text{sw1}})$. Consequently, τ_{island} is extracted using two different methods. The first one, corresponding to full symbols

on figure B.9, uses the average signal measured across the MZI. This signal is however sensitive to the reflection on the central ohmic contact as well as the transmission of the first QPC that is assumed to be at exactly half transmission probability. The second method is based on the characterized $\tau_{\text{island}}(V_{\text{sw1}})$ when $\tau_{\text{qpc1,2}} = 1$. It is assumed that the capacitive crosstalk of the QPCs on sw1 can be corrected by a fixed quantity on V_{sw1}, which is determined for each QPC by matching the recognizable patterns of the $\tau_{\text{island}}(V_{\text{sw1}})$ characterization curve when $\tau_{\text{qpc1,2}} = 1$ to the one when the device is set alternatively to $\tau_{\text{qpc1(2)}} = 1(1/2)$ and $\tau_{\text{qpc1(2)}} = 1/2(1)$. On figure B.9, the result of both methods is displayed, such that for each value of visibility, there is one empty square and one full square. The difference between their abscissa indicates the uncertainty on τ_{island}.

B.5 MZI with an applied voltage bias

B.5.1 Visibility evolution as function of voltage bias

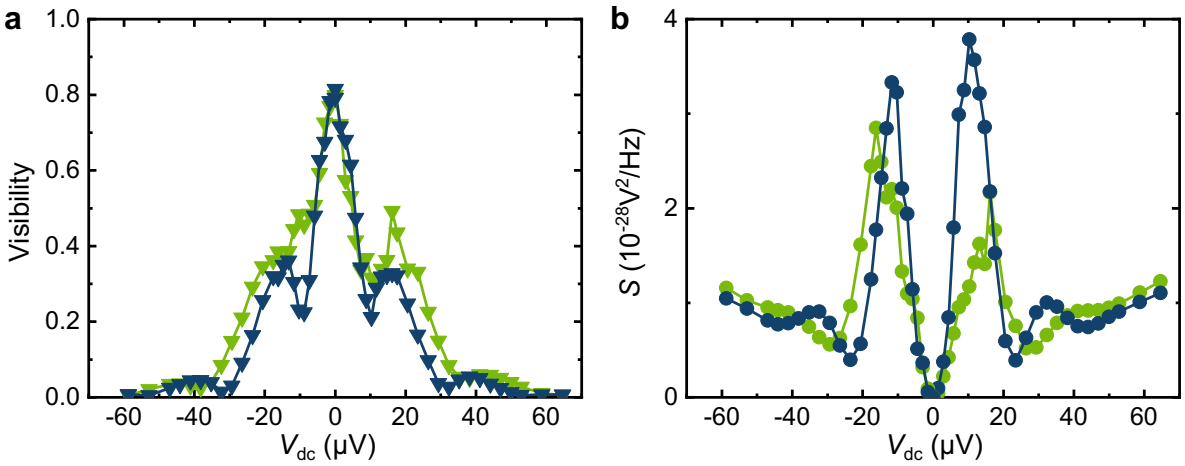

Figure B.10: **a** Median visibility as a function of dc bias applied to the interfering channel **b** Mean excess noise measured simultaneously

It is predicted that in the 1-channel case, the MZI visibility should depend on a new energy scale: the island's charging energy. This can be explored with the voltage bias applied to the interferometer. In figure B.10, the median visibility extracted for both the 1- and 0-channel cases is displayed. It is unfortunately not possible to directly plot the ratio of the two as the lobe energy scale is slightly different from one another as visible particularly at the second node on figure B.10 a, probably due to a slight difference in the paths lengths between both cases. Qualitatively however, it is possible to see that the visibility does indeed die out faster when 1 channel is connected to the island than in the simple MZI case, seem to indicate that the island's charging energy $E_c \approx 26\,\mu$eV does indeed introduce a cutoff in the observed amplitude of the interferences. This smaller robustness of the visibility to the applied bias voltage can

also be seen in the amplitude of the measured excess noise averaged over many periods and shown in figure B.10 b. There, the component of the excess noise that is non-linear in V_{dc} is due to phase noise, as discussed in sections 3.5, 3.7. Here, a side-lobe is visible in the noise.

B.5.2 Phase noise in a MZI (connected to a metallic island)

We provide here one more argument to uphold this idea by the data displayed on figure B.11 a,c. This data was acquired at a bias voltage of $V_{\mathrm{dc}} \approx 18\,\mu\mathrm{V}$, at which point the visibility is still quite substantial ~35%. By simultaneously measuring the MHz noise and the conductance, it is possible to notice that the measured noise boasts peaks each time the derivative of the conductance reaches a maximum, consistent with the first term of equation A.3, the one proportionnal to $\langle\delta\varphi^2(\omega)\rangle$, which is valid when $\langle\delta\varphi^2(\omega)\rangle \ll (2\pi)^2$ as it is obviously the case here because the visibility measured with the lock-in amplifier is still of decent amplitude. The Fourier transform of the Noise (figure B.11 d) effectively boasts a main peak at exactly twice the frequency of the one in the conductance (figure B.11 b). This means that this device has MHz noise which tends to lower the measured visibility at the lock-in amplifier frequencies (~200 Hz).

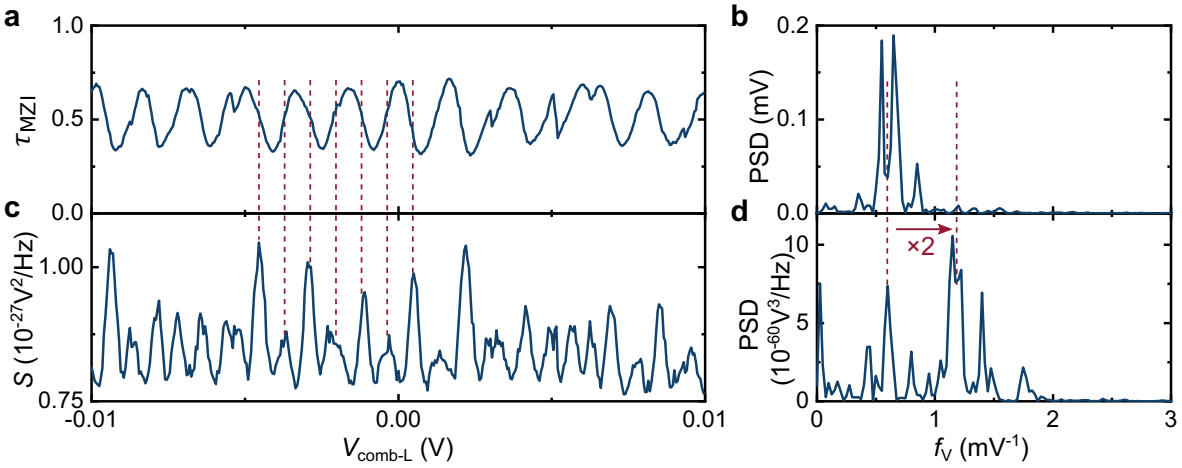

Figure B.11: Data acquired at $V_{\mathrm{dc}} \approx 18\,\mu\mathrm{V}$. **a** Aharonov-Bohm interferences in the differential conductance as a function of the left comb gate (used as a plunger here) and **b** its FFT. **c** Current noise peaks appearing when the derivative of the differential conductance is maximum as indicated for a few peaks by the vertical dashed lines for clarity, this appears in its FFT shown in **d** where the main peak is at twice the frequency of the conductance's.

C

Scattering treatment of the MZI

C.1 Conductance formula in the simple MZI case

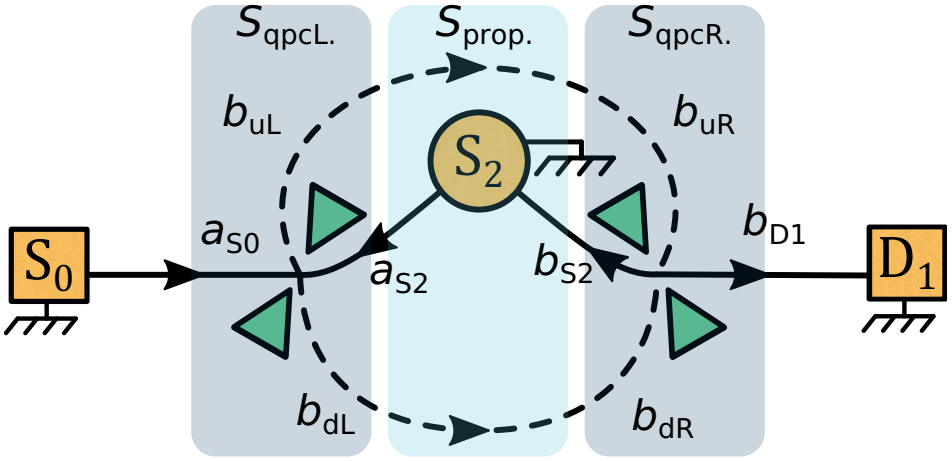

Figure C.1: Schematic of the simple electronic MZI.

It is possible to derive the expression for the conductance accross the MZI using the Landauer-Buttiker formalism. The notations are recapitulated on the schematic of figure C.1, where the a_i, b_i are the annihilation operators for electrons in the channel. The a_i operators are emerging from a contact while the b_i ones are the resulting from a scattering process. It is then possible to express the scattering process at the two QPCs, identified by the dark blue zones on figure C.1, as well as the effect of the phase picked up along the propagation path (light blue zone) with the following scattering

matrices:

$$\begin{pmatrix} b_{\mathrm{uL}} \\ b_{\mathrm{dL}} \end{pmatrix} = S_{\mathrm{qpcL}} \begin{pmatrix} a_{\mathrm{S0}} \\ a_{\mathrm{S2}} \end{pmatrix} = \begin{pmatrix} \sqrt{R_{\mathrm{qpcL}}} & \sqrt{T_{\mathrm{qpcL}}} \\ \sqrt{T_{\mathrm{qpcL}}} & -\sqrt{R_{\mathrm{qpcL}}} \end{pmatrix} \begin{pmatrix} a_{\mathrm{S0}} \\ a_{\mathrm{S2}} \end{pmatrix}$$

$$\begin{pmatrix} b_{\mathrm{uR}} \\ b_{\mathrm{dR}} \end{pmatrix} = S_{\mathrm{prop.}} \begin{pmatrix} b_{\mathrm{uL}} \\ b_{\mathrm{dL}} \end{pmatrix} = \begin{pmatrix} e^{i\phi_u} & 0 \\ 0 & e^{i\phi_d} \end{pmatrix} \begin{pmatrix} b_{\mathrm{uL}} \\ b_{\mathrm{dL}} \end{pmatrix}$$

$$\begin{pmatrix} b_{\mathrm{S2}} \\ b_{\mathrm{D1}} \end{pmatrix} = S_{\mathrm{qpcR}} \begin{pmatrix} b_{\mathrm{dR}} \\ b_{\mathrm{uR}} \end{pmatrix} = \begin{pmatrix} \sqrt{R_{\mathrm{qpcR}}} & \sqrt{T_{\mathrm{qpcR}}} \\ \sqrt{T_{\mathrm{qpcR}}} & -\sqrt{R_{\mathrm{qpcR}}} \end{pmatrix} \begin{pmatrix} b_{\mathrm{dR}} \\ b_{\mathrm{uR}} \end{pmatrix}$$

It is then possible to obtain an expression for b_{D1} in terms of the a_i:

$$b_{\mathrm{D1}} = \left(\sqrt{\tau_{\mathrm{R}}\tau_{\mathrm{L}}} e^{i\phi_d} - \sqrt{(1-\tau_{\mathrm{R}})(1-\tau_{\mathrm{L}})} e^{i\phi_u} \right) a_{\mathrm{S0}} + \left(\sqrt{(1-\tau_{\mathrm{R}})\tau_{\mathrm{L}}} e^{i\phi_u} - \sqrt{\tau_{\mathrm{R}}(1-\tau_{\mathrm{L}})} e^{i\phi_d} \right) a_{\mathrm{S2}}$$

The conductance from the source contact S_0 to drain D_1 reads:

$$\begin{aligned} G^{\mathrm{D1}\leftarrow\mathrm{S0}} =& \frac{e^2}{h} b_{\mathrm{D1}}^{\dagger} b_{\mathrm{D1}} \\ =& \frac{e^2}{h} a_{\mathrm{S0}}^{\dagger} a_{\mathrm{S0}} \left(\tau_R\tau_L + (1-\tau_R)(1-\tau_L) + 2\sqrt{\tau_R\tau_L(1-\tau_R)(1-\tau_L)} \cos(\phi_d - \phi_u) \right) \end{aligned} \tag{C.1}$$

The visibility is simply the ratio between the mean conductance and the amplitude of oscillations:

$$\mathcal{V} = \frac{2\sqrt{\tau_R\tau_L(1-\tau_R)(1-\tau_L)}}{\tau_R\tau_L + (1-\tau_R)(1-\tau_L)} \tag{C.2}$$

C.2 Conductance formula for the MZI with a voltage probe

In this section, the case of an ideal voltage probe connected to one arm of the MZI through a QPC is calculated. This corresponds exactly to the experimental situation of [200].

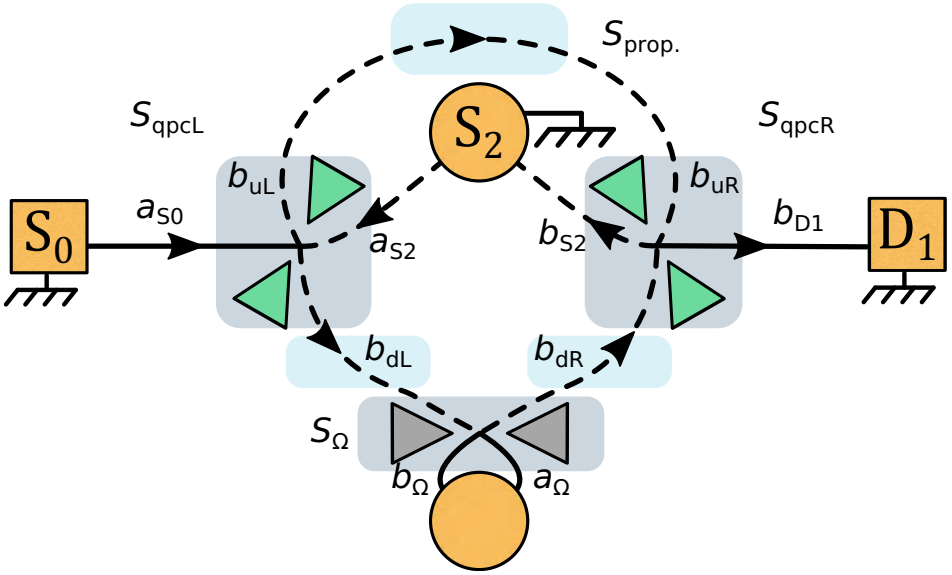

Figure C.2: Schematic of the MZI with a dephasing probe.

$$\begin{pmatrix} b_{\mathrm{uL}} \\ b_{\mathrm{dL}} \end{pmatrix} = \begin{pmatrix} \sqrt{R_{\mathrm{qpcL}}} & \sqrt{T_{\mathrm{qpcL}}} \\ \sqrt{T_{\mathrm{qpcL}}} & -\sqrt{R_{\mathrm{qpcL}}} \end{pmatrix} \begin{pmatrix} a_{\mathrm{S0}} \\ a_{\mathrm{S2}} \end{pmatrix}$$

$$\begin{pmatrix} b_{\mathrm{dR}} \\ b_{\Omega} \end{pmatrix} = \begin{pmatrix} \sqrt{R_\Omega} e^{i\phi_d} & \sqrt{T_\Omega} \\ \sqrt{T_\Omega} & -\sqrt{R_\Omega} \end{pmatrix} \begin{pmatrix} b_{\mathrm{dL}} \\ a_{\Omega} \end{pmatrix}$$

$$b_{\mathrm{uR}} = e^{i\phi_u} b_{\mathrm{uL}}$$

$$\begin{pmatrix} b_{\mathrm{S2}} \\ b_{\mathrm{D1}} \end{pmatrix} = \begin{pmatrix} \sqrt{R_{\mathrm{qpcR}}} & \sqrt{T_{\mathrm{qpcR}}} \\ \sqrt{T_{\mathrm{qpcR}}} & -\sqrt{R_{\mathrm{qpcR}}} \end{pmatrix} \begin{pmatrix} b_{\mathrm{dR}} \\ b_{\mathrm{uR}} \end{pmatrix}$$

With this, we can find an expression for b_{D1} that only depends on source operators (a_i):

$$\begin{aligned} b_{\mathrm{D1}} = &\left(\sqrt{\tau_{\mathrm{R}} \tau_{\mathrm{L}} (1-\tau_\Omega)} e^{i\phi_d} - \sqrt{(1-\tau_{\mathrm{R}})(1-\tau_{\mathrm{L}})} e^{i\phi_u} \right) a_{\mathrm{S0}} \\ &+ \left(\sqrt{(1-\tau_{\mathrm{R}}) \tau_{\mathrm{L}}} e^{i\phi_u} - \sqrt{\tau_{\mathrm{R}} (1-\tau_{\mathrm{L}})(1-\tau_\Omega)} e^{i\phi_d} \right) a_{\mathrm{S2}} \\ &+ \sqrt{\tau_{\mathrm{R}} \tau_\Omega} a_\Omega \end{aligned}$$

Current conservation at the probe imposes , and From the matrices above, it is possible to deduce obtain an expression for $b_\Omega^\dagger b_\Omega$:

$$b_\Omega^\dagger b_\Omega = (\tau_L\tau_\Omega)a_{\mathrm{S0}}^\dagger a_{\mathrm{S0}} + [(1-\tau_L)\tau_\Omega]a_{\mathrm{S2}}^\dagger a_{\mathrm{S2}} + (1-\tau_\Omega)a_\Omega^\dagger a_\Omega \tag{C.3}$$

Plugging in this equation the condition of current conservation at the probe: $a_\Omega^\dagger a_\Omega = b_\Omega^\dagger b_\Omega$, we find:

$$a_\Omega^\dagger a_\Omega = \tau_L a_{\mathrm{S0}}^\dagger a_{\mathrm{S0}} + (1-\tau_L)a_{\mathrm{S2}}^\dagger a_{\mathrm{S2}}$$

It is then possible to evaluate the conductance from contact S0 to contact D1. Therefore the $a_{\mathrm{S2}}^\dagger a_{\mathrm{S2}}$ term is dropped and we find:

$$\begin{aligned}
G^{\mathrm{D1}\leftarrow\mathrm{S0}} =& \frac{e^2}{h} b_{\mathrm{D1}}^\dagger b_{\mathrm{D1}} \\
=& a_{\mathrm{S0}}^\dagger a_{\mathrm{S0}} \left(\tau_R\tau_L(1-\tau_\Omega) + (1-\tau_R)(1-\tau_L) + 2\sqrt{\tau_R\tau_L(1-\tau_\Omega)(1-\tau_R)(1-\tau_L)}\cos(\phi_d-\phi_u) \right) \\
&+ a_\Omega^\dagger a_\Omega(\tau_R\tau_\Omega) \\
=& a_{\mathrm{S0}}^\dagger a_{\mathrm{S0}} \left(\tau_R\tau_L + (1-\tau_R)(1-\tau_L) + 2\sqrt{\tau_R\tau_L(1-\tau_\Omega)(1-\tau_R)(1-\tau_L)}\cos(\phi_d-\phi_u) \right)
\end{aligned}$$

which is the same expression as equation C.1 up to an additional factor of $\sqrt{1-\tau_\Omega}$ in front of the oscillating term. Note that the mean conductance term is identical to the simple MZI one as expected because all current penetrating the probe exits it towards the MZI, such that only the coherence is affected by the presence of the probe along one arm. The visibility reads:

$$\mathcal{V} = \frac{2\sqrt{\tau_R\tau_L(1-\tau_\Omega)(1-\tau_R)(1-\tau_L)}}{\tau_R\tau_L + (1-\tau_R)(1-\tau_L)}$$

and is again identical to equation C.2 up to the $\sqrt{1-\tau_\Omega}$ factor at the numerator.

C.3 Conductance formula for the MZI with a metallic island connected to two channels

In this section, we treat the case of an ideal metallic island (with perfect contacts to the channels) connected to one arm of the MZI through a QPC figure C.3. The nice thing is that all the scattering matrices used above are identical here. The only difference lies

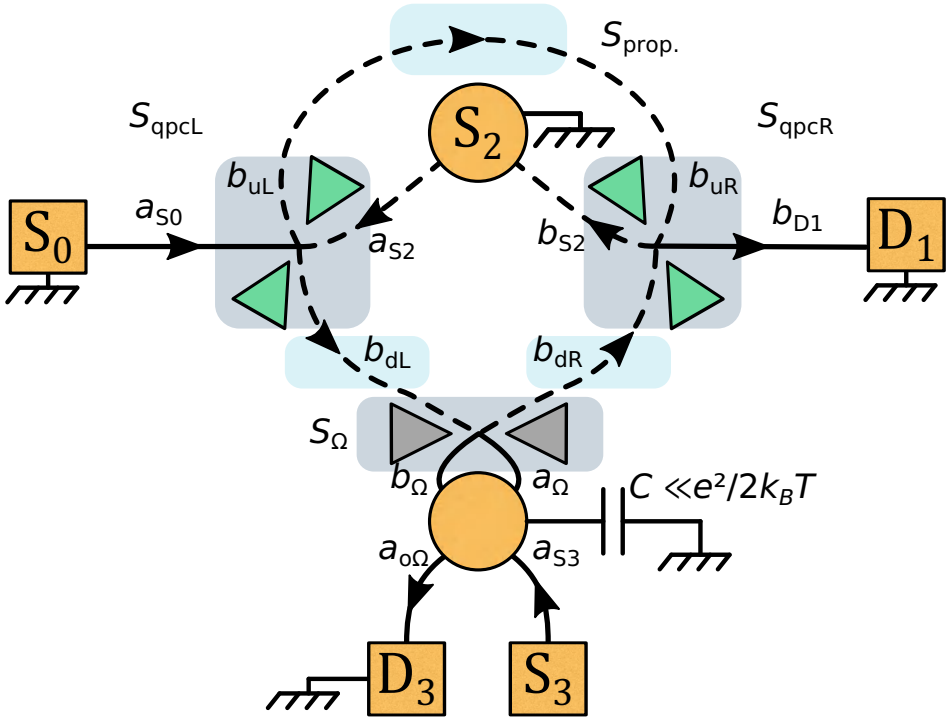

Figure C.3: Schematic of the MZI with a metallic island coupled to one path through a QPC.

in the current conservation at the island, which this time reads:

$$b_\Omega^\dagger b_\Omega + a_{S3}^\dagger a_{S3} = a_\Omega^\dagger a_\Omega + a_{o\Omega}^\dagger a_{o\Omega} \tag{C.4}$$

Morevoer, in this case, an additionnal condition has to be added: the current is equally redistributed in both channels leaving the island which simply follows from the fact that each channel has the same resistance, and it can be expressed as:

$$a_\Omega^\dagger a_\Omega = a_{o\Omega}^\dagger a_{o\Omega}$$

Plugging the latter equirepartition condition in the current conservation one (equation C.4) and using equation C.3, it is possible to find an expression for the current emerging from the island on the MZI side:

$$a_\Omega^\dagger a_\Omega = \frac{\tau_L \tau_\Omega}{1+\tau_\Omega} a_{S0}^\dagger a_{S0} + \frac{(1-\tau_L)\tau_\Omega}{1+\tau_\Omega} a_{S2}^\dagger a_{S2} + \frac{1}{1+\tau_\Omega} a_{S3}^\dagger a_{S3}$$

Once again, the conductance from S0 to D1 does not depend on the $a^\dagger_{S2}a_{S2}$ or $a^\dagger_{S3}a_{S3}$ terms so that we can drop them:

$$
\begin{aligned}
G^{\mathrm{D1}\leftarrow\mathrm{S0}} =& \frac{e^2}{h} b^\dagger_{\mathrm{D1}} b_{\mathrm{D1}} \\
=& \frac{e^2}{h} \Big[a^\dagger_{\mathrm{S0}} a_{\mathrm{S0}} \left(\tau_R\tau_L(1-\tau_\Omega) + (1-\tau_R)(1-\tau_L) \right. \\
& \left. + 2\sqrt{\tau_R\tau_L(1-\tau_\Omega)(1-\tau_R)(1-\tau_L)}\cos(\phi_d - \phi_u) \right) \\
& + a^\dagger_\Omega a_\Omega (\tau_R\tau_\Omega) \Big] \\
=& \frac{e^2}{h} \Big[a^\dagger_{\mathrm{S0}} a_{\mathrm{S0}} \left(\tau_R\tau_L(1-\tau_\Omega) + (1-\tau_R)(1-\tau_L) \right. \\
& \left. + 2\sqrt{\tau_R\tau_L(1-\tau_\Omega)(1-\tau_R)(1-\tau_L)}\cos(\phi_d - \phi_u) \right) \\
& + a^\dagger_{\mathrm{S0}} a_{\mathrm{S0}} \left(\frac{\tau_R\tau_L\tau_\Omega^2}{1+\tau_\Omega} \right) \Big] \\
=& \frac{e^2}{h} a^\dagger_{\mathrm{S0}} a_{\mathrm{S0}} \left(\tau_R\tau_L \left(\frac{1}{1+\tau_\Omega} \right) + (1-\tau_R)(1-\tau_L) \right. \\
& \left. + 2\sqrt{\tau_R\tau_L(1-\tau_\Omega)(1-\tau_R)(1-\tau_L)}\cos(\phi_d - \phi_u) \right)
\end{aligned}
$$

In this case, the oscillating term is multiplied by the same $\sqrt{1-\tau_\Omega}$ term as for the MZI with a probe on one arm but there is also a reduction factor in the direct, non-oscillating, average term, that concerns only the trajectory along the arm interrupted by the island. The visibility in this case is:

$$
\mathcal{V} = \frac{2\sqrt{\tau_R\tau_L(1-\tau_\Omega)(1-\tau_R)(1-\tau_L)}}{\tau_R\tau_L/(1+\tau_\Omega) + (1-\tau_R)(1-\tau_L)} \tag{C.5}
$$

C.4 Scattering treatment of Clerk's metallic dot

It is instructive to derive the prediction for the metallic dot considered in [46] within the scattering formalism and illustrated in figure C.4. Note that this calculation is

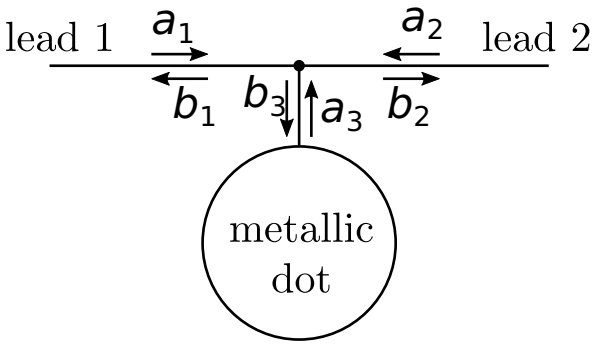

Figure C.4: Metallic dot coupled to two leads in a T-junction geometry as considered in [46,49]

detailed in [49, chap. 5] although a couple of misprints are here corrected, and a few more details are given to reach the author's result. The scattering at the T-junction illustrated in figure C.4 can be expressed as follows:

$$\begin{pmatrix} b_1 \\ b_2 \end{pmatrix} = S_{\text{leads}} \begin{pmatrix} a_1 \\ a_2 \end{pmatrix} + \begin{pmatrix} t'_d \\ t_d \end{pmatrix} a_3$$

$$a_3 = S_{\text{dot}} b_3$$

$$b_3 = \begin{pmatrix} t_d & t'_d \end{pmatrix} \begin{pmatrix} a_1 \\ a_2 \end{pmatrix}$$

where t_d, t'_d, r'_d are the scattering amplitudes of the leads-dot contact, S_{leads} is the 2×2 scattering matrix directly connecting lead 1 to lead 2 and $S_{\text{dot}} = e^{i\phi}$ is the 1×1 scattering matrix of the dot that is here assumed to be fully coherent and therefore only gives a static (energy dependent) phase factor. From the last two equations above, it is possible to find an expression for a_3:

$$a_3 = \frac{S_{\text{dot}}}{1 - S_{\text{dot}} r'_d} \begin{pmatrix} t_d & t'_d \end{pmatrix} \begin{pmatrix} a_1 \\ a_2 \end{pmatrix}$$

and then

$$\begin{pmatrix} b_1 \\ b_2 \end{pmatrix} = \left\{ S_{\text{leads}} + \begin{pmatrix} t'_d \\ t_d \end{pmatrix} \frac{S_{\text{dot}}}{1 - S_{\text{dot}} r'_d} \begin{pmatrix} t_d & t'_d \end{pmatrix} \right\} \begin{pmatrix} a_1 \\ a_2 \end{pmatrix}$$

$$= \left\{ S_{\text{leads}} + t' \frac{S_{\text{dot}}}{1 - S_{\text{dot}} r'_d} t \right\} \begin{pmatrix} a_1 \\ a_2 \end{pmatrix}$$

where the term in curly brackets is the 2×2 scattering matrix S_{T} of the total T-junction, that connects lead 1 to lead 2, when taking into account the effect of the dot. It corresponds to the scattering matrix of eq. 5.1 of [49] (note the sign misprints in eq. 5.1 of [49], the correct expression was provided by the same author in e.g. [212]).

The unitarity of the above scattering matrix is ensured by the 3×3 scattering matrix of the T-junction contact, which can be written as a function of the matrices above:

$$S_{\mathrm{contact}} = \begin{pmatrix} S_{\mathrm{leads}} & t' \\ t & r'_d \end{pmatrix} \tag{C.6}$$

The elements of S_{contact} are given by the polar decomposition (see e.g. [213]) $S_{\mathrm{contact}} = U^\dagger S U$, with:

$$S = \begin{pmatrix} \sqrt{1-\tau} & 0 & \sqrt{\tau} \\ 0 & 1 & 0 \\ \sqrt{\tau} & 0 & -\sqrt{1-\tau} \end{pmatrix}$$

$$U = \begin{pmatrix} e^{\frac{1}{2}i(\delta+\phi)}\cos(\Omega) & e^{-\frac{1}{2}i(\phi-\delta)}\sin(\Omega) & 0 \\ -e^{\frac{1}{2}i(\phi-\delta)}\sin(\Omega) & e^{-\frac{1}{2}i(\delta+\phi)}\cos(\Omega) & 0 \\ 0 & 0 & 1 \end{pmatrix}$$

where $\tau = |t_d|^2 = |t'_d|^2$ is the transmission probability between the leads and dot (and $1-\tau = |r'_d|^2$), δ is the phase acquired by a direct scattering from lead to lead (and is therefore included in S_{leads}), Ω is a parameter characterizing the asymmetry of the dot's coupling to the leads.

Computing S_{contact} and identifying the terms with equation C.6 enables to obtain the T-junction scattering matrix S_{T}, and in particular, the terms that couple both leads:

$$S_{\mathrm{T}12} = S_{\mathrm{T}21} = -\frac{e^{-i\delta}\sin(\Omega)\cos(\Omega)\left(\sqrt{1-\tau}e^{i(2\delta+\phi)} + e^{2i\delta} - \sqrt{1-\tau} - e^{i\phi}\right)}{1+\sqrt{1-\tau}e^{i\phi}}$$

In turn, this gives the conductance from lead 1 to lead 2 through the Landauer formula:

$$G_{21} = \frac{e^2}{h}|S_{12}|^2$$

$$= \frac{e^2}{h}\sin^2(2\Omega)e^{i\phi}\frac{\left(\sqrt{1-\tau}\sin\left(\delta+\frac{\phi}{2}\right) + \sin\left(\delta-\frac{\phi}{2}\right)\right)^2}{\left(\sqrt{1-\tau}+e^{i\phi}\right)\left(1+\sqrt{1-\tau}e^{i\phi}\right)}$$

which, after some algebra, is equivalent to eq. 5.7 in [49]:

$$G_{21} = g_{\max}\sin^2(\delta+\phi(\tau))$$

where $\phi(\tau)$ is defined as

$$e^{2i\phi(\tau)} = \frac{1+\sqrt{1-\tau}e^{-i2\phi}}{1+\sqrt{1-\tau}e^{i2\phi}}$$

Interestingly, when G_{21} is expanded in $\sqrt{1-\tau}$ (eq. 5.10 in [49]), and averaged over the dot's phase, the expression for the conductance across the T-junction simplifies to

$$G_{21} = \frac{1}{2}g_{\max}\left(1-\sqrt{1-\tau}\cos(2\delta)\right)$$

which is the same term as that obtained in the MZI arm interrupted by the probe in section C.2.

D

Experimental Setup and Measurement Procedures

D.1 Conductance Measurement Setup

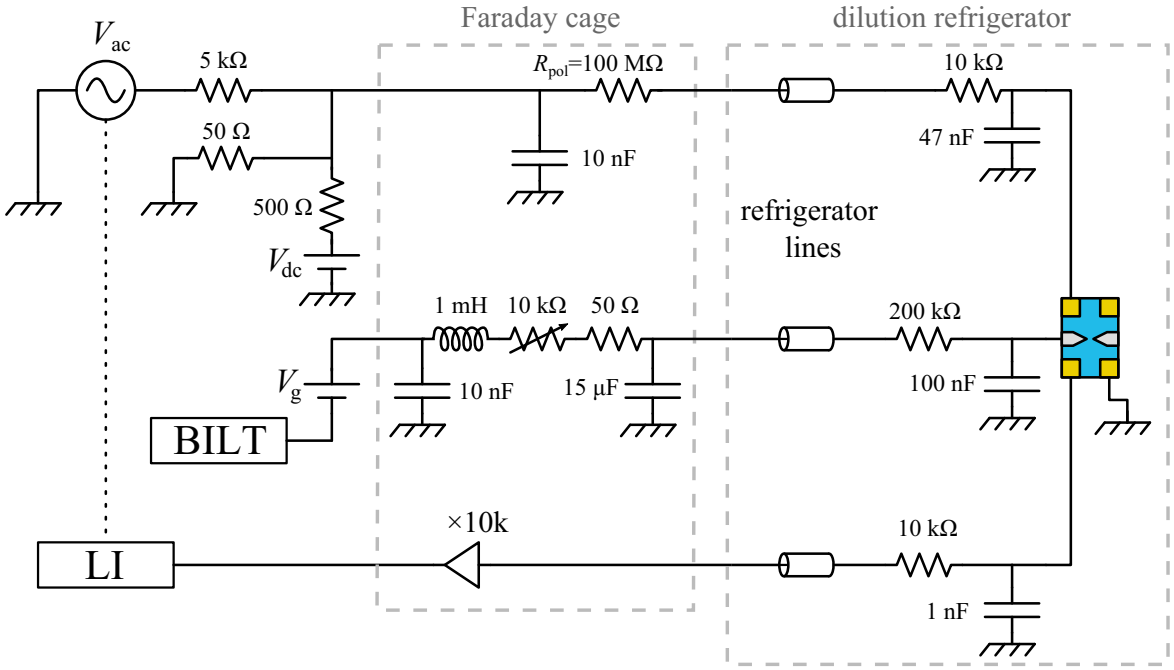

Figure D.1: Schematic of the measurement setup. The lock-in amplifier 'LI' is synchronized with the ac voltage source (dotted line). The 'BILT' controller pilots the gate voltages V_g.

Conductance measurements presented in this manuscript are achieved using a lock-in

technique. An ac voltage source is driven at a frequency in the 100-200 Hz range. The exact frequencies are chosen before starting the measurement campaign, by hooking the injection to ground and measuring the voltage noise spectrum with a spectrum analyser. This enables to identify the zones of least vibration-induced noise on the measurement lines.

The ac signal is then attenuated by a factor of ~ 100 via a voltage divider (the $50\,\Omega$ resistance hooked to ground in parallel with the $5\mathrm{k}\,\Omega$ resistance right after the ac source). It is possible to superpose a dc bias to the ac signal via the dc voltage source (V_{dc}), which is divided by ~ 10. These dividers enable to reduce parasitic signals, e.g. @ 50 Hz, and to combine ac & dc outside the Faraday cage.

Further, a polarization resistance is placed inside the Faraday cage. The purpose of this resistance is to have essentially all the voltage drop across it, in order for the circuit to be current polarized. Effectively, due to the thermal gradient along the lines going down in the refrigerator, a thermo-voltage builds-up. Current polarization also enables to avoid any spurious thermovoltage offset that could occur if we were to use voltage polarization. The other series resistances behind the polarization one, due to the lines going down in the fridge ($\sim 300\,\Omega$), the filter ($\sim 10\,\mathrm{k}\Omega$) placed in the puck, roughly 30 cm away from the sample holder, and the sample itself (from $\sim 100\,\Omega$ under no magnetic field to $\sim e^2/h$ in the quantum Hall regime), are negligible in front of the $R_{\mathrm{pol}} \approx 100\,\mathrm{M}\Omega$. As a consequence, the current input into the on-chip circuit is very well controlled and amounts to $I(t) \approx (V_{\mathrm{dc}}/100 + V_{\mathrm{ac}}(t)/10)/R_{\mathrm{pol}}$ with a relative systematic error of only 0.3% which can be calibrated at a given filling factor and taken into account to correct it.

The low-pass filters right before the sample serve the purpose of getting rid of electric noise potentially picked up on the lines. The multiple shielding layers of the fridge block most of the electromagnetic radiations. However, noise can also originate from triboelectricity: vibrations of the fridge can cause the wires of the coaxial lines to rub against the insulating layer, causing some triboelectric voltage. These vibrations can come from multiple origins: due to the pulse tube or the turbo pump plugged to the fridge, or from outside of the building and propagating through the ground and up the fridge's feet. On top of that, inflated air cushions supporting the fridge's frame serve as mechanical filters which attenuate vibrations. It is possible to try to identify noise sources using a seismometer, plugged to a spectrum analyser, and most importantly, to try to minimize the spectral noise density at the noisiest frequencies.

D.2 On-chip current to voltage converter

The voltage sources in series with the polarization resistance constitute an equivalent current source at the ohmic contacts to which they are attached (denoted Si, for source i on figure D.2). The injected current $I_{\mathrm{inj}}^{\mathrm{S}i\rightarrow}$ then propagates through the sample accord-

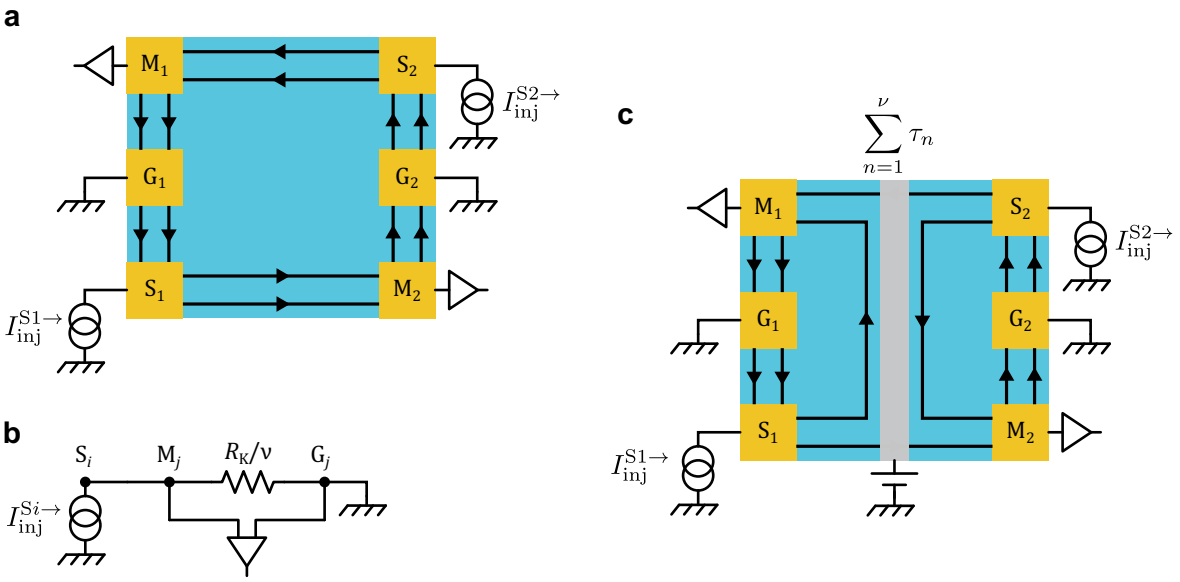

Figure D.2: On-chip current to voltage converter schematics. **a** Schematic of typical contacts configurations and their link to injection and measurement lines. **b** Equivalent circuit of the schematic depicted in **a**: all current injected at source S_i is collected at grounded contact G_j, monitoring the voltage drop across the R_K/ν resistance linking M_j and G_j directly gives the whole injected current in S_i. **c** As long as the measurement contact is always followed by an R_K/ν resistance towards the ground, the voltage drop across this very robust resistance is always yielding an accurate measurement of the impinging current, regardless of the device gates configuration. Here, the device is a simple top gate, but it could be any complicated combination of several gates, as it always boils down to the transmission probabilities of each channel τ_n.

ing to the transmissions determined by the gates voltages configurations (on figure D.2 b, it is a single top gate). In uninterrupted quantum Hall channels, all the voltage drop occur at the ohmic contacts, never within the channels, as beautifully attested by the experiment [214]. Moreover, the measurement contacts are kept floating, consequently, all the current that reaches them can only flow towards the ground via the ν quantum Hall channels thanks to the quantum Hall effect chirality (and also via the input impedance of the pre-amplifier that is however very large $Z_{\text{in}} \approx 100\,\text{M}\Omega \gg R_K$, so that it can safely be neglected). Monitoring the voltage drop across this very stable resistance R_K/ν enables to directly know the current flowing from the source contacts to the drains. Note that this method assumes a negligible resistance of the ohmic contact/2DEG interface, with respect to the pre-amplifier input resistance, which can be directly tested. The amount of current flowing from one source to a drain then gives access to the the transmission coefficient of the device as illustrated in figure D.2 d.

D.3 Determination of the different measurement gains

In general, in our devices, we have several source S_i and measurement M_i contacts. Due to the slight differences between each of the fridge measurement lines' resistance as well as their amplifiers, the measured voltage at the end of each amplification chain might vary slightly from one line to the other. The effective measured voltage at contact M_i is:

$$V_{\text{eff}}^{\text{M}i} = V^{\text{M}i} \times \mathcal{G}_i$$

where $V^{\text{M}i}$ is the actual voltage drop across the R_K/ν resistance and $\mathcal{G}_i$ is the gain of the amplification chain of measurement i. While calibrating the whole amplification chain could be done for each line, it is a long and tedious task that is not necessary for us to deduce the transmission of the device. Effectively, all that is needed is:

- how much current is injected, which does not vary in time for a given excitation voltage and can be calibrated,
- how does this current gets redistributed among all our measurement contacts, which depends on the device configuration (i.e the different gates' voltage).

The injected current from each source can be calibrated when the device is set to 0 transmission for example (as if the gate on figure D.2 c was fully closed), as a consequence we would have for the injected current:

$$\frac{V_{\text{inj}}^{\text{S}_i\rightarrow}}{R_K} = \left.\frac{V_{\text{eff}}^{\text{M}i}/\mathcal{G}_i}{R_K}\right|_{\tau=0}$$

and then, for any gate configuration, one has to recover the full injected current, such

that in terms of the measured quantities, one obtains the following system of equations:

$$\left.\frac{V_{\mathrm{eff}}^{\mathrm{M}_i}}{R_K}\right|_{\tau=0} = \sum_j \frac{\mathcal{G}_i}{\mathcal{G}_j}\frac{V_{\mathrm{eff}}^{\mathrm{M}j}}{R_K}$$

so that it is possible to extract the ratio of gains $\mathcal{G}_i/\mathcal{G}_j$ (note that it is not possible with this technique to get the exact gains individually, but the ratios are enough to fully deduce the transmission coefficients).

E

Sample fabrication

E.1 Air-bridge fabrication review

Building a MZI interferometer necessitates metal bridges to cross the burried 2DEG without affecting its density. Several techniques are known to build air bridges, all imply exposing the bridge's pillars and span locations with different electron doses. The differences lie in the resist(s) layer(s) and their exposure there are three different families:

- the tri-layer technique consisting in coating the sample with low sensitivity PMMA / high-sensitivity MMA / medium-sensitivity PMMA layers. The location of the bridge's span and pillars are then exposed to a base dose with the e-beam, which purpose is to develop only the top two layers. The location of the bridge's pillars is then exposed again to roughly twice the base dose in order to expose the low-sensitivity PMMA bottom layer. Exact doses, acceleration voltage and resist thicknesses can be found in [215,216] and [217] which most probably reveals the secretly kept receipes of the Weizmann Institute as his sample was fabricated there.
- the bi-layer technique uses low-sensitivity PMMA / high-sensitivity MMA or PMMA layers. The span location is exposed to a low dose, while the pillars' are exposed to a larger one. More details are given in [218,219].
- the mono-layer technique uses just a single PMMA or AR-U4000 resist with different exposures for the span and pilars as in [220,221].

In all three cases, resist development is then performed and metal is evaporated and the excess is finally lifted-off.

For this work, the bi-layer technique was chosen, several dose tests were performed in order to determine the optimal dose. A complete overview of the fabrication receipe is given in appendix section E.2

E.2 Sample Fabrication Receipe

Marks

- deoxydazation HCl (37%, 1 vol) / H2O (10 vol) for 10" then rincing H20.
- N2 drying then 2' on hot plate at 95°C
- PMMA 40g/L 4000rpm (4000rpm/s) for 60" then baked 17' on tin hot plate at 170°C
- reflectometry measurement indicates 336nm
- e-beam patterning, base dose 1000µC/cm^2
- development 30" MIBK and 10" IPA.
- metal deposition Ti/Au6 (200/2000 A)
- liftoff trichlo on hot plate at 95°C and acetone rincing

Mesa

- Drying on hot plate at 80°C during 30'.
- Man enduction 4000rpm (4000rpm/s) for 60",
- N2 drying, then bake on hot plate 1' at 95°C.
- reflectometry measurement indicates 665nm
- e-beam patterning with base dose of 450uC/cm2
- development: 20" MIF 826 and 20" H2O (x2)
- thickness 226nm.
- IBE: (clean for 10') then Etch 250V 40° for 4'
- remaining resist thickness on mask 198nm
- man removal: 7' in NaoH 25g/l, then 4' in acetone

Ohmic contacts

- PMMA A6 5000rpm for 60" (acc 3000rpm/s)
- N2 drying then 3' hot plate baked at 170°C
- thickness 385nm.
- e-beam patterning base dose 800µC/cm^2
- development 30" MIBK and 15" IPA and N2 drying.
- deoxydation 30" in HCl (3.7% in H2O), and H2O rincing.
- metal deposition Ni/Au6/Ge/Ni/Au6 (100/100/600/200/1100 A) (with etch before)
- liftoff: trichlo on hot plate at 95°C and acetone rincing

- annealing 1’ at 400°C

Gates

- PMMA A4 4000rpm for 60" (acc 3000rpm/s)
- N2 drying then 1’ hot plate baked at 85°C
- thickness 200nm.
- long bake 1h at 170°C
- e-beam patterning base dose 1000µC/cm^2
- development 45" MIBK and 20" IPA and N2 drying.
- metal deposition: Al 30nm (at 2nm/s)
- liftoff trichlo at 95°C

Air bridges and metal contacts

- PMMA A4 4000rpm for 60" (acc 4000rpm/s)
- N2 drying then 15’ hot plate baked at 170°C
- thickness 210nm.
- MMA 8.5 EL 12 4000rpm for 60" (acc 4000rpm/s)
- thickness 820nm.
- N2 drying then 105’ hot plate baked at 170°C
- e-beam patterning base dose 515µC/cm^2
- development 30" MIBK and 15" IPA and N2 drying.

F

Published papers during this PhD

Macroscopic Electron Quantum Coherence in a Solid-State Circuit

H. Duprez,[1,*] E. Sivre,[1,*] A. Anthore,[1,2] A. Aassime,[1] A. Cavanna,[1] A. Ouerghi,[1] U. Gennser,[1] and F. Pierre[1,†]

[1]*Centre de Nanosciences et de Nanotechnologies (C2N), CNRS, Univ Paris Sud, Université Paris-Saclay, 91120 Palaiseau, France*

[2]*Université de Paris, Univ Paris Diderot, 75013 Paris, France*

(Received 18 December 2018; published 14 May 2019)

The quantum coherence of electronic quasiparticles underpins many of the emerging transport properties of conductors at small scales. Novel electronic implementations of quantum optics devices are now available with perspectives such as "flying-qubit" manipulations. However, electronic quantum interferences in conductors remained up to now limited to propagation paths shorter than 30 μm independent of the material. Here we demonstrate strong electronic quantum interferences after a propagation along two 0.1-mm-long pathways in a circuit. Interferences of visibility as high as 80% and 40% are observed on electronic analogues of the Mach-Zehnder interferometer of, respectively, 24-μm and 0.1-mm arm length, consistently corresponding to a 0.25-mm electronic phase coherence length. While such devices perform best in the integer quantum Hall regime at filling factor 2, the electronic interferences are restricted by the Coulomb interaction between copropagating edge channels. We overcome this limitation by closing the inner channel in micron-scale loops of frozen internal degrees of freedom combined with a loop-closing strategy providing an essential isolation from the environment.

DOI: 10.1103/PhysRevX.9.021030

Subject Areas: Condensed Matter Physics, Mesoscopics, Quantum Physics

I. INTRODUCTION

Ballistic electrons allow for advanced quantum manipulations at the single-electron level in circuits, in the spirit of the manipulation of photons in quantum optics [1–3]. Perspectives notably include a different paradigm for quantum-information processing with a nonlocal architecture based on "flying-qubits" encoded, for example, by the presence or absence of an electron within a propagating wave packet [1,2,4–7]. Electronic edge states topologically protected against disorder constitute promising solid-state platforms. In particular, the emblematic chiral edge channels propagating along a two-dimensional (2D) conductor in the quantum Hall regime are generally considered ideal 1D conductors. Their analogy with light beams, their *in situ* tunability by field effect, and the availability of single-electron emitters were exploited to implement the electronic analogues of optical devices, such as the interferometers of types Fabry-Perot [8], Mach-Zehnder [9], Hanbury-Brown and Twiss [10], and Hong-Ou-Mandel [11]. In contrast to photons, the Coulomb interaction between charged electrons provides a natural correlation mechanism to realize, e.g., CNOT gates [1,2,4,5]. However, the same Coulomb interaction generally entangles the propagating electrons efficiently with numerous degrees of freedom, including the surrounding electrons, which gives rise to quantum decoherence [12] (see Ref. [13] for a notable exception).

In practice, the maximum electron phase coherence length L_ϕ was previously found to reach remarkably similar values at the lowest accessible temperatures in very diverse systems, from diffusive metal ($L_\phi \simeq 20$ μm reported in Ref. [14] at 40 mK) to near ballistic two-dimensional electron gas ($L_\phi \simeq 20$ μm reported in Ref. [15] at 30 mK) and graphene ($L_\phi \simeq 3$–5 μm estimated in Ref. [16] at 260 mK). Along the ballistic quantum Hall edge channels of specific interest for electron quantum optics, $L_\phi \simeq 24$ μm was demonstrated at 20 mK [17] at the most advantageous magnetic field tuning corresponding to filling factor $\nu = 2$ in a Ga(Al)As 2D electron gas. We also point out two promising findings: An important temperature robustness of small conductance oscillations measured across a 6-μm-long Ga(Al)As device, from which a large value of $L_\phi \sim 86$ μm was indirectly inferred [18] and conductance oscillations of very high visibility along a graphene *p-n* junction [19]. Here, we establish a macroscopic electron phase coherence length of 0.25 mm achieved along quantum Hall channels by nanocircuit engineering.

*These authors contributed equally to this work.
†frederic.pierre@c2n.upsaclay.fr

At low temperatures, short-range electron-electron interactions within the *same* chiral edge channel of the integer quantum Hall regime are predicted to increase the electrons' propagation velocity but not to limit their coherence [20,21]. The dominant dephasing mechanism is generally attributed to the interaction between electrons located in *adjacent* edge channels [20,22] (except at $\nu = 1$ and fractional filling factors where the stronger decoherence [23,24] is not clearly understood). This picture is established by complementary signatures including energy transfers [25,26], charge fractionalization [27–29], and Hong-Ou-Mandel characterizations [30]. However, additional dissipative mechanisms yet unidentified were also evidenced experimentally, even in the most canonical $\nu = 2$ case [25–27]. In this work, we demonstrate a circuit design strategy that very efficiently suppresses the essential decoherence mechanisms.

II. NANOENGINEERING THE PHASE COHERENCE LENGTH

The electronic version of the Mach-Zehnder interferometer [MZI, schematically depicted in Fig. 1(a)] essentially consists in a quantum Hall edge channel following two separate paths, and in two quantum point contacts (QPCs) used as tunable beam splitters [9]. The quantum Hall regime is realized in a Ga(Al)As 2D electron gas immersed in a perpendicular magnetic field of 4.3 T corresponding to a filling factor $\nu = 2$, with two copropagating edge channels. The interfering MZI paths involve only the outer edge channel [thick black lines in Fig. 1(a)]. The two beam-splitter QPCs are formed by field effect using split gates [colored orange in Fig. 1(a) with suspended bridges to contact the top parts]. The quantum phase difference between the two paths is proportional to the enclosed magnetic flux. It is here controlled by fine-tuning the lower edge path with the voltage V_{pl} applied to a lateral plunger gate [colored green in Figs. 1(a) and 1(b)]. The quantum interferences are evidenced by sweeping V_{pl} from the resulting oscillations of the transmitted current impinging on the metallic electrode labeled D in Fig. 1(a). Their energy dependence with respect to the bias voltage V_{dc} applied to the source electrode is obtained from a concomitant noise in the transmitted current. The second MZI output is connected to the central metallic electrode (elongated yellow disk in Fig. 1), which is electrically grounded through a suspended bridge. In contrast to previous MZI implementations, our devices include two long surface gates [light gray in Figs. 1(a) and 1(b)] with a particular comb shape with both shafts and teeth placed over the 2D electron gas. This shape is essential for the presently demonstrated strong increase of the electron coherence. As illustrated in Fig. 1(a), these gates can be biased to form inner channel loops along the interfering outer edge channel paths. In order to unambiguously demonstrate and accurately measure very large phase

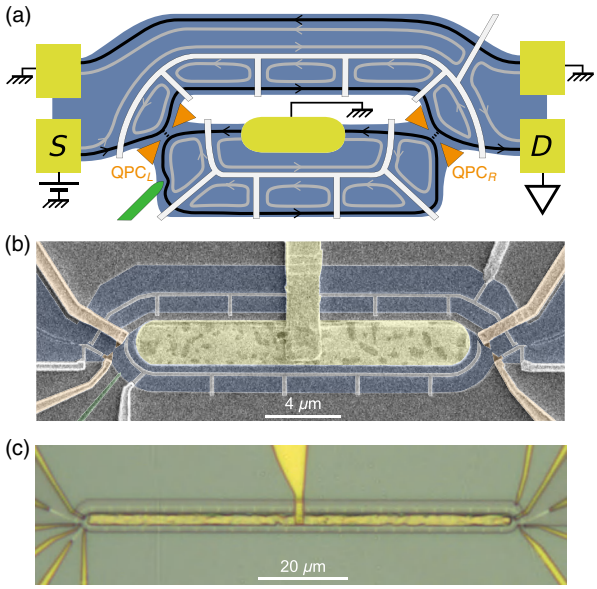

FIG. 1. Nanocircuit engineering of electronic coherence. (a) Sample schematic. Two chiral edge channels (black and gray lines with arrows) propagate along a 2D electron gas (blue) set in the integer quantum Hall regime at filling factor $\nu = 2$. The outer channel (black) follows two separate paths between tunable beam splitters implemented by quantum point contacts (orange), thereby forming a Mach-Zehnder interferometer. The inner edge channel (gray) can be closed into well-separated loops with specific comb-shaped gates (light gray) voltage biased to reflect only this channel. Sweeping the voltage on a lateral plunger gate (green) results in MZI oscillations of the current transmitted from source (S) to detector (D). (b) Colored scanning electron micrograph of the sample with MZI arms of symmetric length $L \simeq 24$ μm. (c) Optical image of the $L \simeq 0.1$ mm MZI. The inner edge channel loops have nominally identical perimeters of 9 μm, except one of 5 μm for the lower left loop of each sample.

coherence lengths, we fabricate two MZIs with extraordinarily long symmetric arms of length $L \simeq 24$ μm [Fig. 1(b)] and 0.1 mm [Fig. 1(c)]. For a straightforward comparison at different L, the two devices are made concurrently (a few millimeters away on the same chip) with identical designs except for the length of the elongated central area and are simultaneously cooled down to 10 mK.

How can L_ϕ be increased? It was initially shown that most of the electrons' energy relaxation can be frozen within the outer edge channel at $\nu = 2$ (along an 8-μm path) by closing into a loop the inner channel [31]. This freezing was explained by the electronic levels' quantization within the loop, which effectively quenches the phase space for inelastic collisions with the inner loop's electrons (for a level spacing larger than the available energy) [31,32]. As inelastic collisions also result in decoherence, a similar approach was subsequently tested on L_ϕ using an electronic MZI [33]. However, the increase in L_ϕ by forming inner channel loops was limited to a factor of 2 [33], relatively

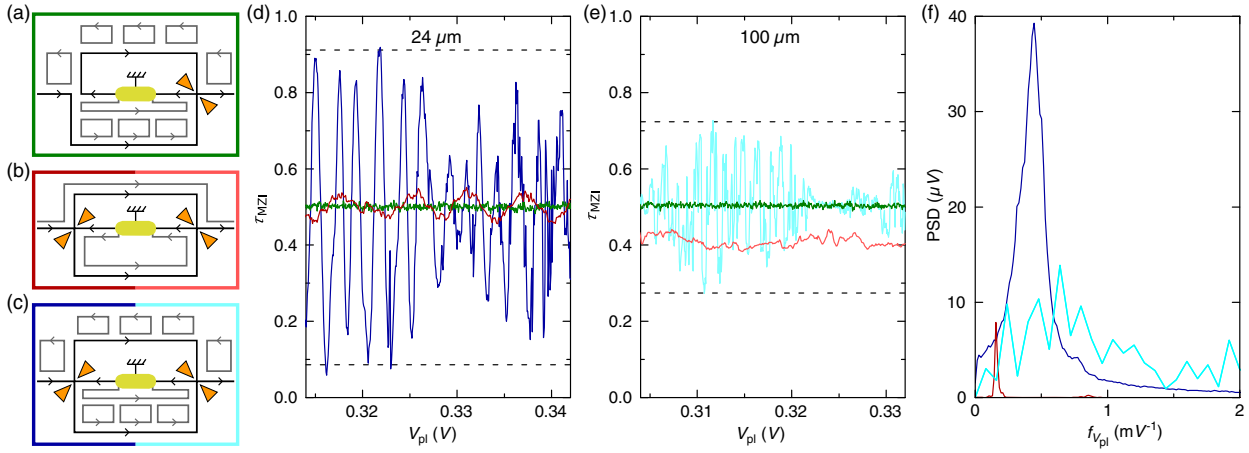

FIG. 2. Quantum oscillations. (a)–(c) Schematics of the different configurations. (d),(e) Continuous lines show versus plunger gate voltage $V_{\rm pl}$, the measured fraction $\tau_{\rm MZI}$ of current transmitted from S to D along the outer channel of the $L \simeq 24$ μm (d) and 0.1 mm (e) MZI [same color as the box enclosing the corresponding schematic in panels (a), (b), or (c); darker shade for the shorter device]. Horizontal dashed lines display the predicted $\tau_{\rm MZI}$ extrema for the same $L_\phi = 0.25$ mm in both MZIs. (f) Continuous lines show the power spectral density of $\tau_{\rm MZI}(V_{\rm pl})$ determined along large $V_{\rm pl}$ sweeps (extending between 50 and 80 mV) measured several times [same color code as in panels (d),(e)]. For the challenging case of $L \simeq 0.1$ mm in configuration (c) (light blue line), the Fourier analysis is restricted to plunger gate-voltage windows exhibiting oscillations larger than 66% of their maximum amplitude.

modest compared to the freezing of energy relaxation. Our conjecture is that the weaker impact on L_ϕ reflects a fundamental design limitation in the MZI implementation of Ref. [33], where an otherwise negligible coupling between two different *outer* edge channels could be mediated by the rigid displacements of the inner loops. These rigid displacements provide an additional mechanism for both decoherence and energy relaxation: Even if the inner loops' electronic degrees of freedom are not excited, the loops' presence can strongly enhance the capacitive coupling between different propagative edge channels adjacent to separate portions of the same loops. The present MZI implementation suppresses this mechanism while preserving a 2D bulk at $\nu = 2$ through a gate design allowing for a much larger separation of the inner loops from additional quantum Hall channels (see Fig. 4 for an illustration, and Sec. II in the Appendix for further discussion).

III. QUANTUM OSCILLATIONS VERSUS LOOP FORMATION

We present in Fig. 2 illustrative MZI oscillations versus plunger gate voltage $V_{\rm pl}$ (a positive bias of $+0.35$ V is applied during cooldown). The displayed $\tau_{\rm MZI}$ corresponds to the transmission probability across the MZI from source S to detector D. It is given by the fraction measured at the electrode D of the current injected into the outer edge channel at the electrode S. The two $L \simeq 24$ μm and 0.1 mm MZIs are each tuned in three different configurations [Figs. 2(a)–2(c)]. The green lines in Figs. 2(d) and 2(e) are data obtained with both devices set in the configuration shown in Fig. 2(a). Their flatness demonstrates directly in the presence of inner channel loops the absence of $\tau_{\rm MZI}$ oscillations when all the transmitted current goes through a single MZI arm (the lower arm; in this specific case $\tau_{\rm MZI} = \tau^R_{\rm QPC}$ since $\tau^L_{\rm QPC} = 1$). The red and blue lines in Figs. 2(d) and 2(e) are obtained with both QPC beam splitters set to half transmission probability for the outer edge channel ($\tau^L_{\rm QPC} \simeq \tau^R_{\rm QPC} \simeq 0.5$, the inner edge channel being always fully reflected at the QPCs) in the configurations illustrated in Figs. 2(b) and 2(c). In the conventional MZI configuration [no loops, Fig. 2(b)], small oscillations of period 6.4 mV are observed only on the $L \simeq 24$ μm device [dark red lines in Figs. 2(d) and 2(f)]. Their visibility $\mathcal{V} \equiv (\tau^{\rm max}_{\rm MZI} - \tau^{\rm min}_{\rm MZI})/(\tau^{\rm max}_{\rm MZI} + \tau^{\rm min}_{\rm MZI}) \approx 6\%$ corresponds to a typical phase coherence length value of $L_\phi \simeq 17$ μm (despite a relatively low temperature $T \simeq 10$ mK) obtained from the standard relationship for a symmetric MZI:

$$\mathcal{V} = 4\sqrt{\tau^R_{\rm QPC}(1-\tau^R_{\rm QPC})\tau^L_{\rm QPC}(1-\tau^L_{\rm QPC})}\,\exp\left(\frac{-2L}{L_\phi}\right), \quad (1)$$

which assumes a perfect absorption of the outer edge channel by the central metallic contact connected to electrical ground (separately checked; see the Appendix). In contrast, for the $L \simeq 0.1$ mm device, no oscillations can be detected without inner channel loops as expected from Eq. (1) ($\mathcal{V} \approx 10^{-5}$ calculated with $L = 0.1$ mm and $L_\phi = 17$ μm). Instead, we observe a slowly evolving $\tau_{\rm MZI}$, which is markedly below 0.5. This low mean value reflects the tunneling of electrons from outer to inner edge channels, which becomes significant over

such a long propagation distance. As a result, a larger (smaller) fraction of the current injected into the outer edge channel is absorbed by the grounded central Ohmic contact (detected at D). Specific measurements of the tunneling between copropagating channels are discussed in the Appendix (Sec. V).

With inner channel loops formed [Fig. 2(c)], high-amplitude oscillations of maximum visibility $\mathcal{V} \approx 80\%$ and 40% are observed for the $L \simeq 24$ μm and 0.1 mm MZIs, respectively. Their sinusoidal shape is, however, perturbed by jumps as well as amplitude modulations, which are attributed to fluctuators such as moving charges in the MZI vicinity. A sudden variation in surrounding charges will indeed appear as a phase jump. In contrast, relatively rapid fluctuations with respect to the experimental integration time (approximately 1 s) but slow with respect to the electron quantum coherence time will artificially reduce the amplitude of MZI oscillations, below their intrinsic value limited by L_ϕ according to Eq. (1). As illustrated with the emblematic single-electron transistor, individual charge fluctuators are usually influenced by surrounding gate voltages. Accordingly, we observe modulations of the phase jump density and of the amplitude of oscillations with gate voltages. Note that two sources of moving charges are specific to the present MZI implementation with inner channel loops: (i) the voltage bias applied to the very long surface gates used to form the loops and (ii) jumps in the number of electrons within each of the many inner channel loops (from the possible tunneling of electrons between outer channel and inner loops). We now further establish by a train of evidence that the large oscillations observed with inner channel loops result from the quantum interferences between the two MZI paths and that their maximum visibility accurately reflects L_ϕ.

IV. OSCILLATION CHARACTERIZATION

First, a well-defined plunger gate-voltage period of 2.2 mV is observed for the smaller $L \simeq 24$ μm MZI, as directly evidenced from the power spectral density [dark blue lines in Figs. 2(d) and 2(f)]. A compatible but broader oscillation periodicity can also be perceived for the $L \simeq 0.1$ mm MZI but only if the FFT analysis is restricted to plunger gate-voltage windows where the oscillation amplitude is relatively large [light blue line in Fig. 2(f)]. The period for $L \simeq 24$ μm with loops is shorter than without, as expected from the stronger influence of the plunger gate voltage. This reduction is a consequence of the quenched screening from isolated inner channel loops hosting a discrete number of electrons as compared to a copropagative inner channel. It also implies that any nearby moving charges will have a stronger impact on the MZI quantum phase.

Second, as shown in Fig. 3(a), the maximum oscillation visibility (highest symbols) follows the hallmark MZI signature $\sqrt{\tau^L_{\rm QPC}(1-\tau^L_{\rm QPC})}$ (continuous lines) when varying the outer edge channel transmission probability across the left QPC beam splitter $\tau^L_{\rm QPC}$. For this purpose, we measure $\tau_{\rm MZI}(V_{\rm pl})$ over many periods on both devices and for various settings of $\tau^L_{\rm QPC}$ at fixed $\tau^R_{\rm QPC} \simeq 0.5$ (see the Appendix). Each symbol in Fig. 3(a) (full and open

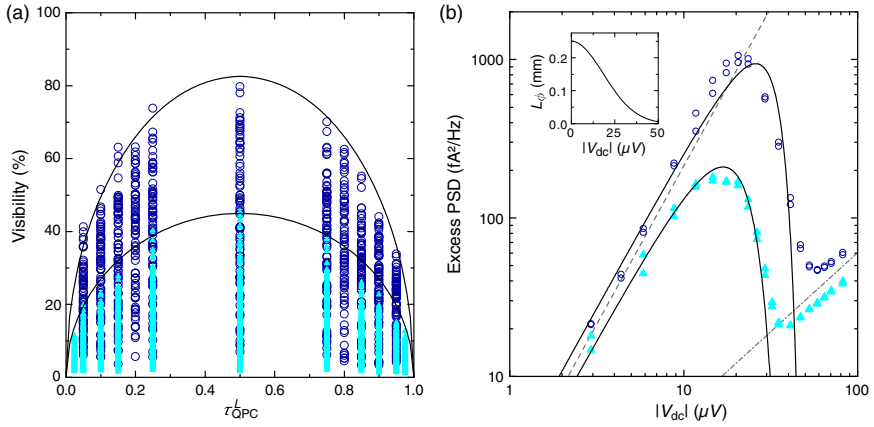

FIG. 3. Beam-splitter and bias-voltage tunings. Open (full) symbols are data points obtained on the $L \simeq 24(100)$ μm MZI. (a) The local quantum oscillations' visibility in the presence of inner channel loops [Fig. 2(c)] separately extracted period per period along large $V_{\rm pl}$ sweeps is displayed as symbols versus the transmission probability $\tau^L_{\rm QPC}$ of the outer channel across the left QPC (at fixed $\tau^R_{\rm QPC} \simeq 0.5$). Continuous lines are Eq. (1)'s predictions for $L_\phi = 0.25$ mm with $L = 24$ μm or 0.1 mm. (b) The excess power spectral density of temporal fluctuations in the transmitted MZI current with respect to zero dc bias and averaged in $V_{\rm pl}$ is shown versus source (S) dc voltage $V_{\rm dc}$. The gray straight lines represent a quadratic (dashed) and linear (dash-dotted) increase. The black continuous lines in the main panel display the noise contribution from phase fluctuations calculated with $L_\phi(V_{\rm dc}) = (0.25\ {\rm mm}) \times \exp[-(V_{\rm dc}/26\ \mu{\rm V})^2]$ (shown in the inset).

corresponding to the $L \simeq 24$ μm and 0.1 mm MZIs, respectively) displays the "locally" extracted visibility of the oscillations obtained by analyzing a restricted plunger gate-voltage window of one period (2.2 mV). The close agreement between the highest data points and MZI expectations confirms that the observed oscillations result from the two-path quantum interferences.

Third, we find a quantitative data or theory agreement with the *same* $L_\phi \approx 0.25$ mm for both devices, despite a factor of 4 in their size. The continuous lines in Fig. 3(a) are calculated using Eq. (1) with $L_\phi = 0.25$ mm, the corresponding MZI length $L = 24$ μm or 0.1 mm, and $\tau^R_{\mathrm{QPC}} = 0.5$. This agreement provides strong evidence that the measured maximum "local" visibility closely captures the intrinsic MZI visibility determined solely by L_ϕ (note that L_ϕ will otherwise be underestimated).

Fourth, as shown in Fig. 3(b), out-of-equilibrium measurements of the transmitted current noise around 0.86 MHz further confirm the presence of MZI interferences accompanied by phase fluctuations and allow probing the energy dependence of L_ϕ. The displayed data points represent measurements of the excess power spectral density of the current impinging on the electrode D versus the dc bias voltage V_{dc} applied to the source electrode S. MZI phase variations, such as those produced by nearby charge fluctuators, are expected to manifest as a quadratic increase of the noise power at low V_{dc} (see the Appendix and Ref. [34]), as we experimentally observe. At larger bias, the generally expected reduction of L_ϕ also progressively diminishes the influence of the quantum phase and, consequently, the current noise induced by phase fluctuations. Experimentally, such a collapse is observed and can be accounted for using the *same* $L_\phi(V_{\mathrm{dc}})$ for both devices: The two black continuous lines (main panel) are calculations based on Eq. (1) (see the Appendix, Eq. (A2)] using the empirically determined $L_\phi = (0.25\ \mathrm{mm}) \times \exp[-(V_{\mathrm{dc}}/26\ \mu\mathrm{V})^2]$ (shown in the inset). Ultimately, a linear noise increase is recovered as expected for the shot-noise contribution [34] (see the Appendix).

V. DISCUSSION

The large phase coherence length presently achieved provides information for the design of novel quantum Hall devices. It sets an upper bound to possibly relevant decoherence mechanisms along the quantum Hall edges in addition to the dominant interchannel coupling and narrows down the mechanisms for a frequently observed but still mysterious additional dissipation [25–27,35].

We establish that nearby metallic gates are completely compatible with large phase coherence lengths, despite the presence of many diffusive electrons. Note their beneficial screening of the long-range part of Coulomb interaction (to approximately 3.5 μm, the loop-gates' period, whether the loops are formed or not), which could otherwise provide an effective decoherence mechanism [36–39] as well as an unwanted coupling to spurious low-energy modes and distant channels [35,40,41]. In practice, a strong capacitive shortcut (100 nF) is included at the low-temperature end of the electrical lines controlling the gates of our samples in order to further suppress both extrinsic and thermal noise sources.

We also find that the additional neutral modes predicted for a realistic smooth confinement potential at the edge [42–44] can essentially be ignored. Either these neutral modes are missing in the outer channel along our etched-defined edges or they are very weakly coupled to the usual charge mode of the same channel. This finding is consistent with thermal conductance measurements across narrow constrictions perfectly transmitting one or several quantum Hall channels at integer bulk filling factors, where the extra heat transfer that would be expected from additional edge modes is not observed [45–47].

Finally, we mention that the two-dimensional quantum Hall bulk does not provide here a substantial path to quantum decoherence, at least when broken into small areas of a few micron squares (within the inner channel loops) and with the long-range part of Coulomb interaction screened by metallic gates. This finding contrasts with the observations of an unexpected heat flow away from the edge at lower filling factors [48–50] and of a long-distance capacitive coupling across the two-dimensional bulk [40,41].

VI. CONCLUSION

We demonstrate that the electron quantum coherence in solid-state circuits can be extended to the macroscopic scale by strongly suppressing through circuit nanoengineering the dominant decoherence mechanism. The present implementation on quantum Hall edge channels is particularly well suited for the coherent control and long-distance entanglement of propagative electrons. Future optimizations include the understanding and suppression of the slow electron phase fluctuations here often, although not systematically, observed. Our work gives access to electron quantum optics devices of a higher complexity level, in line with the direction taken by this field of research [1–3,18]. More generally, increasing the electron phase coherence is essential to progress toward functional quantum devices involving multiple quantum manipulations, such as information processing with electronic flying qubits.

ACKNOWLEDGMENTS

This work is supported by the French RENATECH network, the national French program "Investissements d'Avenir" (Labex NanoSaclay, Grant No. ANR-10-LABX-0035), and the French National Research Agency (project QuTherm, Grant No. ANR-16-CE30-0010-01).

E. S. and H. D. performed the experiment and analyzed the data with inputs from A. Aa., A. An., and F. P.; F. P.

fabricated the sample with input from E. S. and H. D.; A. C., A. O., U. G. grew the 2DEG; F. P. led the project and wrote the manuscript with input from A. Aa., A. An., E. S., H. D. and U. G.; H. D. and E. S. contributed equally to this work.

APPENDIX: EXPERIMENTAL METHODS

1. Samples

Both samples are made of the same Ga(Al)As heterojunction hosting a two-dimensional electron gas of mobility 10^6 cm^2 V^{-1} s^{-1} and density $2.5 10^{11}$ cm^{-2} located 105 nm underneath the surface. They are nanofabricated by *e*-beam lithography, dry etching, and metallic deposition. The central metallic electrode (nickel [30 nm], gold [120 nm], and germanium [60 nm]) forms an Ohmic contact with the 2DEG obtained by thermal annealing (at 440 °C for 50 s) and is set to electrical ground through a suspended bridge. The two arms of each MZI are designed to be as symmetric as possible, such that the thermal smearing of the visibility induced by an asymmetry remains negligible by a large margin as previously observed [17,33]. The elongated shape of the central area is chosen to limit the overall magnetic flux enclosed between the two arms and, hence, the effect of environmental magnetic noise (e.g., from the pulse tube vibrations) on the particularly sensitive MZI phase in these very large devices. Note that a positive bias voltage of +0.35 V is applied to all used gates during cooldown. This is a widespread procedure in Ga(Al)As devices to reduce the charge noise induced by biasing the gates, although it is probably not essential here due to the relatively low bias voltages used to form inner channel loops.

2. Loop gate design

Figure 4 recapitulates the different kinds of inner channel loops in the energy-relaxation experiment [31] [one inner loop enclosed only by the outer channel; see Fig. 4(a)] in the first MZI implementation [33] [inner loops enclosed by a metallic gate, the MZI outer channel, and another counterpropagating outer channel; see Fig. 4(b)] and in the present MZI implementation [inner loops enclosed by a metallic gate and the MZI outer channel; see Fig. 4(c)]. Now focusing on the present implementation, the gates' width of 200 nm reflects a compromise between the separation with additional quantum Hall channels on the other side of the gates, which should be sufficiently large to result in a negligible coupling, and the wish to limit the $\nu = 1$ area underneath the gates, as very weak interferences are often observed if the whole 2D bulk is set to $\nu = 1$ (either by tuning B without gates or using a broad top gate fully covering the 2D bulk; see, e.g., Ref. [24]). The distance between the inner channel loops and the propagative (inner) quantum Hall channel on the other side of the gates (opposite the MZI outer channel) should therefore be larger than 200 nm. This is more than 1 order of magnitude larger than the narrow incompressible strip normally separating adjacent edge channels (typically 10 nm [51]). The loops' perimeter should also be chosen small enough such that the separation between the quantized electronic levels is larger than the available energy of approximately $k_B T$. Assuming a typical drift velocity between 10^4 and 10^5 m/s along the sample edges, we find that the 9-μm loop perimeter corresponds to a level spacing within 4.6 and 46 μeV, always larger than the thermal energy ($3k_B T \simeq 2.6$ μeV at 10 mK) and comparable to the characteristic 26-μV dc bias voltage over which $L_\phi(V_{\rm dc})$ is found to decrease [Fig. 3(b)]. Finally, the gates are designed elongated to minimize their overlap with the outer MZI edge channel, as at these locations their capacitive coupling is maximal and the lateral edge confinement is modified. Note also that one should be particularly careful about the electrical noise introduced by the measurement lines connected to the very long gates used to form the inner channel loops. These gates are indeed much more strongly coupled to the MZI phase than typical lateral plunger gates due to their very long size and because the inner loop efficiently mediates the capacitive coupling between the metallic gate and the MZI outer edge channel.

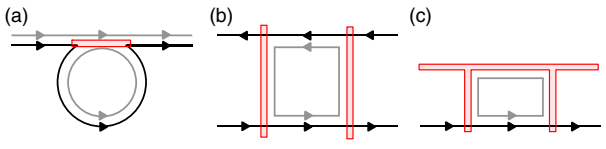

FIG. 4. Loop design. Inner loop design in previous energy-relaxation experiment [31] (a), previous MZI experiment [33], (b) and in the present implementation (c). The outer (inner) edge channel is represented by a black (gray) line. A schematic of the gates used to reflect the inner edge channel is displayed in red.

3. Experimental setup

The two simultaneously cooled devices are thermally anchored to the mixing chamber of a cryo-free dilution refrigerator. Electrical lines connected to the samples include multiple filters and thermalization stages. Note the important RC filter (200 kΩ, 100 nF) implemented at base temperature on the lines connected to the gates, including the long gates used to form the inner channel loops. Spurious high-frequency radiation is screened by two shields at base temperature. The fraction of transmitted current $\tau_{\rm MZI}$ is measured with lock-ins at a frequency below 200 Hz and using an effective integration time close to 1 s per point (corresponding to equivalent noise bandwidth of 0.8 Hz). The power spectral density of temporal current fluctuations is measured over a much larger bandwidth of 180 kHz around 0.86 MHz, using a homemade cryogenic amplifier and a tank circuit based on a superconducting coil. The temperature of electrons in the devices is extracted

from the quantum shot noise across a quantum point contact (the right beam splitter QPC of the $L \simeq 24$ μm MZI set to $\tau^R_{\rm QPC} \simeq 0.5$). See Ref. [52] for further details on the same experimental setup.

4. Central Ohmic contacts characterization

The quality of the grounded central Ohmic contact is characterized by the ratio of reflected to impinging current. Ideally, there should be no reflected current. In practice, if the impinging current is carried only by the outer edge channel (used for the interferometer), the reflected current is found to be negligible for both devices (below 1%). If the impinging current is carried by both the inner and outer edge channels, we find a reflected current in the range of 11%–21% corresponding to a 22%–42% reflection of the inner edge channel from the central Ohmic contact of the $L \simeq 24$ μm paths' MZI, whereas for the $L \simeq 0.1$ mm MZI, the reflected current remains essentially negligible (below 1%). Note that a good Ohmic contact with the outer channel is assumed in Eq. (1) (an imperfect contact will further limit the amplitude of MZI oscillations).

5. Tunneling between inner and outer channels

Tunneling of electrons between adjacent copropagating channels is usually negligible at filling factor $\nu = 2$. However, the propagation distances in the present devices can be considerable. Following standard procedures [53], we determine the electron interchannel tunneling along the MZI arms between the two QPC beam splitters when the inner edge channel is not formed into small loops. Note that the tunneling of electrons in the presence of small inner channel loops is expected to be much smaller because of the electronic level quantization within the loops and because of the Coulomb blockade of tunneling into (nearly) isolated islands (although this tunneling cannot be measured because there is no dc current toward closed loops). The tunneling between copropagative inner and outer edge channels is obtained by applying a small bias selectively on one of the two channels and by measuring at the end of the path the current in the other channel. We find that the tunneling remains small for the $L \simeq 24$ μm MZI [between 2.5% and 5% (approximately 0%) of the injected current is detected on the second channel after propagating along the lower (upper) MZI arm]. The tunneling is more important for the $L \simeq 0.1$ mm MZI [between 30% and 48% (between 10% and 26%) of the injected current is detected on the second channel after propagating along the lower (upper) MZI path].

6. Cross-talk characterization

Changing a gate voltage also slightly influences the other nearby gates. We take into account this small capacitive cross-talk correction on the beam-splitter quantum point contacts (of at most 6% attained for the lateral plunger gate effect on the nearby left QPC).

7. Formation of inner channel loops

The comb-shaped gates of homogeneous width (200 nm) are polarized with a positive voltage of +0.35 V during the cooldown from room temperature. A broad gate-voltage window is found to fully reflect the inner quantum Hall channel while completely letting through the outer channel (with a minimal common window from 0 to 0.13 V that applies simultaneously to each arm of both devices). Such a behavior is usually observed on similar 2DEGs, thanks to the large energy separation between the two lowest Landau levels at filling factor $\nu = 2$. Note that the results corresponding to closed inner channel loops that we present in the manuscript are not specific to a precise gate-voltage setting (chosen within the minimal common window) but representative of the general behavior observed when the inner edge channel loops are completely closed while the outer edge channel is fully propagative.

8. Visibility of conductance oscillations versus QPC transmission

Here we provide more details on the procedure followed to extract the oscillations visibility data displayed in Fig. 3(a). We perform relatively large plunger gate-voltage sweeps of 50 mV corresponding to approximately 21 periods (with a step of 50 μV corresponding to 1/46 of a period) and repeat several times the same sweep (twice for the $L \simeq 24$ μm MZI, 14 times for the more challenging $L \simeq 0.1$ mm MZI). Each sweep is then decomposed into one-period intervals with half a period of overlap between consecutive intervals, and a local visibility of the oscillations in $\tau_{\rm MZI}$ is extracted from $\mathcal{V} \equiv (\tau^{\rm max}_{\rm MZI} - \tau^{\rm min}_{\rm MZI})/(\tau^{\rm max}_{\rm MZI} + \tau^{\rm min}_{\rm MZI})$ in each of these intervals. The symbols in Fig. 3(a) display the many different values of $\mathcal{V}$ obtained by this procedure.

9. Temporal noise spectral density

Here we provide more details on the noise data and calculations displayed in Fig. 3(b). The data points represent the excess power spectral density of the current detected on electrode D [see Fig. 1(a)], i.e., the total noise from which is subtracted the equilibrium noise offset at $V_{\rm dc} = 0$ (that includes the contribution of the amplification chain). To make sure that the noise dependence in the MZI quantum phase is fully averaged out, the displayed data represent the average of many noise measurements equally distributed in a range of the plunger gate voltage corresponding to several periods (240 [40] values of $V_{\rm pl}$ distributed over approximately five [2] periods for the $L \simeq 24[100]$ μm MZI). The displayed calculations (continuous lines) include only the contribution of "slow" fluctuations in the MZI quantum phase $\delta\phi(t)$ detected

within a 180-kHz window around 0.86 MHz and not the quantum shot-noise contribution that we further discuss below. From the relationship $\tau_{\mathrm{MZI}}(t) = 0.5\{1 + \mathcal{V}\sin[\langle\phi\rangle + \delta\phi(t)]\}$, it is straightforward to obtain that the resulting noise in the transmitted current is given by [34]

$$\langle I^2_{\delta\phi}\rangle \propto \frac{V^2_{\mathrm{dc}}e^4}{h^2}\mathcal{V}^2, \tag{A1}$$

with h the Planck constant and e the elementary electron charge. At low V_{dc} bias (as long as the oscillation visibility $\mathcal{V}$ is not significantly reduced), one thus expects a quadratic increase. Using the relationship between visibility and phase coherence length given Eq. (1), this expression becomes

$$\langle I^2_{\delta\phi}\rangle \propto \frac{V^2_{\mathrm{dc}}e^4}{h^2}\exp\left(\frac{-4L}{L_\phi}\right). \tag{A2}$$

The calculations displayed as black continuous lines are obtained from Eq. (A2) using for both devices the same empirical expression $L_\phi(V_{\mathrm{dc}}) = 0.25\ \mathrm{mm} \times \exp[-(V_{\mathrm{dc}}/26\ \mu\mathrm{V})^2]$ (displayed in the inset) the corresponding MZI length $L = 24\ \mu$m or 0.1 mm and where the unknown prefactor (depending on the number and coupling strength of the phase noise sources) is considered here as a free parameter for each device. The smaller quantum shot-noise contribution [not included in Eq. (A2)] is linear in V_{dc} and does not rely on the presence of MZI quantum interferences. As expected, if the vanishing current noise results from a quantum decoherence by "fast" phase fluctuations [34] (compared to the electron quantum coherence), the amplitude of the linear noise is found strongly suppressed compared to the naive expectation $\langle I^2\rangle = 2e(V_{\mathrm{dc}}e^2/h)\langle\tau_{\mathrm{MZI}}\rangle(1 - \langle\tau_{\mathrm{MZI}}\rangle)$ by a factor of 4 (6) for the MZI of arm length $L \simeq 24(100)\ \mu$m.

10. Comparison of voltage-bias robustness with and without inner channel loops

In the absence of inner channel loops, the negligible MZI phase noise does not allow us to probe $L_\phi(V_{\mathrm{dc}})$ through the power spectral density of the transmitted current's temporal fluctuations. However, on the $L \simeq 24\ \mu$m MZI where quantum oscillations are visible without loops, it is possible to determine, versus dc voltage bias, their visibility $\mathcal{V}_{\mathrm{diff}}$ in the transmitted differential current $dI_{\mathrm{MZI}}/dV_{\mathrm{dc}}$. The "diff" subscript is introduced here to clearly distinguish between, on the one hand, this usually measured $\mathcal{V}_{\mathrm{diff}}$ and, on the other hand, the visibility $\mathcal{V}$ of oscillations in the total transmitted current I_{MZI} that is probed through noise measurements [Fig. 3(b)]. These two quantities are simply connected by the relation [54]

$$\mathcal{V}_{\mathrm{diff}} = |\mathcal{V} + V_{\mathrm{dc}}\partial\mathcal{V}/\partial V_{\mathrm{dc}}|. \tag{A3}$$

Measurements of $\mathcal{V}_{\mathrm{diff}}(V_{\mathrm{dc}})$ on the $L \simeq 24\ \mu$m MZI without loops are shown in Fig. 5 as open red circles. We find that $\mathcal{V}_{\mathrm{diff}}$ displays a single side lobe with a first minimum at $|V_{\mathrm{dc}}| \simeq 5\ \mu$V and becomes negligible below our experimental resolution at $|V_{\mathrm{dc}}| \gtrsim 15\ \mu$V. The data can be reproduced by the simple single side-lobe expression derived in Ref. [54] assuming a Gaussian phase averaging (continuous line in Fig. 5):

$$\mathcal{V}^{\mathrm{Gaussian}}_{\mathrm{diff}} = \mathcal{V}_0\left|1 - \frac{V^2_{\mathrm{dc}}}{V^2_0}\right|\exp\left(-\frac{V^2_{\mathrm{dc}}}{2V^2_0}\right), \tag{A4}$$

with $\mathcal{V}_0 = 0.06$ the zero bias visibility and $V_0 = 5\ \mu$V the characteristic voltage scale also corresponding to the position of the intermediate minimum. In order to compare the robustness of MZI interferences with and without inner channel loops, we convert the noise data in Fig. 3(b) into the corresponding $\mathcal{V}_{\mathrm{diff}}$. The resulting $\mathcal{V}_{\mathrm{diff}}$ is displayed in Fig. 5 as open dark blue circles and full light blue triangles for, respectively, the $L \simeq 24$ and 100 μm MZI with loops. This conversion first involves the determination of $\mathcal{V}$ from Eq. (A1) (using the measured noise spectral density from which the linear shot-noise contribution observed at large V_{dc} is subtracted). The unknown proportionality coefficient in Eq. (A1) is fixed by adjusting the visibility at low bias with its direct $V_{\mathrm{dc}} \approx 0$ measurement displayed in Fig. 3(a). The resulting $\mathcal{V}$ is then injected into Eq. (A3) to obtain $\mathcal{V}_{\mathrm{diff}}$.

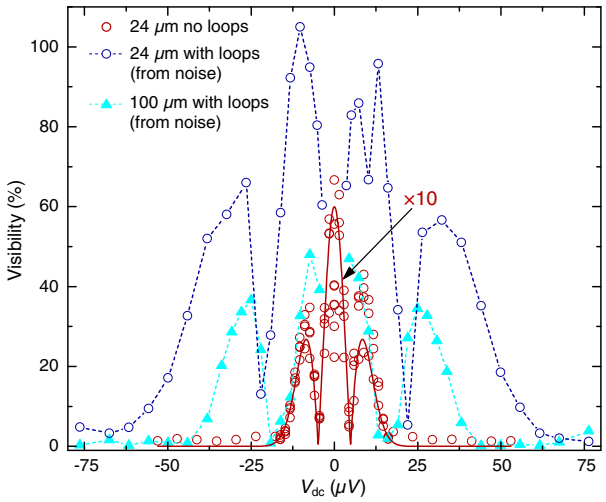

FIG. 5. Out-of-equilibrium visibility in the differential current $\mathcal{V}_{\mathrm{diff}}$. The red circles represent measurements of the visibility of the oscillations in the differential transmitted current across the $L \simeq 24\ \mu$m MZI without inner channel loops as a function of the applied dc bias voltage. The continuous red line is calculated from Eq. (A4) (see text). The dark blue circles (light blue full triangles) connected by dashed lines represent the differential visibility on the $L \simeq 24(100)\ \mu$m MZI with formed inner channel loops, which is extracted from the noise measurements displayed in Fig. 3(b) (see text).

Comparing the two datasets at the same $L \simeq 24$ μm (open circles), we find that the robustness of the MZI visibility with V_{dc} is approximately 4 times larger in the presence of loops (dark blue) than without them (red).

[1] D. Glattli and P. Roulleau, *Levitons for Electron Quantum Optics.*, Phys. Status Solidi B **254**, 1600650 (2017).

[2] C. Bäuerle, D. C. Glattli, T. Meunier, F. Portier, P. Roche, P. Roulleau, S. Takada, and X. Waintal, *Coherent Control of Single Electrons: A Review of Current Progress*, Rep. Prog. Phys. **81**, 056503 (2018).

[3] E. Bocquillon *et al.*, *Electron Quantum Optics in Ballistic Chiral Conductors*, Ann. Phys. (Berlin) **526**, 1 (2014).

[4] A. Bertoni, P. Bordone, R. Brunetti, C. Jacoboni, and S. Reggiani, *Quantum Logic Gates Based on Coherent Electron Transport in Quantum Wires*, Phys. Rev. Lett. **84**, 5912 (2000).

[5] R. Ionicioiu, G. Amaratunga, and F. Udrea, *Quantum Computation with Ballistic Electrons*, Int. J Mod. Phys. B **15**, 125 (2001).

[6] T. Stace, C. Barnes, and G. Milburn, *Mesoscopic One-Way Channels for Quantum State Transfer via the Quantum Hall Effect*, Phys. Rev. Lett. **93**, 126804 (2004).

[7] T. Bautze, C. Sussmeier, S. Takada, C. Groth, T. Meunier, M. Yamamoto, S. Tarucha, X. Waintal, and C. Bauerle, *Theoretical, Numerical, and Experimental Study of a Flying Qubit Electronic Interferometer*, Phys. Rev. B **89**, 125432 (2014).

[8] B. J. van Wees, L. P. Kouwenhoven, C. J. P. M. Harmans, J. G. Williamson, C. E. Timmering, M. E. I. Broekaart, C. T. Foxon, and J. J. Harris, *Observation of Zero-Dimensional States in a One-Dimensional Electron Interferometer*, Phys. Rev. Lett. **62**, 2523 (1989).

[9] Y. Ji, Y. Chung, D. Sprinzak, M. Heiblum, D. Mahalu, and H. Shtrikman, *An Electronic Mach-Zehnder Interferometer*, Nature (London) **422**, 415 (2003).

[10] I. Neder, N. Ofek, Y. Chung, M. Heiblum, D. Mahalu, and V. Umansky, *Interference between Two Indistinguishable Electrons from Independent Sources*, Nature (London) **448**, 333 (2007).

[11] E. Bocquillon, V. Freulon, J.-M. Berroir, P. Degiovanni, B. Placais, A. Cavanna, Y. Jin, and G. Fève, *Coherence and Indistinguishability of Single Electrons Emitted by Independent Sources*, Science **339**, 1054 (2013).

[12] Y. Nazarov and Y. Blanter, *Quantum Transport* (Cambridge University Press, Cambridge, England, 2009).

[13] H. Duprez *et al.*, *Transferring the Quantum State of Electrons across a Fermi Sea with Coulomb Interaction*, arXiv:1902.07569.

[14] F. Pierre, A. B. Gougam, A. Anthore, H. Pothier, D. Esteve, and N. O. Birge, *Dephasing of Electrons in Mesoscopic Metal Wires*, Phys. Rev. B **68**, 085413 (2003).

[15] Y. Niimi, Y. Baines, T. Capron, D. Mailly, F. Y. Lo, A. D. Wieck, T. Meunier, L. Saminadayar, and C. Bauerle, *Quantum Coherence at Low Temperatures in Mesoscopic Systems: Effect of Disorder*, Phys. Rev. B **81**, 245306 (2010).

[16] F. Miao, S. Wijeratne, Y. Zhang, U. C. Coskun, W. Bao, and C. N. Lau, *Phase-Coherent Transport in Graphene Quantum Billiards*, Science **317**, 1530 (2007).

[17] P. Roulleau, F. Portier, D. C. Glattli, P. Roche, A. Cavanna, G. Faini, U. Gennser, and D. Mailly, *Direct Measurement of the Coherence Length of Edge States in the Integer Quantum Hall Regime*, Phys. Rev. Lett. **100**, 126802 (2008).

[18] M. Yamamoto, S. Takada, C. Bäuerle, K. Watanabe, A. D. Wieck, and S. Tarucha, *Electrical Control of a Solid-State Flying Qubit*, Nat. Nanotechnol. **7**, 247 (2012).

[19] D. Wei, T. van der Sar, J. D. Sanchez-Yamagishi, K. Watanabe, T. Taniguchi, P. Jarillo-Herrero, B. I. Halperin, and A. Yacoby, *Mach-Zehnder Interferometry Using Spin- and Valley-Polarized Quantum Hall Edge States in Graphene*, Sci. Adv. **3**, e1700600 (2017).

[20] I. P. Levkivskyi and E. V. Sukhorukov, *Dephasing in the Electronic Mach-Zehnder Interferometer at Filling Factor* $\nu = 2$, Phys. Rev. B **78**, 045322 (2008).

[21] T. Giamarchi, *Quantum Physics in One Dimension* (Oxford University Press, New York, 2003).

[22] P. Roulleau, F. Portier, P. Roche, A. Cavanna, G. Faini, U. Gennser, and D. Mailly, *Noise Dephasing in Edge States of the Integer Quantum Hall Regime*, Phys. Rev. Lett. **101**, 186803 (2008).

[23] L. V. Litvin, A. Helzel, H.-P. Tranitz, W. Wegscheider, and C. Strunk, *Edge-Channel Interference Controlled by Landau Level Filling.*, Phys. Rev. B **78**, 075303 (2008).

[24] I. Gurman, R. Sabo, M. Heiblum, V. Umansky, and D. Mahalu, *Dephasing of an Electronic Two-Path Interferometer*, Phys. Rev. B **93**, 121412(R) (2016).

[25] H. le Sueur, C. Altimiras, U. Gennser, A. Cavanna, D. Mailly, and F. Pierre, *Energy Relaxation in the Integer Quantum Hall Regime*, Phys. Rev. Lett. **105**, 056803 (2010).

[26] K. Itoh, R. Nakazawa, T. Ota, M. Hashisaka, K. Muraki, and T. Fujisawa, *Signatures of a Nonthermal Metastable State in Copropagating Quantum Hall Edge Channels*, Phys. Rev. Lett. **120**, 197701 (2018).

[27] E. Bocquillon, V. Freulon, J.-M. Berroir, P. Degiovanni, B. Plaçais, A. Cavanna, Y. Jin, and G. Fève, *Separation of Neutral and Charge Modes in One-Dimensional Chiral Edge Channels*, Nat. Commun. **4**, 1839 (2013).

[28] H. Inoue, A. Grivnin, N. Ofek, I. Neder, M. Heiblum, V. Umansky, and D. Mahalu, *Charge Fractionalization in the Integer Quantum Hall Effect*, Phys. Rev. Lett. **112**, 166801 (2014).

[29] M. Hashisaka, N. Hiyama, T. Akiho, K. Muraki, and T. Fujisawa, *Waveform Measurement of Charge- and Spin-Density Wavepackets in a Chiral Tomonaga-Luttinger Liquid*, Nat. Phys. **13**, 559 (2017).

[30] A. Marguerite, C. Cabart, C. Wahl, B. Roussel, V. Freulon, D. Ferraro, C. Grenier, J. M. Berroir, B. Placais, T. Jonckheere *et al.*, *Decoherence and Relaxation of a Single Electron in a One-Dimensional Conductor*, Phys. Rev. B **94**, 115311 (2016).

[31] C. Altimiras, H. le Sueur, U. Gennser, A. Cavanna, D. Mailly, and F. Pierre, *Tuning Energy Relaxation along Quantum Hall Channels*, Phys. Rev. Lett. **105**, 226804 (2010).

[32] C. Cabart, B. Roussel, G. Fève, and P. Degiovanni, *Taming Electronic Decoherence in 1D Chiral Ballistic Quantum Conductors*, Phys. Rev. B **98**, 155302 (2018).
[33] P. A. Huynh, F. Portier, H. le Sueur, G. Faini, U. Gennser, D. Mailly, F. Pierre, W. Wegscheider, and P. Roche, *Quantum Coherence Engineering in the Integer Quantum Hall Regime*, Phys. Rev. Lett. **108**, 256802 (2012).
[34] F. Marquardt and C. Bruder, *Effects of Dephasing on Shot Noise in an Electronic Mach-Zehnder Interferometer*, Phys. Rev. B **70**, 125305 (2004).
[35] T. Krähenmann *et al.*, *Auger-Spectroscopy in Quantum Hall Edge Channels: A Possible Resolution to the Missing Energy Problem*, arXiv:1902.10065.
[36] E. Sukhorukov and V. Cheianov, *Resonant Dephasing in the Electronic Mach-Zehnder Interferometer*, Phys. Rev. Lett. **99**, 156801 (2007).
[37] J. Chalker, Y. Gefen, and M. Veillette, *Decoherence and Interactions in an Electronic Mach-Zehnder Interferometer*, Phys. Rev. B **76**, 085320 (2007).
[38] D. Kovrizhin and J. Chalker, *Multiparticle Interference in Electronic Mach-Zehnder Interferometers*, Phys. Rev. B **81**, 155318 (2010).
[39] M. Schneider, D. Bagrets, and A. Mirlin, *Theory of the Nonequilibrium Electronic Mach-Zehnder Interferometer.*, Phys. Rev. B **84**, 075401 (2011).
[40] M. Hashisaka, K. Washio, H. Kamata, K. Muraki, and T. Fujisawa, *Distributed Electrochemical Capacitance Evidenced in High-Frequency Admittance Measurements on a Quantum Hall Device*, Phys. Rev. B **85**, 155424 (2012).
[41] N.-H. Tu, M. Hashisaka, T. Ota, Y. Sekine, K. Muraki, T. Fujisawa, and N. Kumada, *Coupling between Quantum Hall Edge Channels on Opposite Sides of a Hall Bar*, Solid State Commun. **283**, 32 (2018).
[42] A. MacDonald, S. Yang, and M. Johnson, *Quantum Dots in Strong Magnetic Fields: Stability Criteria for the Maximum Density Droplet*, Aust. J. Phys. **46**, 345 (1993).
[43] C. Chamon and X. Wen, *Sharp and Smooth Boundaries of Quantum Hall Liquids*, Phys. Rev. B **49**, 8227 (1994).
[44] I. Aleiner and L. Glazman, *Novel Edge Excitations of Two-Dimensional Electron Liquid in a Magnetic Field*, Phys. Rev. Lett. **72**, 2935 (1994).
[45] S. Jezouin, F. D. Parmentier, A. Anthore, U. Gennser, A. Cavanna, Y. Jin, and F. Pierre, *Quantum Limit of Heat Flow Across a Single Electronic Channel*, Science **342**, 601 (2013).
[46] M. Banerjee, M. Heiblum, A. Rosenblatt, Y. Oreg, D. E. Feldman, A. Stern, and V. Umansky, *Observed Quantization of Anyonic Heat Flow*, Nature (London) **545**, 75 (2017).
[47] E. Sivre, A. Anthore, F. D. Parmentier, A. Cavanna, U. Gennser, A. Ouerghi, Y. Jin, and F. Pierre, *Heat Coulomb Blockade of One Ballistic Channel*, Nat. Phys. **14**, 145 (2018).
[48] C. Altimiras, H. le Sueur, U. Gennser, A. Anthore, A. Cavanna, D. Mailly, and F. Pierre, *Chargeless Heat Transport in the Fractional Quantum Hall Regime*, Phys. Rev. Lett. **109**, 026803 (2012).
[49] V. Venkatachalam, S. Hart, L. Pfeiffer, K. West, and A. Yacoby, *Local Thermometry of Neutral Modes on the Quantum Hall Edge*, Nat. Phys. **8**, 676 (2012).
[50] H. Inoue, A. Grivnin, Y. Ronen, M. Heiblum, V. Umansky, and D. Mahalu, *Proliferation of Neutral Modes in Fractional Quantum Hall States*, Nat. Commun. **5**, 4067 (2014).
[51] D. B. Chklovskii, B. I. Shklovskii, and L. I. Glazman, *Electrostatics of Edge Channels*, Phys. Rev. B **46**, 4026 (1992).
[52] Z. Iftikhar, A. Anthore, S. Jezouin, F. D. Parmentier, Y. Jin, A. Cavanna, A. Ouerghi, U. Gennser, and F. Pierre, *Primary Thermometry Triad at 6 mK in Mesoscopic Circuits*, Nat. Commun. **7**, 12908 (2016).
[53] B. van Wees, E. M. M. Willems, C. J. P. M. Harmans, C. W. J Beenakker, H. van Houten, J. G. Williamson, C. T. Foxon, and J. J. Harris, *Anomalous Integer Quantum Hall Effect in the Ballistic Regime with Quantum Point Contacts*, Phys. Rev. Lett. **62**, 1181 (1989).
[54] P. Roulleau, F. Portier, D. C. Glattli, P. Roche, A. Cavanna, G. Faini, U. Gennser, and D. Mailly, *Finite Bias Visibility of the Electronic Mach-Zehnder Interferometer*, Phys. Rev. B **76**, 161309(R) (2007).

MESOSCOPIC PHYSICS

Transmitting the quantum state of electrons across a metallic island with Coulomb interaction

H. Duprez[1]*, E. Sivre[1]*, A. Anthore[1,2], A. Aassime[1], A. Cavanna[1], U. Gennser[1], F. Pierre[1]†

The Coulomb interaction generally limits the quantum propagation of electrons. However, it can also provide a mechanism to transfer their quantum state over larger distances. Here, we demonstrate such a form of electron teleportation across a metallic island. This effect originates from the low-temperature freezing of the island's charge Q which, in the presence of a single connected electronic channel, enforces a one-to-one correspondence between incoming and outgoing electrons. Such faithful quantum state imprinting is established between well-separated injection and emission locations and evidenced through two-path interferences in the integer quantum Hall regime. The additional quantum phase of $2\pi Q/e$, where e is the electron charge, may allow for decoherence-free entanglement of propagating electrons, and notably of flying qubits.

A disordered environment, with a large number of interacting degrees of freedom, is generally considered unfavorable for quantum technologies. Such an environment is exemplified by a metallic island with a large energy density of states and a small number of connected electronic channels, through which there is no quantum coherent propagation of individual electrons. Indeed, the time that an individual electron spends inside the island (*1*) is typically much longer than the interval between inelastic collisions destroying its quantum coherence (*2*, *3*). In contrast to this conventional wisdom, we show experimentally that the Coulomb interaction in such an island can, under the right circumstances, lead to a near perfect transmission of the quantum state of electrons across it, mediated by the collective surface plasmon modes of the island (*4*, *5*). In the quantum Hall regime implementation, where injection and emission points are physically separated by chirality, this constitutes a form of teleportation of the electrons' state. This phenomenon is different from the standard "quantum teleportation" protocol (*6*) and similar to the "electron teleportation" proposed in (*7*).

The voltage probe model of a metallic island (*8*) is widely used to mimic the electrons' quantum decoherence and energy relaxation toward equilibrium [see, e.g., (*9*)]. However, independent absorption and emission of electrons result in fluctuations of the total island charge Q, with a characteristic charging energy $E_C = e^2/2C$ (C is the geometrical capacitance of the island and e is the elementary electron charge). At low temperatures $T \ll E_C/k_B$ (where k_B is the Boltzmann constant), this energy is not available, and the macroscopic quantum charge state Q is effectively frozen (*5*, *10*) [although not quantized in units of e as long as one channel is perfectly connected (*11*–*13*)]. Consequently, correlations develop between absorbed and emitted electrons. Such correlations are strongest if only one transport channel is connected to the island, in which case theory predicts that the electrons entering it and those concomitantly exiting it are in identical quantum states (*4*, *5*) [see also (*14*) for a related prediction in the presence of strong nonlocal interactions along quantum Hall edges]. Effectively, the electronic states within the connected quantum channel are decoupled from the many quasiparticles within the island, even though the incoming (outgoing) physical electron particles penetrate into (originate from) the island. Another consequence is that heat evacuation from the island's internal states along the channel is fully suppressed (*10*). By contrast, in the presence of two or more open channels, the coherence is lost (*5*), and heat evacuation is restored, in agreement with the recently observed systematic heat Coulomb blockade of one ballistic channel (*15*). The comparable "electron teleportation" proposed in (*7*) also relies on the "all-important" Coulomb charging energy of a small island, which has to prevail over temperature and voltage bias. In this proposal (*7*), the island is superconducting, without subgap states except for Majorana bound states at the injection and emission locations. Such a teleportation process was recently invoked as one possible mechanism for the observed coherent single-electron transport across a hybrid superconductor-semiconductor island in the Coulomb blockade regime (*16*). We additionally point out some similarities with quasiparticle correlations induced by Andreev reflections that take place at the interface between a normal metal and a superconductor (*2*). These correlations can be created nonlocally, through the so-called crossed Andreev reflection involving an electron and a hole separated by at most the superconducting coherence length.

We demonstrate the high-fidelity replication of the quantum state of electrons across a metallic island through quantum interferences. For this purpose, an injected current is first split along two separate paths that are subsequently recombined, thereby realizing an electronic Mach-Zehnder interferometer (MZI).

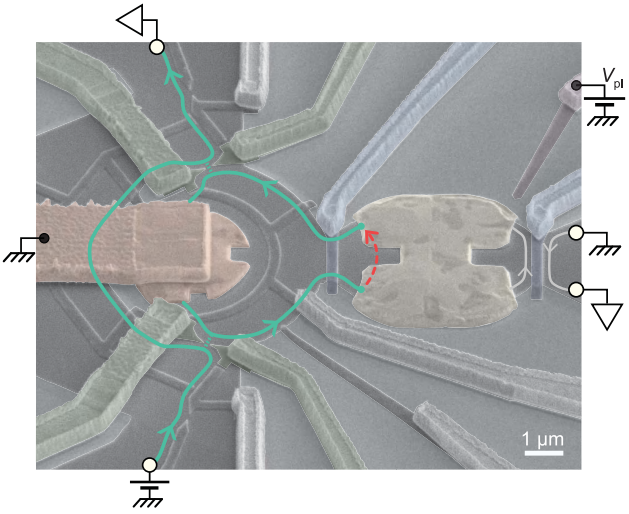

Fig. 1. Device e-beam micrograph. Areas with a Ga(Al)As 2DEG underneath the surface appear darker. The applied perpendicular magnetic field $B \simeq 5$ T corresponds to the integer quantum Hall regime at a filling factor of 2. Capacitively coupled gates colored green and blue control, respectively, the MZI beam splitters for the outer quantum Hall edge channel (lines with arrow, here corresponding to the schematic in Fig. 2B) and the connection to the floating metallic island (sand yellow, in right half) in good ohmic contact with the buried 2D electron gas. One of the two MZI outputs is the central small ohmic contact (light brown, in left half) connected to ground through a suspended bridge. The second one, larger and located farther away, is schematically represented by the top white circle. The MZI phase difference is controlled through B or the plunger gate voltage V_{pl}. The red dashed line visually represents the nonlocal quantum state transfer across the island, between electrons' injection (starting point) and emission (arrow).

[1]Université Paris-Saclay, CNRS, Centre de Nanosciences et de Nanotechnologies (C2N), 91120 Palaiseau, France [2]Université de Paris, C2N, 91120 Palaiseau, France
*These authors contributed equally to this work.
†Corresponding author. Email: frederic.pierre@c2n.upsaclay.fr

In contrast with usual MZI implementations (*17*–*21*), one of the paths can controllably be diverted toward a small floating metallic island (Fig. 1). In that case, any two-path quantum interferences involve both the initial electrons (direct left path) and the reemitted ones (interrupted right path, assuming a perfect contact with the island). Therefore high-visibility interferences directly ascertain a high fidelity of the electron state replication. The Coulomb interaction was previously invoked to account for various observations in electron interferometers, such as the multiple side lobes versus voltage bias in (*22*) or the phase rigidity versus magnetic field in (*23*).

A colorized e-beam micrograph of the measured device is shown in Fig. 1. The sample was nanofabricated from a high-mobility Ga(Al)As two-dimensional electron gas (2DEG) and immersed in a perpendicular magnetic field $B \simeq 5$ T corresponding to the integer quantum Hall filling factor $\nu = 2$, where the electron quantum coherence length is the largest (*18*, *19*, *21*). In this regime, two quantum Hall channels copropagate along the edges (the electron gas was etched away in the brighter areas), and the MZI is formed using only the outer edge channel. The followed paths are represented by thick lines with arrows for the configuration where one MZI arm goes through the floating metallic island (corresponding schematic shown in Fig. 2B). The two MZI beam splitters, each tuned to half transmission, are realized with quantum point contacts formed by field effect using split gates (colored green; the inner quantum Hall channel, not shown, is fully reflected). One of the two MZI outputs is the small central metallic electrode (light brown, in left half of Fig. 1), which is grounded through a suspended bridge. The quantum interferences are characterized by the oscillations of the current transmitted to the second MZI output formed by a much larger electrode 60 μm away (represented in Fig. 1 by the top white circle), while sweeping either the magnetic field B or the voltage V_{pl} applied to a lateral plunger gate (purple). The floating metallic island (sand yellow, in right half of Fig. 1) consists of 2 μm^3 of a gold-germanium-nickel alloy diffused into the Ga(Al)As heterojunction by thermal annealing. The typical metallic density of states of such metals is $\nu_F \approx 10^{47}$ J^{-1} m^{-3} (1.14×10^{47} for gold, the main constituent), corresponding to a very small average electronic level spacing in the island of $\delta \approx 30$ peV. The dwell (wandering) time of individual electrons within this island is given by the expression $\tau_D = \frac{h}{N\delta} \approx \frac{130}{N}$ μs, where h is the Planck constant and N is the number of connected edge channels (*1*). As pointed out in the introduction, this is much longer than the quantum coherence time of electrons in similar metals, which is at most in the 20-ns range (*3*, *24*). The gates barring the broad way on each side of the floating island (blue) are normally tuned to either fully reflect or fully transmit the outer edge channel, in order to implement the MZI configurations schematically represented in Fig. 2, A to C. The second (inner) quantum Hall edge channel is always completely reflected at the barring gate (fig. S1) and can therefore be ignored (*5*). The island charging energy $E_C \simeq k_B \times 0.3$ K was obtained from standard Coulomb diamond measurements [in a specifically tuned tunnel regime; see Fig. 3B and (*25*)]. At the experimental electronic temperature $T \simeq 10$ mK [measured on-chip from shot noise (*26*)], the criterion $k_B T \ll E_C$ for fully developed Coulomb-induced correlations is therefore well verified. The previous experiments were performed in the opposite "high-temperature" regime $k_B T \gg E_C$ of negligible Coulomb correlations, in which case, unsurprisingly, a complete quantum decoherence (*27*) and energy relaxation (*28*) of electrons were observed with a single connected channel. Finally, the transparency of the contact between the floating island and the outer quantum Hall edge channel plays an essential role: If the transparency is poor, many electrons would simply be reflected at the interface. Here, ≳97% of the incoming current penetrates into the floating island (*25*), which is also reflected by the marked changes of behavior detailed later.

In Fig. 2D, we show typical MZI oscillations versus B of τ_{MZI}, the fraction of outer edge channel current transmitted across the device. The measurements were performed in the three configurations depicted in Fig. 2, A to C. The red continuous line in Fig. 2D corresponds to a standard electronic MZI, with the floating metallic island bypassed (schematic in Fig. 2A). In that case, the oscillations are of high visibility $\mathcal{V} \equiv (\tau_{MZI}^{max} - \tau_{MZI}^{min})/(\tau_{MZI}^{max} + \tau_{MZI}^{min}) \approx 90\%$ and, as expected for the Aharonov-Bohm phase, the magnetic field period of 241 ± 3 μT (red symbols in Fig. 2E show consecutive extrema positions) closely corresponds to one flux quantum ($241\ \mu T \times S \simeq 0.98 h/e$ using the nominal area $S \simeq 16.8\ \mu m^2$). A small asymmetry in the τ_{MZI} data (the average is slightly above 0.5) results from a small reflection of the outer edge channel on the grounded central ohmic contact [of ≈5%; see (*25*)]. The black continuous line in Fig. 2D was measured with the right MZI arm deviated to go through the floating ohmic island (edge channel paths displayed in Fig. 1, and schematic in Fig. 2B). We observe first that the visibility of quantum interference remains of the same high amplitude, which corresponds to a perfect fidelity (at experimental accuracy) of the replicated quantum states imprinted on the electrons reemitted from the island, in agreement with low-temperature predictions (*4*, *5*). Second, the magnetic field period of 305 ± 4 μT is found

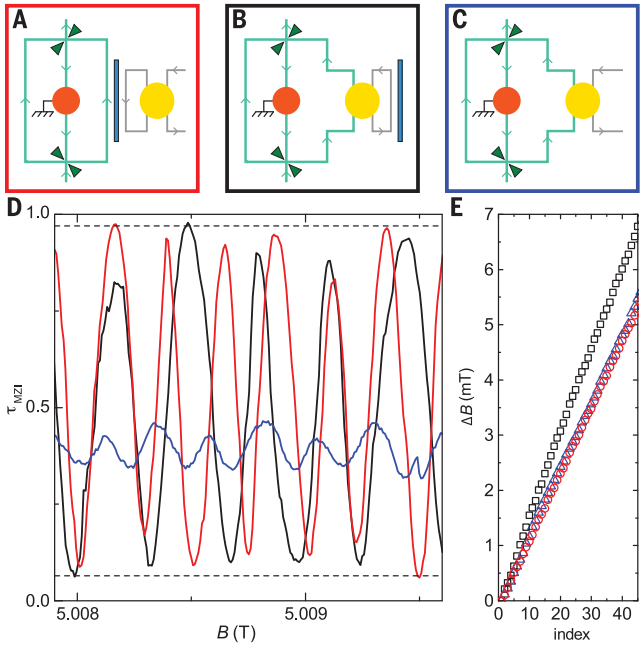

Fig. 2. Quantum oscillations versus magnetic field. (**A** to **C**) Schematics of implemented MZI configurations. (**D**) Fraction τ_{MZI} of the outer edge channel current transmitted across the MZI as a function of B. Continuous lines are measurements performed in the configuration framed by a box of the same color in (A), (B), and (C). The horizontal black dashed lines represent the τ_{MZI} extrema for the standard and floating island MZI configurations [schematics in (A) and (B), respectively], corresponding to a high quantum oscillations visibility of $\mathcal{V} \sim 90\%$. With a second channel connected to the floating island (configuration shown Fig. 2C), the quantum oscillations are strongly reduced to a visibility $\mathcal{V} \sim 20\%$, consistent with the separately characterized small residual reflection of ~3% [see text and (*25*)], and the average τ_{MZI} is diminished as part of the current is transmitted across the island toward a remote electrical ground. (**E**) Symbols display the magnetic field position of consecutive extrema (both peaks and dips increment the index number).

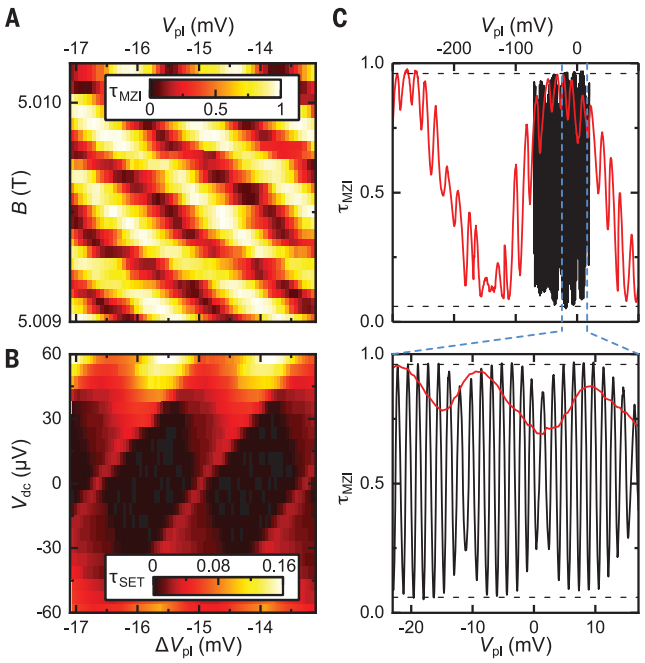

Fig. 3. Quantum phase versus island charge. (**A**) Color plot of $\tau_{MZI}(B, V_{pl})$ in the floating island MZI configuration (schematic in Fig. 2B), with the larger values shown brighter, which establishes the equivalent role of B and V_{pl}. (**B**) Coulomb diamond characterization of the floating island (larger differential conductance τ_{SET} shown brighter; in this configuration, the island is weakly coupled on both sides and V_{dc} is the applied dc bias voltage). A comparison with (A), plotted using the same V_{pl} scale, reveals that the addition of a charge of e on the island precisely corresponds, in the floating island MZI configuration, to an electron quantum phase of 2π (one quantum oscillation period). (**C**) The top and bottom panels display measurements of $\tau_{MZI}(V_{pl})$ with the device set in the floating island MZI configuration (black line) and in the standard MZI configuration (red line, schematic in Fig. 2A). The MZI oscillations' period in V_{pl} is shorter by a factor of 1/160 when the island is connected. An additional modulation of fixed period (≈15 mV) appears in both configurations.

to be larger than in the standard MZI configuration of Fig. 2A (see black symbols in Fig. 2E). This increase is opposite to the reduction that would be expected from the Aharonov-Bohm period with the larger surface enclosed by the outer channel path and the inner boundary of the floating metallic island [see (*25*) for a graphical representation; $S \simeq 18.4\ \mu m^2$ would correspond to an Aharonov-Bohm period of $225\ \mu T \simeq h/eS$]. Such opposite evolution and relatively important discrepancy (36%) establish that the MZI phase does not reduce to the usual Aharonov-Bohm phase acquired by a single electron propagating along two different edge paths. Even a naïve application of the surface modulation that cancels the magnetic field dependence in Fabry-Pérot interferometers dominated by Coulomb interaction (*29*, *30*) would only compensate for the period reduction by the added area enclosed between the metallic island and the barring gate. Instead, the larger period corroborates the transfer of the electrons' state across the island. Indeed, in the presence of an electron path amputated from a section (the 2DEG/metal interface), the closed surface involved in the Aharonov-Bohm phase is no longer well-defined. Whether one can still speak of an Aharonov-Bohm phase with a smaller effective surface, or whether another period reduction mechanism is at play when going through the floating island, is not established. This question calls for further investigations, both theoretical and experimental, with devices implementing different injection-emission distances.

The blue continuous line in Fig. 2D was measured with one MZI arm going through the floating island and in the presence of a second electronic channel connected to it (configuration schematically displayed in Fig. 2C). We find strongly suppressed conductance oscillations corresponding to a full decoherence of the electrons going through the island. The residual visibility $\mathcal{V} \lesssim 0.2$ is consistent with the separately obtained proportion $1 - \tau_{island} \lesssim 3\%$ of reflected electrons, not penetrating into the island (*25*). Indeed, the MZI contribution of the reflected electrons reads $\mathcal{V}(1 - \tau_{island} \ll 1) \simeq \left(\frac{4\mathcal{V}_0}{3}\right)\sqrt{1 - \tau_{island}} \lesssim 0.21$, with $\mathcal{V}_0 \approx 90\%$ the MZI visibility in the standard configuration (*25*, *27*). The magnetic field period of $246 \pm 4\ \mu T$ for these smaller oscillations [see blue symbols in Fig. 2E; a standard fast Fourier transform analysis of these residual oscillations yields the less resolved value $237 \pm 16\ \mu T$ (*25*)] is 9% longer than the 225 μT nominally expected, and is close to the period observed in the standard MZI configuration shown in Fig. 2A. It is plausible that the reflected electrons are those propagating the furthest away from the edge and from the semiconductor-metal interface, effectively corresponding to a smaller surface compatible with the observed longer period. Other possibilities include that the residual electrons' reflection takes place at the level of the barring gate (colored blue, left of island in Fig. 1) or, eventually, a Coulomb-induced compensation in the spirit of Coulomb dominated Fabry-Pérot interferometers (*29*, *30*). Also, the average $\langle \tau_{MZI} \rangle \simeq 0.39$ is shifted below 0.5. This is simply because part of the injected current is evacuated toward a remote electrical ground through the second (right) channel connected to the floating island (the value $\langle \tau_{MZI} \rangle = 0.375$ is expected from current conservation for a floating island and a central ohmic contact both perfectly connected).

We now investigate the relation between the island's charge and the electron phase shift associated with the quantum state transfer. For this purpose, Fig. 3 focuses on the influence on τ_{MZI} of the voltage V_{pl} applied to a plunger gate (colored purple in Fig. 1), which is relatively far from the MZI outer quantum Hall channel but close to the island. The equivalent role on the MZI phase of V_{pl} and B is first directly established, in Fig. 3A, with the device set in the floating island MZI configuration [schematic in Fig. 2B, see also, e.g., (*31*, *32*) for the influence of an electrostatic field on quantum interferences through different mechanisms]. Figure 3B displays Coulomb diamond measurements of the conductance across the island as a function of the same plunger gate voltage V_{pl}. For this purpose, the island is here weakly connected through tunnel barriers, thereby implementing a single-electron transistor of quantized charge Q in units of e (Q is not quantized for the strongly coupled floating island in the MZI configurations). The left MZI arm was disconnected during this measurement, as schematically illustrated in fig. S2 (*25*). Notably, the MZI gate voltage period in Fig. 3A precisely matches the Coulomb diamonds' period in Fig. 3B, as can be seen by directly comparing the two panels plotted using the same V_{pl} scale. In the floating MZI limit of strongly connected channels, $Q = eV_{pl}/\Delta$, with $\Delta \simeq 1.7$ mV being the Coulomb diamond period (*11*–*13*). A quantum phase shift of $2\pi Q/e$ therefore applies to the transferred electrons, as specifically predicted theoretically (*4*, *5*) and in agreement with Friedel's sum rule. Figure 3C shows a comparison of τ_{MZI} oscillations in the standard MZI configuration (red line) and with one arm going through the metallic island (black line); both have maximum visibility $\mathcal{V} \simeq 90\%$ as also seen versus magnetic field in Fig. 2D. However, the V_{pl} period is increased by a large factor of 160, from 1.7 to 270 mV, when the island is disconnected; this reflects the weak coupling of the plunger gate voltage to the MZI outer edge channel [see fig. S3 (*25*) for an

extended V_{pl} range]. This provides further evidence that the edge electrons contributing to the quantum oscillations in the floating island configuration are indeed incorporated into the metal. An additional, smaller signal of fixed period 15 mV is visible in both configurations (in the form of direct oscillations or of an amplitude modulation), which might originate from the progressive charging of a nearby defect.

This experimental work demonstrates that the Coulomb interaction has two facets. It can both destroy and preserve quantum effects. Although a metallic island is often pictured as a floating reservoir of uncorrelated electrons (*8*, *33*), we establish that a high-fidelity electron quantum state transfer can take place across it, enforced by the Coulomb charging energy. This provides a means to overcome limitations imposed by the decoherence of individual electrons. Moreover, the observed universal 2π electron phase shift for one elementary charge e on the island can allow for a strong entanglement of single-electron states, both between themselves or with other quantum degrees of freedom, with a negligible loss of coherence. Such controllable, strong-coupling mechanism constitutes a key element in the context of quantum Hall edges envisioned as platforms for the manipulation and transfer of quantum information via propagating electrons (*21*, *34*–*39*). In particular, it is very well suited to implementing quantum gates for these "flying qubits," such as the CNOT proposal involving a conditional phase shift of π described in (*38*).

REFERENCES AND NOTES

1. P. Brouwer, M. Büttiker, *Europhys. Lett.* **37**, 441–446 (1997).
2. Y. Nazarov, Y. Blanter, *Quantum Transport* (Cambridge Univ. Press, 2009).
3. F. Pierre *et al.*, *Phys. Rev. B Condens. Matter Mater. Phys.* **68**, 085413 (2003).
4. A. Clerk, P. Brouwer, V. Ambegaokar, *Phys. Rev. Lett.* **87**, 186801 (2001).
5. E. G. Idrisov, I. P. Levkivskyi, E. V. Sukhorukov, *Phys. Rev. Lett.* **121**, 026802 (2018).
6. C. H. Bennett *et al.*, *Phys. Rev. Lett.* **70**, 1895–1899 (1993).
7. L. Fu, *Phys. Rev. Lett.* **104**, 056402 (2010).
8. M. Büttiker, *IBM J. Res. Develop.* **32**, 63–75 (1988).
9. Y. M. Blanter, M. Büttiker, *Phys. Rep.* **336**, 1–166 (2000).
10. A. Slobodeniuk, I. Levkivskyi, E. Sukhorukov, *Phys. Rev. B Condens. Matter Mater. Phys.* **88**, 165307 (2013).
11. K. A. Matveev, *Phys. Rev. B Condens. Matter* **51**, 1743–1751 (1995).
12. Y. Nazarov, *Phys. Rev. Lett.* **82**, 1245–1248 (1999).
13. S. Jezouin *et al.*, *Nature* **536**, 58–62 (2016).
14. S.-Y. Lee, H.-W. Lee, H.-S. Sim, *Phys. Rev. B Condens. Matter Mater. Phys.* **86**, 235444 (2012).
15. E. Sivre *et al.*, *Nat. Phys.* **14**, 145–148 (2018).
16. A. Whiticar *et al.*, arXiv:1902.07085 [cond-mat.mes-hall] (2019).
17. Y. Ji *et al.*, *Nature* **422**, 415–418 (2003).
18. P. Roulleau *et al.*, *Phys. Rev. B Condens. Matter Mater. Phys.* **76**, 161309 (2007).
19. L. Litvin, H. Tranitz, W. Wegscheider, C. Strunk, *Phys. Rev. B Condens. Matter Mater. Phys.* **75**, 033315 (2007).
20. E. Bieri *et al.*, *Phys. Rev. B Condens. Matter Mater. Phys.* **79**, 245324 (2009).
21. H. Duprez *et al.*, *Phys. Rev. X* **9**, 021030 (2019).
22. I. Neder, M. Heiblum, Y. Levinson, D. Mahalu, V. Umansky, *Phys. Rev. Lett.* **96**, 016804 (2006).
23. N. Ofek *et al.*, *Proc. Natl. Acad. Sci. U.S.A.* **107**, 5276–5281 (2010).
24. C. Bäuerle *et al.*, *Phys. Rev. Lett.* **95**, 266805 (2005).
25. Materials and methods are available as supplementary materials.
26. Z. Iftikhar *et al.*, *Nat. Commun.* **7**, 12908 (2016).
27. P. Roulleau *et al.*, *Phys. Rev. Lett.* **102**, 236802 (2009).
28. C. Altimiras *et al.*, *Phys. Rev. Lett.* **105**, 226804 (2010).
29. I. Sivan *et al.*, *Nat. Commun.* **7**, 12184 (2016).
30. B. I. Halperin, A. Stern, I. Neder, B. Rosenow, *Phys. Rev. B Condens. Matter Mater. Phys.* **83**, 155440 (2011).
31. R. Schuster *et al.*, *Nature* **385**, 417–420 (1997).
32. A. van Oudenaarden, M. Devoret, Y. Nazarov, J. Mooij, *Nature* **391**, 768–770 (1998).
33. M. de Jong, C. Beenakker, *Physica A* **230**, 219–248 (1996).
34. A. Bertoni, P. Bordone, R. Brunetti, C. Jacoboni, S. Reggiani, *Phys. Rev. Lett.* **84**, 5912–5915 (2000).
35. R. Ionicioiu, G. Amaratunga, F. Udrea, *Int. J. Mod. Phys. B* **15**, 125 (2001).
36. T. M. Stace, C. H. Barnes, G. J. Milburn, *Phys. Rev. Lett.* **93**, 126804 (2004).
37. E. Bocquillon *et al.*, *Ann. Phys. (Berlin)* **526**, 1–30 (2014).
38. D. Glattli, P. Roulleau, *Phys. Status Solidi, B Basic Res.* **254**, 1600650 (2017).
39. C. Bäuerle *et al.*, *Rep. Prog. Phys.* **81**, 056503 (2018).
40. H. Duprez, E. Sivre, A. Anthore, A. Aassime, A. Cavana, U. Gennser, F. Pierre, Data displayed in "Transmitting the quantum state of electrons across a metallic island with Coulomb interaction", Zenodo (2019); doi 10.5281/zenodo.3528156.

ACKNOWLEDGMENTS

We thank P. Brouwer, L. Glazman, C. Mora, H. Sim, and E. Sukhorukov for illuminating discussions. **Funding:** This work was supported by the French RENATECH network, the national French program 'Investissements d'Avenir' (Labex NanoSaclay, ANR-10-LABX-0035), and the French National Research Agency (projects QuTherm, ANR-16-CE30-0010, and SIM-CIRCUIT, ANR-18-CE47-0014-01). **Author contributions:** E.S. and H.D. performed the experiment and analyzed the data with help from A.Aa., A.An., and F.P.; F.P. fabricated the sample with assistance from E.S and H.D.; A.C. and U.G. grew the 2DEG; F.P. led the project and wrote the manuscript with input from A.Aa., A.An., E.S., H.D., and U.G **Competing interests:** The authors declare no competing financial interests. **Data and materials availability:** The data shown in the paper are available at Zenodo (*40*). Correspondence and requests for materials should be addressed to F.P. (frederic.pierre@c2n.upsaclay.fr).

SUPPLEMENTARY MATERIALS

science.sciencemag.org/content/366/6470/1243/suppl/DC1
Materials and Methods
Figs. S1 to S5

24 January 2019; accepted 6 November 2019
10.1126/science.aaw7856

nature COMMUNICATIONS

ARTICLE

https://doi.org/10.1038/s41467-019-13566-8 OPEN

Electronic heat flow and thermal shot noise in quantum circuits

E. Sivre[1,3], H. Duprez[1,3], A. Anthore[1,2], A. Aassime[1], F.D. Parmentier[1], A. Cavanna[1], A. Ouerghi[1], U. Gennser[1] & F. Pierre[1*]

When assembling individual quantum components into a mesoscopic circuit, the interplay between Coulomb interaction and charge granularity breaks down the classical laws of electrical impedance composition. Here we explore experimentally the thermal consequences, and observe an additional quantum mechanism of electronic heat transport. The investigated, broadly tunable test-bed circuit is composed of a micron-scale metallic node connected to one electronic channel and a resistance. Heating up the node with Joule dissipation, we separately determine, from complementary noise measurements, both its temperature and the thermal shot noise induced by the temperature difference across the channel. The thermal shot noise predictions are thereby directly validated, and the electronic heat flow is revealed. The latter exhibits a contribution from the channel involving the electrons' partitioning together with the Coulomb interaction. Expanding heat current predictions to include the thermal shot noise, we find a quantitative agreement with experiments.

[1] Université Paris-Saclay, CNRS, Centre de Nanosciences et de Nanotechnologies (C2N), 91120 Palaiseau, France. [2] Université de Paris, C2N, 91120 Palaiseau, France. [3] Thes authors contributed equally: E. Sivre, H. Duprez. *email: frederic.pierre@c2n.upsaclay.fr

Heating generally drives the crossover from quantum to classical behaviors; nevertheless, heat itself is ruled by quantum mechanics. In recent years, experimental explorations of quantum thermal phenomena have been emerging at a rising pace[1–3]. In particular, the quantum of thermal conductance, a universal basic building block of heat quantum transport, is now firmly established for bosons[1,4], fermions[5,6], and quasiparticles that may be anyons[7], as well as up to macroscopic[8] and room temperature[9,10] scales. However, despite the strong influence of Coulomb interaction on electricity in small quantum circuits[11–14], its impact on the quantum transport of heat remains barely explored experimentally[15–17]. In a first step for perfectly ballistic circuits, where there is no back-scattering along any of the connected electronic channels, a recent observation[16] was made of the predicted[18] heat Coulomb blockade taking place without any concomitant reduction of the electrical conductance. In this limit and at low temperatures, the Coulomb interaction manifests itself as the systematic suppression of a single channel for the evacuation of heat from a small circuit node[16,18]. Here we address elementary quantum circuits including one generic electronic channel of arbitrary electron transmission probability. An unexpected increase in the flow of heat is observed and quantitatively accounted for by an additional quantum heat transport mechanism, involving the association of shot noise and Coulomb interaction.

We obtain the heat current–temperature characteristics by controllably injecting a dc power into a small floating circuit node connecting a quantum channel to a linear resistance, and by monitoring in situ the resulting increase in the electrons' temperature. A complication is that the partition of electrons in the generic channel breaks the Johnson–Nyquist proportionality between excess noise and node temperature increase[19,20], which was previously used for the thermometry of ballistic circuits[5–7,16,17]. We overcome this difficulty with an experimental procedure involving complementary measurements of both the auto- and cross-correlations of electrical fluctuations. This provides us, separately, with the local electronic temperature in the metallic node, as well as with the thermal shot noise. The latter is found in good agreement with predictions derived within the scattering approach[19,21], in which Coulomb effects have been encapsulated in the temperature-dependent conductance (reduced by the dynamical Coulomb blockade[11]). The node temperature increase, both in terms of injected power and electron transmission probability across the channel, exposes an additional heat current contribution involving thermal shot noise.

Results

Test-bed for electronic channels in dissipative environments. An e-beam micrograph of the device is shown in Fig. 1a together with a schematic representation of the measurement setup. The small floating circuit node that is heated is materialized by the central micron-scale metallic island (in brighter gray), of separately characterized self-capacitance $C \simeq 3.1$ fF. It is in essentially perfect electrical contact with a standard Ga(Al)As two-dimensional (2D) electron gas underneath the surface. The 2D gas is immersed in a perpendicular magnetic field corresponding to the integer quantum Hall regime at filling factor two. In this regime, the current flows along two adjacent quantum Hall edge channels depicted by lines with arrows indicating the propagation direction. Three quantum point contacts (QPCs) are formed in the 2D electron gas by applying negative voltages on surface split gates coupled capacitively. A single (spin-polarized) short electronic channel of tunable transmission probability $\tau \in [0, 1]$ is implemented at the left QPC. The top and right QPCs are tuned to a different, ballistic regime: they are set to fully transmit,

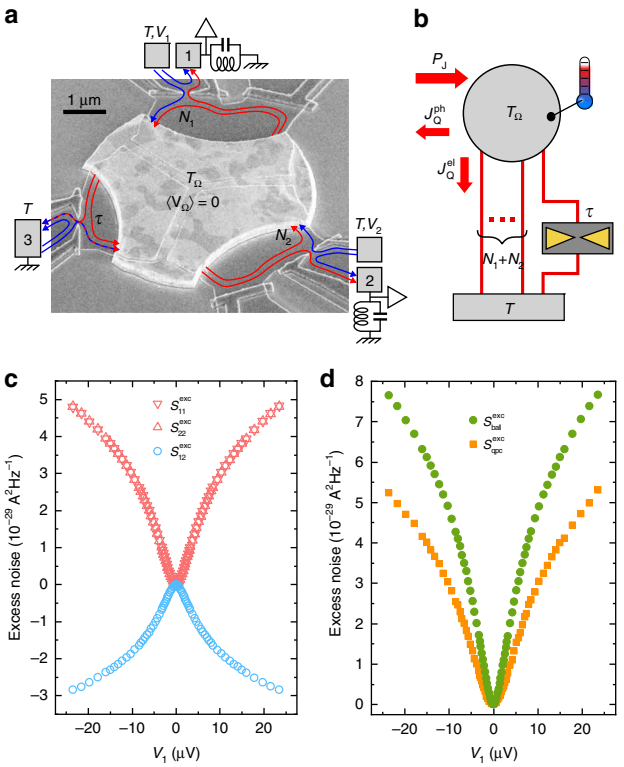

Fig. 1 Experimental approach. a Device e-beam micrograph with measurement setup schematic. A single generic channel of arbitrary electron transmission probability τ, as well as N_1 and N_2 ballistic (perfectly transmitted) channels, are separately connected to a small metallic island. **b** Schematic heat balance representation between injected Joule power (P_J) and outgoing heat currents, from electrons to phonons (J_Q^{ph}) and through the connected electronic channels (J_Q^{el}). **c** Excess auto- and cross-correlation measurements versus $V_1 = -V_2$, in the illustrative configuration $N = 2$ ($N_1 = N_2 = 1$), $\tau \sim 0.5$. **d** Extracted excess noise sources per ballistic channel (S_{ball}^{exc}) and across the generic single-channel quantum point contact of transmission τ (S_{qpc}^{exc}), from the data in **c**.

respectively, N_1 and N_2 channels forming together an adjustable linear resistance[22,23] $R = R_K/N$, with $R_K = h/e^2$ the electrical resistance quantum (h the Planck constant and e the electron charge) and $N = N_1 + N_2$. Further away, the quantum Hall channels are connected to large electrodes at base temperature $T \simeq 8$ mK, represented in Fig. 1a by gray rectangles.

Electronic heat flow determination. The electrons within the central island are heated to T_Ω by dissipating a known Joule power $P_J \simeq (N_1 V_1^2 + N_2 V_2^2)/2R_K$, with V_1 (V_2) the voltage applied to the top (right) large electrode (Methods). The island's dc voltage is pinned to $\langle V_\Omega \rangle = 0$, by imposing $N_1 V_1 = -N_2 V_2$, such that the generic channel experiences a pure temperature bias $T_\Omega - T$ without dc voltage. As illustrated in Fig. 1b, energy conservation in the stationary regime implies $P_J = J_Q^{el} + J_Q^{ph}$, with J_Q^{el} being the heat flow across the connected electronic channels and J_Q^{ph} the heat transferred from the electrons within the island to the phonons. In practice, electron–phonon heat transfers are negligible only for $T_\Omega \lesssim 20$ mK[16]. However, as J_Q^{ph} only depends on temperatures (T_Ω, T), and not on the connected electronic channels (τ, N), it can be calibrated by tuning the circuit to the ballistic regime ($\tau \in \{0, 1\}$). Using the previously established heat

Coulomb blockade predictions for ballistic channels[16,18], we find that all the data with $\tau \in \{0,1\}$, $N \in \{2,3,4\}$ and $T \in \{8,16\}$ mK can be accurately reproduced using the same $J_Q^{\rm ph} \simeq 2.7\times 10^{-8}\left(T_\Omega^{5.7} - T^{5.7}\right)$ W (Methods). At intermediate transmission probability ($0 < \tau < 1$), the unknown electronic heat flow is then obtained by subtracting the above $J_Q^{\rm ph}$ from the injected Joule power ($J_Q^{\rm el} = P_J - J_Q^{\rm ph}$).

Local temperature increase measurement. The island's electronic temperature T_Ω is determined from the low-frequency (MHz) current fluctuations measured on the top (1) and right (2) large electrodes (Methods). The excess auto- and cross-correlation spectral density, from which the zero-bias offset is removed, are plotted in Fig. 1c versus V_1 for the illustrative configuration $N_1 = N_2 = 1$ at $\tau \sim 0.5$. In a nutshell, combining these data gives us access separately to the current noise sources originating from the QPC hosting a single generic channel ($S_{\rm qpc}$) and from the ballistic channels ($S_{\rm ball}$ per channel), both shown in Fig. 1d. This is possible because these two noise sources contribute with the same sign to the experimental autocorrelation signal, while with an opposite sign to the cross-correlation (Methods). The temperature T_Ω is then obtained using solely the ballistic noise source $S_{\rm ball}$, directly resulting from the thermal fluctuations of the electronic states' population in the baths. This robust connection manifests itself as a straightforward, and previously used[5–7,16,17], generalization of the fluctuation-dissipation relation for the thermal noise $S_{\rm ball} = 4k_{\rm B}\bar{T}/R_{\rm K}$, where $\bar{T} = (T_\Omega + T)/2$ is the average temperature[19,24]. In practice, the excess noise data (with respect to $V_{1,2} = 0$) gives us access to the temperature increase $T_\Omega - T$, while T is separately measured (Methods).

Shot noise induced by a temperature difference. Generic channels driven out-of-equilibrium are generally expected to exhibit, in addition to the average thermal noise, a shot noise induced by the electron partitioning into a transmitted electron and a reflected electron[19,21]. In particular, the current noise spectral density at low frequencies ($\omega \ll k_{\rm B}T/\hbar$), for a single channel of transmission probability τ, reads[19]:

$$S_{\rm qpc}^{\rm thy} = \frac{4k_{\rm B}\bar{T}\tau}{R_{\rm K}} + \frac{2\tau(1-\tau)}{R_{\rm K}}\int {\rm d}E\left[f_{T_\Omega}(E) - f_T(E)\right]^2, \qquad (1)$$

with $f_{T,T_\Omega}(E)$ the Fermi distributions in the connected baths at different temperatures and/or voltages. The average thermal noise and the shot noise are, respectively, the first and second term on the right-hand side of Eq. (1). Whereas the shot noise induced by either a voltage difference or a frequency irradiation is experimentally well established (see references in ref. [19] and also ref. [25]), the thermal shot noise resulting from the partition of electrons in the sole presence of a temperature difference was observed only recently[20]. Although convincing, this observation did not allow for a one-to-one comparison of the individual data points with the theory, because the possibly multiple electronic channels were incompletely characterized by the measurement of their parallel conductance. In contrast, in the present work with a single generic channel, the QPC conductance $G_{\rm qpc} = \tau e^2/h$ completely determines the transmission probability τ. In Fig. 2a, following ref. [20], we focus on the thermal shot noise $\Delta S_{\rm qpc}$ obtained by removing the average Johnson–Nyquist noise ($\Delta S_{\rm qpc} = S_{\rm qpc} - 4k_{\rm B}\bar{T}\tau/R_{\rm K}$). The $\Delta S_{\rm qpc}$ data at $N_1 = N_2 = 1$ (symbols) are plotted versus T_Ω for several gate voltage tunings of the single-channel QPC. The predictions (continuous lines), calculated without any adjustable parameter using Eq. (1), closely match the data (for control experiments, see Supplementary Fig. 1 at other $\{N_1, N_2\}$ and Supplementary Fig. 2 at a larger base temperature $T \simeq 16$ mK). Note that the simultaneously measured $G_{\rm qpc} = \tau e^2/h$ depends on the temperatures T and T_Ω, because of the quantum back-action of the series RC circuit[13] also referred to as the dynamical Coulomb blockade[11]. Remarkably, we find that the effect of Coulomb interaction is accurately encapsulated, at experimental resolution, into the renormalized τ injected in Eq. (1). Figure 2b directly reveals the partition origin of the shot noise induced by a temperature difference. The data points represent this experimental shot noise renormalized by the predicted, τ-independent temperature function $\mathcal{F}(T_\Omega, T) = (2/R_{\rm K})\int {\rm d}E\left[f_{T_\Omega}(E) - f_T(E)\right]^2$. The good agreement observed between $\Delta S_{\rm qpc}/\mathcal{F}$ and $\tau(1-\tau)$ attests of the underlying partition mechanism.

Electronic heat flow from a small quantum circuit node. We now address the electronic flow of heat across the QPC and ballistic channels. In conductors, the thermal conductance G_Q is frequently found to be directly proportional to the electrical conductance $G_{\rm el}$, through the so-called Wiedemann–Franz (WF) law $G_Q = \mathcal{L}G_{\rm el}$ with $\mathcal{L} = \pi^2 k_{\rm B}^2/3e^2$ the Lorenz number. While this relation holds between the quantum of thermal and electrical conductances, it generally breaks down in quantum circuits assembled from several interconnected channels. In particular, it was shown that the thermal conductance from a small, heated circuit node connected by ballistic channels is reduced from the WF expectation by precisely one quantum of thermal conductance at low temperatures[16,18], whatever the total number of channels. With such a fixed reduction, the increment by $\mathcal{L}/R_{\rm K}$ of the thermal conductance when adding an extra ballistic channel (starting from at least one) nevertheless follows the WF relation. Is this also the case if the electrical conductance is increased continuously, by sweeping the transmission probability across an electronic channel from $\tau = 0$ to 1? The answer is no, as we will now show.

Figure 3a exhibits as symbols, versus T_Ω, the experimental electronic heat flow $J_Q^{\rm el}$ normalized by the quantum limit per channel $J_Q^{\rm lim} = \pi^2 k_{\rm B}^2(T_\Omega^2 - T^2)/6h$, for different circuit settings spanning the full range of τ at both $N = 2$ and $N = 3$ (see Supplementary Fig. 3b for $N = 4$, and Supplementary Fig. 4 for a control experiment at $T \simeq 16$ mK). The three thick black continuous lines display the full, temperature-dependent heat Coulomb blockade prediction for two (bottom), three (middle), and four (top) ballistic channels[18] (Methods). Note the small, predicted deviations developing with temperature from the complete heat Coulomb blockade of a single channel ($J_Q^{\rm el}/J_Q^{\rm lim} = N - 1$) that only applies in the limit of low temperatures $T_\Omega, T \ll \hbar/k_{\rm B}RC$. Open and full circles (full diamonds) are data points obtained for $N = 2$ ($N = 3$) ballistic channels, with different settings of the generic channel encoded by different colors. The dashed lines represent linear interpolations between ballistic predictions at N and $N+1$ weighted, respectively, by $1-\tau$ and τ measured for the compared data (same color). For example, the brown dashed line in the top part of Fig. 3a (closest to $J_Q^{\rm el}/J_Q^{\rm lim} \sim 2.5$) is given by $\tau(T_\Omega)$ times the prediction for three ballistic channels (thick black line near $J_Q^{\rm el}/J_Q^{\rm lim} \sim 2$; Methods) plus $1-\tau(T_\Omega)$ times the prediction for four ballistic channels (thick black line near $J_Q^{\rm el}/J_Q^{\rm lim} \sim 3$), with $\tau(T_\Omega)$ the renormalized conductance simultaneously measured during the acquisition of the top brown data points of corresponding T_Ω (in practice a linear interpolation is performed between discrete measurements of $\tau(T_\Omega)$). The difference between dashed lines and data points is particularly significant

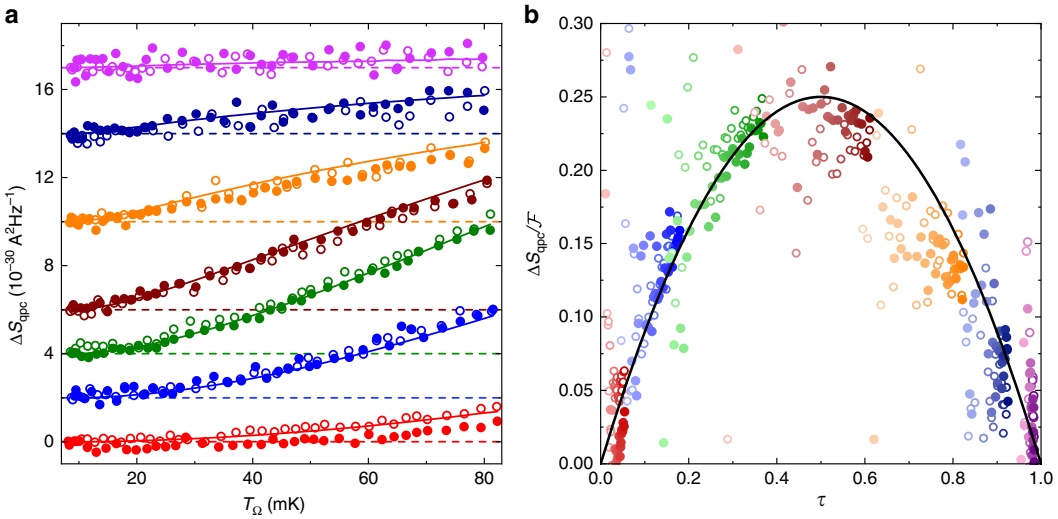

Fig. 2 Thermal shot noise. a Symbols represent the experimental QPC noise at $N = 2$ from which the average thermal noise was removed ($\Delta S_{qpc} = S_{qpc} - 4k_B\bar{T}\tau/R_K$, with $\bar{T} = (T_\Omega + T)/2$). Measurements at different gate voltage tunings of the QPC are shifted vertically, with the applied offsets shown as horizontal dashed lines. Open and full symbols distinguish separate sequences of measurements. Continuous lines display Eq. (1) predictions. **b** The $\tau(1-\tau)$ partition signature is shown as a continuous line versus τ. Symbols represent $\Delta S_{qpc}/\mathcal{F}$, where the τ-independent function $\mathcal{F}(T_\Omega, T)$ is the predicted thermal shot noise's temperature dependence (see text). A lighter (darker) symbol coloring indicates a low (large) $T_\Omega - T$ corresponding to a higher (lower) experimental uncertainty.

at intermediate τ. This shows that the thermal conductance increase does not reduce to a linear, WF-like, function of the electrical conductance. In contrast, quantitative predictions based on the Langevin approach in ref. [18] but including the partition noise from the generic channel (colored continuous lines, Methods) lie close to the data, without any adjustable parameter. At low temperatures $T_\Omega, T \ll \hbar/k_B RC$, the difference between theory (thy) predictions J_Q^{thy} and the WF extension (linear in τ) of heat Coulomb blockade predictions for ballistic channels $(N + \tau - 1) \times J_Q^{lim}$, reads:

$$J_Q^{thy} - (N + \tau - 1) \times J_Q^{lim} \simeq \frac{\tau(1-\tau)}{N+\tau} \times J_Q^{lim}. \qquad (2)$$

Note that $J_Q^{thy} = 0$ for $N = 0$ at low temperatures, whatever the value of τ (see refs. [26–28] for the electrons' state preservation concomitant to the absence of heat transfers). The $\tau(1-\tau)$ numerator attests of the role of electron partition in this additional heat transport mechanism. We also point out that this heat current contribution vanishes at higher temperatures, when Coulomb effects become negligible (Methods). This shows straightforwardly the essential role of Coulomb interaction, which combines with electron partition into a different form of quantum heat transport. Figure 3b provides direct experimental evidences for an underlying partition mechanism (see also Supplementary Fig. 3a, c), by subtracting from the renormalized electronic heat flow at $N = 2$ (symbols in Fig. 3a) the corresponding WF (linear) interpolation (dashed lines in Fig. 3a). Focusing here on the temperature range $T_\Omega \in [17, 65]$ mK where measurements are most accurate (see error bars in Fig. 3a), a convincing agreement is found with $\tau(1-\tau)/(2+\tau)$ plotted as a continuous line versus τ.

Discussion

We have experimentally investigated the heat flow and thermally induced shot noise in an elementary quantum circuit composed of one small metallic node (island) connected by several ballistic channels and by one generic electronic channel of arbitrary electron transmission probability. Applying a temperature bias, without dc voltage across the generic channel, we measured the thermal shot noise[20] and determined the overall electronic heat flow from the island. The former is found in direct quantitative agreement with thermal shot noise predictions computed using the known transmission probability[19]. The latter displays an additional heat flow contribution. The underlying mechanism involves in particular the Coulomb charging energy of the island, which effectively freezes its total charge at low temperatures and thereby induces correlations between the heat carrying electrical current fluctuations propagating along the connected channels[18] (Methods). In a fully ballistic circuit (without thermal shot noise), these correlations amount to the recently observed systematic blockade of a single channel for the flow of heat, independently of the total number of channels[16,18]. Here, with a generic channel, a thermal shot noise is impinging on the island and fractionalized among all the outgoing channels by the frozen island charge imposed by Coulomb interaction[29]. This combination of Coulomb interaction and thermal shot noise underpins the presently observed additional heat transport mechanism (Methods).

Advancing our understanding of the mechanisms of quantum heat transport and establishing the thermal shot noise contribution is essential for exploiting heat and noise to unveil exotic physics[17,30,31], and is bound to play a role in the thermal and signal to noise management of future quantum devices. The present work also demonstrates measurement strategies widening the range of experimental systems eligible for thermal explorations: by exploiting complementary auto- and cross-correlation measurements of the electrical fluctuations, we have shown that the different sources of noise can be accessed separately. We expect that such advanced combinations of fluctuation measurements will play an increasing role in the thermal and noise investigations of quantum circuits.

Methods

Sample. The Al(Ga)As 2DEG has an electron density of 2.5×10^{11} cm^{-2}, a mobility of 10^6 cm^2 V^{-1} s^{-1} and is located 105 nm below the surface. The central island is formed from a metallic layering of nickel (30 nm), gold (120 nm), and germanium (60 nm), which is thermally annealed at 440 °C for 50 s to make an electrical contact with the 2DEG. The two quantum Hall edge channels at filling factor $\nu = 2$

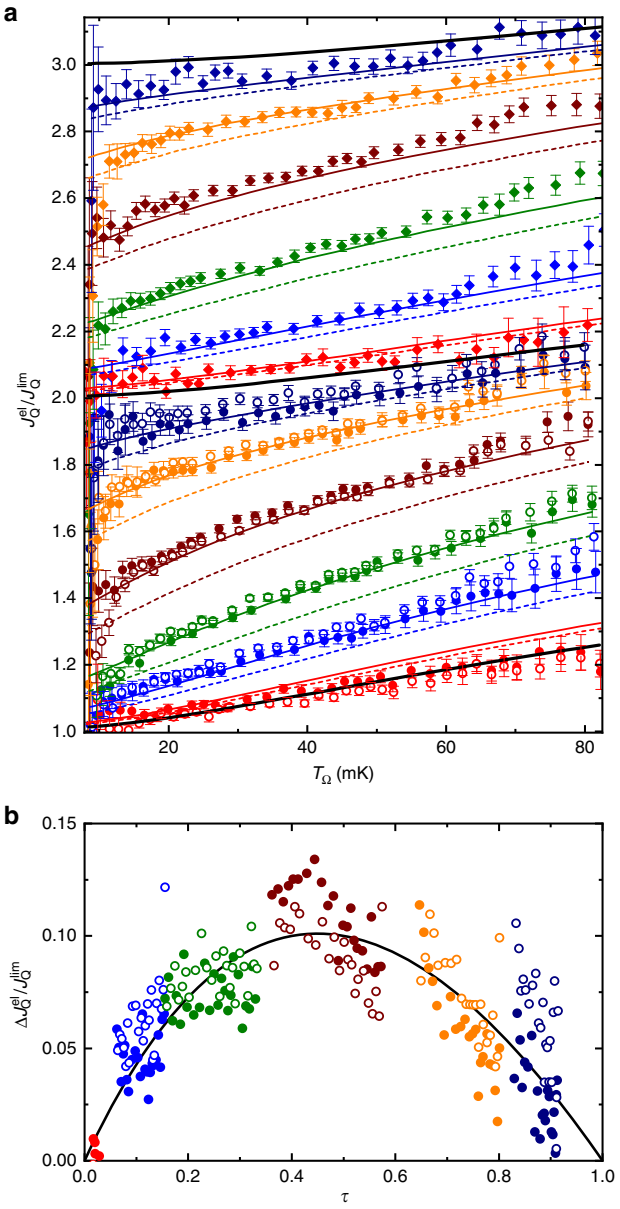

Fig. 3 Electronic heat flow. a Experimental J_Q^{el}/J_Q^{lim} (with $J_Q^{lim} = \pi^2 k_B^2 (T_\Omega^2 - T^2)/6h$) are plotted as symbols versus T_Ω with $N = 2$ (circles) and $N = 3$ (diamonds), for a broad range of QPC tunings (colors). Error bars represent the standard statistical error. Black continuous lines are predictions at $\tau = 0$ for $N = 2$ (bottom), 3 (middle), and 4 (top). Dashed lines are interpolations between ballistic predictions, linear in the measured τ. Continuous lines are theoretical predictions. **b** Symbols represent the difference ΔJ_Q^{el} between experimental J_Q^{el} ($N = 2$, $T_\Omega \in [17, 65]$ mK in panel **a**) and the corresponding interpolation between ballistic predictions, normalized by J_Q^{lim}. The continuous line displays versus τ the low-temperature prediction $\tau(1-\tau)/(N+\tau)$ for $N = 2$.

are found in near perfect contact with the island, with a reflection probability below 6×10^{-3} (see Methods in ref. [14] for a detailed description of the characterization procedure). The short ~1 μm distance between metallic island and QPC combined with the low temperatures ($T_\Omega \lesssim 80$ mK) ascertains that the interaction between co-propagating channels can be safely ignored (see e.g. ref. [32]), as in previous works with the same sample[14,23,33–35]. The self-capacitance of the island $C \simeq 3.1$ fF (corresponding to a charging energy $E_C = e^2/2C \approx k_B \times 0.3$ K) is obtained from standard Coulomb diamond measurements (with all channels connected to the device tuned in the tunnel regime).

Noise measurement setup. The time-dependent current fluctuations $\delta I_1(t)$ and $\delta I_2(t)$ impinging, respectively, on electrodes 1 and 2 are first amplified with a cryogenic amplifier located on the 4K stage of a dilution refrigerator, and with a room temperature amplifier. They are then digitized at 10 Mbit/s and sent to a computer. The Fourier auto- and cross-correlations analysis are performed over a 180 kHz bandwidth centered on 0.855 MHz (the resonant frequency of the LC oscillators shown in Fig. 1a). The amplification gains $G_{1,2}^{amp}$ are separately calibrated from the same standard shot-noise vs voltage bias measurements used to determine the base temperature T (see corresponding section). We find that $G_{1,2}^{amp}$ are stable along each run, but slightly different from cooldown to cooldown. Averaging 862 (2840) shot noise vs voltage bias sweeps, the statistical uncertainty on $G_{1,2}^{amp}$ is below 0.09% (0.04%) for the first (second) experimental run shown here. The cross-correlation gain G_X^{amp} is also impacted by the matching between the two resonators. For a perfect match, $G_X^{amp} = \sqrt{G_1^{amp} G_2^{amp}}$. In general, a correction factor c_{12} needs to be introduced $G_X^{amp} = \sqrt{G_1^{amp} G_2^{amp}} \times c_{12}$. This factor c_{12} is experimentally characterized at $\tau = 0$ ($N_{1,2} \neq 0$) from the robust relation $\Delta S_{11} = \Delta S_{22} = -\Delta S_{12}$, which directly results from the negligible charge accumulation on the island at the measurement frequencies. In practice, we find an essentially perfect resonators' match ($c_{12} \approx 1.000$ and 0.993 for the first and second cooldown, respectively).

Dissipated Joule power. The bulk of the Joule power dissipated within the electronic fluid in the metallic island is given by the expression $P_J \simeq (N_1 V_1^2 + N_2 V_2^2)/2R_K$. We also include the small additional contributions P_J^{ac} due to the extra power dissipated from the small ac voltages $V_{1,2,3}^{ac} \simeq 0.23$ μV_{rms} applied (at different low frequencies) to the three source electrodes (to simultaneously measure with lock-in the conductances across each of the three QPCs), as well as a separately characterized small triboelectric voltage from the pulse tube vibrations specifically developing on the source electrode 1 (feeding the top QPC) $V_1^{tribo} \simeq 0.4$ μV_{rms}:

$$P_J^{ac} = \frac{1}{2R_K(N+\tau)} \times [\{(V_1^{ac})^2 + (V_1^{tribo})^2\} N_1 (N_2 + \tau) + (V_2^{ac})^2 N_2 (N_1 + \tau) + (V_3^{ac})^2 \tau N]. \quad (3)$$

In practice, $P_J^{ac} \in [2, 6]$ aW is below 1% of P_J at $T_\Omega \gtrsim 20$ mK. It corresponds to a temperature increase in the island of ~0.3 mK at zero dc bias (see section Base electron temperature). Note that we avoid possible mismatch from the thermoelectric voltage developing along the measurement lines by applying a current dc bias. It is converted onchip into a voltage exploiting the well-defined quantum Hall resistance R_K/ν connecting current biased electrodes and cold electrical grounds.

Base electron temperature. The base electronic temperature T is extracted from standard shot-noise measurements, applying a dc bias voltage directly to a QPC set to a transmission probability of one half, with the floating island bypassed using side gates (see Methods in ref. [34] for further details).

Due to the small P_J^{ac} (see section Dissipated Joule power), the temperature of the floating island is slightly higher than T even in the absence of a dc voltage. This small temperature increase is obtained by measuring the cross-correlations at zero dc bias $V_1 = V_2 = 0$ (carefully calibrating instrumental offsets just before and after each measurement sequence), from the relation:

$$T_\Omega(V_{1,2} = 0) - T \simeq -\frac{R_K}{2k_B} \frac{N+\tau}{N_1 N_2} S_{12}(V_{1,2} = 0), \quad (4)$$

which straightforwardly relies on the generalized fluctuation-dissipation relation. Although there are deviations from the generalized fluctuation-dissipation relation in the presence of a generic channel, as studied in this work, this approximation is excellent for small $T_\Omega(V_{1,2} = 0) - T \ll T$ such as in the present case. We find $T_\Omega(V_{1,2} = 0) - T \sim 0.3$ mK (always below 0.6 mK), consistent with expectations based on the value of P_J^{ac} given by Eq. (3). This small temperature difference is included in the experimental determination of T_Ω.

Excess electron temperature and shot noise. This section details how are obtained the excess electron temperature, $\Delta T_\Omega = T_\Omega - T_\Omega(V_{1,2} = 0)$, and the resulting excess noise generated across the generic QPC, $S_{qpc}^{exc} = \langle \delta I_{qpc}^2 \rangle - \langle \delta I_{qpc}^2 \rangle (V_{1,2} = 0)$. A schematic representation of the circuit is shown in Fig. 4 with arrows indicating the chirality also corresponding to the convention used for positive currents. The large electrodes labeled E_n ($n \in \{1, 2\}$) include each a measurement electrode M_n and a voltage biased source electrode S_n. The floating central metallic node is labeled Ω.

First, let us separately consider a current fluctuation δI_{qpc} generated across the generic QPC (see Fig. 4), and determine the resulting current fluctuations $\delta I_{M1,M2}^{qpc}$ impinging on the measurement electrodes $M_{1,2}$. As the corresponding charge accumulated in the island relaxes very fast compared to the measurement frequencies ($1/R_K C \sim 10$ GHz $\gg 1$ MHz), the current δI_{qpc} injected in the island is compensated by the outgoing current from the resulting voltage fluctuation δV_Ω of the floating island. This reads $\delta I_{qpc} = (N + \tau)\delta V_\Omega / R_K$ (for a treatment of

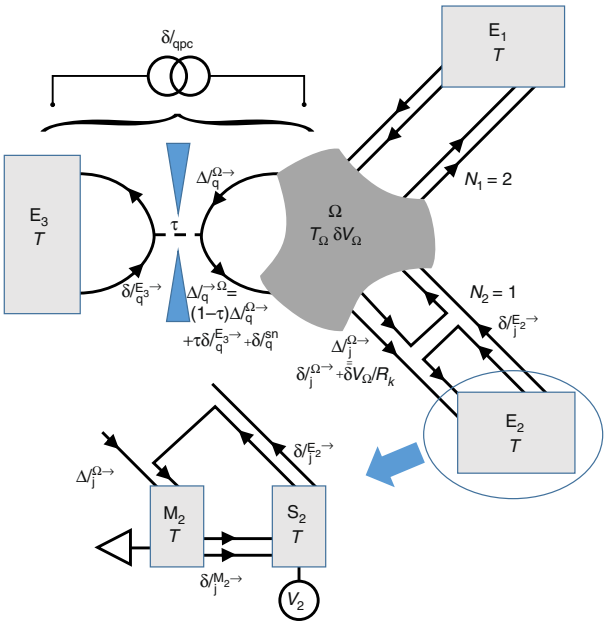

Fig. 4 Noise schematic. Graphical representation of the different current and voltage fluctuations discussed in the text.

charge relaxation at arbitrary frequencies see section Heat Coulomb blockade predictions). Then, $\delta I^{\rm qpc}_{M1(2)} = N_{1(2)}\delta V_\Omega/R_{\rm K} = \delta I_{\rm qpc}N_{1(2)}/(N+\tau)$. Consequently, the QPC noise's contribution to the autocorrelation signal is

$$S^{\rm qpc}_{11(22)} = S_{\rm qpc}N^2_{1(2)}/(N+\tau)^2, \tag{5}$$

and its contribution to the cross-correlation signal is

$$S^{\rm qpc}_{12} = S_{\rm qpc}N_1N_2/(N+\tau)^2. \tag{6}$$

Second, we separately consider a current fluctuation $\delta I_j^{\Omega\to}$ emitted from the island, by the thermal fluctuations of electronic states' population at T_Ω, into a ballistic channel j. From the fast charge relaxation of the island pointed out in the previous paragraph, one obtains $\delta V_\Omega/R_{\rm K} = -\delta I_j^{\Omega\to}/(N+\tau)$. On the one hand, the current fluctuation measured on the electrode M_1 if the channel j propagates toward the electrode M_2 ($j \in M_2$) is then $\delta I^{\Omega\to 2}_{\rm M1} = -N_1/(N+\tau)\delta I^{\Omega\to}_{j\in M2}$. The corresponding autocorrelation signal on M_1, resulting from the thermal current fluctuations emitted toward M_2 (summing all $j \in M_2$) therefore reads:

$$S^{\Omega\to 2}_{11} = \frac{N_1^2}{(N+\tau)^2}\sum_{j=1}^{N_2}\langle(\delta I_j^{\Omega\to})^2\rangle = N_2\times\frac{N_1^2}{(N+\tau)^2}\langle(\delta I^{\Omega\to})^2\rangle, \tag{7}$$

where the unimportant channel index j is omitted in $\langle(\delta I^{\Omega\to})^2\rangle \equiv \langle(\delta I_j^{\Omega\to})^2\rangle$ (independent of j). On the other hand, the current fluctuation measured on the electrode M_1 if the channel j is also connected to the electrode M_1 ($j \in M_1$) includes both the direct term $\delta I^{\Omega\to}_{j\in M1}$ and the smaller δV_Ω contribution: $\delta I^{\Omega\to 1}_{\rm M1} = [1 - N_1/(N+\tau)]\delta I^{\Omega\to}_{j\in M1}$. As a result

$$\begin{aligned} S^{\Omega\to 1}_{11} &= \left(1-\frac{N_1}{N+\tau}\right)^2\sum_{j=1}^{N_1}\langle(\delta I_j^{\Omega\to})^2\rangle \\ &= N_1\times\left(1-\frac{N_1}{N+\tau}\right)^2\langle(\delta I^{\Omega\to})^2\rangle, \end{aligned} \tag{8}$$

and

$$S^{\Omega\to 1}_{12} = -N_1\times\left(1-\frac{N_1}{N+\tau}\right)\frac{N_2}{N+\tau}\langle(\delta I^{\Omega\to})^2\rangle. \tag{9}$$

Summing up the independent contributions from the QPC ($\delta I_{\rm qpc}$) and from all ballistic channels (emitted $\delta I_j^{\Omega\to}$ and absorbed $\delta I_j^{E_n\to}$), one straightforwardly obtains for the autocorrelation signal:

$$\begin{aligned} S_{11(22)} = N_{1(2)}&\left[\left(1-\frac{N_{1(2)}}{N+\tau}\right)^2+\frac{N_1N_2}{(N+\tau)^2}\right]\langle(\delta I^{\Omega\to})^2\rangle \\ &+\frac{N^2_{1(2)}}{(N+\tau)^2}S_{\rm qpc}+\frac{N^2_{1(2)}N}{(N+\tau)^2}\langle(\delta I^{E\to})^2\rangle + S_{\rm offset1(2)}, \end{aligned} \tag{10}$$

with $S_{\rm offset1(2)}$ a noise offset mostly corresponding to the amplification chain, and also including the thermal noise along the $2 - N_{1(2)}$ reflected channels and along the 2 quantum Hall channels propagating from measurement (M) to source (S) contacts (for the experimental bulk filling factor $\nu = 2$; see Fig. 4). Similarly, one gets for the cross-correlation signal:

$$S_{12} = \frac{N_1N_2}{(N+\tau)^2}[-(N+2\tau)\langle(\delta I^{\Omega\to})^2\rangle + S_{\rm qpc} + N\langle(\delta I^{E\to})^2\rangle]. \tag{11}$$

Focusing on the excess signal with respect to $V_{1,2} = 0$, one obtains from Eqs. (10) and (11):

$$S^{\rm exc}_{\rm ball} = \frac{S^{\rm exc}_{11}}{2N_1}+\frac{S^{\rm exc}_{22}}{2N_2}-\frac{S^{\rm exc}_{12}N}{2N_1N_2}, \tag{12}$$

with $S^{\rm exc}_{\rm ball} = \langle(\delta I^{\Omega\to})^2\rangle - \langle(\delta I^{\Omega\to})^2\rangle(V_{1,2}=0)$ the excess noise generated across one ballistic channel. From the Johnson–Nyquist-type relation well established in the ballistic case[5–7,16–18] $\langle(\delta I^{\Omega\to})^2\rangle = 2k_{\rm B}T_\Omega/R_{\rm K}$, the excess island's temperature reads:

$$\Delta T_\Omega = \frac{R_{\rm K}}{2k_{\rm B}}\left(\frac{S^{\rm exc}_{11}}{2N_1}+\frac{S^{\rm exc}_{22}}{2N_2}-\frac{S^{\rm exc}_{12}N}{2N_1N_2}\right). \tag{13}$$

Solving Eqs. (10) and (11) also provides $S^{\rm exc}_{\rm qpc}$:

$$S^{\rm exc}_{\rm qpc} = (N+2\tau)\left(\frac{S^{\rm exc}_{11}}{2N_1}+\frac{S^{\rm exc}_{22}}{2N_2}\right)+S^{\rm exc}_{12}\frac{(N+\tau)^2+\tau^2}{2N_1N_2}. \tag{14}$$

Heat Coulomb blockade predictions. In this section we derive the predictions shown as continuous lines in Fig. 3 and Supplementary Figs. 3 and 4, for the electronic flow of heat $J^{\rm el}_Q$ in the presence of a generic quantum channel. We follow the Langevin approach developed for ballistic systems in ref. [18], and expand it to the case where the current is partially reflected with a probability $1-\tau$ on a QPC inserted along one of the channels (the other channels remaining ballistic, see schematic in Fig. 4). The three main differences with ref. [18] are: (i) the symmetry between channels is broken, (ii) a partition noise emerges at the generic QPC, (iii) the transmission probability τ depends on the temperatures due to dynamical Coulomb blockade.

The heat flow $J^{\rightarrow}_{Qj}$ propagating in one direction ($\rightarrow$) along one electronic channel (j) is obtained from the time-dependent electrical current fluctuations $\Delta I_j^{\rightarrow}$ propagating in the same direction at the considered location[18]:

$$J^{\rightarrow}_{Qj} = \frac{\hbar}{2e^2}\int_{-\infty}^{\infty}{\rm d}\omega\left(\langle(\Delta I_j^{\rightarrow})^2\rangle - \langle(\Delta I_j^{\rightarrow})^2\rangle_{\rm vacuum}\right), \tag{15}$$

with $\langle\rangle_{\rm vacuum}$ referring to the vacuum fluctuations at zero temperature.

If $\Delta I_j^{\rightarrow}$ directly originates from the large, voltage biased electrodes ($S_{1,2,3}$ in $E_{1,2,3}$), then it only includes the emitted thermal current fluctuation $\delta I_j^{E_n\to}$ (see Fig. 4). These thermal fluctuations are assumed uncorrelated ($\langle\delta I_j^{E_n\to}\delta I_k^{E_m\to}\rangle = 0$ for $j \neq k$ even at $m = n$) and of variance given by the usual thermal noise expression at the base temperature T[18]:

$$\langle(\delta I_j^{E_n\to})^2\rangle(\omega) = \frac{\hbar\omega/R_{\rm K}}{-1+\exp[\hbar\omega/k_{\rm B}T]}. \tag{16}$$

Note the factor two difference with the standard low-frequency expression $2k_{\rm B}T/R_{\rm K}$, in which the contribution at positive and negative frequencies are added. Injecting Eq. (16) into Eq. (15), one obtains the usual expression $J^{\rightarrow}_{Qj} = (\pi k_{\rm B}T)^2/6h$.

In contrast to the voltage biased electrodes, the floating metallic node's electrochemical potential exhibits fluctuations δV_Ω (related to charge fluctuations as, e.g., in the voltage probe and dephasing probe models, see ref. [19] and references therein). These result in the emission of identical current fluctuations $\delta V_\Omega/R_{\rm K}$ in all outgoing channels[18,19]. Such current fluctuations add up with the thermal emission $\delta I_j^{\Omega\to}$ of electrons from the central node: $\Delta I_j^{\Omega\to} = \delta I_j^{\Omega\to} + \delta V_\Omega/R_{\rm K}$, with $\langle\delta I_j^{\Omega\to}\delta I_k^{\Omega\to}\rangle = 0$ for $j \neq k$ and a variance $\langle(\delta I_j^{\Omega\to})^2\rangle$ given by the same Eq. (16) but with the island temperature T_Ω instead of T. The integrand in Eq. (15) therefore includes such correlations as $\langle\delta I_j^{\Omega\to}\delta V_\Omega\rangle$. These can be obtained from the connection to the island's charge fluctuations $\delta Q = C\delta V_\Omega$ ($\delta Q = Q - \langle Q\rangle$ with Q the overall charge of the island, and C its self-capacitance), which obey the charge

conservation relation:

$$\begin{aligned} i\omega\delta Q &= \sum_{j=1}^{N+1}(\Delta I_j^{\to\Omega} - \Delta I_j^{\Omega\to}) \\ &= \Delta I_q^{\to\Omega} - \delta I_q^{\Omega\to} - \delta Q/R_K C \\ &\quad + \sum_{j=1}^{N}(\delta I_j^{E\to} - \delta I_j^{\Omega\to}) - N\delta Q/R_K C, \end{aligned} \tag{17}$$

where we separated in the second equality the generic channel labeled with the index q (first line) from the N ballistic channels (second line). In channel q, the incoming current fluctuations toward the island $\Delta I_q^{\to\Omega}$ include three contributions:

$$\Delta I_q^{\to\Omega} = \tau\delta I_q^{E_3\to} + (1-\tau)\left(\delta I_q^{\Omega\to} + \delta Q/R_K C\right) + \delta I_q^{\rm sn}, \tag{18}$$

with the third term corresponding in the Langevin description to an uncorrelated noise source induced by the electrons' partition at the QPC. At equilibrium ($T = T_\Omega$), the Johnson–Nyquist relation at low frequencies imposes $2\langle(\delta I_q^{\rm sn})^2\rangle = \tau(1-\tau)\times 4k_{\rm B}T/R_{\rm K}$ (the factor two is because positive and negative frequencies are included for this comparison). In the non-equilibrium regime ($T \neq T_\Omega$), the information needed on $\delta I_q^{\rm sn}$ for the heat current will be directly obtained from energy flow conservation at the input and output of the QPC (see below). Note that we neglect in Eq. (18) the small time delay associated with the round loop path island-QPC-island (a delay of about 20 ps using a typical velocity of 10^5 m/s), and that the transmission probability τ is taken as a frequency independent value (that depends on T and T_Ω due to dynamical Coulomb blockade, see e.g. ref. [23]). Combining Eqs. (17) and (18) allows us to write δQ as a function of uncorrelated noise sources:

$$\begin{aligned} (i\omega + \tau_\Omega/R_K C)\delta Q &= \tau(\delta I_q^{E_3\to} - \delta I_q^{\Omega\to}) \\ &\quad + \delta I_q^{\rm sn} + \sum_{j=1}^{N}(\delta I_j^{E\to} - \delta I_j^{\Omega\to}), \end{aligned} \tag{19}$$

where we introduced τ_Ω defined as the sum of the transmission probabilities of the channels connected to the island:

$$\tau_\Omega = N + \tau. \tag{20}$$

This straightforwardly makes it possible to formulate the integrands $\langle(\Delta I_q^{\to\Omega})^2\rangle$ and $\langle(\Delta I_q^{\Omega\to})^2\rangle$ as functions of uncorrelated noise sources (independently of δV_Ω). As an illustration, we obtain for the latter:

$$\begin{aligned} \langle(\Delta I_q^{\Omega\to})^2\rangle &= \frac{\langle(\delta I_q^{\rm sn})^2\rangle + (\tau_\Omega - \tau(1-\tau))\langle(\delta I^{E\to})^2\rangle}{\tau_\Omega^2 + (\omega R_K C)^2} \\ &\quad + \left(1 + \frac{\tau_\Omega - \tau(1-\tau) - 2\tau\tau_\Omega}{\tau_\Omega^2 + (\omega R_K C)^2}\right)\langle(\delta I^{\Omega\to})^2\rangle, \end{aligned} \tag{21}$$

where the arbitrary index j is omitted. The only missing ingredient is $\delta I_q^{\rm sn}$. As pointed out above, the required information can be obtained most robustly from global heat conservation at the QPC: $J_{Qq}^{E_3\to} + J_{Qq}^{\Omega\to} = J_{Qq}^{\to E_3} + J_{Qq}^{\to\Omega}$, with $J_{Qq}^{E_3\to}$ the flow of heat from the large electrode E_3 toward the QPC, $J_{Qq}^{\Omega\to}$ the flow of heat from the island toward the QPC, $J_{Qq}^{\to E_3}$ the flow of heat from the QPC toward E_3, and $J_{Qq}^{\to\Omega}$ the flow of heat from the QPC toward the island. Using Eq. (15), this equality reads:

$$\begin{aligned} &\int_{-\infty}^{\infty} {\rm d}\omega\ \langle(\delta I_q^{\rm sn})^2\rangle \times \left[1 + \frac{\tau_\Omega - \tau(1-\tau) - 2\tau\tau_\Omega}{\tau_\Omega^2 + (\omega R_K C)^2}\right] \\ &= \int_{-\infty}^{\infty} {\rm d}\omega\ \tau(1-\tau)\left[1 + \frac{\tau_\Omega - \tau(1-\tau) - 2\tau\tau_\Omega}{\tau_\Omega^2 + (\omega R_K C)^2}\right] \\ &\quad \times \left\{\langle(\delta I_q^{E_3\to})^2\rangle + \langle(\delta I_q^{\Omega\to})^2\rangle\right\}. \end{aligned} \tag{22}$$

Summing up the contributions of all channels and performing the integration in Eq. (15), we obtain for the net heat flow from the metallic island:

$$\begin{aligned} J_Q^{\rm thy} &= \sum_{j=1}^{N+1}\left(J_{Qj}^{\Omega\to} - J_{Qj}^{\to\Omega}\right) \\ &= \tau_\Omega\frac{\pi^2 k_{\rm B}^2}{6h}(T_\Omega^2 - T^2) - \tau_\Omega\frac{h(\tau_\Omega - \tau(1-\tau))}{(2\pi R_K C)^2} \\ &\quad \times \left[\Im\left(\frac{h\tau_\Omega/R_K C}{2\pi k_{\rm B}T_\Omega}\right) - \Im\left(\frac{h\tau_\Omega/R_K C}{2\pi k_{\rm B}T}\right)\right], \end{aligned} \tag{23}$$

with the function $\Im$ given by

$$\Im(x) = \frac{1}{2}\left[\ln\left(\frac{\rm x}{2\pi}\right) - \frac{\pi}{\rm x} - \psi\left(\frac{\rm x}{2\pi}\right)\right], \tag{24}$$

with $\psi(z)$ the digamma function. Equation (23) was used to calculate the predictions shown as continuous lines in Fig. 3a, Supplementary Fig. 3b and Supplementary Fig. 4.

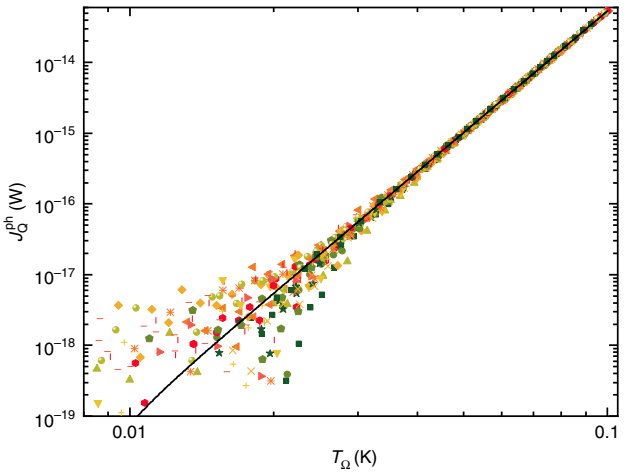

Fig. 5 Electron–phonon heat transfers. Symbols represent the flow of heat $J_Q^{\rm ph}$ from the electrons within the metallic island to the phonons at $T \simeq 8$ mK. Different symbols represent data points from different configurations $N \in \{2,3,4\}$ and $\tau \in \{0,1\}$, including measurements performed in two different cooldowns. All the data collapse on $J_Q^{\rm ph} = 2.752\times 10^{-8}(T_\Omega^{5.709} - T^{5.709})$ W (continuous line).

At $\tau = 0$ or 1, Eq. (23) reduces to the expression derived for a ballistic system[18] (see Methods in ref. [16] for a similar formulation). At high temperatures, Eq. (23) reduces to the non-interacting result matching the widespread Wiedemann–Franz law (without additional contribution from the partition noise):

$$\begin{aligned} J_Q^{\rm thy}\left(T, T_\Omega \gg \frac{h\tau_\Omega}{k_{\rm B}R_K C}\right) &\simeq \tau_\Omega\frac{\pi^2 k_{\rm B}^2}{6h}(T_\Omega^2 - T^2) \\ &\simeq \tau_\Omega J_Q^{\rm lim}. \end{aligned} \tag{25}$$

At low temperatures, Eq. (23) simplifies into:

$$\begin{aligned} J_Q^{\rm thy}\left(T, T_\Omega \ll \frac{h\tau_\Omega}{k_{\rm B}R_K C}\right) &\simeq \left(\tau_\Omega - 1 + \frac{\tau(1-\tau)}{\tau_\Omega}\right)\frac{\pi^2 k_{\rm B}^2}{6h}(T_\Omega^2 - T^2) \\ &\simeq \left(\tau_\Omega - 1 + \frac{\tau(1-\tau)}{\tau_\Omega}\right)J_Q^{\rm lim}. \end{aligned} \tag{26}$$

In this case, in addition to the systematic blockade of one ballistic channel (-1) with respect to the non-interacting case (τ_Ω), we find an additional contribution to the flow of heat whose partition character is signaled by the characteristic $\tau(1-\tau)$ dependence.

Electron–phonon heat transfers. The Fig. 5 displays the amount of heat transferred from electrons in the metallic island to cold phonons at base temperature $T \simeq 8$ mK. It is obtained by subtracting from the injected Joule power P_J the known electronic heat flow $J_Q^{\rm el}$ when the circuit is tuned in the ballistic regime (for the subtracted expression of $J_Q^{\rm el}$, see Eq. (23) with $\tau \in \{0,1\}$ or refs. [16,18]). The data from all ballistic configurations ($N \in \{2,3,4\}$, $\tau \in \{0,1\}$) collapse on the same curve, fitted by $J_Q^{\rm ph} = \Sigma(T_\Omega^\alpha - T^\alpha)$ with $\Sigma = 2.752\times 10^{-8}$ W K$^{-\alpha}$ and $\alpha = 5.709$. We checked that this power law also precisely accounts for $J_Q^{\rm ph}$ at the larger temperature $T \simeq 16$ mK (data not shown).

Data availability

The data that support the findings of this study are available from the corresponding author upon reasonable request.

Received: 4 July 2019; Accepted: 8 November 2019;
Published online: 10 December 2019

References

1. Schwab, K., Henriksen, E., Worlock, J. & Roukes, M. Measurement of the quantum of thermal conductance. *Nature* **404**, 974–977 (2000).

2. Giazotto, F. & Martínez-Pérez, M. J. The Josephson heat interferometer. *Nature* **492**, 401–405 (2012).
3. Ronzani, A. et al. Tunable photonic heat transport in a quantum heat valve. *Nat. Phys.* **14**, 991–995 (2018).
4. Timofeev, A. V., Helle, M., Meschke, M., Möttönen, M. & Pekola, J. P. Electronic refrigeration at the quantum limit. *Phys. Rev. Lett.* **102**, 200801 (2009).
5. Jezouin, S. et al. Quantum limit of heat flow across a single electronic channel. *Science* **342**, 601–604 (2013).
6. Srivastav, S. et al. Universal quantized thermal conductance in graphene. *Sci. Adv.* **5**, eaaw5798 (2019).
7. Banerjee, M. et al. Observed quantization of anyonic heat flow. *Nature* **545**, 75–79 (2017).
8. Partanen, M. et al. Quantum-limited heat conduction over macroscopic distances. *Nat. Phys.* **12**, 460 (2016).
9. Mosso, N. et al. Heat transport through atomic contacts. *Nat. Nanotechnol.* **12**, 430–433 (2017).
10. Cui, L. et al. Quantized thermal transport in single-atom junctions. *Science* **355**, 1192–1195 (2017).
11. Grabert, H. & Devoret, M. (eds) *Single Charge Tunneling* (Plenum, New York, 1992).
12. Likharev, K. Single-electron devices and their applications. *Proc. IEEE* **87**, 606–632 (1999).
13. Parmentier, F. D. et al. Strong back-action of a linear circuit on a single electronic quantum channel. *Nat. Phys.* **7**, 935–938 (2011).
14. Jezouin, S. et al. Controlling charge quantization with quantum fluctuations. *Nature* **536**, 58–62 (2016).
15. Dutta, B. et al. Thermal conductance of a single-electron transistor. *Phys. Rev. Lett.* **119**, 077701 (2017).
16. Sivre, E. et al. Heat Coulomb blockade of one ballistic channel. *Nat. Phys.* **14**, 145–148 (2018).
17. Banerjee, M. et al. Observation of half-integer thermal Hall conductance. *Nature* **559**, 205–210 (2018).
18. Slobodeniuk, A., Levkivskyi, I. & Sukhorukov, E. Equilibration of quantum Hall edge states by an Ohmic contact. *Phys. Rev. B* **88**, 165307 (2013).
19. Blanter, Y. & Büttiker, M. Shot noise in mesoscopic conductors. *Phys. Rep.* **336**, 1–166 (2000).
20. Lumbroso, O., Simine, L., Nitzan, A., Segal, D. & Tal, O. Electronic noise due to temperature differences in atomic-scale junctions. *Nature* **562**, 240–244 (2018).
21. Martin, T. & Landauer, R. Wave-packet approach to noise in multichannel mesoscopic systems. *Phys. Rev. B* **45**, 1742–1755 (1992).
22. Jezouin, S. et al. Tomonaga-Luttinger physics in electronic quantum circuits. *Nat. Commun.* **4**, 1802 (2013).
23. Anthore, A. et al. Circuit quantum simulation of a Tomonaga-Luttinger liquid with an impurity. *Phys. Rev. X* **8**, 031075 (2018).
24. Blanter, Y. M. & Sukhorukov, E. V. Semiclassical theory of conductance and noise in open chaotic cavities. *Phys. Rev. Lett.* **84**, 1280–1283 (2000).
25. Reydellet, L.-H., Roche, P., Glattli, D. C., Etienne, B. & Jin, Y. Quantum partition noise of photon-created electron-hole pairs. *Phys. Rev. Lett.* **90**, 176803 (2003).
26. Duprez, H. et al. Transmitting the quantum state of electrons across a metallic island with Coulomb interaction. Preprint at https://arXiv.org/abs/1902.07569 (2019).
27. Idrisov, E., Levkivskyi, I. & Sukhorukov, E. Dephasing in a Mach-Zehnder Interferometer by an Ohmic Contact. *Phys. Rev. Lett.* **121**, 026802 (2018).
28. Clerk, A., Brouwer, P. & Ambegaokar, V. Interaction-induced restoration of phase coherence. *Phys. Rev. Lett.* **87**, 186801 (2001).
29. Idrisov, E., Levkivskyi, I. & Sukhorukov, E. Quantum ammeter. Preprint at https://arXiv.org/abs/1906.10902 (2019).
30. Altimiras, C. et al. Chargeless heat transport in the fractional quantum hall regime. *Phys. Rev. Lett.* **109**, 026803 (2012).
31. Inoue, H. et al. Proliferation of neutral modes in fractional quantum Hall states. *Nat. Commun.* **5**, 4067 (2014).
32. leSueur, H. et al. Energy relaxation in the integer quantum Hall regime. *Phys. Rev. Lett.* **105**, 056803 (2010).
33. Iftikhar, Z. et al. Two-channel Kondo effect and renormalization flow with macroscopic quantum charge states. *Nature* **526**, 233–236 (2015).
34. Iftikhar, Z. et al. Primary thermometry triad at 6 mK in mesoscopic circuits. *Nat. Commun.* **7**, 12908 (2016).
35. Iftikhar, Z. et al. Tunable quantum criticality and superballistic transport in a 'charge' Kondo circuit. *Science* **360**, 1315–1320 (2018).

Acknowledgements

This work was supported by the French RENATECH network, the national French program Investissements d'Avenir (Labex NanoSaclay, ANR-10-LABX-0035) and the French National Research Agency (projects QuTherm, ANR-16-CE30-0010, and SIM-CIRCUIT, ANR-18-CE47-0014-01). We thank Y. Jin for providing the cryogenic HEMTs used for the noise measurements, and E. Sukhorukov for fruitful discussions.

Author contributions

E.S. and H.D. performed the experiment with inputs from A. Aassime, A. Anthore, and F.P.; A. Anthore, E.S., F.P. and H.D. analyzed the data and expanded the theory with help from A. Aassime; F.D.P. fabricated the sample using developments from A. Anthore; A.C., A.O., and U.G. grew the 2DEG; F.P. led the project and wrote the manuscript with contributions from A. Aassime, A. Anthore, E.S., H.D., and U.G.

Competing interests

The authors declare no competing interests.

Additional information

Supplementary information is available for this paper at https://doi.org/10.1038/s41467-019-13566-8.

Correspondence and requests for materials should be addressed to F.P.

Peer review information *Nature Communications* thanks Tomonori Arakawa, Liliana Arrachea and Elke Scheer for their contribution to the peer review of this work.

Reprints and permission information is available at http://www.nature.com/reprints

Publisher's note Springer Nature remains neutral with regard to jurisdictional claims in published maps and institutional affiliations.